**Electrochemical Properties of Two-Dimensional (2D) MXenes
and Their Hybrid/Hetero-Structures**

by

Armin VahidMohammadi

A dissertation submitted to the Graduate Faculty of
Auburn University
in partial fulfillment of the
requirements for the Degree of
Doctor of Philosophy

Auburn, Alabama
August 3, 2019

Keywords: Two-Dimensional Transition Metal Carbides, MXenes, Heterostructures,
Electrochemistry, Batteries, Supercapacitors

Approved by

Majid Beidaghi, Chair, Assistant Professor of Materials Engineering
Jeffrey Fergus, Professor of Materials Engineering
Dong-Joo Kim, Professor of Materials Engineering
Minseo Park, Professor of Physics
Tae-Sik Oh, Assistant Professor of Chemical Engineering

Dedications

To my father Bahram
  and my mother Nasim
    for all the sacrifices you made for me in your life
      and for all your love and unconditional support

To Aida
  for your encouragement in my work

To Aidin
  for your inspiration in my research and computer graphics

To Mehrnaz
  for all your love, motivation, and understanding during all these years

Abstract

Two-dimensional (2D) transition metal carbides and nitrides (MXenes) have gained huge

interest over the past few years for electrochemical energy storage applications because of their

exceptional physical and (electro)chemical properties. Since their discovery in 2011, many

researchers around the world have investigated the electrochemical properties of MXenes in

various energy storage systems. Despite the substantial work done on these materials, the work on

MXenes is still in its infancy. For instance, electrochemical investigations of MXenes have been

largely limited to aqueous supercapacitors and monovalent ion batteries (lithium or sodium ion

batteries), and their performances in multivalent battery systems have been barely studied.

Batteries based on multivalent ion chemistry, such as aluminum batteries, are emerging as potential

alternative technologies to current Li-ion batteries because of their higher safety and (theoretically

achievable) energy densities. Lack of high-performance cathode materials for these systems,

however, is the main challenge facing their development. The high potential of MXenes as

electrode materials for multivalent ion batteries have been suggested by theoretical studies.

Therefore, the experimental investigation of MXenes in these systems is important and needs to

be carried out. On the other hand, although, to date around 30 different MXene materials have

been experimentally synthesized, most of the researches have only focused on one MXene

composition, $Ti_3C_2T_x$. The lack of systematic and controlled methods for the synthesis of many

MXenes in their 2D (delaminated) form, as well as their chemical instabilities, are some of the

underlying reasons that have hampered their applications, particularly in aqueous systems where

they are more prone to oxidation and degradation. Moreover, establishing practical forms of 2D MXenes can enable fabrication of 2D vertical heterostructures based on different compositions of them with new and improved properties; an emerging field that has received enormous attention among researchers. My Ph.D. research aimed to shed light on some of these challenges (to the extent possible) and lay down a scientific understanding about them, provide solutions, and finally demonstrate the high-performance of MXenes and their hybrid/hetero-layered structures in different electrochemical energy storage systems. The outcomes of my Ph.D. research will directly impact the ongoing research on 2D MXenes in complex electrochemical systems and fabrication of advanced electrode materials based on them.

Acknowledgments

friendship and support. I am thankful to Dr. Nuala M. Caffery at Trinity College Dublin in Ireland for her help with DFT calculations in my research. I am grateful to Dr. Zhe Cheng at Florida International University for all the laboratory skills he taught me when I moved to the US. I should also thank Dr. Babak Anasori at Drexel University for his efforts in preparation of the first MXene book and our valuable discussions during the MRS meetings.

I am thankful to my dear friends, Dr. Sadegh Behdad, Dr. Ali Karbasi, and Dr. Ali Hadjikhani for all their care and support in the past six years. I am grateful for all the valuable discussions I had with them at different stages of my Ph.D.

I am also grateful to all the people I have not named here; for our conversations, their help, and all the fun during my Ph.D. years.

Lastly, I should thank Mehrnaz for her love, support, and understanding during all these years. I am very lucky that I have her by my side. She has been my friend and my research collaborator. On the research side, she led the MXene nanopore and DNA sensing projects, and helped me with STEM images. Also, as a life partner, she has always been there for me. Her support has been unconditional, inspired me, and encouraged me to do what I am doing, and to reach for the stars.

Table of Contents

List of Tables

List of Figures

List of Abbreviations

LiBs	Lithium ion Batteries
NaBs	Sodium ion Batteries
AlBs	Aluminum Batteries
PANI	Polyaniline
PPy	Polypyrrole
2D	Two-Dimensional
TMDs	Transition Metal Dichalcogenides
TMOs	Transition Metal Oxides
CV	Cyclic Voltammetry
EIS	Electrochemical Impedance Spectroscopy
CE	Counter Electrode
WE	Working Electrode
XPS	X-ray Photoelectron Spectroscopy
SEM	Scanning Electron Microscopy
EDS	Energy Dispersive Spectroscopy
TEM	Transmission Electron Microscopy
STEM	Scanning Transmission Electron Microscopy
XRD	X-ray Diffraction
FTIR	Fourier-Transform Infrared Spectroscopy

ML   Multilayer

FL   Few Layer

TBAOH   Tetrabutylammonium Hydroxide

HF   Hydrofluoric Acid

HCl   Hydrochloric Acid

Chapter 1

Introduction

Over the past decade, synthesis of two-dimensional (2D) materials through intercalation and delamination of three-dimensional (3D) materials with layered structures has received significant attention because of its scalability and relatively easy processing method, as well as abundance of naturally available precursor layered materials.[1,2] Separation and isolation of atomically thin layers of these materials[3] was a crucial step toward fundamental understanding of the dimensional-dependent properties of these materials, as well as designing structures based on them that deliver improved specific properties in a variety of applications. It was not until 2004 and isolation of single-layer graphene sheets by K. S. Novoselov[4] that scientists realized this important concept. The proof that such free-standing 2D atomic crystals can exist and pose high crystal quality prepared the ground for extensive research on 2D materials. It is important that in the beginning of this dissertaion, the term "2D materials" be clarified as atomically thin single-layer or few-layers flakes with thicknesses ranging from 1 to less than 5 nm.[3,5–7] In the quest to find and study properites of the 2D materials, delamination (separation of 3D layered structures into single or few-layer flakes) of different layered materials such as graphite, transition metal dichalcogenides, and hexagonal boron nitride (h-BN) have been widely shown over the past two decades.[3,6,8]

Arguably, 2D transition metal carbides and nitrides, collectively called MXenes, are among the most recent and notable members of the family of 2D materials.[7,9,10] Discovered in 2011,[10] MXenes were the first examples of 2D materials produced by selective extraction of strongly bonded layered crystal structures. The name "MXene" was selected by removing the "A" from the name of their parent MAX phases, a large group of hexagonal layered structure ternary carbides and nitrides, to indicate the selective removal of A layers from MAX phases, and also the "ene" was added to the end of the "MX" to resemble the "graphene" name and indicates the 2D nature of these materials.[9] Synthesis of MXenes by selective etching and exfoliation distinguishes these materials from other 2D materials such as graphene, MoS_2, and h-BN, where their bulk counterparts are weakly bonded van der Walls layered structures and can be easily exfoliated to 2D flakes through sonication in liquids or by mechanical separation methods.[11] However, as I will discuss throughout my dissertation, such methods cannot be directly used to produce MXenes because the nature of atomic bonds between M and A layers in their parent materials, MAX phases, is of strong metallic bonding and not the van der Waals attractions.[10,12] Therefore, so far it has not been possible to separate MX and A layers through mechanical work or exfoliation.[13] Since the bonding between M and X layers is of strong covalent/ionic nature, however, the A layers can be selectively removed from the MAX phase structure producing weakly bonded stacks of MX layers, that can later be separated with intercalation or sonication.[7] Over the past few years MXenes have received much attention in the literature due to their exceptional physical and (electro)chemical properties. High conductivity of MXenes (arising from their metal-carbide core layers), their compositional diversity, their functional surfaces, and the possibility to manipulate and modify their surface chemistry have rendered these materials as promising candidates for variety of applications including energy storage,[14–23] electromagnetic interference shielding,[24,25] water

desalination,[26,27] gas sensing,[28,29] wireless communications,[30] fabrication of organic hybrid structures,[31,32] gas separation,[33] and disease therapy[34–38] to name a few. In particular, MXenes have largely been recognized as potential energy materials for a wide variety of electrochemical energy storage and conversion applications.

The focus of my Ph.D. research over the past four years was on electrochemical characterization of advanced electrode architectures based on 2D MXenes and their hybrid and 2D heterostructures, both in aqueous supercapacitors and organic multivalent aluminum batteries. The first step toward fabrication of MXene electrodes was the synthesis and delamination of these materials. Therefore, a significant portion of my time was spent on optimizing the synthesis conditions for both MAX phases and MXenes based on the different reports in the literature. After designing the MXene materials and electrodes, I was facing some key issues such as chemical instability of some MXenes (i.e. V_2CT_x and Ti_2CT_x) after their delmination into single/few layer flakes. Eventually, the investigations and studies performed over different steps of my research resulted in new findings on how to control those delminated MXenes in their dry form and suppress their rapid oxidation in the ambient atmosphere as well as during electrochemical measurements. As one of the main goals of my research, controlling MXene compositions other than $Ti_3C_2T_x$, enabled us to desing stable electrodes based on them and test them in aqueous and non-aqueous systems. The different synthesized MXenes were tested in organic Aluminum battery (AlB) multivalent chemistry. One of the main challenges of carrying out the AlB experiments was the preperation of ultra-high purity ionic-liquid based electrolyte. In addition, this electrolyte which is commonly used in AlBs, and as I will discuss in chapter 6, is very corrosive and therefore, I had to prepare handmade Teflon or pouch cells to carry out the experiments. Throughout different

tasks of my research, we could establish methods to perform standard AlB tests and carefully study MXenes' performance in this new and emerging battery chemistry.

In the next chapters of my dissertation, I will initially (in chapter 2) provide a background and literature review about 2D MXenes and their applications in electrochemical energy storage systems to discuss the current and important status of the research on MXenes for energy storage applications. Then, in chapter 3, I will discuss the methods and experimental conditions for the synthesis of MAX phases and MXenes used in different steps of my Ph.D. Research. In Chapter 4, as the first steps toward preparation of MXene hybrid structures, my work on the synthesis of MXene (with $Ti_3C_2T_x$ as the example) and polyaniline hybrid structures is presented that provides information and scientific insights about the rational design of MXene-polymer hybrids for supercapacitor applications. Following up this section, Chapter 5 discusses my work on self-assembly of MXenes multilayers and 2D heterostructures and detailed electrochemical characterization of the fabricated pillared or superlattice structures. Electrochemical characterization and performances of MXenes in organic AlBs are discussed in chapter 6 where different electrode structures developed throughout different parts of my research have been examined in the emerging multivalent aluminum chemistry. In the end, I will discuss and suggest some of the future works that can be carried out to improve the results and findings presented here as part of my dissertation, shall other researchers wish to work and build upon on them.

Chapter 2

Background and Literature Survey

This chapter provides background information about MAX phases and MXenes, their structure, synthesis methods, and applications with focus on their performances in electrochemical energy storage devices. The last portion of this chapter will cover literature information on aluminum batteries with organic electrolytes. As it will be explained in detail and at different parts of this dissertation, the synthesis of MXenes invloves a selective etching process in which 2D sheets of metal-carbides/nitrides are produced from a group of layered ternary carbide and nitrides called MAX phases. Therefore, it is crucial to initially introduce the MAX phases in this chapter and explain the synthesis steps of MXenes from them.

2.1. MAX Phases and Synthesis of 2D MXenes From Them

2D MXenes are produced by selective extraction and exfoliation of a large group of layered hexagonal strcuture (space group $P6_3/mmc$) ternary transition metal carbides and nitrides, called MAX Phases.[9] MAX phases have a general formula of $M_{n+1}AX_n$, where M is an early transition metal such as Ti, V, Nb, Cr, Mo, etc. (red elements in **Figure 2.1**), A is usually a group 13 or 14 element such as Al, In, Si, etc. (blue elements in **Figure 2.1**), and X represents carbon, nitrogen, or both. In this formula, n can be 1, 2 or 3.[9,12] These materials are machinable, conductive, highly damage tolerant, and have high oxidation and thermal shock resistance.[9,12]

Figure 2.1. Table of elements. Different elements so far reported in the structure of MAX phases have been highlighted, including different transition metals (in red color), group 13 and 14 (in blue color), and carbon and/or nitrogen (in black color).

To date, more than 70 different compositions[13] of MAX phases have been successfully synthesized. Based on the "n" value in the formula of the MAX phases, these materials are categorized under three different structures: M_2AX (i.e. Ti_2AlC), M_3AX_2 (i.e. Ti_3AlC_2), and M_4AX_3 (i.e. Ta_4AlC_3). These structures are schematically shown in **Figure 2.2**.

As it can be seen in this figure, the crystal structure of MAX phases can be explained as individual M-X layers (carbon/nitrogen (X) atoms are placed in octahedral sites, sandwiched between layers of transition metals) that are separated by A layer atoms.[1,7] The M-X bonds in MAX phases are of covalent-ionic nature, and the M-A bonds are metallic.[7,9] The metallic bonding present between M and A layers in MAX phases, differentiates these materials from van der Waals layered compounds, where different layers are held together by weak van der Waals bonds.[11] This strong bonding between MX and A layers in MAX phases makes their mechanical exfoliation extremely difficult and practically impossible.[1,7,10] It is noteworthy to mention that the M layer of MAX phases can contain two transition metals in a solid solution (random, i.e. $(Ti,V)_3AlC_2$) or ordered phase (i.e., $(Mo_2Ti)AlC_2$ which is an ordered double transition metals MAX Phase).[39]

The presence of solid solution or ordered Structures in M layer of MAX phases provides versatile opportunities in material design. For example, in the ordered $(Mo_2Ti)AlC_2$ phase, the M-X layers contain Ti layers that are sandwiched between two Mo layers. The combination of Mo and Ti transition metals, makes this material promising for applications where for example, high conductivity of Ti atoms at the core and high redox-activity of Mo atoms at the surface are required.[39] This is in contrast to the solid solution phase of $(Ti,V)_3AlC_2$ where Ti and V atoms are randomly distributed. Also, as mentioned earlier, the "X" sites of MAX phases can be occupied by C, N or both resulting in a ternary carbonitride structures such as $Ti_3Al(CN)$.
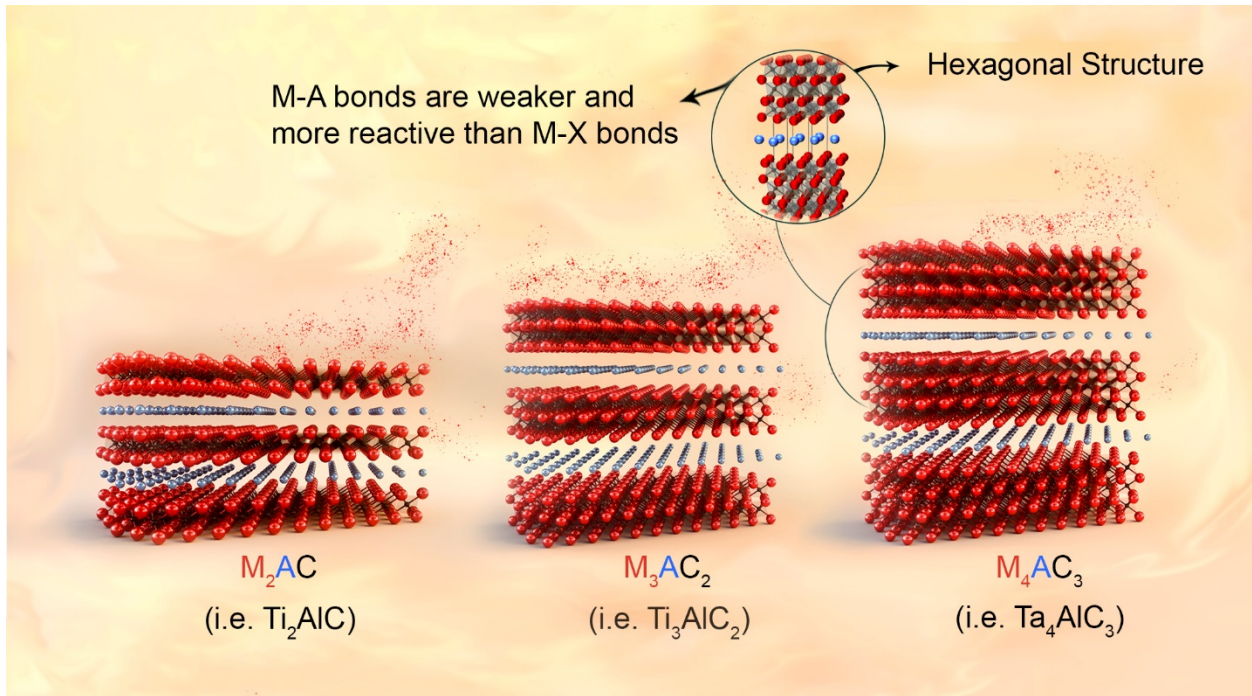
Figure 2.2. Different structures of MAX phases, from left to right: 211, where two layers of transition metal and a layer of carbon are separated by A-layer elements, 312 where the M-X layers consist of three layers of transition metal and two layers of carbon, and 413, where M-X layers consist of four layers of transition metal and three layers of carbon in between them.

In MAX phases, since M-A bonds are weaker than M-X bonds, and also in most MAX phases, A layer elements are chemically more reactive than the M-X layers, A layers can be selectively removed from MAX phase structures.[1,9] In fact, this difference in the reactivity of A layers compared to M-X layers is the basis for selective etching of the A layers in dilute fluoride containing acidic solutions, and synthesis of MXenes.[1,7,13] This slective process used in the synthesis of MXenes, as indicated in the previous chapter, was kept in mind in selection of the "MXene" name, which is derived from MAX phases ("A" is removed from "MAX" to indicate selective removal of A atoms from MAX phases) and by adding "ene" to bring the dimensionality analogy of these materials to graphene.[9,10] **Figure 2.3** schematically shows this selective etching process where A layers are removed, and stacks of weakly bonded $M_{n+1}X_n$ are left. It is important to note that, since the etching process is done in fluoride containing aqueous acidic solutions, upon etching and removal of the A layer elements, the outer transition metals in the M-X stacks are usually functionalized with -O, -OH, and -F groups.[7] For the sake of brevity, in literature, these functional groups are shown with "T_x" in the general formula of MXenes ($M_{n+1}X_nT_x$), where T_x represents a combination of all these surface terminations present at the surface of outer layer transition metals.

The MXene discovery started with the synthesis of $Ti_3C_2T_x$, and by selective exfoliation of Ti_3AlC_2 MAX phase in diluted hydrofluoric acid (HF).[10] Since then, HF has been known as the most common etchant for the synthesis of MXenes from MAX phases containing Al atoms in their "A" layers. Considering HF as the etchant, the reactions involved in the chemical etching of MAX phases can be assumed as follow:[9]
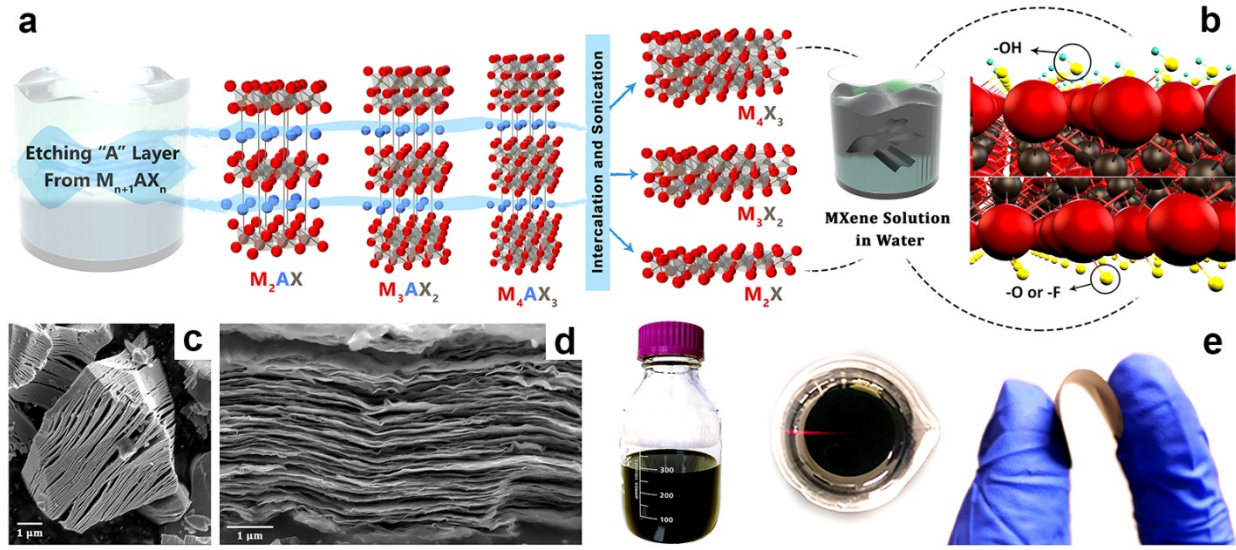
Figure 2.3. Schematic of the selective etching process of MXenes. a) The selective etching process of MXenes is schematically shown where, the A layer of different MAX phase structures shown in **Figure 2.2** can be selectively removed in fluoride containing acids, resulting in exfoliation of 2D M-X layers. b) The presence of surface functional groups on the outer transition metal layers are shown in this image. c) The produced MXenes can be delaminated and form stable solutions, which can be filtered to form freestanding flexible films (called MXene paper). d) The cross-sectional scanning electron microscopy (SEM) of MXene paper and e) SEM image of MXene particle are shown.

$$M_{n+1}AlX_n + 3HF = M_{n+1}X_n + AlF_3 + 1.5H_2 \quad (1)$$

$$M_{n+1}X_n + 2H_2O = M_{n+1}X_n(OH)_2 + H_2 \quad (2)$$

$$M_{n+1}X_n + 2HF = M_{n+1}X_nF_2 + H_2 \quad (3)$$
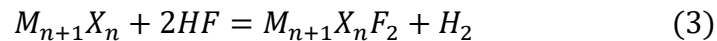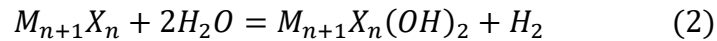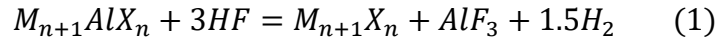
Equations (1) is the essential reaction for etching of MAX phases in HF solutions. As the result of etching reaction of the MAX phase powders with HF, hydrogen gas (H_2) will be released, which is evident in experimental work as after addition of MAX phase powders to the HF solutions, usually bubbles form that indicates a severe reaction and release of H_2 gas.[10] In this process, it is suggested that equations (2) and (3) occur simultaneously and after equation (1).[9,10] This selective etching process in aqueous solutions results in functionalized MXene surfaces, where different functional groups such as O, OH, F, and Cl are present based on the type of the

etchant used (shown in Figure **2.3.c**).[7,40] After etching process, the powders are washed in several steps with DI water to remove the acid after which the product is usually a multilayered MXene particle (shown in **Figure 2.3.e**). These multilayered powders can be delaminated into single-layer flakes through subsequent intercalation and sonication steps, as it will be discussed later in this chapter, to produce delaminated MXene solutions and freestanding films and MXene papers (shown in **Figure 2.3.d and e**). The final 2D structure and some important properties of different MXenes with different number of atomic layers in their structure are shown in **Figure 2.4**.
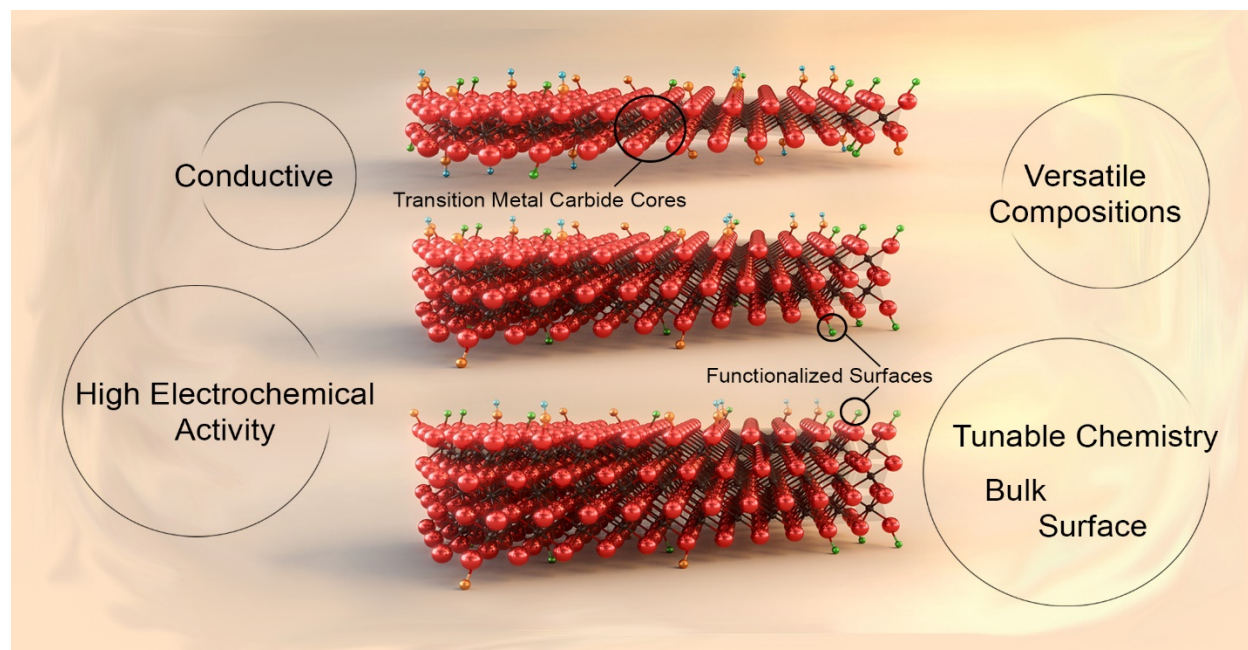
Figure 2.4. Schematic of final 2D structures for single-layer MXenes with different number of atomic layers in their structures. Some of the most important properties of MXenes that have made these materials one of the hottest topic of research in recent years are marked and shown on the schematic.

If etching of MAX phases is complete and successful, all the XRD peaks corresponding to MAX phase structure should typically disappear and only the peaks corresponding to M-X basal planes (000l) broaden and shift to lower angles.[7] This shift and broadening is mainly observed with a large downshift for the peak corresponding to (0002) basal planes.[7] **Figure 2.5** shows this change in the XRD patterns of four different MAX phases after etching. For many MXene compositions, however, the current developed etching processes, cannot result in complete removal of A layers, and therefore, the XRD patterns of their multilayered particles still contain some of the main and strong MAX phase basal plane peaks. Despite this partial etching and remaining MAX phase impurities, the etched particles can be delaminated and separated from the unreacted MAX phase particles through subsequent intercalation and centrifugation steps which will be explained further in this chapter. As explained, the etching process (with HF) usually results in stacks of M-X layers that are weakly bonded together due to the presence of surface termination groups.[7,10] Sonication of these MXene particles in water results in the formation of thin and electron-transparent 2D $M_{n+1}X_n$ layers, but with a very low production yield.[10]

Some of the notable MXene compositions that are synthesized to date are Ti_2CT_x, V_2CT_x, Nb_2CT_x, Mo_2CT_x, $(Ti,V)_2CT_x$, $(Ti,Nb)_2CT_x$, $Ti_3C_2T_x$, $(Ti,V)_3C_2T_x$, $(Cr,V)_3C_2T_x$, $Ti_3(C,N)_2T_x$, $Zr_3C_2T_x$, $(Mo_2Ti)C_2T_x$, $(Cr_2Ti)C_2T_x$, $Ti_4N_3T_x$, $Nb_4C_3T_x$, $Ta_4C_3T_x$, $(Ti,Nb)_4C_3T_x$, $(Nb,Zr)_4C_3T_x$, and $(Mo_2Ti_2)C_3T_x$.[13]
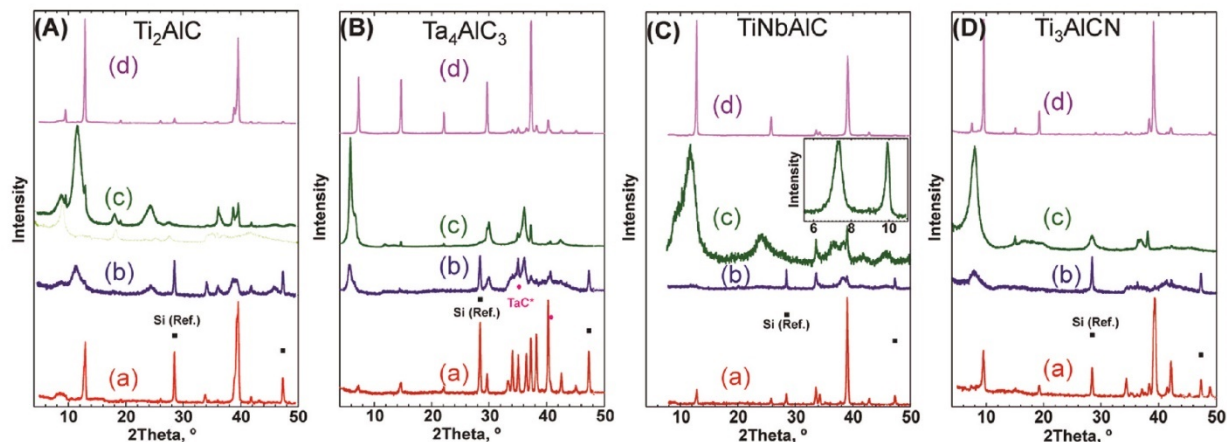
Figure 2.5. XRD patterns of different MAX phases and their corresponding MXenes after the etching process. a) Ti_2AlC, b) Ta_4AlC_3, c) $(Ti,Nb)AlC$, d) Ti_3AlCN. Adapted and reproduced with permission from ref. 9 (Copyright © 2012 American Chemical Society).

2.2. Delamination of Multilayered MXenes into Single-Layer Flakes

Delamination of MXenes into single/few-layer flakes plays an important role in achieving their full potential in different applications, particularly in energy storage systems. Similar to other 2D materials, it is shown that delamination of multilayered MXene particles into single/few-layer flakes can significantly affect their properties. For example, delaminated MXene flakes have shown better electrochemical performances in different energy storage applications.[15,19,41–43] Therefore, it is crucial to successfully delaminate MXenes into single-layer flakes and harness their unique 2D properties. Mechanical cleavage or the so-called "scotch tape" technique have been used to isolate single-layer flakes of a variety of layered materials with strong in-plane bonds and weak van der Waals bonds between their layers.[3] Although this technique allows scientists to isolate single-layer 2D flakes and study their properties, its limited scalability prevents large-scale synthesis of 2D materials. Liquid exfoliation methods have also been widely applied to delaminate single-layer flakes of layered materials.[8] As mentioned earlier in this section, however, 2D

MXenes cannot be directly produced through mechanical cleavage or direct liquid exfoliation of their parent MAX phases due to the nature of interlayer bonds in these ternary carbides. The MX layers of MAX phases are bonded with strong primary bonds (M-A bonds), which mostly have metallic character.[7] M-A bonds, however, are more reactive than M-X bonds (with mixed ionic and covalent character), and therefore, under certain conditions, the "A" atoms can be selectively removed in acidic environments. The readers are referred to chapter 2.1 of my dissertation for more details about this selective removal process. The resulting products of this process are usually multilayered particles of MXene and have a microstructure that resembles that of exfoliated graphite.[7]

The separation of the individual single/few-layer flakes from the MXene particles is not always straightforward. In many cases, the interactions between the layers in the multilayered MXenes are very strong. Therefore, to delaminate ML-MXenes into single/few-layer flakes usually an additional step (usually a liquid-based delamination method) for expanding the interlayer space and weakening the interaction between layers is required. This is usually achieved by chemical intercalation of large organic/inorganic molecules between the MXene layers. In principle, intercalation of large molecules and ionic species results in an increased interlayer spacing and weakens the out-of-plane interactions between weakly stacked MXene (M-X) layers.[11] This is usually followed by a substantial swelling of the MXene powders due to co-intercalation of water molecules. The outcome of this intercalation process, if proper intercalants and process conditions are selected, is reduction of the energy barrier for delamination of MXenes.[7,43] As a result, subsequent sonication of intercalated MXene particles in water leads to delamination of single-/few-layer MXene flakes. In the continues of this section, the delamination process of MXenes will be briefly discussed in a case by case fashion as different MXenes require different

delamination conditions. **Figure 2.6** schematically shows different approaches reported to date for delamination of multilayered MXenes into single/few-layer flakes.

Ti$_3$C$_2$T$_x$ is the most studied MXene in terms of synthesis, exfoliation, and delamination methods. In the early reports on the synthesis of this material, the large-scale delamination of single/few-layer Ti$_3$C$_2$T$_x$ flakes was carried out by chemical intercalation of dimethyl sulfoxide (DMSO) into multilayered (ML-) Ti$_3$C$_2$T$_x$ powders produced by selective etching of Al from Ti$_3$AlC$_2$ in a concentrated HF solution (50%) at room temperature.[15,43] This intercalation process resulted in the expansion of layer spacing and a large increase (about 15.4 Å) in the c-lattice parameter (c-LP) of ML-Ti$_3$C$_2$T$_x$.[15,43] Co-intercalation of water molecules has been mentioned as the reason for such large change in the c-LP upon DMSO intercalation.[7]

Furthermore, intercalation and delamination of multilayered Ti$_3$CNT$_x$ and TiNbCT$_x$ MXene phases has also been shown through the use of hydrazine, N,N-dimethylformamide (DMF), Urea, dimethyl sulphoxide (DMSO).[43] Intercalation of these large molecules in multilayered MXene particles, similarly, results in a significant downshift of (0002) planes of MXenes, corresponding to larger d-spacing and c-lattice parameter (c-*LP*), and therefore, reduced interactions between individual flakes.
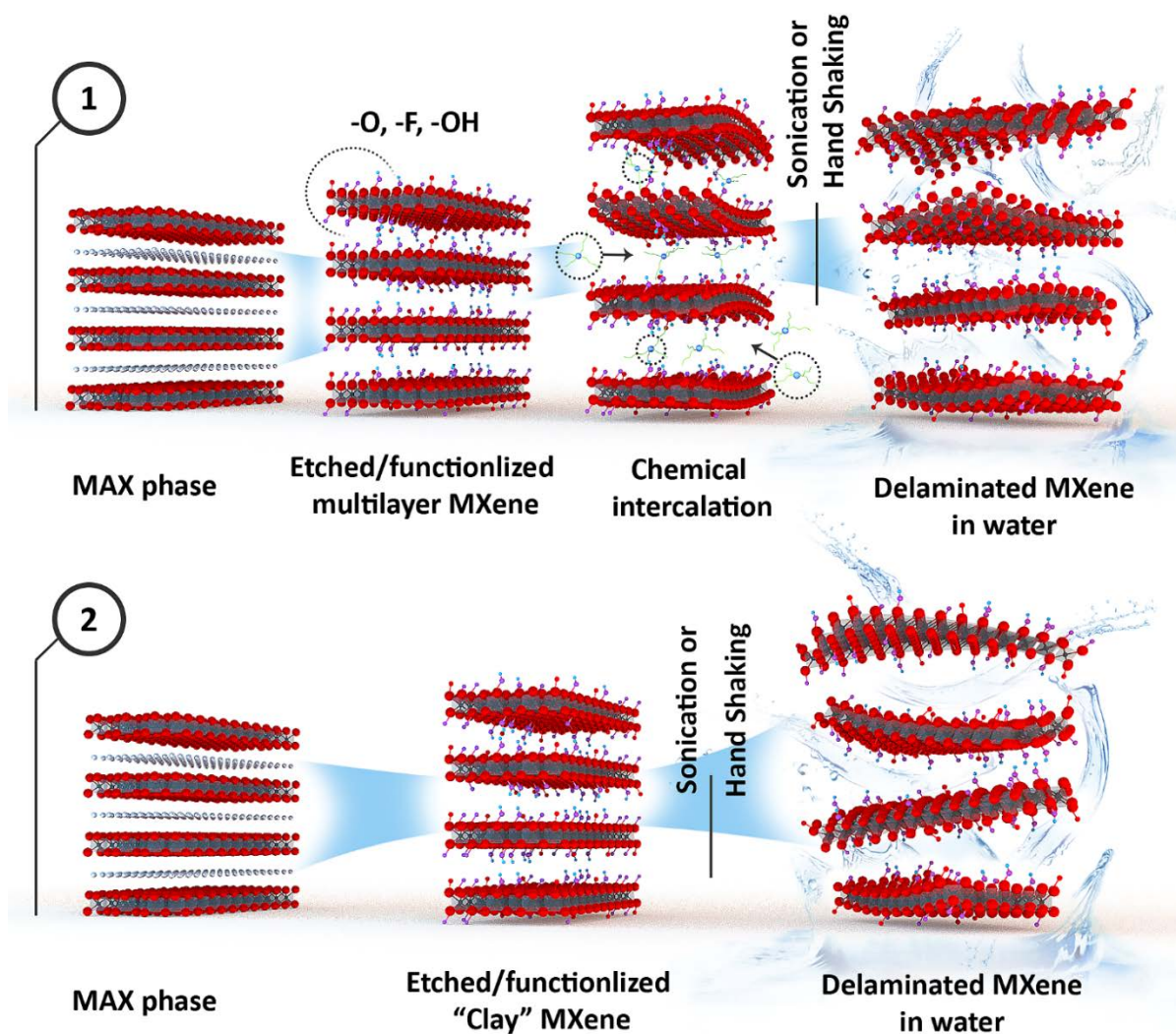
Figure 2.6. Schematic illustration of the reported techniques for the delamination of MXenes into single/few-layer flakes. Technique (1) is usually applied to multilayered MXene produced by etching the MAX phases in concentrated HF solutions. After the etching process, the ML-MXenes are intercalated with large organic molecules and then delaminated by sonication or handshaking. Technique (2) applies to those MXenes that can be etched in the mixture solutions of metal salts and acids. This technique is a single-step etching and delamination process for producing few/single-layer flakes. The M_2XT_x MXene structure is used in the schematics as an example. As explained and discussed in this chapter, other MXene structures can also be synthesized and delaminated by these methods. Adapted with permission from Chapter 11: Techniques for MXene delamination into single-layer flakes, of "2D Metal Carbides and Nitrides (MXenes)" book (Copyright © 2019 Springer Nature Switzerland AG).

The increase in the c-LP significantly weakens the interaction between M-X layers and the sonication of interlayer-expanded ML-Ti$_3$C$_2$T$_x$ in water results in the delamination of single/few layer MXene flakes. This two-step etching and delamination process (schematically illustrated as technique 1 in **Figure 2.6**) has been successfully used for delamination of various other MXene compositions (by using a variety of intercalants). In 2014, Ghidiu et al. reported a facile and efficient one-step method for the synthesis of Ti$_3$C$_2$T$_x$.[41] In this method (shown as technique 2 in **Figure 2.6**), instead of concentrated HF solutions, a mixture solution of lithium fluoride (or other fluoride salts) and hydrochloric acid is used as the etchant. During the etching process, Al atoms are removed from Ti$_3$AlC$_2$, and the hydrated Li ions are simultaneously intercalated between the M-X layers, leading to their delamination into single/few-layer Ti$_3$C$_2$T$_x$ flakes. Later, it was shown that the synthesis conditions can be tuned to produce large and high quality Ti$_3$C$_2$T$_x$ single-layer flakes.[44] Although, this method is a much more facile synthesis procedure compared to HF etching, and results in higher quality of the produced MXene sheets, it has not been much effective for single step delamination or even etching of other MAX phases.[13] This largely is due to the differences in bond energies between different transition metals and aluminum.[13] Therefore, further work is required to develop methods for etching, delamination, and processing of other MXene compositions, which indeed might result in MXenes with new surface chemistries and chemical/electrochemical properties.

Naguib et al,[45] showed that by using large molecules organic bases such as tetrabutylammonium hydroxide (TBAOH), choline hydroxide, or *n*-butylamine, several different multilayered MXenes other than Ti$_3$C$_2$T$_x$ (produced with HF etching method) can be delaminated into single/few layers and result in stable water dispersions having negative zeta potential. However, many MXenes delaminated with this technique are chemically unstable in their

single/few layer form and quickly oxidize in air or water.[45] It is important to note that the specific conditions for the delamination of MXenes, such as the type of intercalant, are dependent on the etching method. Therefore, it is essential to consider the etching process when looking for a delamination method for a particular MXene composition.

In contrast to $Ti_3C_2T_x$, information on the delamination of other MXenes into stable solutions containing single/few layer flakes is very limited in the literature. This is despite the fact that multilayered powders of a variety of MXenes have been experimentally produced and some shown exceptional properties in various applications.[16,19] Some of the approaches that are already proven to be effective for delamination of $Ti_3C_2T_x$ and were discussed earlier in this section have not been successful in delamination of other MXene compositions. This has prevented extended studies of the properties and applications of delaminated single/few layer flakes of MXenes other than $Ti_3C_2T_x$. So far, the most significant report on the large-scale delamination of other MXenes is the work by Naguib et al.[45] in which they successfully delaminated MXenes such as V_2CT_x and Ti_3CNT_x using an intercalation and gentle sonication approach, similar to that shown as technique 1 in **Figure 2.6**. However, in order to delaminate V_2CT_x and Ti_3CNT_x large organic bases were used as the intercalants in the pre-intercalation step. It should be noted that the one-step etching and delamination technique used by a mixture of metal salts and acids has not been reported to be effective for the direct delamination of other MXenes (except for Ti_2CT_x and Mo_2CT_x).[46–48]

V_2CT_x and Ti_3CNT_x (representatives of M_2X and M_3X_2 family of MXenes) were delaminated using immersion of the multilayered powders (etched in 48% HF for 92h for V_2CT_x and 30% HF for 18h for Ti_3CNT_x) in TBAOH, choline hydroxide, and *n*-butylamine in a ratio of 1g MXene powder to 10 mL of intercalant solution for different time periods of 2, 4, and 21 h.[45] In this method, after washing and removal of excess TBAOH (or other intercalants) from the

treated powders, both V_2CT_x and Ti_3CNT_x powders become swollen. By adding water and handshaking them, black colloidal solutions of single and few layers MXenes can be obtained.

In general, the chemical pre-intercalation and sonication method seems to be a very effective method for delamination of all MXene compositions. One problem associated with delaminated MXenes beyond $Ti_3C_2T_x$ is their instability and fast oxidation in the water. For example, delaminated V_2CT_x flakes dispersed in water are reported to quickly degrade over a few hours when exposed to air in an open container.[45] Therefore, for future characterization of these MXene flakes methods for proper storage of their dispersions and new techniques for their delamination should be developed.

2.3. Electrochemical Properties of MXenes

2.3.1. Aqueous Supercapacitors

Since their discovery, MXenes have been studied for a wide variety of applications from water filtration and desalination to electromagnetic interference shielding and biomolecule sensing.[24,28,29,49–52] Despite the increased attention to MXenes for different applications, most of the studies on these materials are still about their performances in electrochemical energy storage devices. The layered structure, high conductivity, and functionalized surfaces of MXenes, render these materials as promising electrodes for electrochemical energy storage devices.[13] The earliest and one of the most significant works that demonstrated the high potential of MXenes for energy storage devices was carried out by Lukatskaya et al.[15] in 2013. They demonstrated, for first time, that a wide variety of cations with different sizes and charges can chemically and electrochemically intercalate $Ti_3C_2T_x$ from aqueous solutions, resulting in high volumetric capacitances up to 400 F cm^{-3} (when tested as an electrode material for supercapacitors). **Figure 2.7.** shows the CVs and

capacitances of $Ti_3C_2T_x$ in various aqueous electrolytes.[15] Later it was shown that the clay-$Ti_3C_2T_x$ nanosheets produced by the LiF-HCl method (salt and acid mixture etching technique explained in section 2.1), can deliver capacitances as high as 900 Fcm^{-3} when tested in the sulfuric acid electrolyte.[41] The possibility of fabricating delaminated $Ti_3C_2T_x$ into freestanding flexible films, either through vacuum filtration of its delaminated water dispersions or rolling of its "clay" particles, opened numerous opportunities in terms of MXene electrode fabrication and design for supercapacitors and batteries. Presence of binders and conductive additives usually are not favorable but are unavoidable for many conventional materials such as metal oxides as they are not conductive, and therefore, to improve the charge transfer inside the electrode, it is necessary to add conductive additives alongside a polymeric binder which holds the particles together.[53] 2D MXenes, however, are highly conductive (~1500 S cm^{-1} for rolled films of $Ti_3C_2T_x$[41]), and since the individual flakes can slide with respect to each other in the freestanding films fabricated with vacuum filtration (making the produced films flexible), the need for conductive additives and binders is mostly eliminated. This results in a higher mass of active material (MXene) per area of the electrode and therefore, higher gravimetric and volumetric energy densities.[41,54]
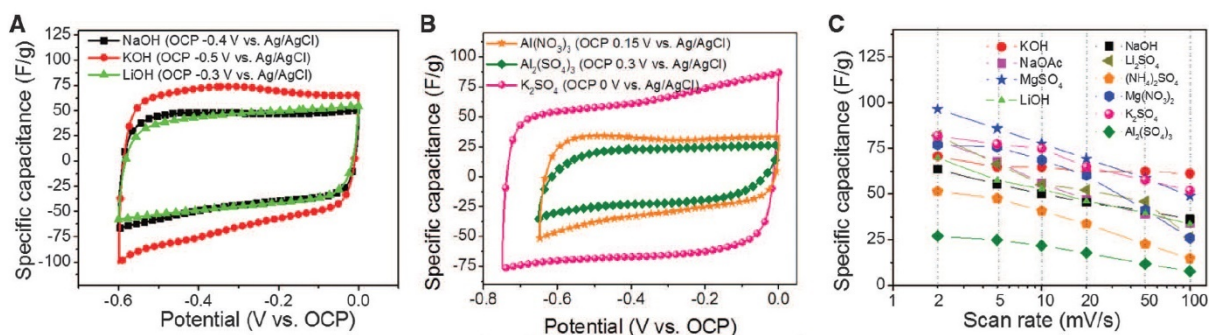
Figure 2.7. Electrochemical properties of titanium carbide MXene in aqueous electrolytes. A) CVs of $Ti_3C_2T_x$ in aqueous electrolytes of hydroxide salts. B) CVs of $Ti_3C_2T_x$ in aqueous electrolytes with sulfate-based salts. C) Gravimetric capacitances of $Ti_3C_2T_x$ in various electrolytes. Reproduced with permissions from ref. 15 (Copyright © 2013 American Association for Advancement of Science.

19

Recently, Lukatskaya et al.[17] reported on structurally engineered hydrogel and microporous $Ti_3C_2T_x$ electrodes with outstanding capacitances at ultra-high-rates of up to 10 V s^{-1}. They reported on capacitances as high as 1500 F cm^{-3} in the 3 M sulfuric acid electrolyte at low rates, and an exceptional gravimetric capacitance of 210 F g^{-1} at an ultra-high-rate of 10 V s^{-1}. These numbers are unprecedented among pseudocapacitive electrode materials. **Figure 2.8** shows typical cyclic voltammetry curves with signature redox peaks for $Ti_3C_2T_x$ MXene thin film electrodes and its rate-performance in 3 M sulfuric acid.[17]
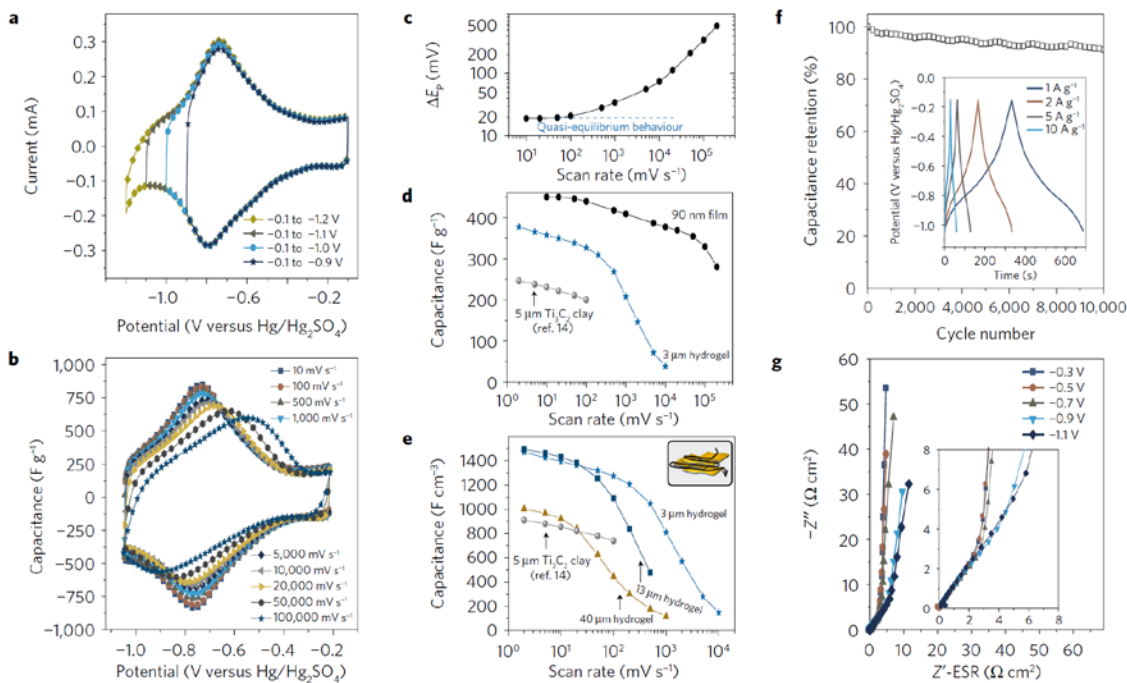
Figure 2.8. Ultrahigh-rate electrochemical performance of 2D titanium carbide MXene. a) Cyclic voltammetry (CV) profiles for a $Ti_3C_2T_x$ electrode collected in different potential windows at a scan rate of 5 mV s^{-1}. b) CV profiles at different scan rates for a 90-nm thick $Ti_3C_2T_x$ electrode. c) Peak separation, ΔE_p, for different scan rates extracted from CV analysis of 90nm MXene film. The blue dashed line indicates the domain of the quasi-equilibrium. d) the gravimetric capacitance of different $Ti_3C_2T_x$ electrodes. e) The volumetric capacitance of different $Ti_3C_2T_x$ electrodes. f) Capacitance retention of a $Ti_3C_2T_x$ hydrogel electrode at a rate of 10 A g^{-1}. g) Electrochemical impedance spectroscopy (EIS) results at different potentials for a $Ti_3C_2T_x$ paper electrode. Adapted with permission from ref. 17 (Copyright © 2017 Macmillan Publishers Ltd.).

More recently, a thickness-independent capacitance was reported for vertically aligned $Ti_3C_2T_x$ MXene liquid crystalline electrodes, where binder-free electrodes with thicknesses of up to 200 µm showed an electrochemical performance almost independent of their thicknesses.[55] These results show the promise of MXenes for practical supercapacitor devices where usually a minimum electrode thickness of ~100 µm is required.[55] Without a doubt, these reports have rendered 2D MXenes very promising for pseudocapacitive energy storage application. To date, however, most of the research on MXenes for aqueous supercapacitor have been only focused on $Ti_3C_2T_x$ composition and other compositions have not been systematically investigated in aqueous systems. In fact, of the 30 different MXenes that have been synthesized so far, only $Ti_3C_2T_x$ has been systematically investigated as a pseudocapacitive electrode material for ECs. Lack of established methods for delamination of MXenes other than $Ti_3C_2T_x$, as well as the lower (electro)chemical stability of some of the MXene compositions in their 2D (delaminated) form, are among the reasons that have hampered the investigation of other promising MXenes.[56] In this direction, a recent theoretical study has predicted the high performance of many MXenes other than $Ti_3C_2T_x$ for pseudocapacitive energy storage.[57] Notably, the pseudocapacitive properties of completely delaminated (single/few layers) M_2CT_x MXenes, such as $d-V_2CT_x$ and $d-Ti_2CT_x$, have remained unexplored. When these MXene are delaminated to single/few-layer sheets they show poor chemical stability in ambient conditions, or in the presence of water and oxygen.[13,45] It is important to note that, complete exfoliation and delamination of MXenes (or generally any layered material) for pseudocapacitive charge storage applications is a crucial step toward achieving their best performance, because delaminated single/few layer flakes pose higher surface area and redox active sites compared to their multilayered counterparts, as well as a faster ion diffusion (intercalation) kinetics as the interlayer spacing of individual sheets is now significantly

larger.[15,43,58] M_2CT_x (M= V, Ti, Nb,..) MXenes can potentially offer better electrochemical properties compared to $Ti_3C_2T_x$ ($M_3C_2T_x$) because of their similar functionalized surfaces but lower weights as well as higher valance state of the transition metals in certain cases such as V_2CT_x.[13,59] For example, multilayered V_2CT_x, which has shown the highest Li ion intercalation capacity among all MXenes,[16,19] quickly oxidizes in water or air when delaminated to 2D flakes (d-V_2CT_x). Very recently, Shan et al showed the promise of V_2CT_x MXene as aqueous supercapacitor electrode in a short report.[60] However, despite a promising electrochemical performance, the V_2CT_x showed low electrochemical stability, which was attributed to either oxidation of MXene or dissolution of V in aqueous electrolytes.[60]

Therefore, methods that can enable the possibility of investigating other MXene compositions for aqueous energy storage are required to be developed.

Since we talked about performance of MXenes in systems with aqueous electrolytes, it is important to mention that the charge storage mechanism of MXenes in aqueous electrolytes has been demonstrated to be intercalation pseudocapacitance (with pronounced redox couple peaks in acidic electrolytes),[13,17,61,62] which is fast and reversible redox reactions that occur in the bulk of a material through ultrafast intercalation of ions.[63] It is noteworthy that, pseudocapacitive materials can store more charge and deliver higher energy densities compared to conventional electric double layer capacitors (EDLCs) through these fast and reversible surface redox reactions.[15,56,64–69] This is because in conventional electrochemical capacitors (ECs) or the so called electric double-layer capacitors (EDLCs), charge storage is based on the electrosorption of ions on the surface of carbonaceous electrode materials and therefore, the amount of stored charge is limited by the surface area of the electrodes.[56,65,70] For most pseudocapacitive materials (e. g., metal oxides such as $RuO_2 . nH_2O$[68] and MnO_2[65]), however, the redox reactions are limited to the surface or near-

22

surface of the electrodes, which greatly underutilizes the bulk of electrode material in charge storage.[56] For some oxides such as T-Nb$_2$O$_5$[63] the pseudocapacitance occurs in the bulk of the material through fast intercalation of ions resulting in high specific capacitances and energy densities. However, transition metal oxides suffer from low electrical conductivities which hinders their rate-handling capability, power density, and cyclic performance.[15,17,71] Therefore, since MXenes are highly conductive, they have shown superior intercalation-based pseudocapacitive properties compared to many other previously reported materials. There have been some comprehensive studies which have investigated the pseudocapacitive charge storage mechanism of Ti$_3$C$_2$T$_x$ in sulfuric acid in detail. Through these studies, it has been shown that the potential of electrode changes almost linearly with an oxidation state of titanium, and this change is accompanied by protonation of oxygen functional groups present on the surface of a transition metal.[17,61]

2.3.2. MXenes-Organic Hybrids

Hybrid structures of MXenes and polymers have been investigated as pseudocapacitive electrode materials in literature with some promising performances.[31,32,72] It is important that in this section, I point out that an advantage of 2D materials, such as MXenes, over the conventional EC electrode materials is that they can be assembled into freestanding and flexible electrodes and devices using simple and binder-free fabrication methods (e. g. through vacuum filtration or layer-by-layer deposition methods). As mentioned earlier in previous section, it has been shown that the thin freestanding Ti$_3$C$_2$T$_x$ electrodes can deliver specific capacitances as high as 450 F g^{-1}.[17,41,73] However, similar to the other 2D materials, MXene sheets tend to restack during electrode fabrication, which severely reduces the ion transport in the structure of the electrode. This problem is more pronounced in the case of thicker electrodes and, as a result, freestanding electrodes

fabricated by direct assembly of the 2D sheets usually show highly thickness-dependent performances.[41] Restacking significantly affects the rate capability of $Ti_3C_2T_x$ electrodes and limits their charge storage capacity to far below the theoretical value of ~ 615 C g^{-1}.[17,48,74–76] To overcome this problem, various approaches have been applied to engineer the structure of the MXene electrodes and improve their ion transport properties. These include fabrication of microporous and hydrogel $Ti_3C_2T_x$ films[17] and designing hybrid electrodes of $Ti_3C_2T_x$ and carbon nanomaterials such as carbon nanotubes (CNTs)[73] and graphene.[76,77] While some of these strategies are effective in improving ion transport and high-rate electrochemical performance of the electrodes, they often reduce the electrode density resulting in decreased volumetric capacitance, rate capability, and energy density of the electrodes, particularly at higher electrode thicknesses.[17,76]

Previously, it has been demonstrated that the electrochemical properties of freestanding MXene electrodes can be improved by deposition of conductive polymers such as polypyrrole (PPy) and Poly(3,4-ethylenedioxythiophene) (PEDOT) on the surface of MXene sheets. **Figure 2.9.** schematically shows the structure of the produced MXene and PPy hybrids as well as some strcuctural characterization of the produced hybrid materials.[31] Hybrid electrodes of $Ti_3C_2T_x$ and PPy have shown to deliver specific capacitances as high as 416 F g^{-1} in 1M H_2SO_4.[31] The performance of the electrodes fabricated using PEDOT deposited $Ti_3C_2T_x$ sheets were also improved compared to the electrodes fabricated using pristine $Ti_3C_2T_x$.[72] The improved performance of these hybrid electrodes does not stem from the contribution of the polymers to charge storage. PPy and PEDOT are both electrochemically inactive in the potential range that $Ti_3C_2T_x$ shows its highest electrochemical activity in acidic aqueous electrolytes (-0.7 V to +0.2 V vs. Ag/AgCl). In other words, in these cases, the deposited polymers only act as conductive spacers that prevent restacking of $Ti_3C_2T_x$ sheets in the electrode structure.

This is a unique application of conductive polymers in designing high performance electrodes as these materials are more often considered as the active materials in various electrochemical energy storage systems.[78–80] However, previous studies have not fully explored this interesting electrode design strategy. For example, the effects of polymer loading in the hybrid electrodes and the thickness of the deposited polymer on electrochemical performance have not been investigated. In addition, the application of hybrid $Ti_3C_2T_x$/polymer sheets in designing high performance freestanding electrode with very high thicknesses has not been reported either.
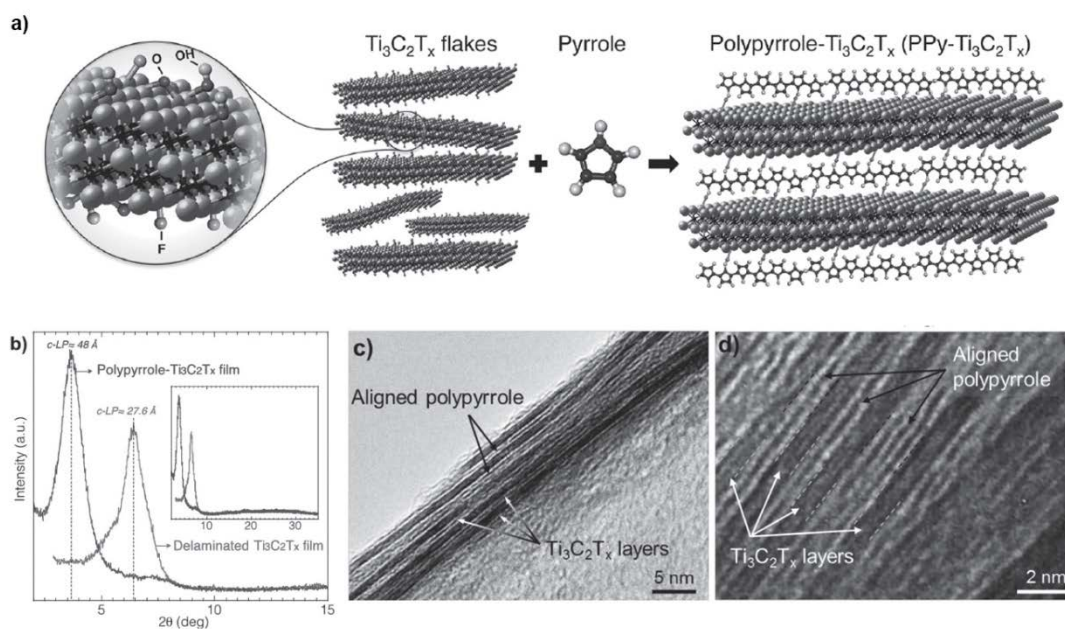
Figure 2.9. Hybrid structures of $Ti_3C_2T_x$ and PPy. a) schematic structure of $Ti_3C_2T_x$ MXene flakes and the process used for polymerization of pyrrole monomers on the surface of MXene nanosheets. b) XRD patterns of the pristine $Ti_3C_2T_x$ film and the $Ti_3C_2T_x$/PPy hybrid film, showing the change in d-spacing of the hybridized film as the result of polymerization of pyrrole monomers at the surface of MXene sheets. c and d) High resolution TEM images form the cross-section of the hybrid films demonstrating aligned PPy layers between MXene sheets. Reproduced with permission from ref. 31 (Copyright © 2016 Wiley-VCH Verlag GmBH & Co.).

2.3.3. MXene Heterostructures

Two-dimensional (2D) materials, due to their low-dimensionality and highly accessible and redox-active surfaces, offer interesting properties for electrochemical energy storage applications. Fast transport of ions, abundant intercalation sites, exceptional charge transport properties, and excellent mechanical robustness, are among the promising properties of 2D materials.[58] To date, however, no individual 2D material has shown to offer all of these properties together.[58,81,82] Additionally, in many cases inherent properties, as well as highly exposed surfaces of 2D materials, can result in unwanted side reactions with electrolyte and other cell components, resulting in their poor cyclic stability (i.e., many 2D metal oxides suffer from these issues).[58] Vertical stacking of different 2D materials to produce heterostructure is an approach that allows combining different atomically thin materials into hetero-layered structures with superior physical and (electro)chemical properties.[58,81,83–85] Such 2D heterostructures not only can potentially eliminate shortcomings of individual 2D materials, but also enable the realization of numerous new electrode compositions for batteries and supercapacitors.[58]

As discussed earlier in this chapter, MXenes distinguish themselves from other 2D materials by their versatile compositions as well as having different number of atomic layers in their structure. To date, around 30 different MXenes are experimentally synthesized and many more theoretically predicted.[13,86] Therefore, this large family of 2D materials provides an interesting avenue for the development of new 2D heterostructures.[13]

Recently, a few heterostructures of $Ti_3C_2T_x$ MXene with other 2D materials have been reported.[76,87–92] While these early studies have suggested enhanced properties for the final hetero (or composite) materials, they often do not demonstrate an ordered and uniform vertical stacking of the different 2D layers and only briefly discuss their structural properties. They rather only display the promise of such structures without investigating or controlling the stacking of 2D layers

into superlattice structures. In addition, these early reports have only focused on the combination of 2D $Ti_3C_2T_x$ with graphene or 2D metal oxides and dichalcogenides; leaving behind other promising pseudocapacitive MXene compositions such as Ti_2CT_x and V_2CT_x, as well as the possibility of fabricating 2D heterostructures only based on the vertical stacking of different MXene sheets. Therefore, it can be assumed that the proper stacking of different 2D MXene sheets into vertical heterostructures might enable practical superlattice materials that address shortcomings of individual MXenes and result in dozens of new 2D heterostructures with superior properties. To date and at the time of my dissertation, however, there are no reports on such all-MXene vertical 2D heterostructures.

2.3.4. MXenes in Batteries with Non-Aqueous Electrolytes

MXenes have also attracted interest as intercalation-type electrodes for energy storage systems with non-aqueous (organic or ionic-liquid) electrolytes such as rechargeable batteries and Li- and Na-ion capacitors. High power of multilayered Ti_2CT_x MXene nanosheets was shown for Na-ion storage at an early stage of research on MXenes.[18] Similarly, different MXene compositions such as $Ti_3C_2T_x$, Ti_2CT_x, V_2CT_x, and Nb_2CT_x were used as anode materials for Li-ion batteries which showed promising performances comparable to, or higher than conventional graphite anodes.[16,43,93] Despite these promising performances in monovalent battery systems, so far, MXene electrodes have shown capacitive behavior with no distinct plateaus in their charge and discharge profiles. This capacitive behavior of MXenes in Li and Na ion batteries has generally hindered their development as battery materials.[71]. Nevertheless, over the past few years significant researches on MXenes as building blocks for fabrication of battery electrodes have been carried out. Examples of these are fabrication of hybrid electrodes based on MXenes and metal

27

oxides,[94–96] fabrication of porous MXene electrodes,[20,97–99] and fabrication of pillared or hollow structures of MXenes.[100–102]

Most of the battery research on MXenes has been focused on Li- and Na-ion batteries, where insertion of Li and Na cations were shown inside different (multilayered) MXene materials such as $Ti_3C_2T_x$, Ti_2CT_x, V_2CT_x, and Nb_2CT_x.[16,18,43,103] In these systems, MXenes behave as anode materials that are capable of high-rate handling capabilities.[16] Theoretical studies have predicted promising and high performance of different MXene compositions in beyond Li-ion batteries, and in particular, multivalent-ion batteries such as Magnesium and Aluminum batteries.[13,59,104] In spite of these theoretical predictions, there have been a handful of studies on applications of MXenes in multivalent-ion batteries.[19,105,106] Therefore, the knowledge on behavior and responses MXenes in these systems is very limited.

It might be asked, why when LiBs are capable of powering all of our gadgets and electric vehicles (EVs), why we should spend money and time on development of new batteries based on multivalent chemistry. Therefore, it is important to discuss why the research on multivalent battery systems is important in the field of electrochemical energy storage deviecs. From a sustainable energy standpoint, lithium resources are very limited and cannot be considered as the only means of battery manufacturing in the next few years, particualrly when the electric vehicles (Evs) start to dominate the market.[107] In addition, LiBs suffer from flammability issues, and Li metal cannot be directly used as the anode since lithium forms dendrites and results in cell shortage.[108,109] Na is considerably more abundant than Li, however, most of the other issues associated with LiBs exist for Na-ion batteries as well. One can argue that the flammability issue and safety concerns of Li and Na batteries can be solved through technological advancements such as the development of solid-state batteries where no flammable organic electrolyte is used. Even in that case, the scarcity

and availability issues of Li metal would still hinder leaning on Li technology as the only source of energy storage for the future. Therefore, over the past few years, significant research has been carried out on the design and fabrication of rechargeable battery systems based on multivalent-ions (Ca^{2+}, Mg^{2+}, Zn^{2+}, and Al^{3+}).[108,110–113] Apart from the higher abundance of any of these metals compared to Li (please see **Figure 2.10.**), utilization of multivalent ions in a battery system enables possibility of achieving significantly higher energy densities suitable for applications in developing EVs.[108] This is because they can offer multiple-electron redox reactions (compared to Li^+ where only one electron is transferred per each inserting ion) during the charge and discharge processes of the battery, resulting in higher capacities (**Figure 2.10**) and therefore, exceptionally higher energy densities.[107,108,114]

One important aspect of batteries based on multivalent chemistry is that multivalent metals can be directly used as anodes in these systems, eliminating the need for development of substitute anodes. This is because early researches have shown that unlike Li, metals such as Mg, Ca, and Al since electrodeposition of these metals (Mg^{2+}, Ca^{2+}, Al^{3+}) does not result in dendrite formation.[107,108] They rather deposit uniformly during the charging process of the battery on the metallic anode. In contrast, as mentioned earlier, Li deposits as dendrites on its metal and therefore, the surface area of Li metal anodes increases significantly during battery cycling, resulting in increased cell resistance, cell shortage, and even may lead to disastrous fire events.[53,108]
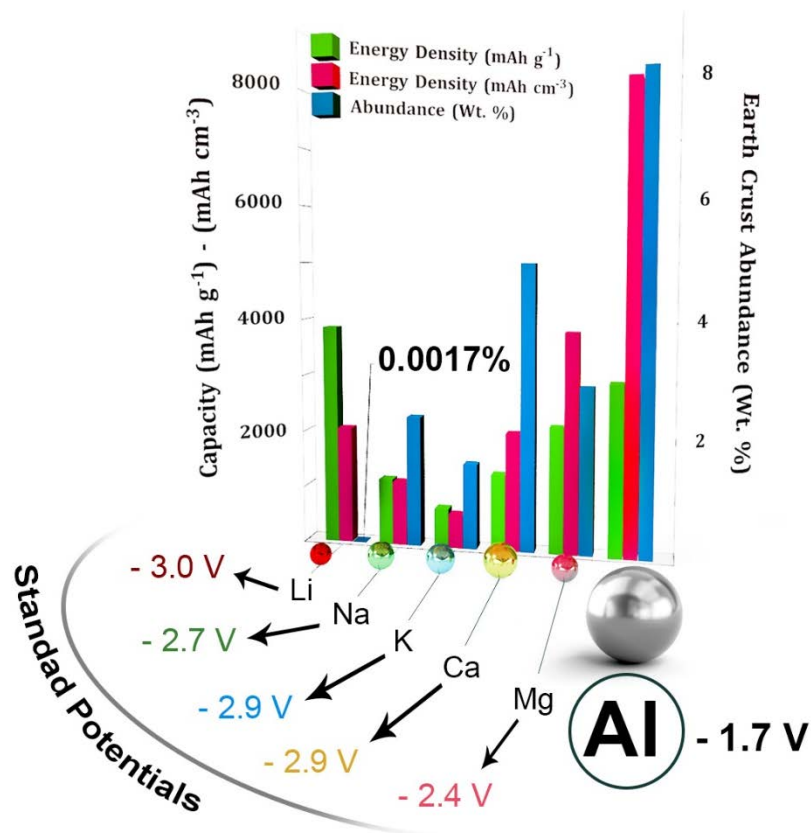
Figure 2.10. Comparison between abundance, and theoretical gravimetric (normalized by weight), and volumetric (normalized by volume) capacitances of different metal anodes.

However, similar to any new-born battery technology, the main challenge facing multivalent-ion batteries is the development of novel positive electrode (cathode) materials that can host multivalent-ions with different charge densities. Unfortunately, conventional cathode materials used in current Li-ion batteries have shown not to be active for hosting different multivalent ions.[107,108,114] In this direction, nanomaterials and in particular, a few layered and 2D materials such as graphene and MoS_2 have shown to be promising cathode materials for multivalent-batteries.[115–119] MXenes, however, have fallen short in the literature to be investigated for these battery systems. This is while their diverse compositions with the possibility of having different and multiple transition metals[39] inside their structure as well as their already proven

30

capability in hosting different ions with different charges and sizes (from aqueous electrolytes)[15], renders them as promising materials for multivalent-ion batteries. Therefore, research on the application of MXenes for such electrochemical systems is crucial and can lead to new findings in literature toward the development of safer and higher energy density battery technologies.

Among different multivalent battery chemistries, over the past few years rechargeable aluminum batteries (AlBs) have received significant attention as promising alternatives to LiBs for applications such as electric vehicles (EVs) and gird-scale storage.[107] This high interest in AlBs arises from the fact that aluminum is the most abundant metal in Earth crust (~8.1% vs. 0.0017% for Li), is much cheaper, does not catch fire, and is highly accessible for manufacturing purposes.[107,114] These alongside high theoretical capacity of the aluminum metal anode (8040 mAh cm^{-3} and 2980 mAh g^{-1}) stemming from its relatively light weight and three-electron redox capability, have rendered aluminum batteries as a potential technology of choice for future electrical energy storage. The main challenge facing AlBs, however, is lack of proper cathode materials that can hos high charge density Al^{3+} cations. Unfortunately, similar to insertion of Mg^{2+}, conventional electrode materials have shown high diffusion barrier for intercalation of Al^{3+} and are not capable of hosting these cations inside their strcuture.[108] Therefore, there is a great need for development of new cathode materials for these systems.

At the time of my dissertation, a few studies had shown experimental results on the performance of $Ti_3C_2T_x$ MXene and its hybrid electrode structures for Magnesium (Mg) hybrid Li/Mg batteries.[42,105,106] Except these few reports in organic Mg-ion batteries, however, at the time of my dissertation, applications of MXenes in other promising multivalent chemistries such as Al batteries.

Chapter 3

Materials and Methods

This chapter will cover the details of the general experimental work done for different sections of my Ph.D. research including MAX phases and MXenes' synthesis procedures and their structural characterizations. The specific details for different experiments and techniques discussed in chapter 4, 5, and 6 are explained in their corresponding chapters.

3.1. Chemicals

The following materials were used for different experiments as mentioned accordingly in each topic, except where otherwise is indicated.

Titanium powder (99.5%, 325 mesh, Alfa Aesar), TiC powder (99.5%, ~ 2 microns, Alfa Aesar), Aluminum powder (99.5%, 325 mesh, Alfa Aesar), Graphite powder (99%, 325 mesh, Alfa Aesar), Niobium powder (99.8%, 325 mesh, Alfa Aesar), Vanadium powder (99.5%, 325 mesh, Alfa Aesar), Chromium powder (99%, 325 mesh, Alfa Aesar), Aluminum chloride (AlCl$_3$, anhydrous, 99.999+% or 99+%, Alfa Aesar), Aniline (99+%, Alfa Aesar), Calcium chloride (anhydrous, 93%, Alfa Aesar), Carbon Black Super P (99+%, Alfa Aesar), Diethyl ether (DEC, 99+%, Alfa Aesar), Dimethyl Carbonate (DMC, 99%, Alfa Aesar), Hexadecyltrimethylammonium bromide (CTAB, BioXtra 99%, Sigma Aldrich), Hydrochloric Acid (HCl, ACS grade, BDH), Lithium chloride (LiCl, anhydrous, 99%, Alfa Aesar), Lithium

fluoride (LiF, 98.5%, 325 mesh, Alfa Aesar), Lithium metal (ribbon, 0.75 mm, 99.9%, Sigma Aldrich), Lithium sulfate monohydrate (99%, Alfa Aesar), Magnesium chloride ($MgCl_2$, anhydrous, 99%, Alfa Aesar), Magnesium perchlorate ($Mg(ClO_4)_2$, anhydrous, ACS, Alfa Aesar), Magnesium sulfate ($MgSO_4$, anhydrous, 99.5%, Alfa Aesar), Molybdenum Foil (99.95% 0.1 mm thick, Alfa Aesar), N-Methyl-2-Pyrrolidone (NMP, 99+%, Alfa Aesar), Potassium chloride (99%, Alfa Aesar), Potassium hydroxide (pellets, 85%, Alfa Aesar), Potassium sulfate (K_2SO_4, 99%, Alfa Aesar), Propylene carbonate (PC, 99%, Alfa Aesar), Sodium chloride (NaCl, 99%, Alfa Aesar), Sodium metal (cubes, 99%, Sigma Aldrich), Sodium dodecyl sulfate (SDS, 99+%, Sigma Aldrich), Sodium hydroxide (NaOH, 98%, Alfa Aesar), Sodium perchlorate (98%, Alfa Aesar), Sodium sulfate (Na_2SO_4, anhydrous, 99%, Alfa Aesar), Sulfuric acid (reagent, 18 M, VWR), Hydrofluoric Acid (HF, ACS grade, BDH), tetra-n butyl ammonium hydroxide (40% w/w aqueous solution of TBAOH, Alfa Aesar), Zinc sulfate heptahydrate (ACS 99+%, Alfa Aesar), 1-Butyl-3-methylimidazolium chloride (BMImCl, HPLC 99+%, Sigma Aldrich), 1-Ethyl-3-methylimidazolium chloride (EMImCl, 98+%, Alfa Aesar).

3.2. MAX Phase Synthesis

- <u>Ti_2AlC MAX Phase</u> powder was prepared through mixing TiC (99.5%, ~ 2 microns, Alfa Aesar), Ti, and Al powders in 0.85:1.15:1.05 molar ratio and ball milled for 24h using zirconia grinding balls. The ball milled powders were then heated to 1400 ºC in a tube furnace under a flowing argon atmosphere at a heating rate of 5 ºC/min and were kept there for 4 hrs. Synthesized bulk Ti_2AlC was milled using titanium carbide tips and sieved through a 400 mesh to obtain powders with an average particle size of ~32 microns.[32]

- <u>Ti$_3$AlC$_2$ MAX phase</u> powder was synthesized according to previous reports in the literature.[15] In summary, Ti$_2$AlC (~400 Mesh or average particle size of ~ 32 μm) and TiC (99.5%, ~ 2 microns, Alfa Aesar) powders were mixed in a 1:1 molar ratio and ball milled for 24h using zirconia grinding balls. The ball milled powders were then heated to 1400 ºC in a tube furnace under a flowing argon atmosphere at a heating rate of 5 ºC/min and were kept there for 2 hrs. Synthesized bulk Ti$_3$AlC$_2$ was milled using titanium carbide tips and sieved through a 400 mesh to obtain powders with an average particle size of ~32 microns.

- <u>V$_2$AlC MAX Phase</u> was synthesized by mixing vanadium powder (99.5%, 325 mesh, Alfa Aesar), aluminum powder (99.5%, 325 mesh, Alfa Aesar), and graphite powder (99%, 325 mesh, Alfa Aesar) in a 2:1.3:1 ratio and ball milled using zirconia balls for 18 h. Then the mixture was sintered at 1500 ºC with a heating rate of 3 ºC/min for 4h under flowing argon atmosphere. The synthesized MAX phases were crushed, milled, and sieved through a 400 mesh to obtain powders with an average particle size of ~32 micron.[19]

- <u>Cr$_2$AlC MAX Phase</u> was prepared through mixing the elemental powders of Cr, Al, and C in a 2:1.1:1 ratio, and ball milling them for 12h. Then the mixed powders were sintered at 1400 ºC for 1h with a heating rate of 5 ºC/min.

- <u>Nb$_2$AlC MAX phase</u> was prepared similarly to Cr$_2$AlC where the elemental powders of Nb, Al, and C were mixed in a 2:1.1:1 ratio, ball milled for 18h, and then sintered at 1600 ºC for 4h. The heating rate was 5 ºC/min.

XRD results for the synthesized MAX Phases are shown in **Figure 3.1**.
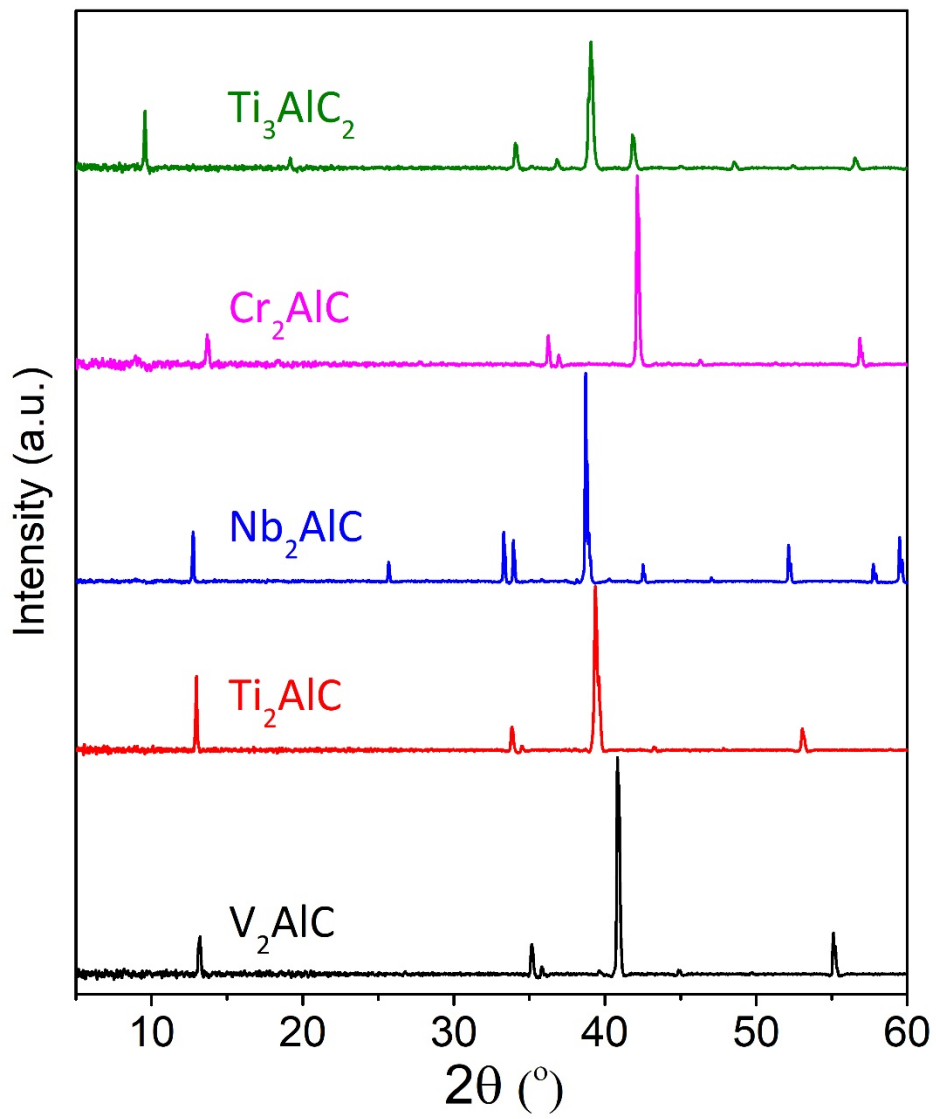
Figure 3.1. XRD patterns of all different 211 and 312 MAX phase compositions synthesized in our laboratory.

3.3. MXene Synthesis: Powders, Solutions, Films

- <u>$Ti_3C_2T_x$ MXene</u> was prepared according to the minimally intensive layer delamination (MILD) method.[44,120] Typically, 1g LiF (98.5%, Alfa Aesar) was added to 20 mL solution of 6 M HCl (ACS grade, BDH). The solution was stirred until the LiF powder was completely dissolved. Then 1g of Ti_3AlC_2 MAX phase powder was slowly added to the LiF-HCl etching solution (in over ~10 minutes). An ice bath was used to dissipate the excess heat from the etching solution while adding the MAX phase powder. The solution was continuously stirred at 550 rpm using a Teflon coated magnetic bar for 24h at 35 ℃. The etched powder was then washed several times by DI water, hand-shaken for at least 1 minute, and centrifuged at 3500 rpm for 5 minutes until obtaining a dark green supernatant or when the pH of the supernatant became higher than 5. At this point, etched particles were probe sonicated (with 35% amplitude/~250 W power) in deaerated DI water (~1g powder in 200 mL water) for 1h. Again, an ice bath was used to avoid excessive heat generation and oxidation of MXene during probe sonication. The final solution (referred to as $Ti_3C_2T_x$ MXene solution in the text) was obtained by centrifugation of the sonicated powders at 3500 rpm for 1h. The concentration of resulting MXene solutions was calculated by filtering a known volume of solution and measuring the weight of the resulting freestanding $Ti_3C_2T_x$ film after it was completely dried.[32]

- <u>Ti_2CT_x MXene:</u> The methods for preparation of Ti_2CT_x is similar to $Ti_3C_2T_x$ with the exception that the produced powders do not readily delaminate and the etching results in multilayered particles. In order to delaminate Ti_2CT_x, the synthesized multilayered powders after etching (pH of supernatant ~ 4.5) were collected and intercalated with tetra n-butyl ammonium hydroxide (TBAOH, 40 % w/w aqueous solution in water, Alfa Aesar) by adding 200 mg of Ti_2CT_x powder to 4 mL of TBAOH solution and stirring for 2h at room temperature. Then the obtained

solution was diluted with DI water and shaken for 2 minutes, followed by centrifugation at 2000 rpm for 10 minutes. Again, the first supernatant (slightly dark red color) was poured out as it contained residual TBAOH. Then, DI water was added to the sediments, the solutions were shaken for 2 minutes followed by centrifugation at 2000 for 30 minutes. The obtained dark red supernatant was collected and labeled as d-Ti$_2$CT$_x$.

- <u>V$_2$CT$_x$ MXene</u>: V$_2$AlC MAX phase was treated with 50% concentrated Hydrofluoric Acid (HF, ACS grade, BDH) in a 2 g powder to 40 mL etchant ratio for 92 h at room temperature while stirring with a Teflon coated magnetic bar at 200 rpm. The etched powder was then washed several times by using DI water and centrifuging at 4500 rpm for 5 minutes until the pH of the supernatant was higher than 4. The MXene powder was then filtered using a Celgard® porous membrane, rinsed with DI water and absolute ethanol, and collected and dried.[19] Similar to Ti$_2$CT$_x$, the obtained powders do not delaminate after the etching process. The delamination process was done by intercalation of MXene particles with tetra-n butyl ammonium hydroxide (40% w/w aqueous solution of TBAOH, Alfa Aesar) for 4 h at RT. To intercalate MXenes with TBA$^+$ cations, the produced multilayered powders were stirred in a TBAOH solution at 1000 rpm in a ratio of 200 mg MXene powder to 4 mL of TBAOH solution. The intercalated powders were then dispersed in 45 mL of DI water and transferred to centrifuge tubes. The dispersions were shaken by hand for 2 minutes and subsequently centrifuged for 10 minutes at 2 000 rpm. The supernatant obtained after the first round of shaking and centrifuge processes contained low concentrations (light green color) as well as residual TBAOH. Therefore, it was not used for studies. The delamination process was continued by adding DI water to the precipitate powder and repeating the skaing and centrifuge steps. After the centrifugation, the resulting supernatant (labeled as d-V$_2$CT$_x$) was collected. **Figure 3.2.** schematically shows the process.[56]
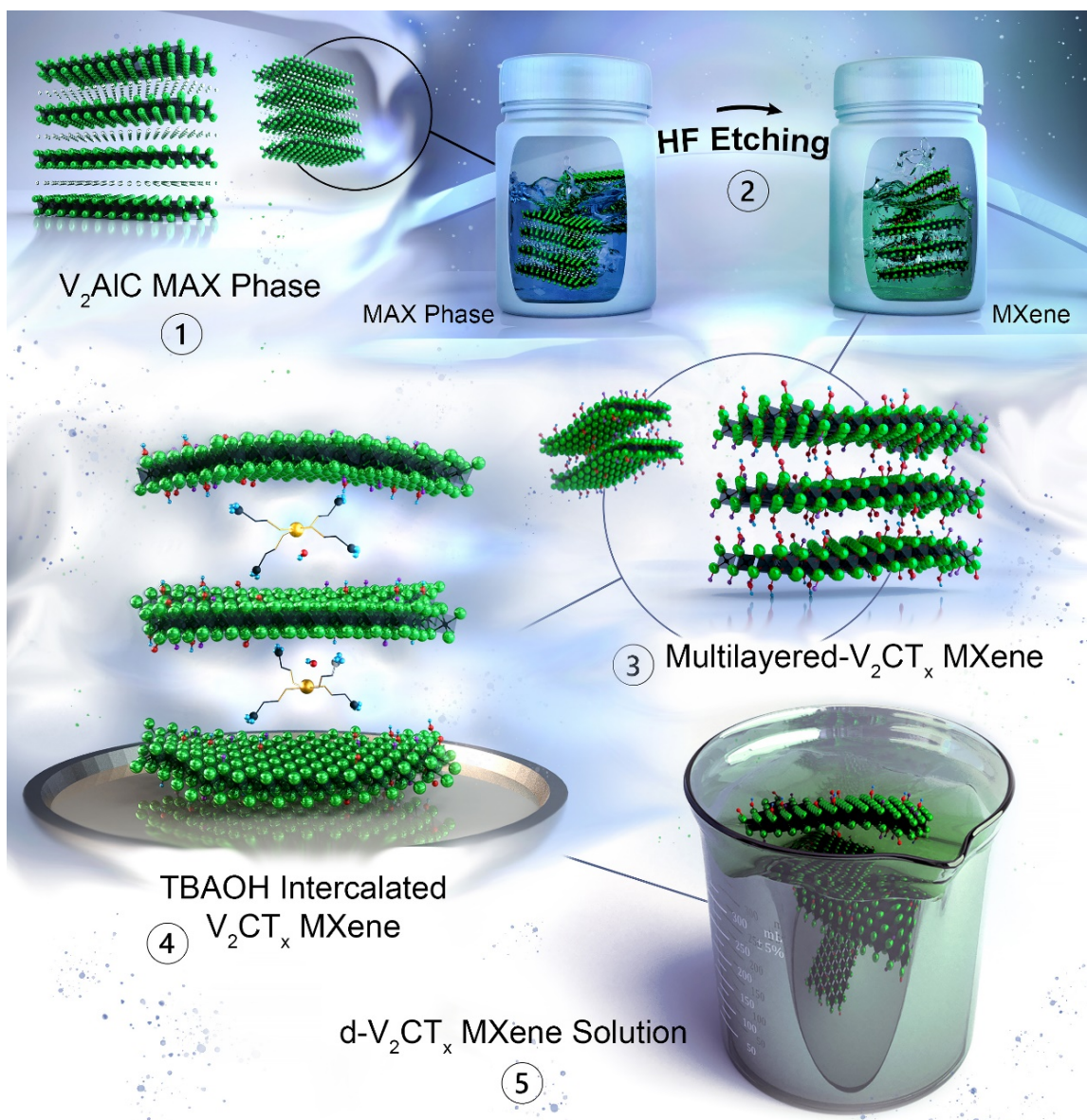
Figure 3.2. Schematic illustration of the synthesis and delamination of V_2CT_x. The synthesis method relies on expanding the interlayer spacing in the MAX phase in order to weaken interlayer interactions and facilitate delamination.[19,45,121] 1, Structure of V_2AlC MAX phase. 2, Selective etching of the V_2AlC in 50% HF solution for 92 h, where Al atoms are selectively etched. 3, Structure of the multilayered V_2CT_x (ML-V_2CT_x) showing the presence of different functional groups on the surface of the exfoliated MXene sheets. 4, Intercalation of tetrabutylammonium cations (TBA$^+$) through treatment of the MXene powders in a solution of tetrabutylammonium hydroxide (TBAOH) at room temperature resulting in expansion of interlayer spacing of ML-V_2CT_x. 5, Delaminated V_2CT_x (d-V_2CT_x) solution obtained by handshaking of the TBA$^+$ intercalated ML-V_2CT_x in water. Adapted with permission from ref. 56 (copyright © 2019 Wiley-VCH Verlag GmBH & Co.).

- $\underline{Nb_2CT_x \; MXene}$ was prepared with a method similar to V_2CT_x. The only difference was the etching time in which the MAX phase powders were etched in HF for 48h, and the reaction temperature was controlled at 55 ℃. The resulting products after etching are multilayered (ML) Nb_2CT_x which can be delaminated according to a similar process to that of V_2CT_x.

Synthesis conditions for multilayered and delaminated MXenes prepared as part of my dissertation research are summarized in **Table 3.1.**

Table 3.1. Etching conditions and delamination procedure for various MXenes.

MXene	Etchant	Etching Condition	Powder/Batch	Delamination Procedure	
				Chemical	Condition
Ti_2CT_x	40 mL 6 M HCl + 2 g LiF	35 ℃ / 24 h	2 g	40 wt.% TBAOH	200 mg/4 mL 4h Stir
$Ti_3C_2T_x$	40 mL 6 M HCl + 2 g LiF	35 ℃ / 24 h	2 g	Already delaminated (No need)	
V_2CT_x	40 mL 48% HF	RT / 92 h	2 g	40 wt.% TBAOH	200 mg/4 mL 4h Stir
Nb_2CT_x	20 mL 48% HF	55 ℃ / 50 h	2 g	40 wt.% TBAOH	200 mg/4 mL 4h Stir

* RT: Room Temperature

SEM images of the synthesized MAX phases and their corresponding multilayered MXene particles are shown in **Figure 3.3**.
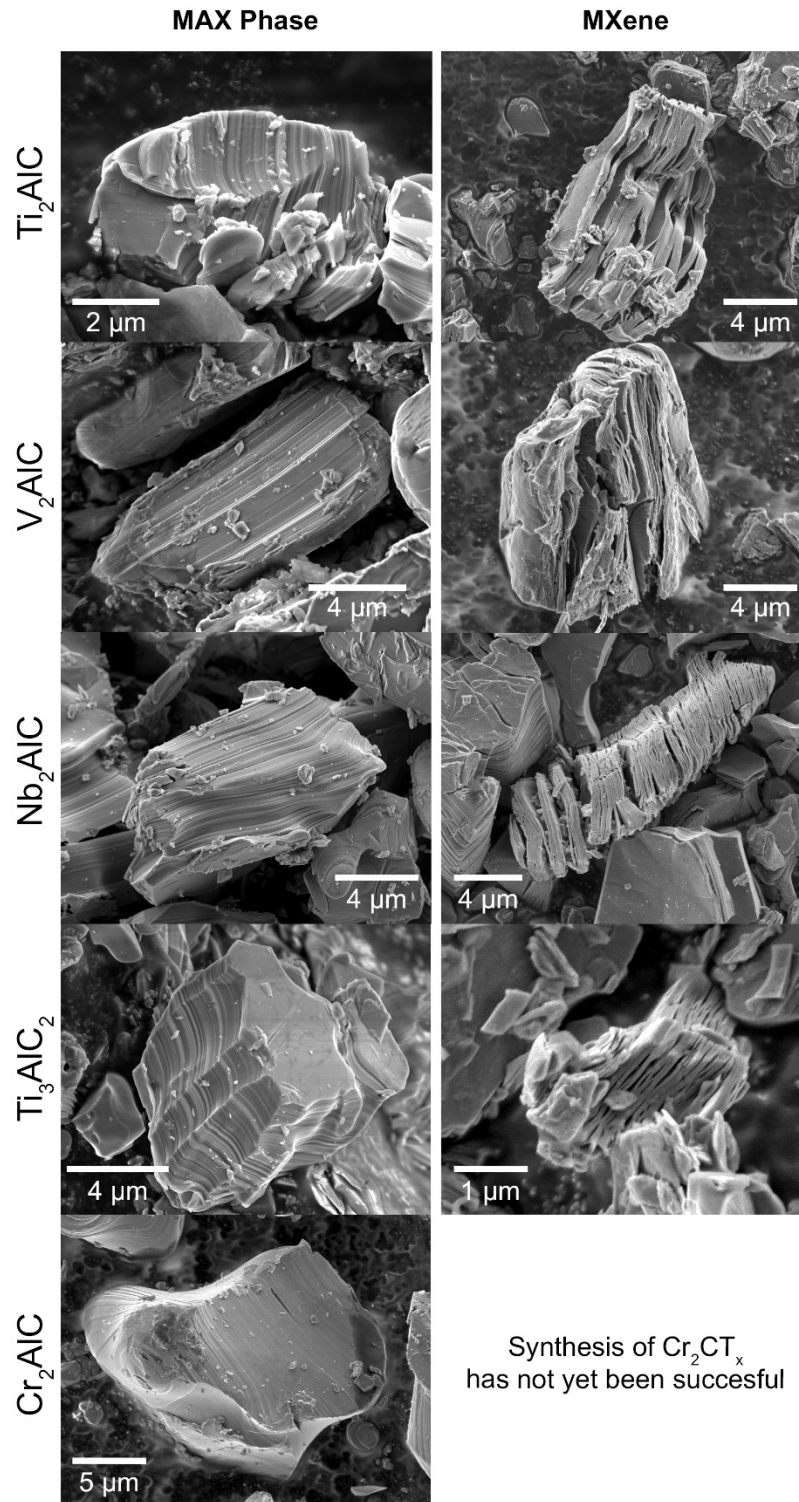
Figure 3.3. SEM images of MAX phases and their corresponding multilayered MXene particles. It is noteworthy that so far neither we nor no one else in literature has been able to selectively etch Cr_2AlC and produce Cr_2CT_x MXene.

Figure 3.4 to 3.6 show the XRD and AFM characterization results for the produced Ti$_3$C$_2$T$_x$, Ti$_2$CT$_x$, and V$_2$CT$_x$, respectively. **Figure 3.7** shows the XRD characterization results for the synthesized Nb$_2$CT$_x$ MXenes. **Figure 3.8** shows different tools and instruments used in my research for materials synthesis and electrochemical cell fabrication and measurements.
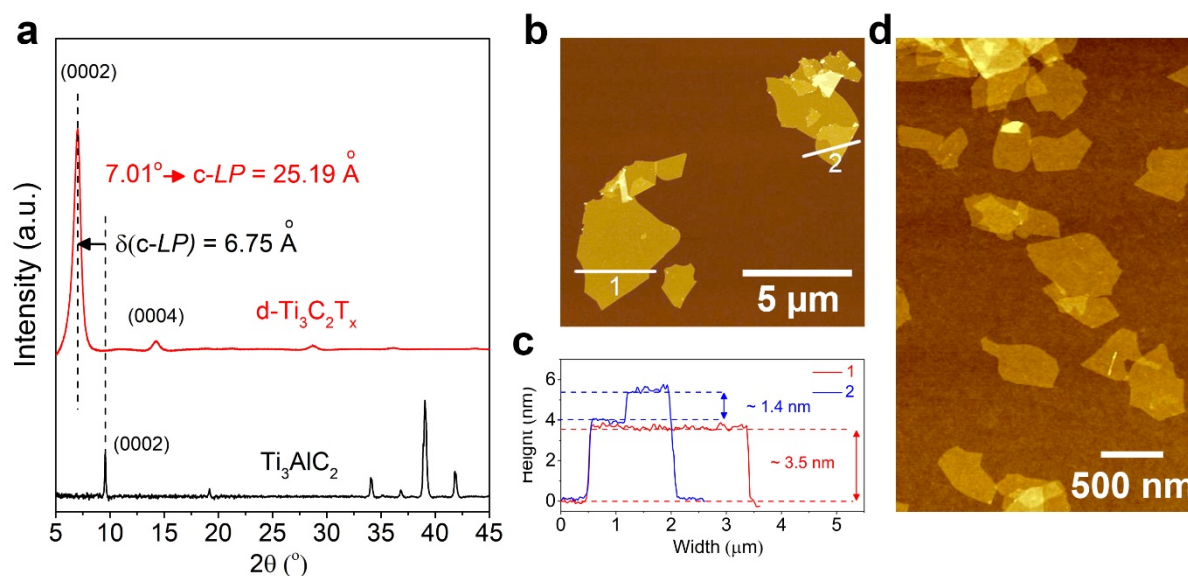
Figure 3.4. XRD and AFM analysis results of the Ti$_3$C$_2$T$_x$ MXene. (a) XRD of the Ti$_3$AlC$_2$ MAX phase and delaminated Ti$_3$C$_2$T$_x$ (prepared by route 2 in Figure 3.2), showing an increase of 6.75 Å in the c-lattice parameter (c-*LP*) upon etching. (b) AFM images of synthesized Ti$_3$C$_2$T$_x$ MXenes before sonication (delamination was done by handshaking). (c) Corresponding height profile of the Ti$_3$C$_2$T$_x$ flakes. (d) AFM image of the Ti$_3$C$_2$T$_x$ flakes after delamination using sonication, showing considerably smaller sizes of the flakes after sonication. Panels "b" and "c" are adapted with permission from ref. 52 (copyright © 2019 American Chemical Society). Panel "d" is adapted by permission from ref. 122 (copyright © 2019 Macmillan Publishers Ltd.).
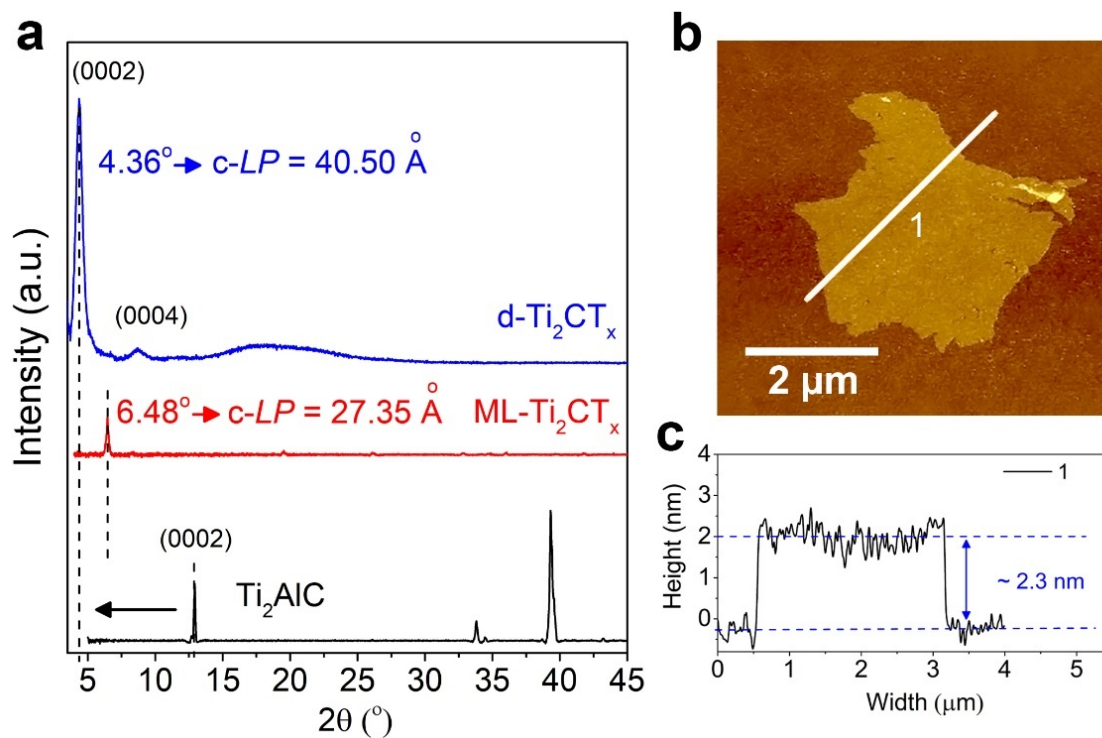
Figure 3.5. XRD and AFM analysis results of the Ti_2CT_x MXene. (a) XRD of the Ti_2AlC MAX phase, multilayered (ML), and delaminated (d-) Ti_2CT_x (prepared by route 1 in Figure 3.2). (b) AFM image of d-Ti_2CT_x MXene flake. (c) Corresponding height profile of the d-Ti_2CT_x flake. Panels "b" and "c" are adapted with permission from ref. 52 (copyright © 2019 American Chemical Society).
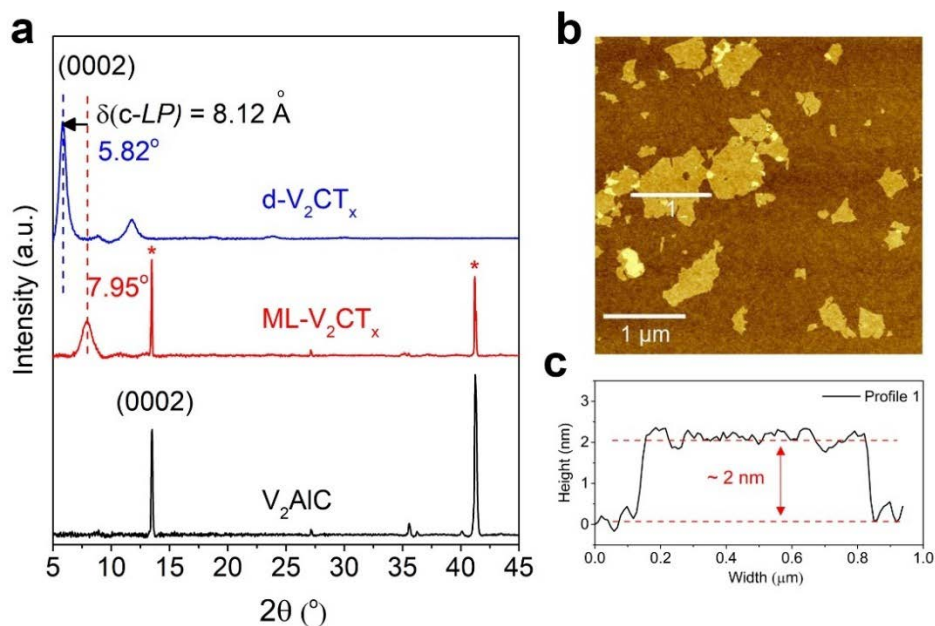
Figure 3.6. XRD and AFM analysis results of the V_2CT_x MXene. (a) XRD of the V_2AlC MAX phase, multilayered (ML), and delaminated (d-) Ti_2CT_x (prepared by route 1 in Figure 3.2). An increase of 8.12 Å was observed after complete delamination of V_2CT_x by TBAOH intercalation. (b) AFM image of d-V_2CT_x MXene flakes. (c) Corresponding height profile of the d-V_2CT_x flake.
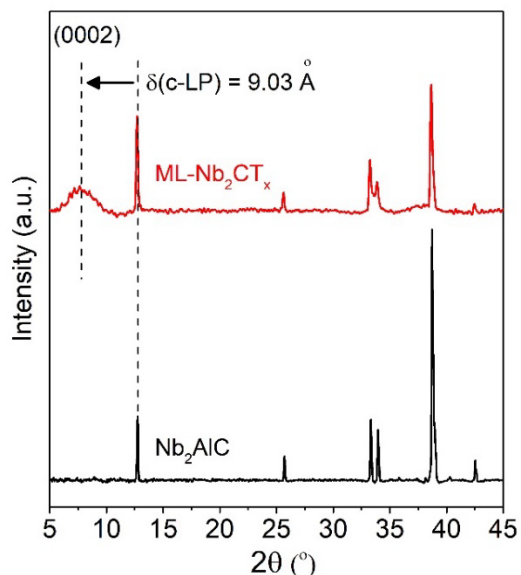
Figure 3.7. XRD patterns of Nb_2AlC MAX phase and multilayered (ML) Nb_2CT_x MXene. We are still working on complete delamination of this MXene.
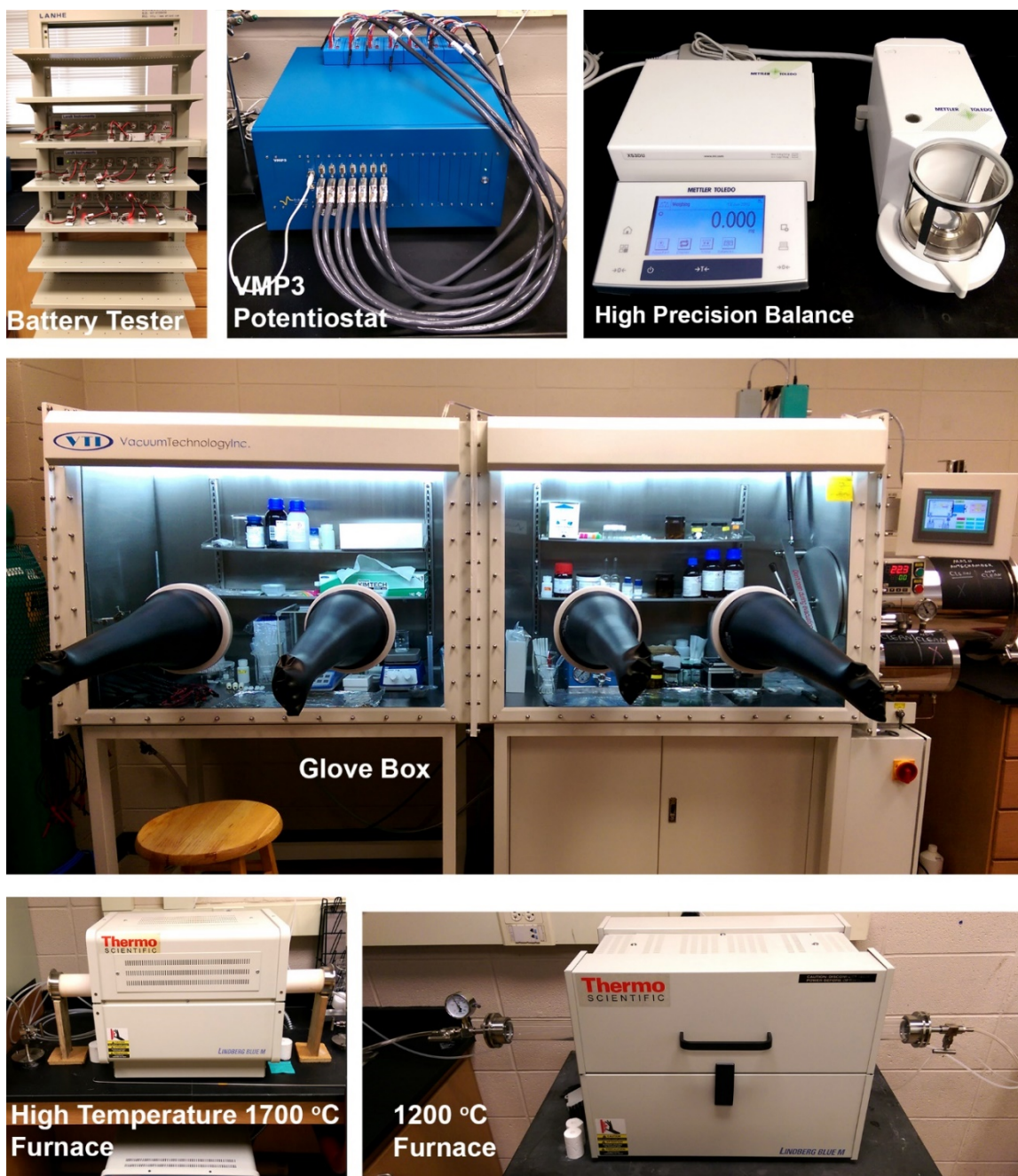
Figure 3.8. Digital photographs of the tools and instruments used for MAX phase and MXene synthesis, as well as electrochemical measurements. From top to bottom: Landt battery tester, BioLogic VMP3 potentiostat, High precision balance, argon-filled glovebox, Thermo Scientific high temperature tube furnace (1700 °C), and Thermo Scientific intermediate temperature tube furnace (1200 °C).

3.4. Electrochemical Measurements and Analyses Techniques

This sections, explains the details for general electrochemical measurements and practices during my Ph.D. research. Specific experiments and methods for different research tasks are explained in more details in the corresponding chapter.

All electrochemical measurements for supercapacitors were done using BioLogic VMP3 potentiostat. As for the battery experiments, cyclic voltammetry (CV) and some galvanostatic charge discharge tests were done using VMP3. Some portions of the charge discharge experiments, particularly for experiments performed using coin cells were also performed using the Landt battery cycler. All supercapacitor experiments in a three- and two-electrode setups were carried out in plastic Swagelok cells where glassy carbon electrodes were used as current collectors for the working and counter electrodes. **Figure 3.9 a** schematically shows the Swagelok setup and **Figure 3.9 b** shows the digital photographs of the cell components, as well as an example of the final assembled cell. Ag wire coated with AgCl immersed in 1 M KCl was used as the reference electrode for all the tests. Working electrodes (WE) were prepared by directly punching the freestanding MXene films into the desired size. A piece of over-capacitive activated carbon film (YP-50) was used as the counter electrode (CE) in the cells. The CE electrode was prepared by mixing a slurry of 95 wt.% activated carbon and 5 wt.% PTFE over the night at 45 °C and then the thick slurry was rolled into freestanding films and punched to the required size for the cell assembly. The size and mass of the CE electrode was controlled to be much higher than the working electrode. Aqueous electrolytes were prepared by solving metal salts in desired molar ratio in DI water as indicated in each chapters' experiments. After preparation of the aqueous electrolytes they were Argon bubbled for at least 2 h to reduce the dissolved oxygen in them, and therefore increase their potential window stability. For the supercapacitor experiments, usually all

cells were initially stabilized by 50 CV cycles at a scan rate of 20 mV s^{-1} prior to electrochemical measurements. CV experiments were done at scan rates ranging from 2 mV s^{-1} to 10 Vs^{-1}. The operating potential window of the MXene electrodes in each electrolyte was determined by using CV test where the potential window was gradually increased until signs of electrolyte decomposition and/or MXene oxidation was observed. In all electrolytes, usually, the upper cut-off potential was found to be the same as open circuit potential (OCP). Electrochemical impedance spectroscopy (EIS) data were collected in the same three-electrode setup, in the 100 mHz to 1,000 kHz frequency range. The EIS experiments were carried out at OCP and the applied potential amplitude was 10 mV. Symmetric supercapacitors were assembled by using V$_2$CT$_x$ films (with equal weight) as both working and counter electrodes to evaluate the performance of fabricated V$_2$CT$_x$ electrodes in full cells (two-electrode setup). The specific capacitance of each cell was calculated based on the total weight (or volume) of both MXene electrodes.

Capacitance and rate-dependence charge storage mechanism calculations. The capacitance of MXene electrodes was calculated from the reduction portion of the CV graphs at different scan rates by using the following equation:[41]

$$C = \frac{1}{\Delta V} \int \frac{j \, dV}{s} \qquad (3.1)$$

where C is the normalized capacitance (F cm^{-3} or F g^{-1}), ΔV is the voltage window (V), j is the current density (mA cm^{-3} or mA g^{-1}), V is voltage (V), and s is the scan rate (mV s^{-1}). The specific energy (E) and power (P) densities of the symmetric cells were calculated from CV graphs at different scan rates using the following equations:[15]

$$E = (\frac{1}{2} \times C \times V^2) / 3600 \quad [\text{Wh cm}^{-3}] \qquad (3.2)$$

$$P = E \times \frac{s}{V} \times 3600 \qquad [\text{W cm}^{-3}] \qquad (3.3)$$

where C is the normalized capacitance of the cell (F cm^{-3}), V is the cell operating potential window (V), and s is the scan rate (V/s).

The kinetics of the charge storage in the electrodes were evaluated at different scan rates by considering a power-law relationship between the current, i, and scan rate, v (i=av^b). A b value of 0.5 corresponds to a diffusion-controlled process and a b value of 1 represents a surface-controlled charge storage mechanism.[63] To distinguish these two processes, the total current value of each potential point was considered to have two different capacitive controlled and diffusion controlled contributions according to the following equation:[41]

$$i(V) = k_1 v + k_2 v^{0.5} \qquad (3.4)$$

where V is the potential and k_1 and k_2 are adjustable variables. $k_1 v$ determines capacitive contribution and $k_2 v^{0.5}$ represents the diffusion-controlled contribution of the total charge stored.

3.5. Structural Characterization Techniques

XRD analyses of the different samples were using Bruker X-ray diffractometer (D8 Discover) with 40 kV and 40 mA Cu-kα radiation at a scan speed of 0.2 seconds per 2θ step, except where indicated otherwise. SEM/EDS analyses of the samples were done using a JEOL JSM-7000F scanning electron microscope equipped with an energy dispersive spectrometer (EDS detector) was used. For atomic force microscopy (AFM) measurements usually the diluted MXene solutions were drop casted on SiO$_2$ coated silicon wafers. Prepared samples were characterized by Park Instruments NX10 AFM using a non-contact mode cantilever. S/TEM and XPS analyses were performed by our collaborators outside of the Auburn University and details of them are explained in experimental section of each chapter.
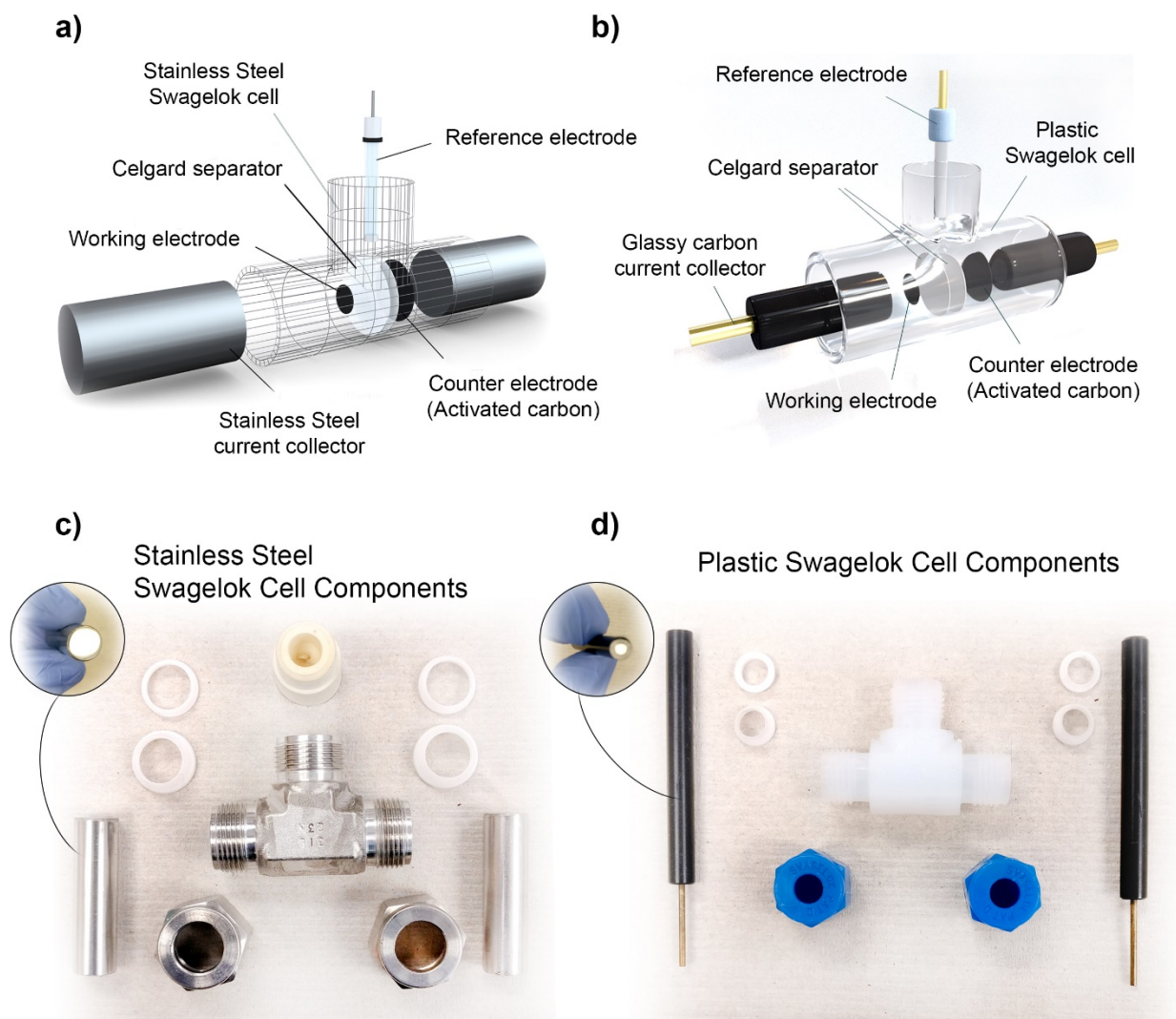
Figure 3.9. Schematic illustration of the three electrode Swagelok setup used in my experiments. The setup is shown for two different type of Swagelok cells: a) for stainless steel (SS) Swagelok cells where SS rods are used as current collectors and b) for plastic Swagelok cells where glassy carbon electrodes were used as current collector. These setups were chosen for each experiment based on the type of the electrolyte and potential window of the electrochemical test. c-d) Digital photographs of the Swagelok cells and their components for SS Cells and Plastic Cells, respectively. Panel "a" is reproduced with permission from ref. 32 (copyright © 2018 Royal Society of Chemistry).

Chapter 4

Electrochemical Properties of MXene-Polyaniline Hybrid Structures

This chapter presents the results of my research on preparation and evaluation of MXene-polyaniline (PANI) hybrid structures as freestanding electrodes for aqueous supercapacitors. My research provide basic understanding on rational design and optimization of MXene and organic materials' hybrid structures for applications in fast energy storage devices. Here it is shown that the amount of the PANI, an example of conductive polymer materials, inside the structure of the final hybrid material plays an important role in improving the charge storage properties of MXenes. The final goal of this research was to identify the optimum synthesis condition and electrode composition for the fabricated MXene/PANI hybrid materials as well as identifying the role of polymer in the charge storage of the MXene material. The results of this chapter are published as a peer-reviewed article (ref. 32) titled: "Thick and Freestanding MXene/PANI Pseudocapacitive Electrodes with High Specific Capacitance", in the Journal of Materials Chemistry A, 2018, 6 (44), 22123-22133.

4.1. Introduction

In this research, a design strategy for fabrication of hybrid electrodes of delaminated $Ti_3C_2T_x$ MXene and polyaniline (PANI) with outstanding electrochemical performances is explained. Hybrid $Ti_3C_2T_x$/PANI sheets were synthesized by *in situ* and oxidant-free polymerization (i. e., without use of additional oxidizing chemicals) of aniline monomers on the

surface of single-layer $Ti_3C_2T_x$ sheets. It is shown that controlling the amount of deposited polymer is a critical parameter affecting the electrochemical performance of the electrodes. By minimizing the amount of polymer deposited on the surface of $Ti_3C_2T_x$ flakes, it was possible to fabricate electrodes with high ion transport properties and improved high-rate electrochemical performance compared to previously reported electrodes based on MXenes. An important advantage of the produced hybrid electrodes compared to pristine $Ti_3C_2T_x$ electrodes is that they can be fabricated in very high thicknesses without significantly scarifying their electrochemical performance. For example, a 13 µm thick $Ti_3C_2T_x$/PANI hybrid film with a mass loading of 3.3 mg cm^{-2} delivered specific capacitances as high 458 F g^{-1} and 1163 F cm^{-3}, a performance similar to thin $Ti_3C_2T_x$ electrodes while maintaining a better rate-capability at higher scan rates compared to them.

4.2. Experimental Section

Preparation of $Ti_3C_2T_x$/PANI Hybrid Electrodes. To prepare the MXene/PANI hybrids, first 300 µL of aniline monomer (99+%, Alfa Aesar) was dissolved in 20 mL solution of 1M HCl. Then, the aniline/HCl solution was slowly added to a dispersion $Ti_3C_2T_x$ in water (with the desired aniline to MXene weight ratio), and the mixture was stirred for 10 minutes. The addition of aniline/HCl solution to the MXene dispersion resulted in the precipitation and crumpling of $Ti_3C_2T_x$ sheets after absorption of aniline. The prepared solutions with different MXene to aniline ratios were sealed and kept at ~ 4 ºC for 5h. The final solutions were centrifuged at 3500 rpm for 1 minute and washed with DI water two times to remove any residual and unreacted aniline monomer. Each time 45 mL of water was added to the centrifuge tube and after the centrifugation the obtained clear supernatant was decanted. After the final wash, $Ti_3C_2T_x$/PANI hybrid sheets were dispersed in ~30 mL DI water by handshaking and the dispersion was filtered on a Celgard®

membrane filter to fabricate freestanding MXene/PANI hybrid films. The hybrid films were punched into desired sizes and were directly used as electrodes for electrochemical measurements.

It is noteworthy that based on my experience, simply mixing the aniline monomer with $Ti_3C_2T_x$ MXene solution could also result in the polymerization of the monomer on the surface of MXene sheets. To do this, first the aniline should be dispersed in a proper amount of water to obtain a stable and uniform dispersion of aniline monomers in the water. Then the prepared solution of aniline can be mixed with MXene solution in desired weight ratio. The mixture requires to be stirred between 12 h to 24 h to obtain the MXene and PANI hybrid samples. The time of the stirring effects the polymerization, however, in my experiments I noticed that this method usually decreases the quality of the produced hybrid materials, since stirring the mixture solution in large amount of water for that elongated period, can also oxidize MXene sheets. Therefore, the first method was chosen for sample preparation.

The synthesis steps for $Ti_3C_2T_x$ MXene solution preparation, as well as the procedure for preparation of the $Ti_3C_2T_x$ MXene/PANI hybrid freestanding films through *in situ* and oxidant-free polymerization of the aniline monomers at the surface of MXene sheets are shown schematically in **Figure 4.1**.[32]
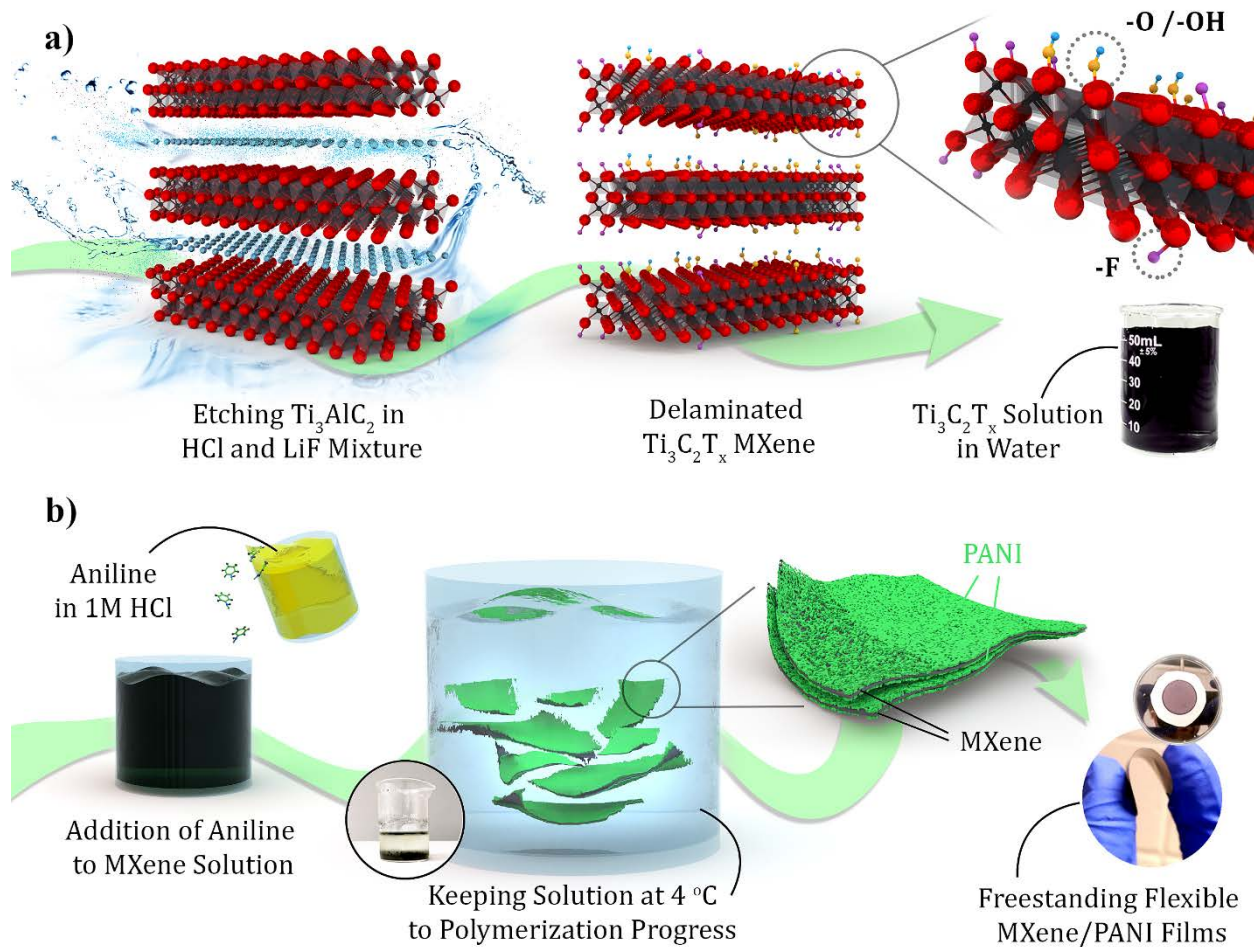
Figure 4.1. Schematic illustration of the synthesis of $Ti_3C_2T_x$ MXene by selective etching of Al layer for the structure of layered Ti_3AlC_2 MAX phase (shown in a). After the synthesis the surface of $Ti_3C_2T_x$ is terminated with various functional groups. b) Schematic representation of the process used for the synthesis of $Ti_3C_2T_x$/PANI hybrid electrodes. Adapted with permission from ref. 32 (copyright © 2018 Royal Society of Chemistry).

Electrochemical Measurements. All electrochemical experiments were carried out by a BioLogic VMP3 potentiostat in a three-electrode setup using Swagelok cells. The details of electrochemical cell fabrication, capacitance calculations, and other electrochemical analyses can

be found in Chapter 3 (section 3.4). The working electrode was prepared by punching the filtered MXene and MXene/PANI films. In all experiments, the electrolyte was 3M H_2SO_4 solution and two layers of Celgard® membranes were used as separators. Cyclic voltammetry (CV) experiments were performed at scan rates ranging from 2 mV s^{-1} to 10 V s^{-1} in a -0.7 V to +0.2 V potential window (vs. Ag/AgCl). All cells were first pre-cycled for 50 times at scan rate of 20 mV s^{-1} before any further measurements. To evaluate the cyclic performance of the electrodes, CV experiments were carried out at a scan rate of 20 mV s^{-1} over 10,000 cycles. Galvanostatic charge/discharge experiments were performed between -0.7 V to +0.2 V (V vs. Ag/AgCl) at current densities of 5, 10, 20, 30, and 50 A g^{-1}.

Materials Characterization Techniques. Structure and morphology of the synthesized MXene and MXene/Polymer hybrid films were characterized using a Bruker X-ray diffractometer (40 kV and 40 mA Cu-kα radiation) and JEOL JSM-7000F scanning electron microscope (SEM) equipped with an energy dispersive spectrometer (EDS). XRD analysis was done directly on the freestanding MXene films with a scan speed of 2 degrees/min. To investigate the polymerization of aniline monomer on $Ti_3C_2T_x$ nanosheets, Fourier transform infrared spectroscopy (FTIR) measurements were carried out using Perkin Elmer spectrum 100 ATR-FTIR spectrometer with a resolution of 4 cm^{-1}. Raman measurements were performed using a Renishaw InVia Qontor Raman Spectrometer with a 532-nm laser as the excitation source. For all measurements a 2400 L mm^{-1} grating was used in a range of 100–3200 cm^{-1} using a 100x long-distance objective lens. The spectra were recorded using 10% of the laser power, an exposure time of 10 seconds, and 10 accumulations for each spectrum. Thermogravimetric analysis (TGA) was performed using a TA instruments Q50 under O_2 atmosphere. First the temperature was ramped up to 120 ℃ with a heating rate of 10 ℃/min and the sample was kept at this temperature for 30 min to evaporate all

the moisture. Then, the sample was heated up to 800 ℃ with the same rate and was hold at that temperature for 45 min. Atomic force microscope (AFM) measurements were carried out by Park Instruments NX10 AFM using a non-contact mode cantilever. AFM samples were prepared by drop casting diluted MXene solutions on silicon wafers or immersing silane-coated silicon wafers in well-dispersed and diluted solutions of $Ti_3C_2T_x$ or $Ti_3C_2T_x$/PANI.

4.3. Results and Discussions

The chemical deposition of PANI on a substrate or on the surface of different materials usually follows an oxidative polymerization process, where an oxidizing agent, such as ammonium persulfate (APS), is used to initiate the polymerization process.[123–126] The protonation of nitrogen atoms in the deposited polymer and its doping with anions (such as Cl⁻) are important for achieving high quality conductive PANI through chemical deposition methods.[123] However, as explained further below, during our initial studies in this work, we found that aniline can spontaneously polymerize on surface of $Ti_3C_2T_x$ sheets even in the absence of an oxidant. This is in agreement with previous reports that have shown oxidant-free deposition of PPy and PEDOT on $Ti_3C_2T_x$ nanosheets.[31,72] Chen et al. used a combination of experimental and theoretical studies to show that 3,4-ethylene dioxythiophene (EDOT) monomer can polymerize on surface of MXene as long as a charge transfer occurs between the monomer and MXene and the energy cost for polymerization decreases as the charge loss from monomer increases.[31,72] **Figure 4.1 a** schematically shows the process used for synthesis of $Ti_3C_2T_x$ and $Ti_3C_2T_x$/PANI hybrids. PANI was deposited on the synthesized MXene sheets by adding a solution of aniline dissolved in 1M hydrochloric acid (HCl). As shown in **Figure 4.1 b** after the gradual addition of the prepared solution to $Ti_3C_2T_x$ dispersion, the absorption of aniline by MXene flakes and their crumpling due to low pH of the mixture solution results in the flocculation of a hybrid material. Importantly, the color of supernatant in the

54

MXene/aniline mixture solution is clear in contrast to the yellowish color of solution of aniline in HCl. The crumpled $Ti_3C_2T_x$/aniline solution was kept at a low temperature (~ 4 ℃) to complete the polymerization process. Then, the crumpled hybrid material was dispersed in water by handshaking and used for fabrication of freestanding films through vacuum filtration.

For comparison, freestanding films of pristine $Ti_3C_2T_x$ as well as $Ti_3C_2T_x$ sheets treated in 1 M HCl solutions were also prepared using the same fabrication method. It should be noted that addition of HCl solution to $Ti_3C_2T_x$ dispersions also results in crumpling of MXene flakes.[127] **Figure 4.2 a** shows the X-ray diffraction (XRD) patterns of the films prepared using $Ti_3C_2T_x$/PANI crumpled flakes, $Ti_3C_2T_x$ crumpled with HCl, and pristine $Ti_3C_2T_x$. As shown in this figure, for the $Ti_3C_2T_x$/PANI hybrid film the peak corresponding to the (0002) plane of MXene downshifts to about 6.53º from its position for the pristine $Ti_3C_2T_x$ (at around 6.9º).
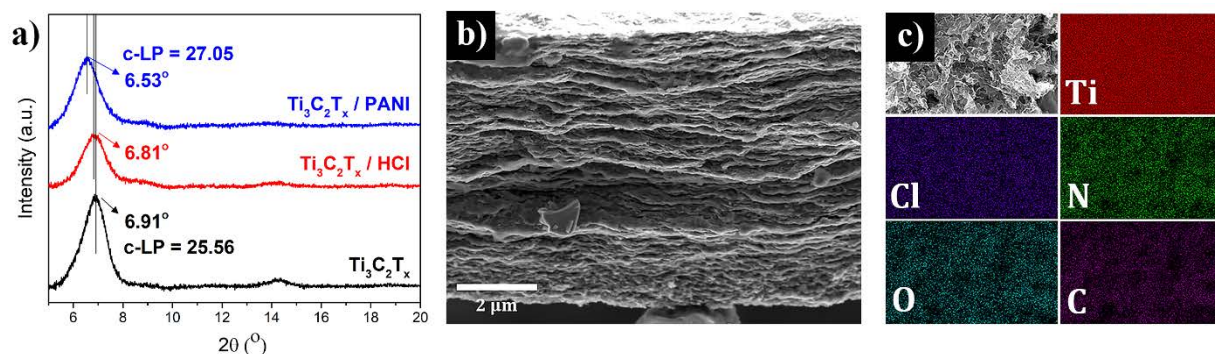
Figure 4.2. Characterization results for MXene/PANI hybrids. a) XRD patterns of freestanding films of $Ti_3C_2T_x$, $Ti_3C_2T_x$ crumpled with HCl, and Ti_3CT_x/PANI hybrids films. The (0002) peak of the MXene shifts from 6.91º to about 6.53º as a result of PANI deposition on MXene flakes. b) A cross-sectional SEM image of the fabricated hybrid films. c) EDS mapping of Ti_3CT_x/PANI electrodes showing presence of N from the deposited PANI along with Ti, Cl, O and C from $Ti_3C_2T_x$. Adapted with permission from ref. 32 (copyright © 2018 Royal Society of Chemistry).

This shift in the (0002) basal planes peak corresponds to a 1.5 Å increase in the c-lattice parameter (c-LP) and 0.75 Å increase in the d-spacing after the PANI deposition. However, the

calculated increase in d-spacing was only about 0.18 Å in case of the sample prepared after treatment in HCl solution. (Fig. S1). The cross-sectional scanning electron microscopy (SEM) image of a $Ti_3C_2T_x$/PANI film shows the layered structure formed during the directional assembly of the hybrid flakes using vacuum filtration (**Figure 4.2 b**). The energy dispersive spectroscopy (EDS) mapping of the top surface of the hybrid films showed the presence of nitrogen in the electrodes after PANI deposition (**Figure 4.2 c**). EDS also showed a decrease in the oxygen content of the MXene to 15.7 at.% from 25 at.% before PANI deposition (**Table 4.1**).

Table 4.1. EDS results showing atomic percentage of different elements present in the pristine $Ti_3C_2T_x$ and $Ti_3C_2T_x$/PANI hybrids for a sample prepared with high loading of aniline monomer. Adapted with permission from ref. 32 (copyright © 2018 Royal Society of Chemistry).

	Ti	O	Cl	F	N
As prepared MXene	23.69%	24.59%	2.18%	10.22%	0%
After PANI deposition	9.88%	15.71%	0.89%	4.13%	33.3%

It is also worth noting that in order to understand the effect of the amount of deposited PANI on the performance of electrodes, hybrid $Ti_3C_2T_x$/PANI flakes were prepared using different $Ti_3C_2T_x$ to aniline ratios in the synthesis process. As expected, further increase in interlayer spacing was observed for samples synthesized using a higher ratio of aniline and the largest increase in d-spacing (~6.12 Å) was observed for a sample prepared using a MXene to aniline ratio of 1:500. This is shown in **Figure 4.3** where the XRD patterns of the films prepared using MXene to aniline weight ratios of 1:2, 1:4, and 1:500 are shown. As the ratio of aniline increases, the

(0002) peak of MXene in the fabricated freestanding film shifts to lower angles which is an indication of increased interlayer spacing of $Ti_3C_2T_x$ flakes. For a film prepared by a precursor solution with very high aniline content (1:500 sample), the (0002) peak shifted down to 4.7° corresponding to a c-lattice parameter (c-LP) of 37.8 Å.
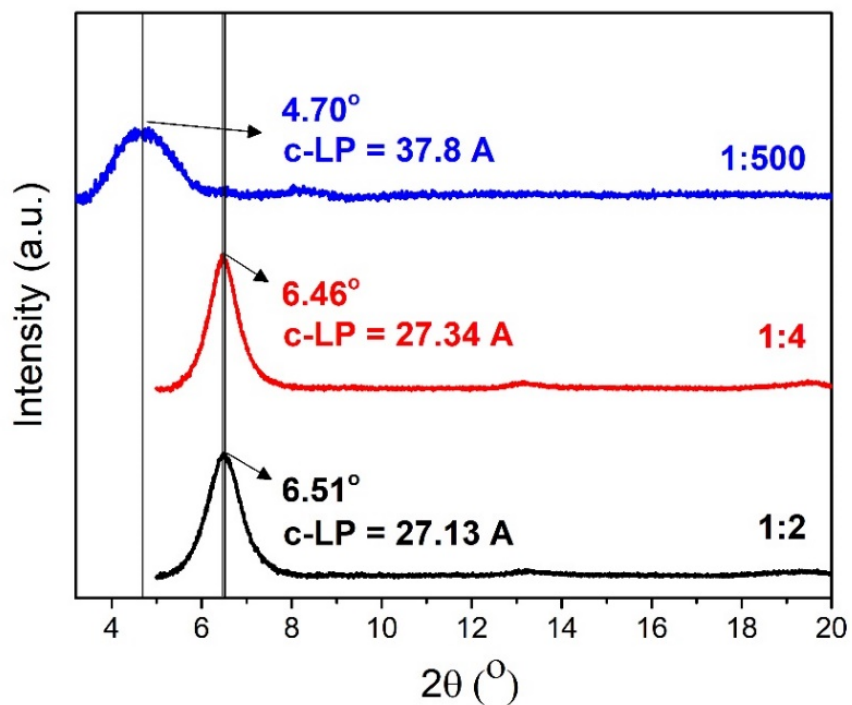
Figure 4.3. XRD patterns of the hybrid $Ti_3C_2T_x$/PANI films prepared using different MXene to aniline ratios of 1:2, 1:4, and 1:500. By increasing the aniline to MXene ratio, the (0002) peak slowly shifts to lower angles and for very high ratio of 1:500 the intensity of MXene peaks decrease due to loss of ordering in the MXene/PANI films. Adapted with permission from ref. 32 (copyright © 2018 Royal Society of Chemistry).

In fact, the amount of PANI deposited on the MXene sheets can be precisely controlled by controlling the $Ti_3C_2T_x$ to aniline ratio during the synthesis of hybrid sheets. This allows preventing the restacking of the $Ti_3C_2T_x$ sheets by depositing a very thin layer of PANI on their

surface and reducing the amount of the inactive component (dead weight) in the electrodes. The results of thermogravimetric analysis (TGA) are shown in **Figure 4.4** for two different MXene to Aniline weight rations of 1:2 and 1:500. As it can be seen, the amount of PANI in the hybrid $Ti_3C_2T_x$/PANI electrodes with weight ratio of 1:2 for MXene to aniline is only about ~3.2 wt.%, while for the 1:500 sample the weight loss attributed to PANI is around 20%. These are in good agreement with larger d-spacing from the XRD results and indicate an increased amount of the deposited PANI.

The best electrochemical performance, however, was achieved for samples with $Ti_3C_2T_x$ to aniline ratio of 1:2. The change in the capacitance of the hybrid materials with respect to the amount of the aniline used in the precursor mixture are shown in **Figure 4.5 a**. As it can be seen, the 1:2 ratio sample shows the best overall performance while increasing the ratio to 1:5 and 1:10 results in the capacitance of the hybrid electrodes. The details and underlying reasons for the decrees in the capacitance will be explained later on this chapter, however, here I briefly note that the deposited PANI on MXene sheets does not directly contribute to the charge storage in the fabricated electrode as it is not electrochemically active in the potential window that $Ti_3C_2T_x$ is active in sulfuric acid electrolytes. PANI only acts as a conductive spacer between the MXene layers. Therefore, the presence of excessive amounts of PANI in the hybrid electrodes' structure will increase the inactive component (deadweight) of the electrodes and reduces the specific capacitance of the hybrid material. This explains why the capacitance of the electrode with MXene to aniline ratios of 1:5 and 1:10 is lower than the electrodes with a ratio of 1:2.
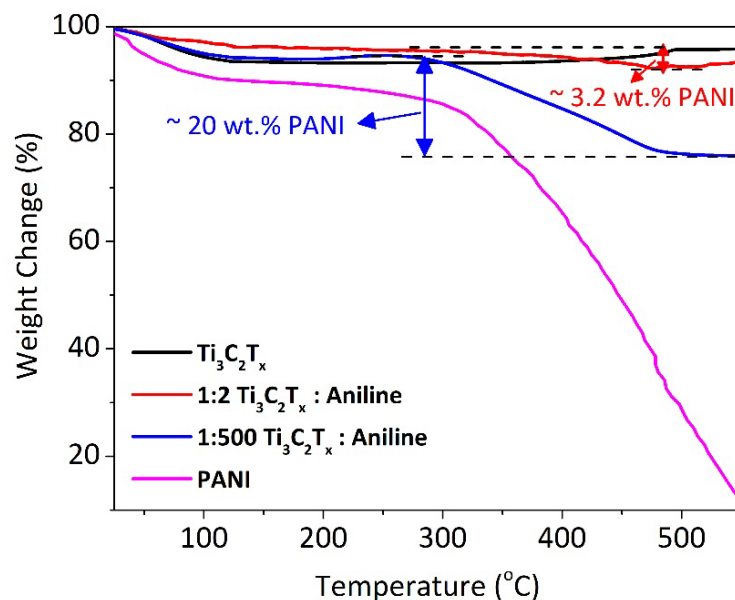
Figure 4.4. Thermogravimetric analysis (TGA) data of MXene/PANI samples. TGA data are shown for a pristine $Ti_3C_2T_x$ films, a hybrid film prepared using the $Ti_3C_2T_x$ to aniline ratio of 1:2, a hybrid film prepared using the $Ti_3C_2T_x$ to aniline ratio of 1:500, and pure PANI. The TGA experiments were carried out under O_2 atmosphere. Adapted with permission from ref. 32 (copyright © 2018 Royal Society of Chemistry).
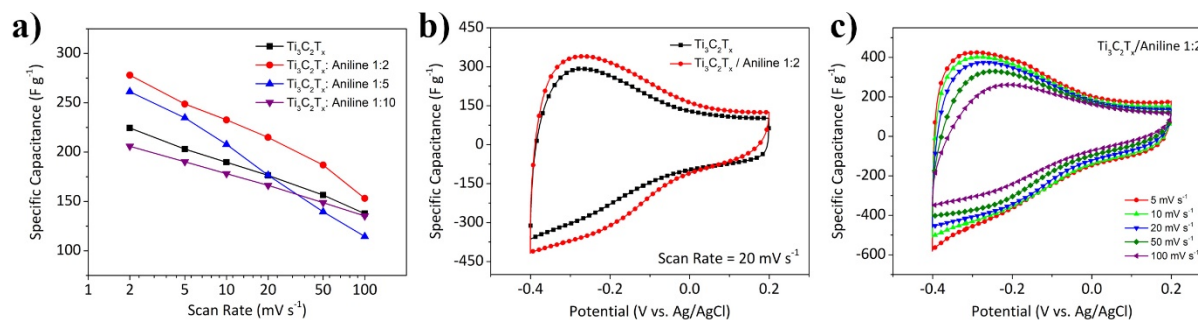
Figure 4.5. Electrochemical performance of hybrid electrode prepared using various MXene to aniline ratios. These experiments were done in our earlier electrochemical tests and using stainless steel rods as current collectors in a narrower potential window. a) Capacitance of different hybrid films at different scan rates. A sample prepared using MXene to aniline ratio of 1:2 shows the highest specific capacitance at all scan rates. b) CV curves of a $Ti_3C_2T_x$ electrode and $Ti_3C_2T_x$/aniline (1:2) hybrid electrode. c) CV curves of $Ti_3C_2T_x$/PANI electrode at different scan rates of 5 mV s^{-1} to 100 mV s^{-1} in a potential window of -0.4 V to +0.2 V (V vs Ag/AgCl) in 1 M H_2SO_4. Adapted with permission from ref. 32 (copyright © 2018 Royal Society of Chemistry).

Figures 4.5 b and c show the comparison between the CVs of the pristine $Ti_3C_2T_x$ with that of 1:2 hybrid material, and the CVs of the 1:2 hybrid material at different scan rates in a narrow potential window of -0.4 V to 0.2 V (V vs Ag/AgCl), respectively. As it can be seen improved capacitive performance of the PANI hybrid samples are notable in this CV experiments that were done initially using the SS Swagelok cell setup. Therefore, $Ti_3C_2T_x$: Aniline samples with a ratio of 1:2 (referred to as $Ti_3C_2T_x$/PANI in the following) were selected for detailed characterization.

The Fourier transform infrared spectroscopy (FTIR) spectra of a $Ti_3C_2T_x$/PANI film and a pristine $Ti_3C_2T_x$ are shown in **Figure 6**. After PANI deposition, the intensities of absorption bands corresponding to O, OH and F surface functional groups of $Ti_3C_2T_x$ (1651, 1437, 1379, 1362, and 1081 cm^{-1})[128,129] are decreased, which is consistent with the decrease in the measured F and O content shown by EDS. Furthermore, a few new bands appear in the spectrum of the hybrid films that suggest the deposition PANI on the surface of MXene sheets. These include the bands corresponding to C=C stretching vibrations of quinoid and benzenoid rings at 1546 and 1453 cm^{-1}, respectively, and the C-N stretching vibrations at 1303 and 1228 cm^{-1}. The bands corresponding to the C-H stretching of the aromatic amine appear at 1145 and 1136 cm^{-1} and the peak at 802 cm^{-1} can be assigned to aromatic C-H out-of-plane bending vibration.[130]

For comparison, FTIR analysis was also performed on a $Ti_3C_2T_x$/PANI hybrid film with higher mass loading of deposited PANI prepared using MXene to aniline weight ratio of 1:500 (**shown in Figure 4.7**). As expected, the peaks related to polymer were intensified in this sample. The peak at 1566 cm^{-1} corresponds to C=C stretching vibrations of quinonoid ring and the peaks at 1366 cm^{-1} and 1217 cm^{-1} correspond to C-N stretching vibrations. The peak at 1164 cm^{-1} can be assigned to C-H stretching of aromatic amine. Also, the transmittance peaks observed at 106 cm^{-1} and 802 cm^{-1} correspond to C-H out-of-plane vibration of the benzene ring.
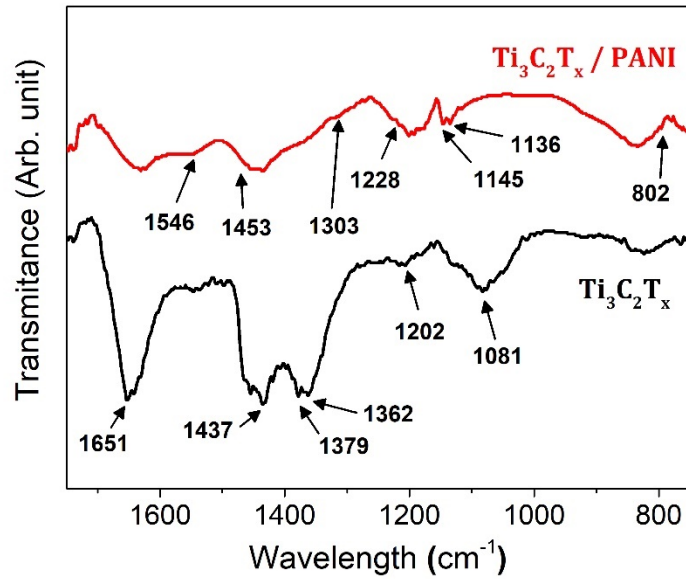
Figure 4.6. FTIR spectra of a delaminated $Ti_3C_2T_x$ film and a $Ti_3C_2T_x$/PANI hybrid film. Adapted with permission from ref. 32 (copyright © 2018 Royal Society of Chemistry).
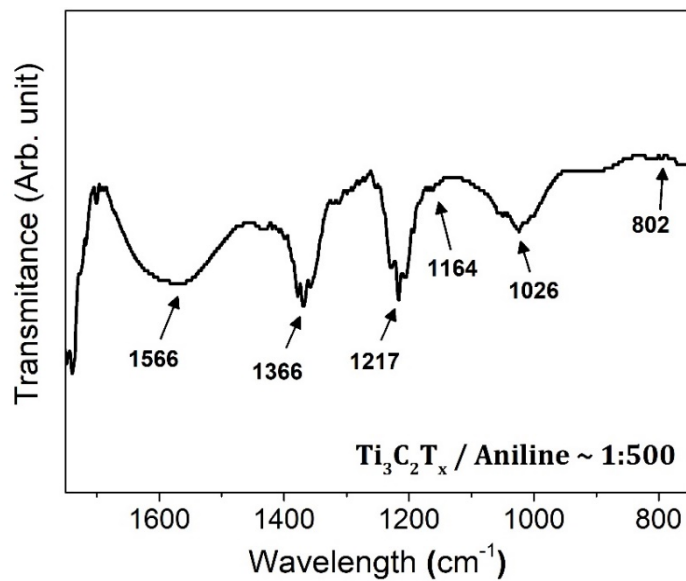
Figure 4.7. FTIR spectrum of $Ti_3C_2T_x$/PANI hybrid films prepared using MXene to aniline ratio of 1:500. Adapted with permission from ref. 32 (copyright © 2018 Royal Society of Chemistry).

Raman analysis of Ti$_3$C$_2$T$_x$/PANI hybrid films (**Figure 7**) showed decreased intensity of MXene peaks after PANI deposition as well as appearance of main characteristic peaks of PANI at 1160 and 1185 cm^{-1} (C-H stretching vibration of benzenoid ring), 1497 cm^{-1} (C=N stretching of quinoid ring), and 1595 cm^{-1} (C-C stretching of benzenoid ring).[78,125] Also, the two newly peaks observed at 1356 and 1398 cm^{-1} indicate the presence of PANI in its highly conductive emeraldine form.[125]
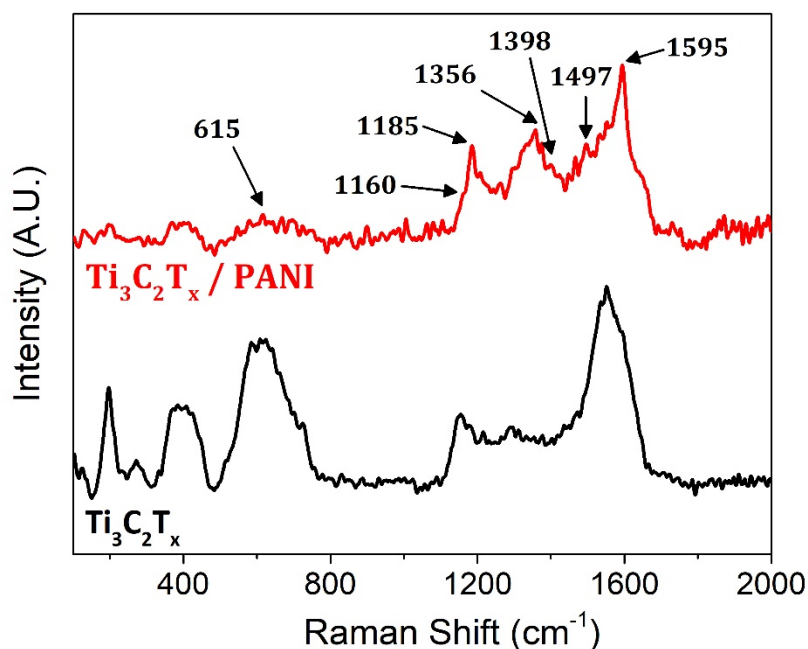
Figure 4.8. Raman Spectra of a delaminated Ti$_3$C$_2$T$_x$ film and a Ti$_3$C$_2$T$_x$/PANI hybrid film. Adapted with permission from ref. 32 (copyright © 2018 Royal Society of Chemistry).

Furthermore, atomic force microscopy (AFM) analysis of $Ti_3C_2T_x$ flakes before and after aniline polymerization confirmed the deposition of PANI on the MXene flakes. The results of AFM analyses are shown in **Figure 4.9**.
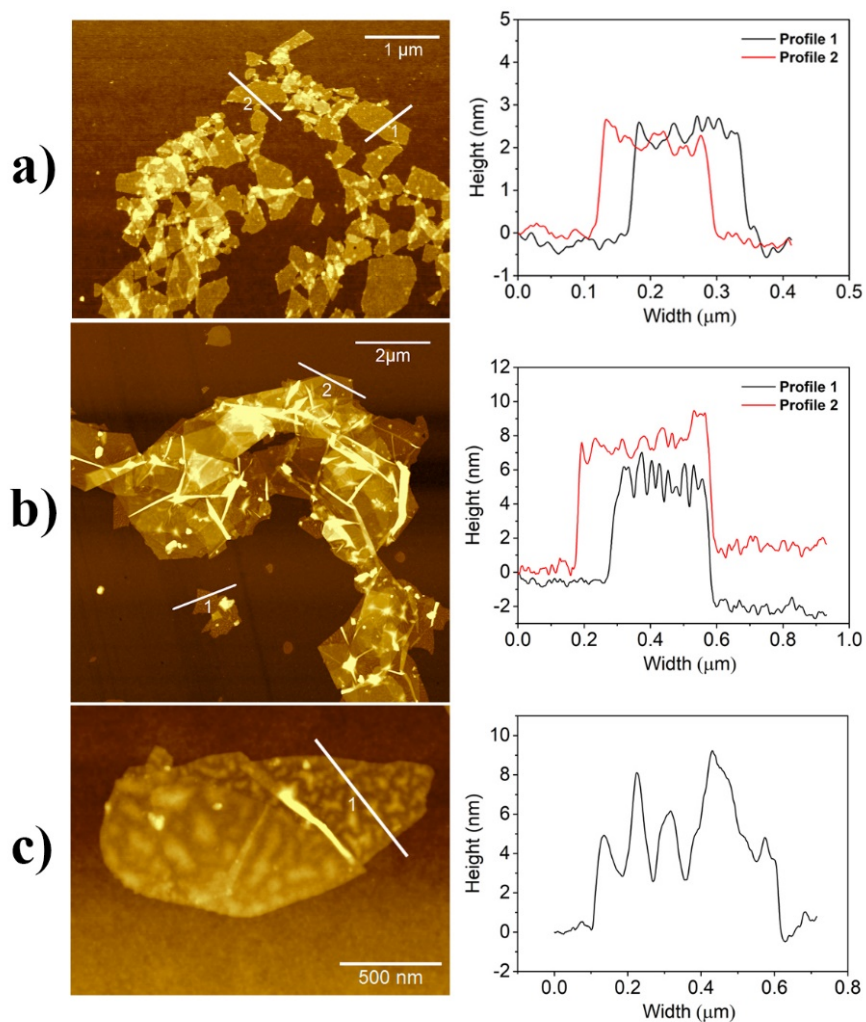
Figure 4.9. Atomic force microscopy (AFM) images and corresponding height profiles for MXene ad MXene/PANI. a) as synthesized $Ti_3C_2T_x$. b) and c) $Ti_3C_2T_x$/PANI hybrids (with 1:2 MXene to aniline ratio) prepared in this study. The formation of island shape PANI chains on MXene flakes can be seen in these images. Thickness of single layer flakes of $Ti_3C_2T_x$ is ~2.7 nm. However, after polymerization of aniline on surface of MXene, the functionalized $Ti_3C_2T_x$ sheets are crumpled and their thicknesses increases to about ~6 nm. Adapted with permission from ref. 32 (copyright © 2018 Royal Society of Chemistry).

We speculate that deposition of PANI on the surface of $Ti_3C_2T_x$ sheets follows the charge transfer induced polymerization mechanism previously proposed for the polymerization of EDOT on the surface of MXene.[72] **Figure 4.10** schematically shows the suggested mechanism for the polymerization of aniline on the surface of $Ti_3C_2T_x$ flakes. Polymerization starts after the oxidation of aniline by the oxygen and hydroxyl functional groups present on the surface of $Ti_3C_2T_x$, which produces aniline cation radicals and/or neutral radicals.[123,131] The oxidation of aniline is the rate-liming step of the polymerization and after its completion the polymerization process can continue by the electrophilic substitution of the hydrogen atom in the benzene rings of the oxidation products to form aniline dimers. Since oxidation potential of produced dimers is much lower than that of aniline monomer, upon formation, the dimers can quickly oxidize and react with other aniline monomers through subsequent oxidation or deprotonation to form oligomers and polymer.[131]
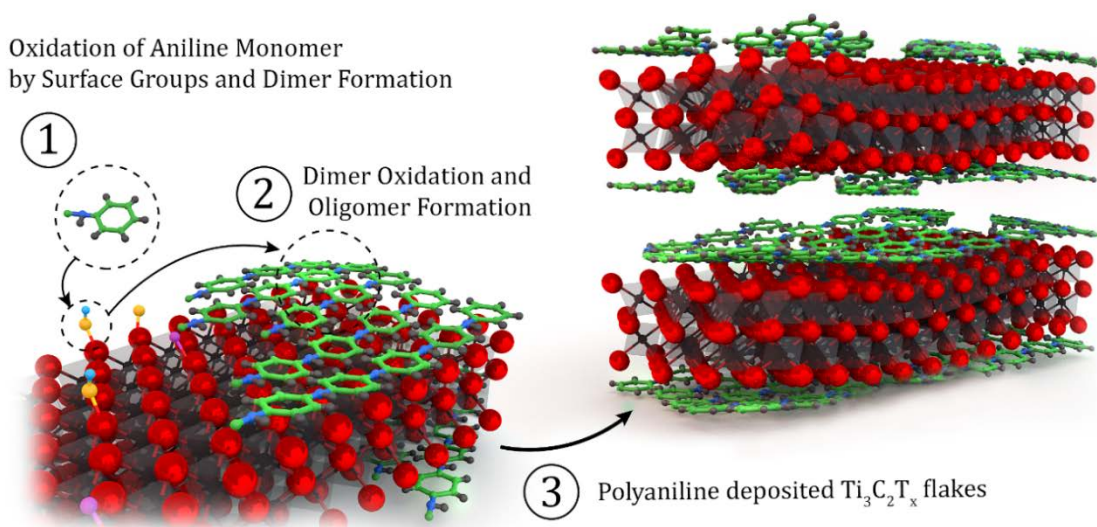
Figure 4.10. Suggested mechanism for polymerization of aniline on the surface of $Ti_3C_2T_x$ MXene. (1) Hydroxyl and oxygen surface groups initiate oxidation of aniline and the oxidation products form dimers at the surface of MXene. (2) Produced dimers are oxidized to form oligomers and polymers. (3) PANI is deposited on the surface of $Ti_3C_2T_x$ flakes. Adapted with permission from ref. 32 (copyright © 2018 Royal Society of Chemistry).

The electrochemical characterization of the fabricated hybrid films was performed using a three-electrode setup with glassy carbon current collectors in 3 M H_2SO_4 solution as the electrolyte. Glassy carbon electrodes have a large overpotential for hydrogen evolution reaction and using these electrodes instead of the more commonly used stainless steel current collectors allows accessing a larger operating potential window for $Ti_3C_2T_x$ in the sulfuric acid electrolytes.[17] **Figure 4.11 a** shows cyclic voltammetry (CV) profiles of a freestanding $Ti_3C_2T_x$/PANI electrode with a thickness of ~4 µm (mass loading of 1.34 mg cm^{-2}) collected at scan rates ranging from 5 mV s^{-1} to 1,000 mV s^{-1}. The CV curves recorded at low scan rates show the signature redox peaks of $Ti_3C_2T_x$ and, as expected, at higher scan rates the redox peaks become broader.

At a scan rate of 2 mV s^{-1}, a specific capacitance of ~503 F g^{-1} (or ~1682 F cm^{-3}) was calculated for the $Ti_3C_2T_x$/PANI hybrid electrode. At the time of the publication of this work, the reported gravimetric capacitance was the highest capacitance value reported for MXene-based electrodes surpassing those previously reported for MXene/rGO and MXene hydrogel electrodes with comparable electrode thicknesses.[17,76] In addition, the $Ti_3C_2T_x$/PANI electrode showed a very high rate-handling capability. An electrode tested at various scan rates retained about 60% (~300 F g^{-1}, 1,000 F cm^{-3}) and 40% (~203 F g^{-1}, 677 F cm^{-3}) of its low scan rate capacitance at higher scan rates of 100 mV s^{-1} and 1,000 mV s^{-1}, respectively (**Figure 4.11 c**). Even at an extremely high scan rate of 10 Vs^{-1}, the hybrid electrode showed a capacitance of ~80 F g^{-1}.
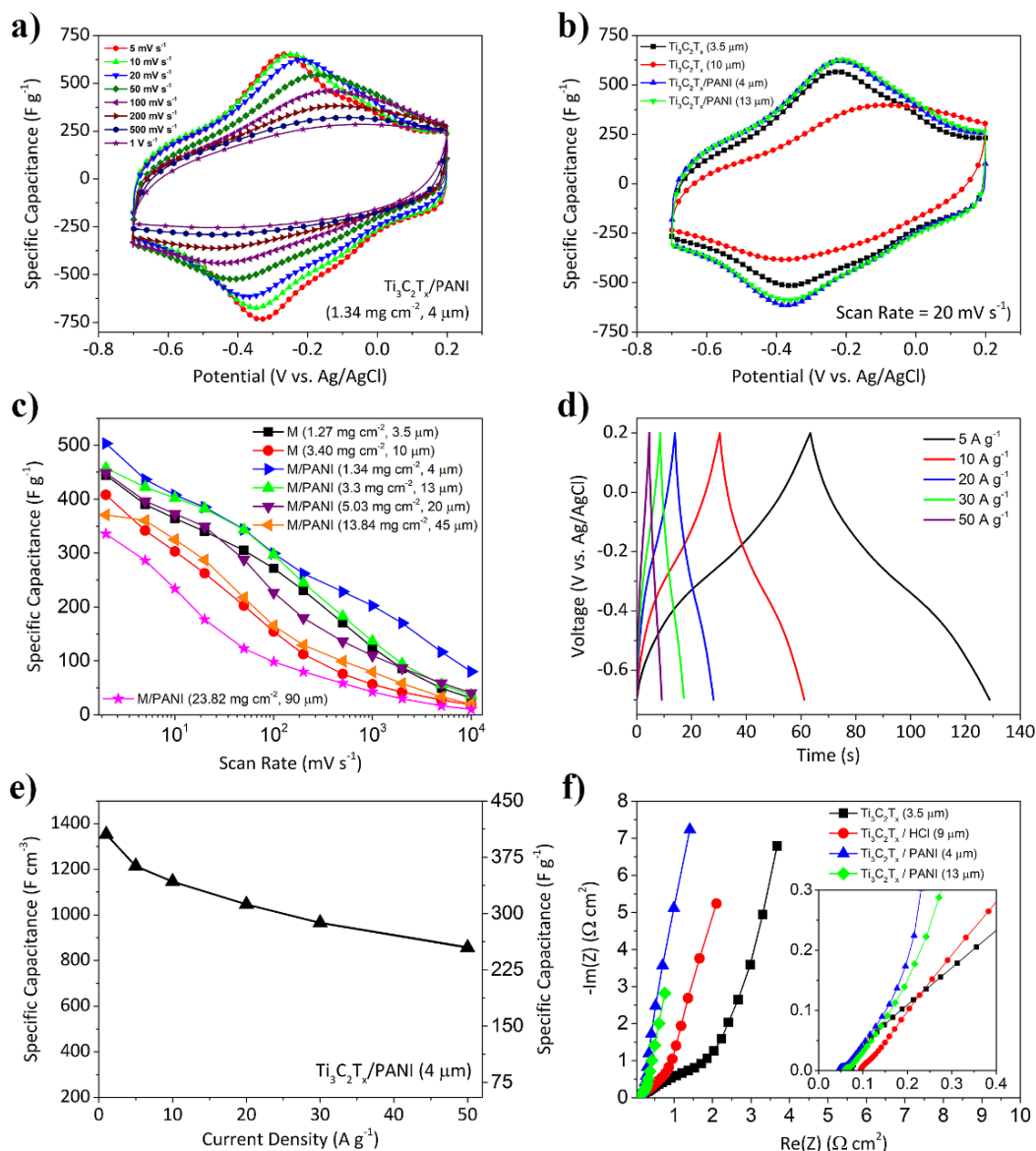
Figure 4.11. Electrochemical analyses of MXene/PANI electrodes. a) Cyclic voltammetry (CV) curves of a freestanding $Ti_3C_2T_x$/PANI electrode (4 µm thickness) at scan rates of 5 mV s^{-1} to 1,000 mV s^{-1} in 3 M H_2SO_4 electrolyte. b) Comparison of the CV profiles of two $Ti_3C_2T_x$/PANI electrodes (4 and 13 µm thicknesses) and two pristine $Ti_3C_2T_x$ electrodes (3.5 and 10 µm thickness). c) Gravimetric capacitance of electrodes with different thicknesses and mass-loadings. M represents pristine $Ti_3C_2T_x$ electrodes and M/PANI indicates a hybrid $Ti_3C_2T_x$/PANI electrode. d) Galvanostatic charge/discharge profiles of $Ti_3C_2T_x$/PANI (4 µm thickness) electrode at different current densities of 1, 5, 10, 20, 30, and 50 A g^{-1}. e) Specific capacitances of the $Ti_3C_2T_x$/PANI electrode (4 µm thickness) at different current densities. f) Electrochemical impedance spectroscopy data for hybrid $Ti_3C_2T_x$/PANI electrodes (4 and 13 µm thicknesses), $Ti_3C_2T_x$/HCl, and $Ti_3C_2T_x$ electrodes, showing improved ion transport and lower resistance of $Ti_3C_2T_x$/PANI electrodes. Adapted with permission from ref. 32 (copyright © 2018 Royal Society of Chemistry).

The high specific capacitance and excellent rate-handling capability of the $Ti_3C_2T_x$/PANI films can be explained by the increase in the interlayer spacing of MXene sheets in the structure of the hybrid electrodes. This facilitates the ion transport inside the electrode structure and increases the electrolyte's ions (protons) accessibility to the redox-active sites at the surface of $Ti_3C_2T_x$. It is important to note that PANI does not directly contribute to charge storage in the fabricated electrodes as it is electrochemically inactive in the potential window that $Ti_3C_2T_x$ is active. Therefore, in the fabricated electrodes PANI only act as a conductive spacer that improves the ionic and electronic conductivity of the electrodes. However, conductive polymers such as PANI are a much more effective conductive spacer compared to carbon nanomaterials (such as CNT) that are commonly used in design and fabrication of freestanding electrodes based on 2D materials.[31,72]

The improved ionic and electronic conductivity of the electrodes after PANI deposition allows fabrication of electrodes with much higher thicknesses and mass loadings compared to what is normally achieved for freestanding electrodes of 2D materials. Fig. 5b compares the CV curves of two $Ti_3C_2T_x$/PANI electrodes with thicknesses of 4 µm and 13 µm to CV curves of two pristine $Ti_3C_2T_x$ electrode with thicknesses of 3.5 µm and 10 µm at a scan rate of 20 mV s^{-1}. Increasing the thickness of the pristine $Ti_3C_2T_x$ films from 3.5 µm (mass loading of 1.27 mg cm^{-2}) to 10 µm (mass loading of 3.4 mg cm^{-2}) resulted in a significant loss of capacitance (from 340 F g^{-1} to 262 F g^{-1}). This observation is in agreement with previous reports on the effects of thickness on the performance of freestanding MXene electrodes.[41] In contrast, in the case of $Ti_3C_2T_x$/PANI films, the electrode with 13 µm thickness (mass loading of 3.3 mg cm^{-2}) showed a pseudocapacitive response similar to the one with 4 µm thickness and delivered an almost equal gravimetric capacitance of ~383 Fg^{-1} at 20 mV s^{-1} (~385 F g^{-1} for the 4 µm thick electrode). The calculated

specific capacitance of the 13 µm thick $Ti_3C_2T_x$/PANI electrode is higher than the capacitance of both 3.5 µm and 10 µm thick pristine MXene electrodes by about 13% and 47%, respectively.

These results clearly show that the performance of the hybrid electrodes is much less thickness-dependent compared to pristine $Ti_3C_2T_x$ electrodes. **Figure 4.11 c** shows the rate-dependence of gravimetric capacitance of $Ti_3C_2T_x$/PANI electrodes with different thicknesses and mass loadings. The hybrid electrodes with the thicknesses of 4 µm and 13 µm show very similar rate-dependent behavior as their capacitance drops at higher CV scan rates. Both electrodes show a higher capacitance compared to the pristine MXene electrodes at all scan rates. More importantly, the specific capacitance of hybrid electrode with a thickness of 20 µm is almost similar to that of 3.5 µm thick $Ti_3C_2T_x$ electrode at almost all scan rates (**Figure 4.11 c**). Also, the performance of a hybrid electrode with thickness of ~45 µm is similar to the performance of 10 µm thick $Ti_3C_2T_x$ electrodes at all scan rates. Both electrode show a specific capacitance of about 325 F g^{-1} at 10 mV s^{-1}. As shown in Fig. 5c even at a very high thickness of ~90 µm, the fabricated hybrid electrodes still show much higher capacitance values compared to conventional supercapacitor electrodes based on activated carbon and other porous carbon materials.[132]

Figure 4.11 d and e show charge-discharge profiles and specific capacitance of the 4 µm thick $Ti_3C_2T_x$/PANI electrode at current densities ranging from 5 to 50 A g^{-1}, respectively. The charge/discharge profiles are typical of Ti_3C_2Tx electrodes with near triangular shapes and broad humps that indicate the pseudocapacitive response of the material. The 4 µm $Ti_3C_2T_x$/PANI film could deliver a volumetric capacitance of about 1353 F cm^{-3} at 1 A g^{-1} and retains about 64% of its capacitance at a very high current density of 50 A g^{-1}.

Figure 4.11 f shows the results of electrochemical impedance spectroscopy (EIS) performed on $Ti_3C_2T_x$/PANI electrodes of various thicknesses as well as a pristine $Ti_3C_2T_x$

electrode and an electrode assembled using Ti₃C₂Tₓ crumpled by HCl treatment. Nyquist plots of both 4 µm and 13 µm hybrid films show the low ion transport resistance of the electrodes with near vertical rise of the imaginary impedance at low frequencies. However, for the 3.5 µm thick Ti₃C₂Tₓ, the 45-degree linear part of the impedance (Warburg impedance related to ion transport resistance) is much larger compared to hybrid electrodes. The length of the Warburg region decreases for the electrodes fabricated using the HCl treated Ti₃C₂Tₓ, but it is still much larger than the same region in the hybrid electrodes.

Figure 4.12 compares the CV profiles of different MXene and MXene/PANI samples at scan rates of 2 mV s^{-1} and 100 mV s^{-1}. As it can be seen, the pristine MXene samples quickly lose their capacitive performance at higher rates by increasing the thickness compared to MXene/PANI samples. **Figure 4.13** also shows the CV profiles of different samples tested in this study at scan rates from 5 mV s^{-1} to 1000 mV s^{-1}.
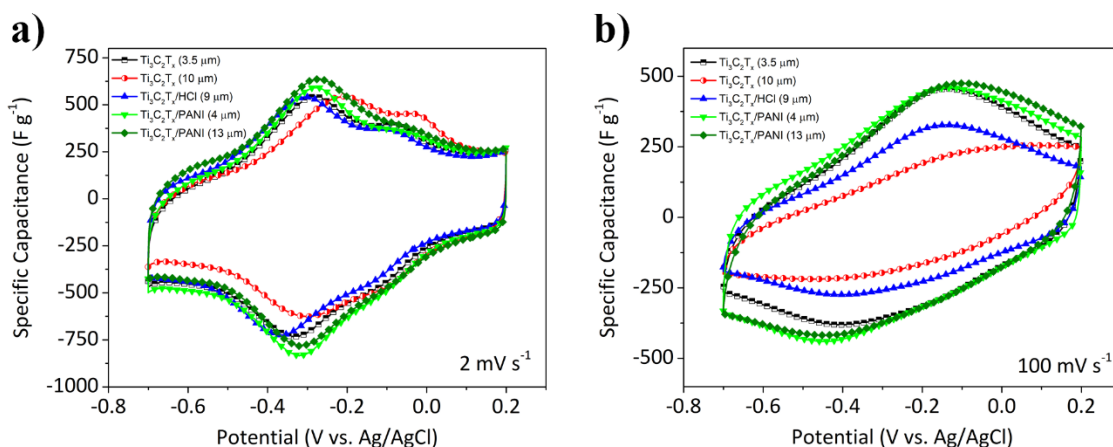
Figure 4.12. Comparison of CVs of MXene and MXene/PANI hybrid electrodes reported in this study at scan rates of a) 2 mV s^{-1} and b) 100 mV s^{-1}. Adapted with permission from ref. 32 (copyright © 2018 Royal Society of Chemistry).
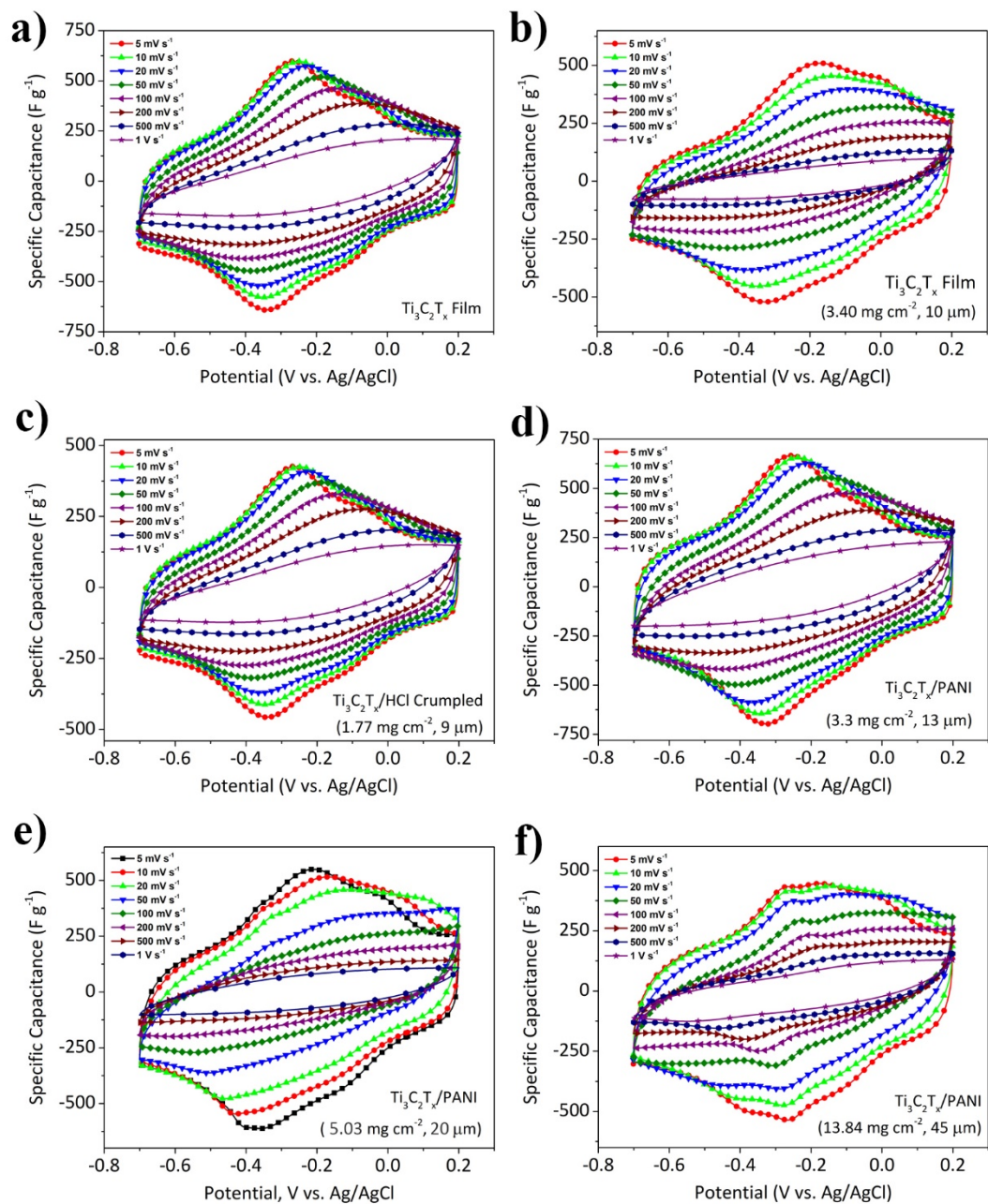
Figure 4.13. CV curves of MXene/PANI electrodes. a) a 3.5 µm thick $Ti_3C_2T_x$ electrode, b) a 10 µm thick $Ti_3C_2T_x$ electrode, c) a 9 µm thick $Ti_3C_2T_x$ crumpled with HCl, d) a 13 µm thick $Ti_3C_2T_x$/PANI hybrid electrode, e) a 20 µm thick$Ti_3C_2T_x$/PANI hybrid electrode, and f) a 45 µm thick $Ti_3C_2T_x$/PANI electrode at scan rates ranging from 5 mV s^{-1} to 1 V s^{-1}. Adapted with permission from ref. 32 (copyright © 2018 Royal Society of Chemistry).

Figure 4.14 a shows the logarithm of CV peak current versus the logarithm of the scan rate for various fabricated electrodes. This graph can be used to explain the kinetics of charge storage in the electrodes. Considering a power-law relationship between peak CV current, i_p, and scan rate, v, we can write:[63]

$$i_p = av^b \qquad (4.1)$$

where a and b are adjustable variables. Therefore, a plot of $\log(i_p)$ vs. $\log(v)$ would be a straight line with a slope of b.[17,63] In equation 1, a b-value of 0.5 implies a diffusion-controlled charge storage mechanism while b=1 is representative of surface-controlled capacitive storage.[63] As it can be seen in Fig. 6a, for a 4 µm thick $Ti_3C_2T_x$/PANI film the b-value is close to 1 for scan rates up to 5 V s^{-1}. However, for the 13 µm and 20 µm thick hybrid electrode the b-value remains close to 1 up to a scan rate of 500 mV s^{-1}, whereas a 10 µm thick $Ti_3C_2T_x$ only showed capacitive behavior up to a scan rate of 50 mV s^{-1}. The fabricated hybrid electrodes also showed very good cycle life performance. As shown in **Figure 4.14 b**, a 20 µm thick $Ti_3C_2T_x$/PANI electrode retained 98.3% of it is initial capacitance after 10,000 cycles at a CV scan rate of 20 mV s^{-1}.
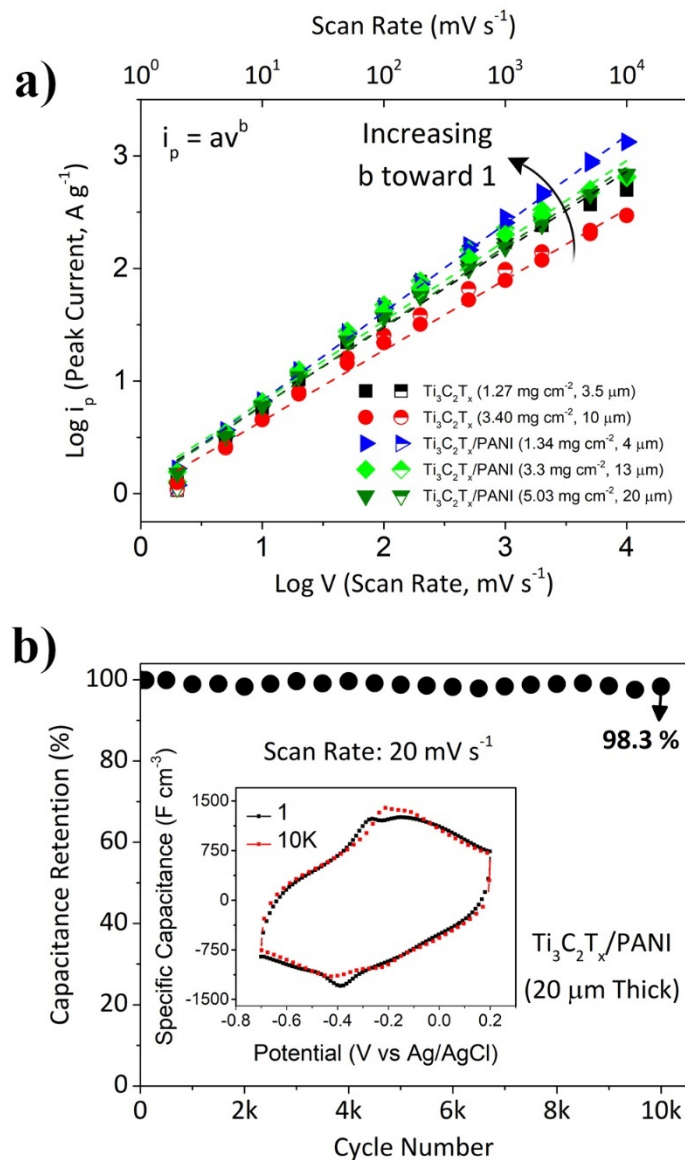
Figure 4.14. Electrochemical analyses of MXene/PANI electrodes and their life cycle. a) Logarithm of cathodic (solid symbols) and anodic (half-filled symbols) peak currents versus logarithm of scan rate for various $Ti_3C_2T_x$/PANI electrodes for determination of b-values. b) Cyclic performance of a 20 µm thick $Ti_3C_2T_x$/PANI hybrid electrode tested at a scan rate of 20 mV s^{-1} showing 98.3% capacitance retention after 10,000 cycles. Inset shows CV profiles before and after 10,000 cycling. Adapted with permission from ref. 32 (copyright © 2018 Royal Society of Chemistry).

Further analysis of the charge storage mechanism of the fabricated electrodes was performed using the method explained by Wang et al.[133] to separate the contribution of surface-controlled and diffusion-controlled processes to their charge storage during CV experiments. Fi **Figure 4.15 a and b** show the CV profiles of a 13 µm thick $Ti_3C_2T_x$/PANI electrode at scan rates of 2 and 20 mV s^{-1}, respectively. The hatched portions of graphs show the capacitive contributions (an indication of charge storage mechanism with surface controlled redox reactions) to the total charge stored in the electrode at each scan rate.[41] At the lower scan rate of 2 mV s^{-1}, about 82% of the charge stored in the hybrid electrodes is due to capacitive contributions. As expected, as the scan rate is increased to 20 mV s^{-1} the contribution of the diffusion-limited processes decreases and about 94% of the capacitance stems from pseudocapacitance charge storage. It is worth noting that capacitive contribution was about 58% and 81% for a 10 µm thick $Ti_3C_2T_x$ electrode at scan rates of 2 and 20 mV s^{-1}, respectively. **Figure 4.16** shows these analyses for other samples.
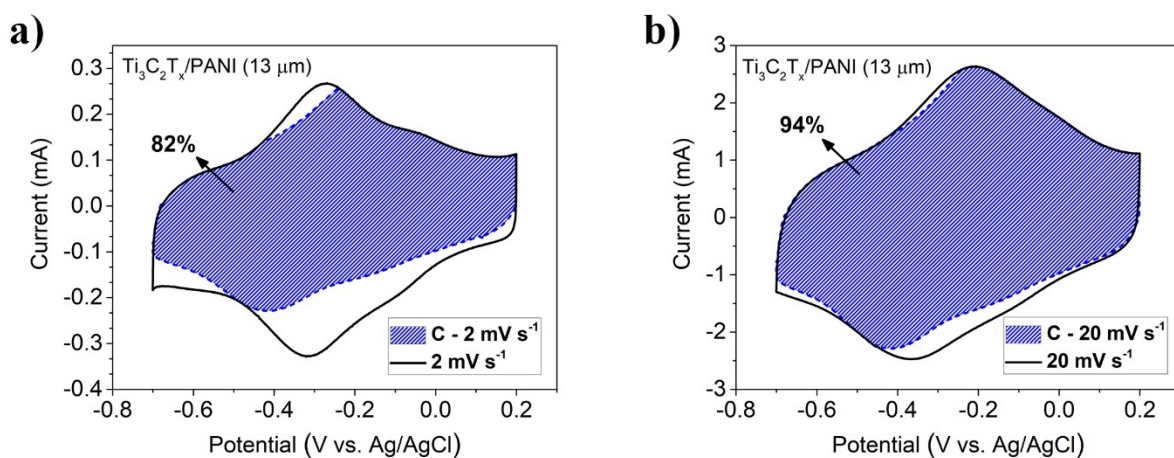
Figure 4.15. CV charge analyses of a $Ti_3C_2T_x$/PANI electrode (13 µm thickness) at a) 2 mV s^{-1} and b) 20 mV s^{-1}. The hatched portions of the graphs represent the contribution of surface-controlled processes (capacitive/pseudocapacitive) to the charge storage. Adapted with permission from ref. 32 (copyright © 2018 Royal Society of Chemistry).
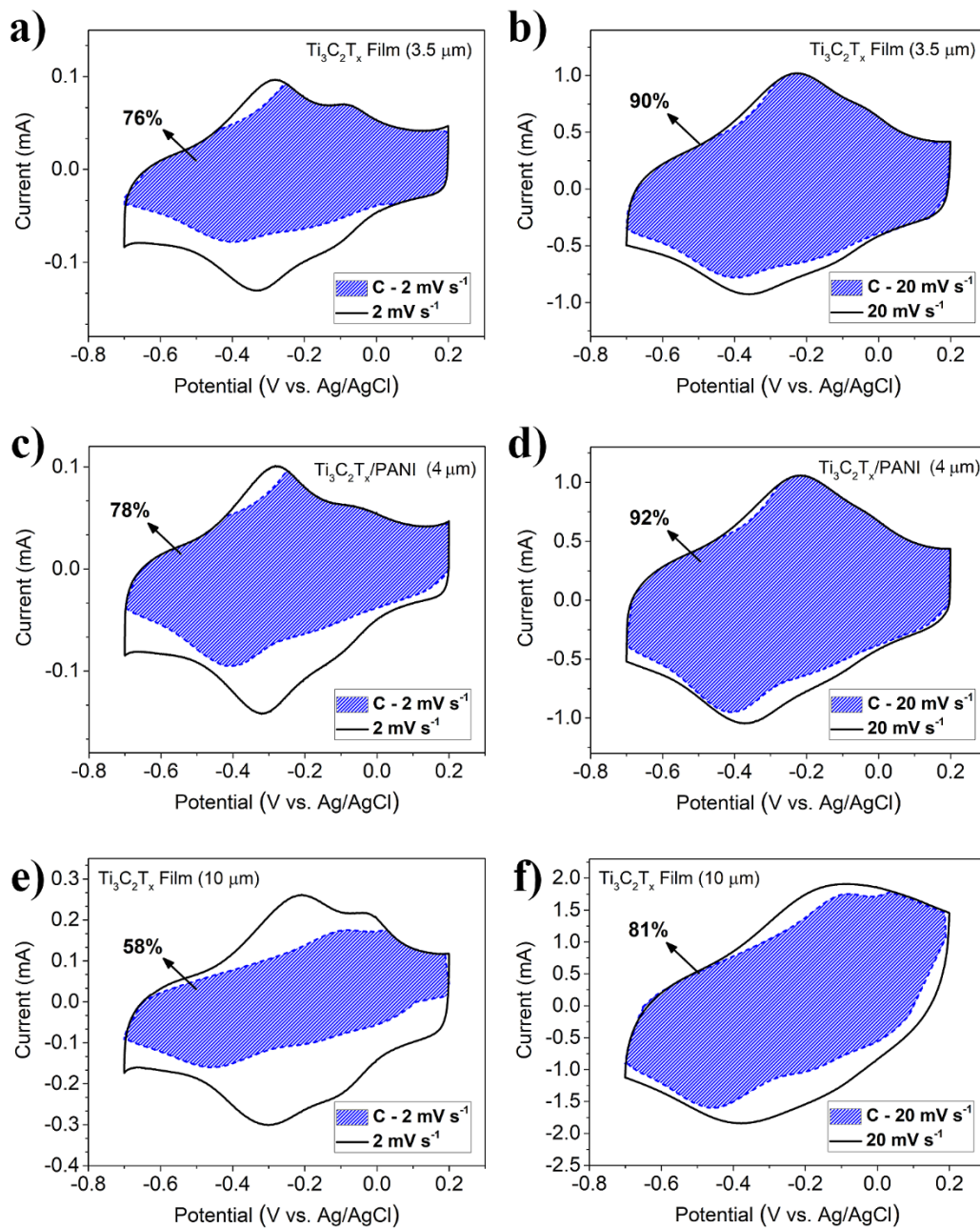
Figure 4.16. Capacitive charge storage contribution of MXene and MXene/PANI electrodes. Shown for a 3.5 μm thick $Ti_3C_2T_x$ electrode at scan rate of (a) 2 mV s^{-1} and (b) 20 mV s^{-1}, for a 4 μm thick $Ti_3C_2T_x$/PANI hybrid electrode at scan rate of (c) 2 mV s^{-1} and (d) 20 mV s^{-1}, and for a 10 μm thick $Ti_3C_2T_x$ film at scan rate of (e) 2 mV s^{-1} and (f) 20 mV s^{-1}. Adapted with permission from ref. 32 (copyright © 2018 Royal Society of Chemistry).

Figure 4.17 a shows the volumetric capacitances of various electrodes fabricated in this study. The addition of PANI and the increased interlayer spacing of MXene sheets lead to the lower density of the hybrid electrodes compared to the pristine $Ti_3C_2T_x$ electrodes. Therefore, the impact of PANI deposition on the volumetric capacitance of the electrodes is less than its impact on the gravimetric capacitance of the electrodes. The hybrid electrodes with thicknesses of 13 µm (3.3 mg cm^{-2}) , 20 µm (5.03 mg cm^{-2}), and 90 µm (23.82 mg cm^{-2}) showed excellent volumetric capacitances of about 1163 F cm^{-3}, 1129 F cm^{-3}, and ~889 F cm^{-3} (~47% less than the capacitance of 4 µm thick $Ti_3C_2T_x$/PANI electrode) at a scan rate of 2 mV s^{-1}, respectively. Therefore, an important advantage of synthesized hybrid materials over the pristine $Ti_3C_2T_x$ is that they can be used for fabrication of very thick electrodes. This is a critical property since in many perceived applications of advanced ECs, such as energy storage in wearable and portable devices and self-powered microsystems, there is a limited area available for the device and increasing the electrode thickness can enhance the energy density.[134] Therefore, materials that can be assembled in thick electrodes and still show high specific capacitance are highly desirable for these applications. The hybrid $Ti_3C_2T_x$/PANI electrode could be an excellent option for devices fabricated in a limited footprint area as high thickness of the electrodes increases their areal capacitance (capacitance normalized by the geometric area of the electrode). For example, an areal capacitance of about 2.26 F cm^{-2} was calculated for the 20 µm thick hybrid electrode (5.03 mg cm^{-2} mass loading) at 2 mV s^{-1} (**Figure 4.17 b**) Moreover, an electrode with thickness of ~90 µm (23.82 mg cm^{-2} mass loading) delivered an unprecedented areal capacitance of ~8 F cm^{-2} at 2 mV s^{-1} (~1 F cm^{-2} at 1 V s^{-1}), exceeding the performance of previously reported microporous and hydrogel MXene electrodes (~ 4 F cm^{-2}).[17]
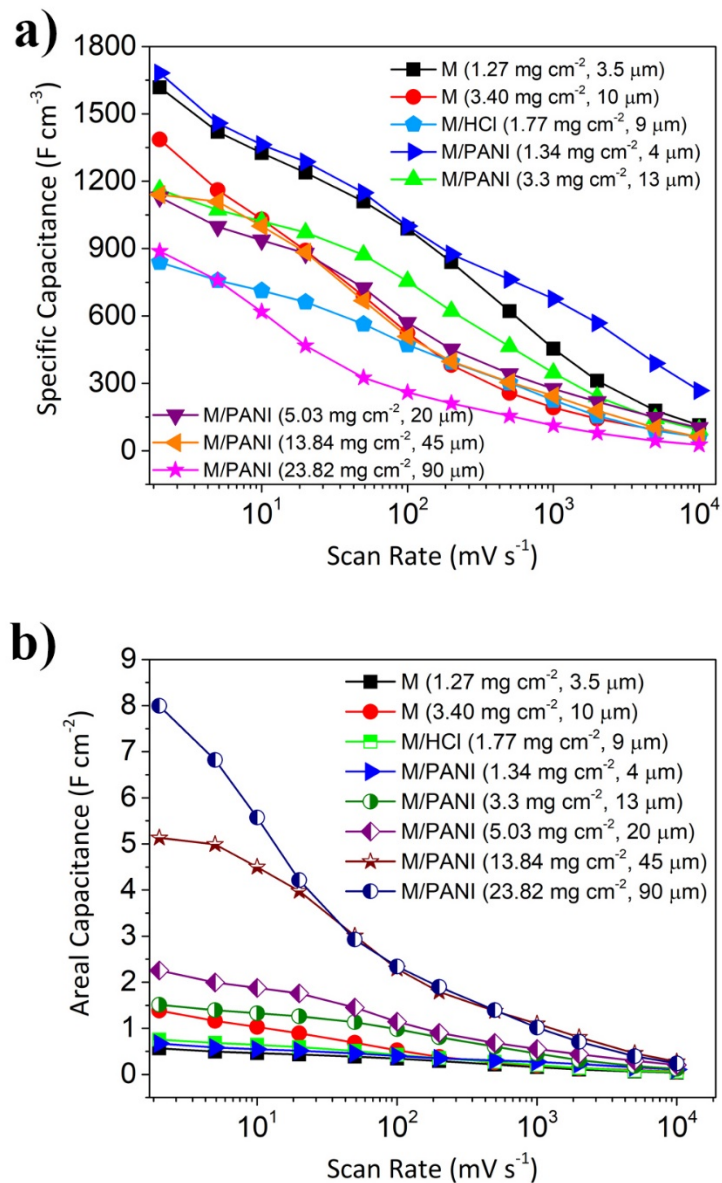
Figure 4.17. a) volumetric and b) areal capacitance of pristine $Ti_3C_2T_x$ electrode (M) and hybrid $Ti_3C_2T_x$/PANI electrode (M/PANI) with different mass loading and thicknesses. Adapted with permission from ref. 32 (copyright © 2018 Royal Society of Chemistry).

We also prepared symmetric supercapacitors using $Ti_3C_2T_x$/PANI (4 µm) electrodes to evaluate the performance of the electrodes in full cells. CV curves and specific capacitances of the symmetric supercapacitor (in 3 M H_2SO_4) are shown in **Figure 4.18**. The symmetric cell showed specific capacitances of ~130 F g^{-1} and ~575 F cm^{-3} (considering the total weight and volume of the active materials) at a scan rate of 2 mV s^{-1}. The symmetric supercapacitor based on $Ti_3C_2T_x$/PANI could deliver an ultrahigh energy density of 79.8 Wh L^{-1} at a power density of ~ 575 W L^{-1} (Ragone plots are shown in **Figure 4.19**), surpassing the previously reported values for MXene/rGO symmetric supercapcaitors.[25]
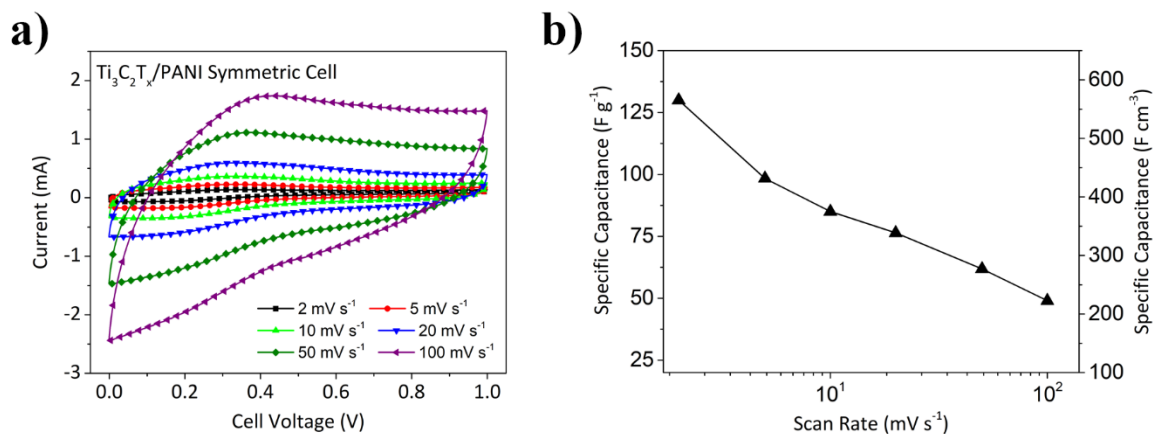
Figure 4.18. A symmetric supercapacitor prepared with two $Ti_3C_2T_x$/PANI hybrid electrodes (4 µm thickness) in 3 M H_2SO_4. a) CVs at various scan rates ranging from 2 mV s^{-1} to 100 mV s^{-1} in a 1 V voltage window and b) Corresponding gravimetric and volumetric capacitances of the cell at different scan rates. Adapted with permission from ref. 32 (copyright © 2018 Royal Society of Chemistry).
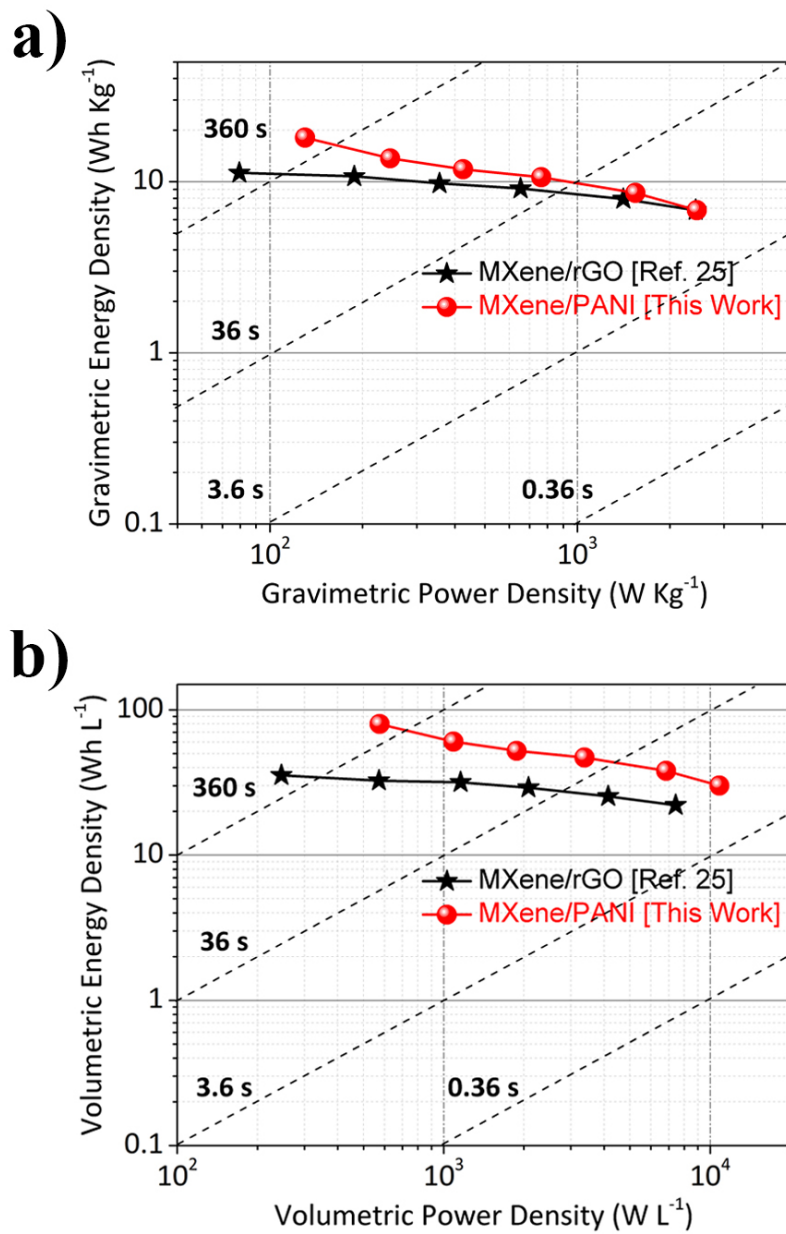
Figure 4.19. Ragone plots of the symmetric MXene/PANI supercapacitor with a) gravimetric and b) volumetric power and energy densities of the cell compared to a previously reported symmetric supercapacitor based on MXene/graphene hybrid electrodes.[76] Adapted with permission from ref. 32 (copyright © 2018 Royal Society of Chemistry).

4.4. Conclusions

In summary, high performance MXene/PANI hybrid electrodes were prepared through an oxidant-free *in situ* polymerization process. The freestanding hybrid electrodes were fabricated by vacuum filtration of hybrid sheets and showed an increased interlayer spacing compared to the films fabricated using pristine $Ti_3C_2T_x$. Both thin and thick $Ti_3C_2T_x$/PANI hybrid electrodes showed significantly enhanced pseudocapacitive charge storage compared to the pristine $Ti_3C_2T_x$ electrodes. The thinner $Ti_3C_2T_x$/PANI electrodes showed very high capacitances of about 503 F g^{-1} and 1682 F cm^{-3} at 2 mV s^{-1} scan rate. The most important impact of PANI deposition on the performance of the electrodes was enhancing the ion transport properties of the electrodes. Consequently, the thickness and mass loading of the hybrid electrodes could be increased without a severe impact on their performance. Even a very thick electrode (~45 µm thickness) prepared using $Ti_3C_2T_x$/PANI hybrid sheets could deliver specific capacitances of about 371 F g^{-1} (1141 F cm^{-3}) and 287 F g^{-1} (884 F cm^{-3}) at scan rates of 2 mV s^{-1} and 20 mV s^{-1}, respectively. With a capacitance retention of over 98% after 10,000 cycles and areal capacitance of up to 8 F cm^{-2}, the performance of the fabricated $Ti_3C_2T_x$/PANI hybrid electrodes matches or surpasses the state-of-the-art EC electrodes based on carbon nanomaterials and previously reported MXene electrodes.[17,31,41,76]

Chapter 5

Electrochemical Properties of Pillared MXene Multilayers Prepared by Self-Assembly of Their Colloidal Solutions

Following the previous chapter and my work on hybridization of the MXenes with organic materials, this chapter presents my research results on fabrication of hybrid MXene materials in form of pillared multilayers. The results presented in this chapter demonstrate how pillaring 2D MXenes into multilayered structures through introducing interlayer cations can affect their electrochemical properties and stability. Pillared multilayers of MXenes were prepared by self-assembly of delaminated MXene solutions. It is shown that alkali-cation pillared 2D V_2CT_x and Ti_2CT_x multilayers show superior (electro)chemical stability compared to their as delaminated flakes. This finding can render V_2CT_x MXene as another practical 2D material for a wide variety of applications, and basically as an analogy to the widely studied $Ti_3C_2T_x$. Therefore, arguably the scientific impact and importance of the superior properties of the cation pillared V_2CT_x MXene structures are beyond just their electrochemical performance. Most portions of the research presented in different sections of this chapter are published as a peer-reviewed article (ref. 56) titled: "Assembling 2D MXenes into Highly Stable Pseudocapacitive Electrodes with High Power and energy Densities", in the Journal of Advanced Materials, 2019, 31 (8), 1806931.

5.1. Introduction

Fast storage and delivery of electrical energy for powering mobile electronics and electric vehicles is an evolving challenge in the field of energy storage. Despite considerable progress in the design and fabrication of the state-of-the-art batteries, their charging rates and lifespans have remained insufficient for many applications.[64,65] In contrast, electrochemical capacitors (ECs), also known as supercapacitors, can be charged and discharged in seconds and deliver high power densities for thousands of cycles.[15,17,65,134,135] However, in conventional ECs or electric double-layer capacitors (EDLCs), charge storage is based on the electrosorption of ions on the surface of carbonaceous electrode materials and therefore, the amount of stored charge is limited by the surface area of the electrodes. Pseudocapacitive materials, an alternative sub-class of ECs, can store more charge and deliver higher energy densities as compared to EDLCs through a storage mechanism that involves fast and reversible surface redox reactions.[15,64–69] For most materials in this category (e. g., metal oxides such as $RuO_2 \cdot nH_2O$[68] and MnO_2[65]), the redox reactions are limited to the surface or near-surface of the electrodes, which greatly underutilizes the bulk of electrode material in charge storage. For some oxides such as $T-Nb_2O_5$[63] the pseudocapacitance occurs in the bulk of the material through fast intercalation of ions resulting in high specific capacitances and energy densities. However, transition metal oxides suffer from low electrical conductivities which hinders their rate-handling capability, power density, and cyclic performance.[15,17,71]

As discussed, MXenes exhibit high electrical conductivities, can be intercalated with various organic and inorganic ions, and can undergo fast redox reactions at their surfaces.[13] Such properties are ideal for pseudocapacitive charge storage. Intercalation-based pseudocapacitive charge storage in MXenes was first reported for delaminated $Ti_3C_2T_x$ (d-$Ti_3C_2T_x$), where

freestanding electrode films showed volumetric capacitances of over 400 F cm^{-3} in aqueous electrolytes.[15] In addition, volumetric capacitances as high as ~900 F cm^{-3} was reported for freestanding d-Ti$_3$C$_2$T$_x$ films in sulfuric acid electrolytes.[41] Recently, Lukatskaya et al.[17] demonstrated that some electrochemical properties of MXene electrodes, such as their specific capacitance and rate-handling capability, can be further improved by designing microporous and hydrogel electrode structures. However, of the 30 different MXenes that have been synthesized so far, only Ti$_3$C$_2$T$_x$ has been systematically investigated as a pseudocapacitive electrode material for ECs, mainly due to the low chemical or electrochemical stability of 2D flakes of other MXene compositions. Notably, the pseudocapacitive properties of completely delaminated (single/few layers) M$_2$CT$_x$ MXenes, such as d-V$_2$CT$_x$ and d-Ti$_2$CT$_x$, have remained unexplored. When these MXene are delaminated to single/few-layer sheets they show poor chemical stability in ambient conditions, or in the presence of water and oxygen.[13,45] For example, multilayered V$_2$CT$_x$, which has shown the highest Li ion intercalation capacity among all MXenes,[16,19] quickly oxidizes in water or air when delaminated to 2D flakes (d-V$_2$CT$_x$). Very recently, Shan et al showed the promise of V$_2$CT$_x$ MXene as aqueous supercapacitor electrode in a short report.[60] However, despite a promising electrochemical performance, the V$_2$CT$_x$ showed low electrochemical stability, which was attributed to either oxidation of MXene or dissolution of V in aqueous electrolytes.[60] To date, the low chemical and electrochemical stability of V$_2$CT$_x$ and other M$_2$C MXenes has prevented the systematic study of their pseudocapacitive properties.

This chapter will demonstrate my research results on preparation of highly stable, freestanding, and flexible pseudocapacitive electrodes fabricated by the cation-driven assembly of otherwise unstable V$_2$CT$_x$ flakes. The assembled flakes have a layered structure that can be intercalated by a variety of inorganic cations and can deliver outstanding high-rate electrochemical

performances with volumetric capacitances in excess of 1300 F cm^{-3}. The fabricated V$_2$CT$_x$ films exhibit superior stability in ambient atmospheres and aqueous electrolytes with capacitance retention of ~77% after one million charge/discharge cycles, an unprecedented performance for MXene electrodes. In addition, symmetric cells fabricated with assembled V$_2$CT$_x$ electrodes could deliver some of the highest values reported for supercapacitors to date.

5.2. Experimental Section

Synthesis of MAX phases and MXenes. MAX phases and MXenes used in this chapter were prepared according to the methods explained in chapter 3.

Cation-driven assembly of MXenes and fabrication of freestanding films. To assemble delaminated MXene sheets, saturated aqueous solutions of LiCl (anhydrous, 99%, Alfa Aesar), NaCl (99%, Alfa Aesar), MgCl$_2$ (anhydrous, 99%, Alfa Aesar), and Mg(ClO$_4$)$_2$ (anhydrous, ACS grade, Alfa Aesar) were first prepared in such a way that the total mass of the salt in the solutions was at least 100 times higher than the mass of MXenes in their dispersions. The saturated salt solutions were then added slowly to the delaminated MXene solutions at room temperature. Upon addition of the salt solutions, the MXene flakes gradually assembled and precipitated at the bottom of the container (Figure S2). The solutions containing the assembled MXene flakes were slowly stirred, sealed, and kept for 30 min to allow all the assembled MXene flakes to precipitate. Then the clear supernatant was decanted and the assembled MXenes flakes were washed two times with DI water to remove any residual salt. After washing, 30 mL of water was added to the MXene flakes and the solution was slowly shaken by hand for 1 minute to get a uniform dispersion of restacked flakes. These dispersions were filtered on Celgard membranes to obtain freestanding MXene films. It is worth mentioning that for the MXenes assembled with Li$^+$ cations, strong

shaking resulted in partial disassembly and redispersion of assembled flakes in water. Therefore, strong shaking was avoided to prevent disassembly of the MXenes flakes. The freestanding MXene films were labeled as $C-V_2CT_x$, where C is the cation used in the assembly process (Li^+, Na^+, or Mg^{2+}). In addition, freestanding films of delaminated MXenes without assembly ($d-V_2CT_x$ and $d-Ti_2CT_x$) were fabricated by directly filtering their corresponding dispersion on filter membranes.

Electrochemical measurements. All electrochemical measurements were carried out in plastic Swagelok cells where glassy carbon electrodes were used as current collectors for the working and counter electrodes. Ag wire coated with AgCl immersed in 1 M KCl was used as the reference electrode for all the tests. Working electrodes (WE) were prepared by directly punching the freestanding MXene films into the desired size. A piece of over-capacitive activated carbon film (YP-50) was used as the counter electrode (CE) in the cells. Aqueous solutions of 5 M LiCl, 1 M Li_2SO_4, 1 M Na_2SO_4, 1 M $MgCl_2$, 1 M Mg_2SO_4, 1 M KOH, 0.5 M K_2SO_4, and 3 M H_2SO_4 were used as electrolytes in the cells. All cells were initially stabilized by 50 charge and discharge cycles at a scan rate of 20 mV s^{-1} prior to electrochemical measurements. CV experiments were done at scan rates ranging from 2 mV s^{-1} to 10 Vs^{-1}. The operating potential window of the MXene electrodes in each electrolyte was determined by using CV test cycling where the potential window was gradually increased until signs of electrolyte decomposition and/or MXene oxidation was observed. In all electrolytes, the upper cut-off potential was found to be the same as open circuit potential (OCP). The operating potential window in 5 M LiCl and 1 M Li_2SO_4 electrolytes was set to be from 0 V to -1 V, in 1 M Na_2SO_4, 1 M $MgSO_4$, 1 M $MgCl_2$, and 0.5 M K_2SO_4 it was set from 0 V to -0.8 V, and in 1 M KOH it was set between -0.6 and -1.2 V (All potential values vs Ag/AgCl). In 3 M H_2SO_4 the upper cut-off potential was +0.2 V while the two lower cut-off

potentials of -0.4 V and -0.6 V were studied. To evaluate the cycle life of the electrodes, galvanostatic charge/discharge experiments at current densities of 10 and 100 A g^{-1} were carried out for 10 000 cycles in the corresponding potential window of each electrolyte.

Electrochemical impedance spectroscopy (EIS) data were collected in the same three-electrode setup, in the 100 mHz to 1000 kHz frequency range. The EIS experiments were carried out at OCP and the applied potential amplitude was 10 mV. Symmetric supercapacitors were assembled by using V_2CT_x films (with equal weight) as both working and counter electrodes to evaluate the performance of fabricated V_2CT_x electrodes in full cells (two-electrode setup). The specific capacitance of each cell was calculated based on the total weight (or volume) of both MXene electrodes.

Characterization techniques. XRD analyses of the samples were done directly on the fabricated freestanding films using Bruker X-ray diffractometer (D8 Discover) with 40 kV and 40 mA Cu-kα radiation at a scan speed of 0.2 seconds per 2θ step. For *ex situ* XRD analyses, the electrodes were pre-cycled at a scan rate of 20 mV s^{-1}, and then cycled at 2 mV s^{-1} and stopped at corresponding potentials. The cells were quickly opened and the electrodes were washed with DI water before analysis. For SEM analysis of the samples, a JEOL JSM-7000F scanning electron microscope equipped with an energy dispersive spectrometer (EDS detector) was used. A FEI Scios dual beam system with gallium ion beam source was used to prepare lamellae from cross-section of Na-V_2CT_x, Li-V_2CT_x, and d-V_2CT_x electrode films for further characterization with electron microscopy. S/TEM analyses were done by Mehrnaz Mojtabavi and Dr. Wentao Liang at Northeastern University in Boston. To prepare TEM samples, lamellas were thinned to a thickness of less than 100 nm and placed on a TEM grid. Some TEM samples were also prepared by drop casting the redispersed assembled V_2CT_x flakes on TEM grids. A probe-corrected FEI Titan

Thermis 300 S/TEM with ChemisSTEM technology was employed for imaging lamellas in both HR-TEM and STEM imaging modes and studying samples' structures. Furthermore, EDS analysis was performed at 300 kV using a SuperX EDS system for elemental analysis of samples and confirming the presence of cations in between the V_2CT_x layers. XPS analyses were performed in University of Alabama. A Kratos AXIS 165 surface analysis instrument with a 165-mm hemispherical analyzer (HAS) was used to carry out X-ray photoemission spectroscopy analysis on the samples. The XPS chamber was purged with nitrogen and XPS spectra were recorded in fixed analyzer transmission (FAT) mode at 12 mA and 15 kV by using a monochromatic aluminum source. The step size for all measurements was 0.05 eV with 500 ms dwell time. Ar sputtering was done at 4 kV for 10 minutes with a large spot size of ~2 mm^2. The resolution of the XPS machine was measured from FWHM of the Ag3d$_{5/2}$ peak to be 1.0 eV and the incidence of the X-ray beam had an angle of 54.7^o relative to the specimen normal. To calibrate the XPS energy scale, the Ag3d$_{5/2}$ line of clean silver was set to exactly 368.3 eV referenced to the Fermi level. Delaminated MXene solutions or cation assembled MXene dispersions were drop casted on SiO_2 wafers for atomic force microscopy (AFM) measurements. Prepared samples were characterized by Park Instruments NX10 AFM using a non-contact mode cantilever.

Computational methods. Density functional theory calculations are performed using the VASP code.[136–138] The Perdew-Burke-Ernzerhof (PBE)[139] functional was employed. The plane wave basis set was converged using a 500eV energy cutoff. Structural relaxations of the supercell were carried out using a 3×3×2 k-point Monkhorst-Pack mesh.[140] The electronic structure was then calculated using a 9×9×4 mesh. Dispersion forces were included using the semi-empirical approach of Grimme (DFT-D3).[141] The surface sites of a 3×3 V_2C supercell were covered with mixed –O, and –F groups placed directly above the V atom on the opposite surface. Calculations

were carried out considering full coverage of MXene surfaces with functional groups (nominal stoichiometry formula of $V_2CF_{0.88}O_{1.11}$). As the number of –OH groups on the surface is typically found to be reduced or even eliminated after alkali atom intercalation,[59,142,143] this termination type was not considered. Li atoms were intercalated at a concentration of $Li_{0.22}$-V_2CT_x, close to what was found experimentally. A full structural relaxation was performed. After Li intercalation the c lattice parameter increased by 1 Å (from 13.7 Å to 14.7 Å). Computational studies were performed by Dr. Nuala M. Caffrey at Trinity College Dublin in Ireland.

5.3. Results and Discussions

V_2CT_x is expected to be an excellent pseudocapacitive material as the multiple oxidation states of V can potentially lead to a high charge storage capacitance.[16,59] Delaminated V_2CT_x flakes (d-V_2CT_x) was synthesized by delaminating multilayered V_2CT_x (ML-V_2CT_x) particles, which were in turn synthesized by selectively etching Al atoms from a V_2AlC MAX phase powder. The final product of the synthesis process is a dispersion of d-V_2CT_x flakes in water. **Figure 5.1** shows the atomic force microscopy (AFM) of the as prepared fresh d-V_2CT_x flakes. As shown in **Figure 5.2 a**, when the dispersion is kept in ambient atmosphere, d-V_2CT_x flakes quickly oxidize and disintegrate within a few hours, as evidenced by a change in color of the dispersion from dark green to pale yellow. Deaeration of the produced dispersion and storage in a sealed container slows the degradation of d-V_2CT_x flakes. AFM images (**Figure 5.2 b and c**), however, suggested that even the flakes stored in deaerated containers oxidize and disintegrate in about two days. In addition, freestanding MXene films fabricated by vacuum filtration of fresh d-V_2CT_x dispersions showed little flexibility and their color changed from grayish brown to black after one week of exposure to ambient atmosphere at room temperature (**Figure 5.3**). The fabricated films disintegrated, and their color further darkened after one month.
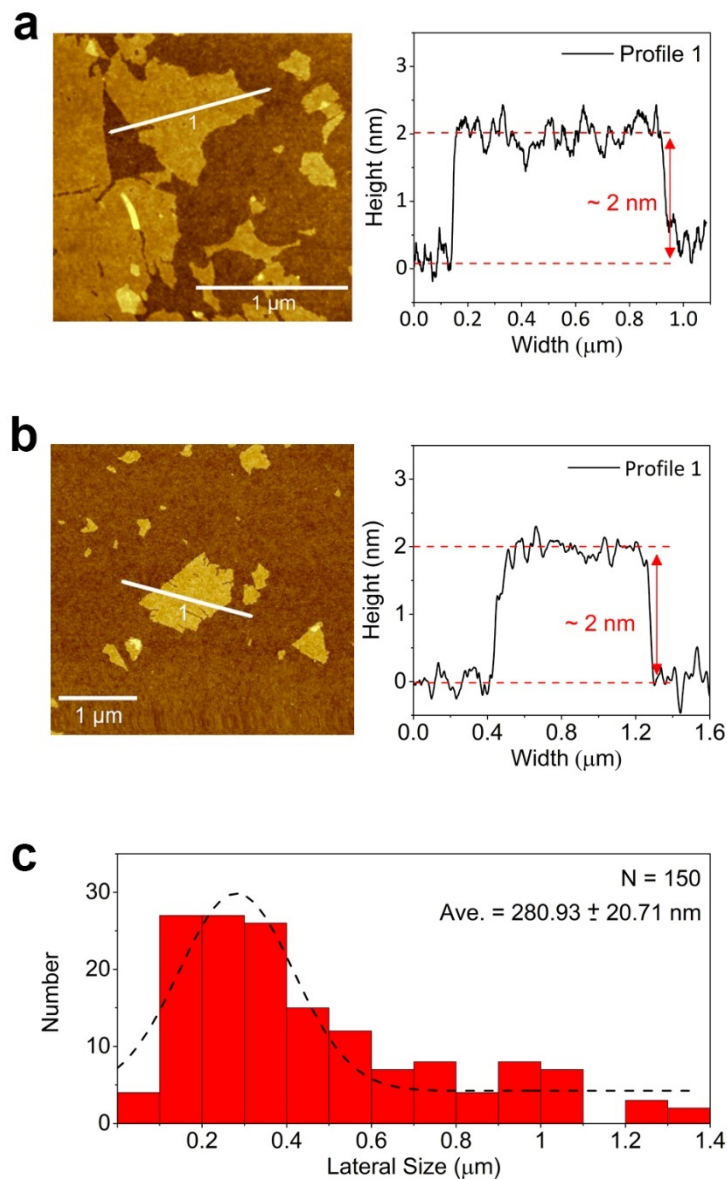
Figure 5.1. Atomic force microscopy (AFM) images of V_2CT_x MXene. a and b) AFM images and corresponding height profiles of the delaminated V_2CT_x (d-V_2CT_x) showing mostly single layer flakes in the delaminated solutions with an apparent thickness of ~ 2 nm. The higher than theoretical thickness observed here is due to the interactions between the silicon substrate and different functional groups present on the surface of MXene flakes. Similar observations have been reported for AFM measurements of $Ti_3C_2T_x$ flakes.[10,44] d) Average lateral size and size distribution of the synthesized V_2CT_x MXene flakes calculated by measuring the size of 150 individual flakes using AFM. The produced d-V_2CT_x solutions showed an average lateral flake size of 280.93 ± 20.71 nm. Adapted and reproduced with permission from ref. 56 (copyright © 2019 Wiley-VCH Verlag GmBH & Co.).
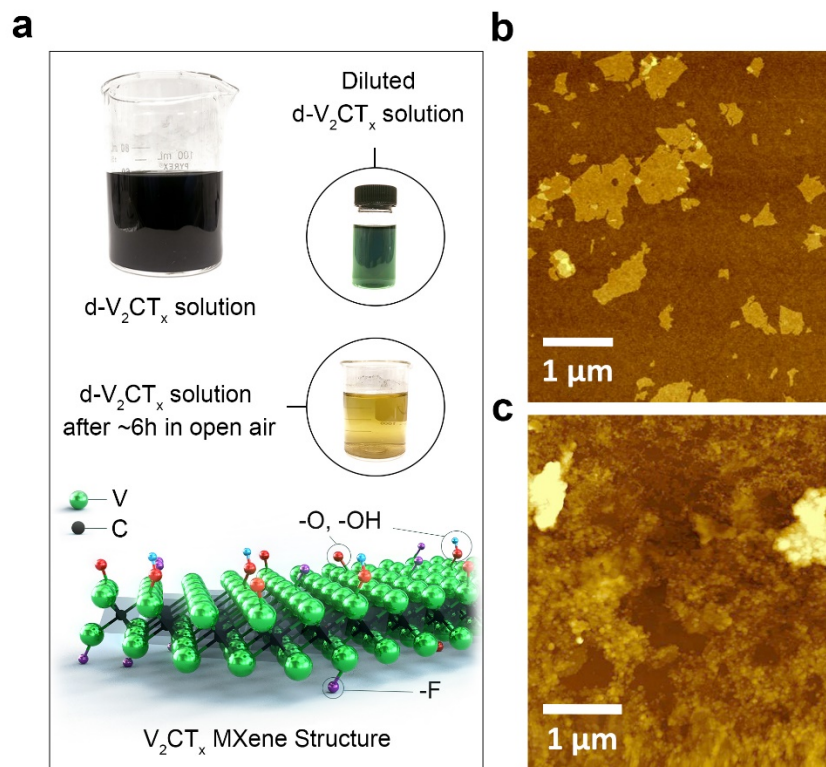
Figure 5.2. Photographs of 2D vanadium carbide MXene solutions and observation of their oxidation with AFM. a) Digital photographs of a fresh d-V$_2$CT$_x$ solution and a diluted d-V$_2$CT$_x$ solution, showing an initial green color which changes to a pale yellow in few hours due to oxidation of the d-V$_2$CT$_x$ flakes. Schematic of the structure of V$_2$CT$_x$ MXene is shown at the bottom of this panel. b) An AFM image of a fresh single layer d-V$_2$CT$_x$ MXene. c) An AFM image of d-V$_2$CT$_x$ flakes from a deaerated solution kept in a sealed container for 2 days. Adapted and reproduced with permission from ref. 56 (copyright © 2019 Wiley-VCH Verlag GmBH & Co.).
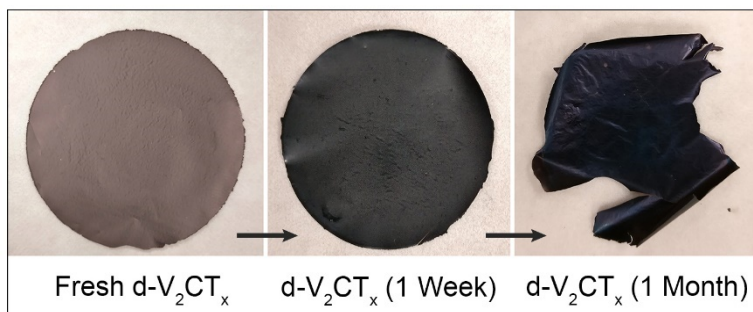
Figure 5.3. Digital photographs of d-V$_2$CT$_x$ films indicating oxidation and color change in ambient atmosphere after a week and disintegration in a month (change in color from a grayish brown to black). Adapted with permission from ref. 56 (copyright © 2019 Wiley-VCH Verlag GmBH & Co.).

The X-ray photoelectron spectroscopy (XPS) spectrum (V2p region) of a freshly prepared d-V_2CT_x film (**Figure 5.4 a**) showed that vanadium is mostly present in its V^{4+} oxidation state, indicating the termination of MXene surface with functional groups and presence of surface oxide monolayers, in agreement with previous studies.[16,19] However, the XPS spectrum of a one-month-old film (**Figure 5.4 b**) confirmed the oxidation of V_2CT_x flakes, as the V species were dominated by V^{5+}, indicating the formation of V_2O_5. Previous studies[144,145] have shown that the products of $Ti_3C_2T_x$ MXene oxidation at room temperature are amorphous oxide particles and carbon. This also appears to be the case for V_2CT_x oxidation. The X-ray diffraction (XRD) pattern of the oxidized d-V_2CT_x films (**Figure 5.4 c**) showed a significant loss of intensity for the (0002) MXene peak. However, no peaks related to vanadium oxide species were observed, implying that the produced vanadium oxide is amorphous in nature.

The self-restacking of the d-V_2CT_x flakes and their instability adversely affect the electrochemical performance of the fabricated freestanding MXene films. **Figure 5.4 d** show cyclic voltammetry (CV) profiles and cycle life of a d-V_2CT_x film electrode in a 5 M LiCl aqueous electrolyte. This electrode displayed good pseudocapacitive performance at low scan rates, but its capacitive behavior declined at scan rates above 10 mV s^{-1}, suggesting a high ion transport resistance between the restacked MXene flakes.[17,55] In addition, due to the gradual oxidation of the electrodes during cycling, a significant drop in the electrode capacitance (to ~69% of the initial capacitance) was observed in less than 1500 cycles (**Figure 5.4 e**). To date, the instability of d-V_2CT_x in air and water has hindered its applications, and studies of the electrochemical properties of V_2CT_x MXenes have been mostly limited to more stable multilayered particles or to non-aqueous electrolytes to avoid oxidation.[16,19,121]
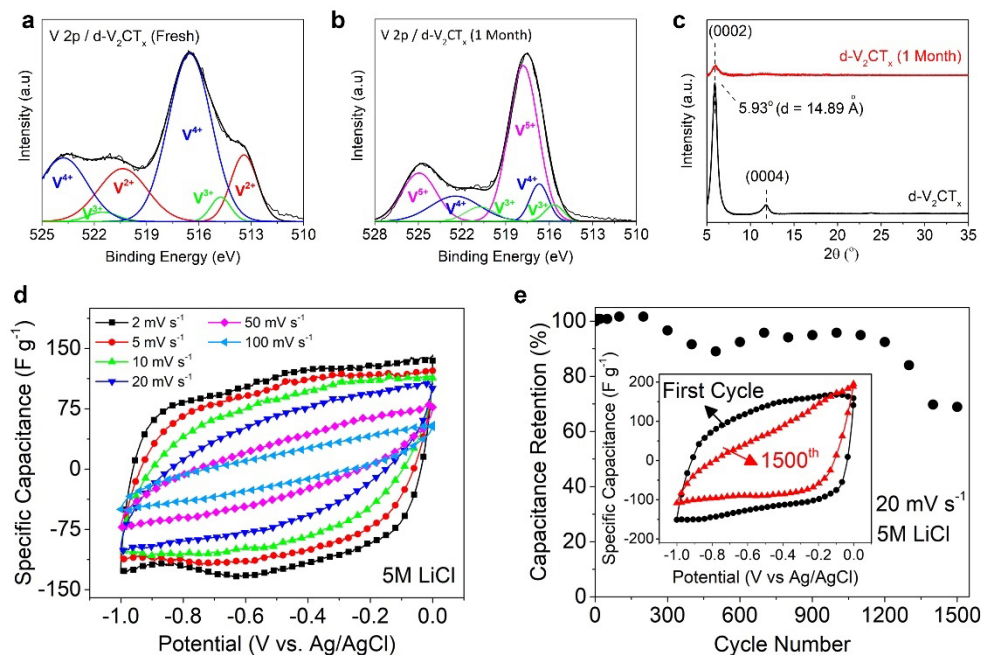
Figure 5.4. a) High-resolution V 2p XPS spectrum of a fresh d-V$_2$CT$_x$ film. b) High-resolution V 2p XPS spectrum of a d-V$_2$CT$_x$ film after one month. (c) XRD patterns of fresh and one-month old d-V$_2$CT$_x$ films showing a significant reduction in the intensity and broadening of the characteristic (0002) peak of MXene. (d) CVs of a fresh d-V$_2$CT$_x$ film fabricated by vacuum filtration in 5 M LiCl at scan rates ranging from 2 mV s^{-1} to 100 mV s^{-1}. (e) Cyclic performance of a d-V$_2$CT$_x$ film in 5 M LiCl at 20 mV s^{-1}. Adapted and reproduced with permission from ref. 56 (copyright © 2019 Wiley-VCH Verlag GmBH & Co.).

Figure 5.5 also shows the shape of the V 2p XPS spectra shown in **Figure 5.4 a and b** before removal of the XPS Shirley background and their corresponding XPS fits. As it can be noted, it was found that a better fit for the 1 month old can be achieved only considering the V^{4+} and V^{5+} species in deconvolution. The end results and conclusions obtained from XPS analysis, however, are the same with or without removal of the Shirley background. In this figure also the C 1s XPS spectra for the two sample are provided. The C-C and C-O peaks are attributed to the adventitious contaminations.[16] As it can be seen the V-C peak is completely vanished in the one-month old sample indicating disintegration of the V-C species and formation of amorphous carbon and vanadium oxide species.
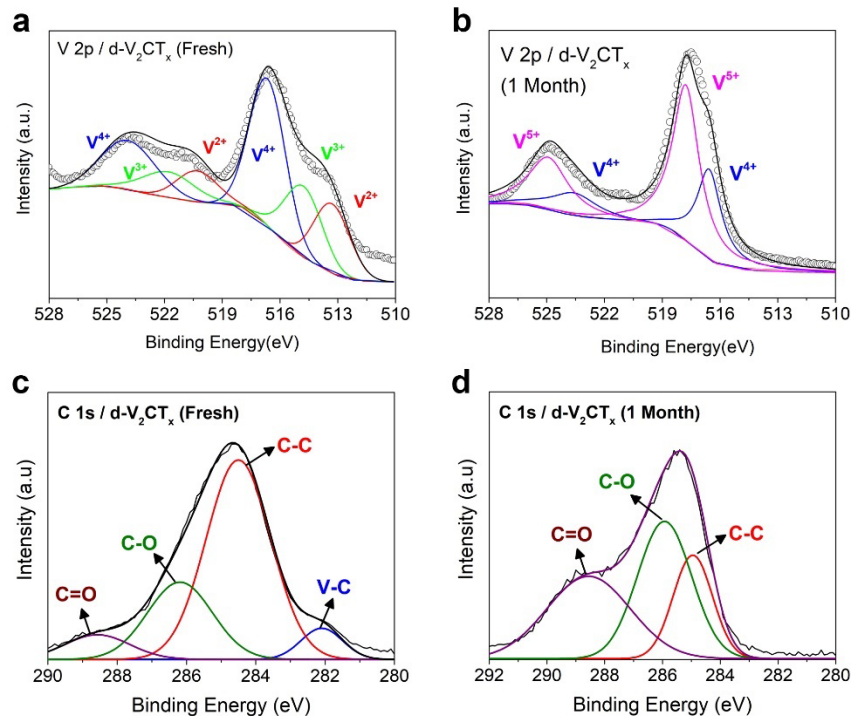
Figure 5.5. High-resolution V 2p XPS spectra of a) fresh d-V_2CT_x film and b) d-V_2CT_x film after one month (shown in the previous graph in panels a and b) before removal of the XPS Shirley background. C 1s spectra of c) fresh d-V_2CT_x film and d) d-V_2CT_x film after one month. Panels a and b are adapted and reproduced with permission from ref. 56 (copyright © 2019 Wiley-VCH Verlag GmBH & Co.).

The assembly of 2D transition metal oxides into layered structures mediated by alkali metal cations has been recently utilized to synthesize pre-intercalated oxide materials for energy storage applications.[146–149] This simple and rapid assembly method relies on the electrostatic attraction of negatively charged 2D oxide flakes to alkali cations, forming ordered layered structures with improved electrochemical performance.[146,147,150] In the case of MXenes, it was recently reported that addition of alkali hydroxide solutions to d-$Ti_3C_2T_x$ dispersions results in flocculation of MXene flakes and formation of porous aggregates with crumpled morphologies.[99] Here, my results show that the cation-driven assembly not only significantly improves the electrochemical properties V_2CT_x, but also converts the chemically (and electrochemically) unstable MXene flakes to highly stable films and electrodes.

As schematically illustrated in **Figure 5.6 a**, upon addition of concentrated alkali metal chloride solutions to dispersions of d-V_2CT_x flakes in water, an electrostatic attraction between metal cations and the negatively charged MXene flakes leads to the assembly of multilayer restacked V_2CT_x flakes pillared by metal cations. **Figure 5.6 b and c** compare the scanning electron microscopy (SEM) images of d-V_2CT_x flakes drop-casted onto alumina membranes before and after assembly using a concentrated solution of LiCl. In contrast to the d-V_2CT_x flakes, which were transparent to the electron beam, the V_2CT_x flakes assembled by Li^+ cations (Li-V_2CT_x) appeared to be much thicker and opaque.

Figure 5.6 d shows a cross-sectional SEM image of a Li-V_2CT_x film where ordered stacking of MXene flakes resulted in a layered structure. XRD analyses of the C-V_2CT_x films showed the characteristic MXene peaks for all samples (**Figure 5.6 e** and **Figure 5.7**). The change in the position of the peak associated with the (0002) plane of the MXene is due to the dependence of the interlayer spacing on the type of cation present between the layers. Interestingly, the appearance of (0004), (0006), and (0008) MXene peaks in the XRD patterns of the assembled flakes suggests a more ordered structure for all C-V_2CT_x films compared to the one prepared using d-V_2CT_x.[99,146] For Li-V_2CT_x films, the (0002) peak shifted from 5.93° for d-V_2CT_x to 7.26°. This corresponds to a decrease in the Li-V_2CT_x d-spacing of about 2.73 Å, which is probably caused by the attraction of the MXene layers to the interlayer Li^+ cations. Nevertheless, the assembled MXene films still showed quite high interlayer spacings, which suggests that the intercalated cations during assembly are in a (partially) hydrated state in the structure of the assembled V_2CT_x films.[151,152] **Figure 5.6 f and g** display HR-STEM images of the fabricated Li-V_2CT_x and Na-V_2CT_x films, showing the ordered layered structure of the films and confirming the d-spacing calculated from XRD.
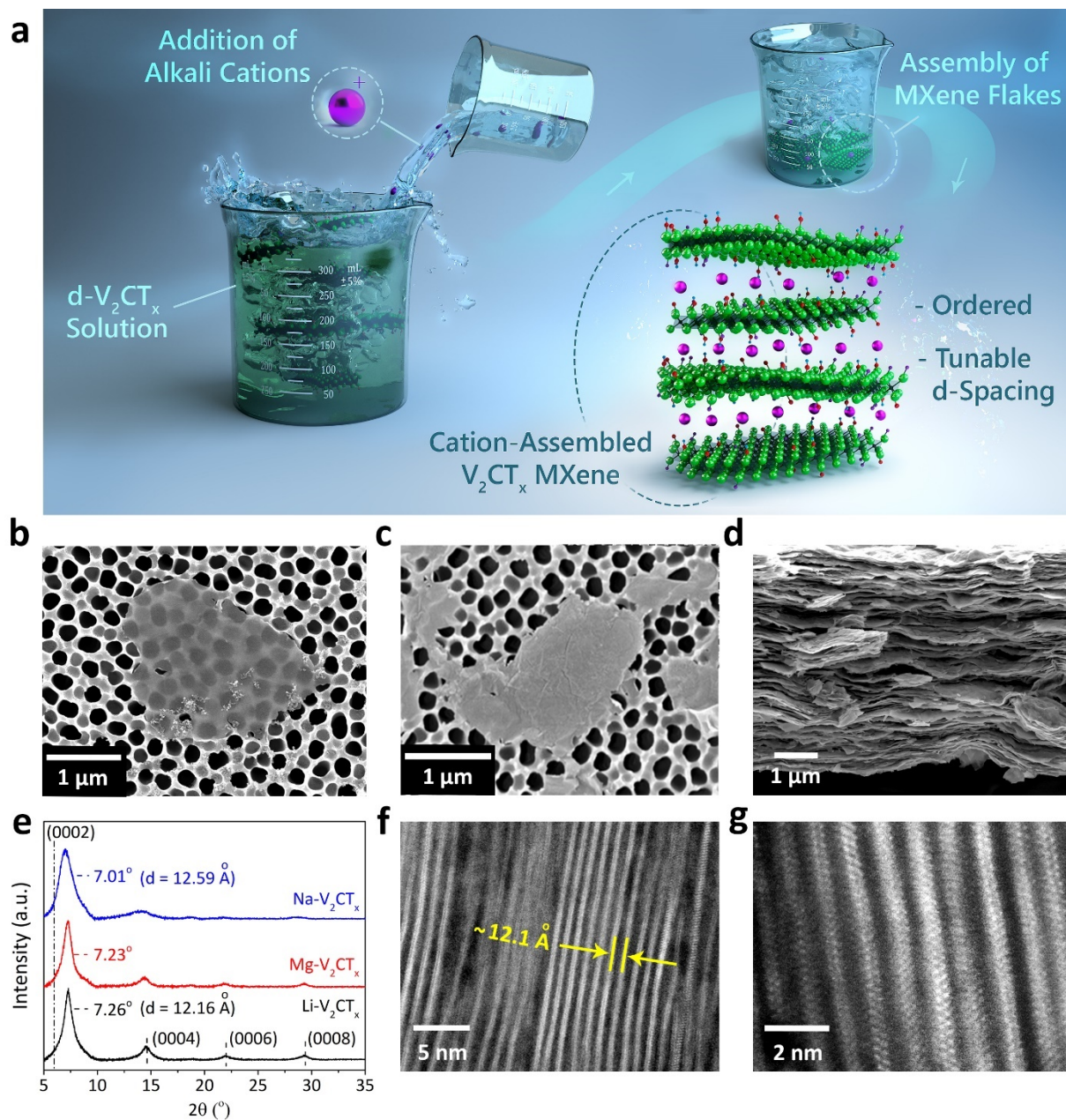
Figure 5.6. Schematic illustration of the cation-driven assembly process used for fabrication of the ordered and highly stable V_2CT_x flakes (shown in a). b) SEM image of a freshly synthesized single-layer d-V_2CT_x on an alumina oxide (AAO) substrate. c) SEM image of V_2CT_x flakes restacked using Li^+ cations (Li-V_2CT_x) on an AAO filter. d) Cross-sectional SEM image of a Li-V_2CT_x film. e) XRD patterns of films fabricated using flakes assembled with various cations. The dashed line on the left of the graph indicates original position of the (0002) peak for d-V_2CT_x film. f) TEM image of a Li-V_2CT_x film showing its layered structure. (g) Atomic resolution STEM image of the Na-V_2CT_x. Adapted and reproduced with permission from ref. 56 (copyright © 2019 Wiley-VCH Verlag GmBH & Co.).
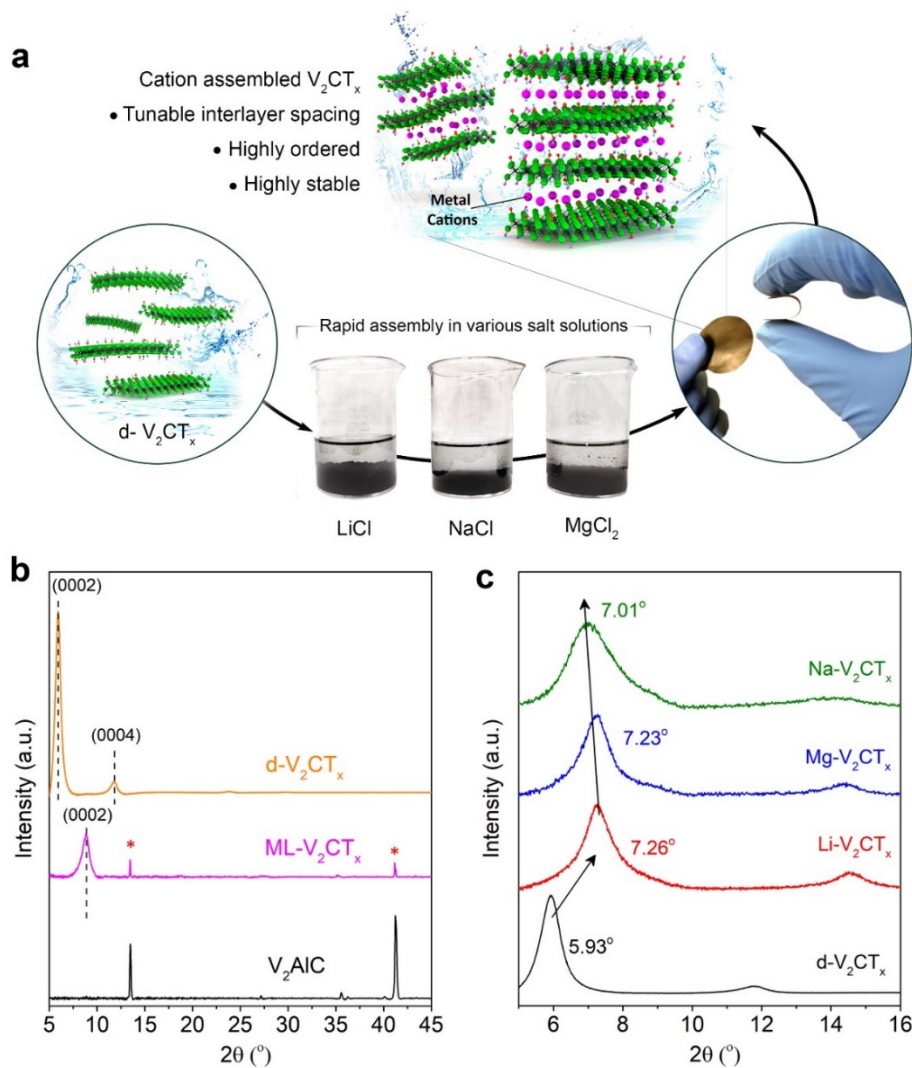
Figure 5.7. Assembly of V_2CT_x flakes and X-ray diffraction (XRD) characterization of fabricated M-V_2CT_x films (M: Li, Na, Mg). a) Schematic of d-V_2CT_x structure, digital photographs of the MXene dispersion after the addition of LiCl, NaCl, and MgCl$_2$ solutions, digital photographs of the freestanding flexible films fabricated with vacuum filtration of the assembled MXene flakes, and schematic illustration of the assembled flakes. (=b) XRD patterns of V_2AlC MAX phase, multilayered (ML) V_2CT_x, and delaminated V_2CT_x (d-V_2CT_x). After HF treatment and selective removal of Al atoms, the intensities of the MAX phase peaks were significantly reduced and a new peak corresponding to (0002) plane of MXenes appeared at ~8.86° (d-spacing: 9.97 Å, c-LP: 19.94 Å). After TBA$^+$ intercalation and complete delamination of V_2CT_x, residual MAX phase powders were separated from delaminated MXene flakes by centrifugation. XRD pattern of the d-V_2CT_x films showed a large downshift in the (0002) peak position to 5.93° (d-spacing: 14.89 Å, c-LP: 29.78 Å). Also, another peak corresponding to (0004) plane of MXene was appeared at ~ 11.75°. c) Enlarged portion of the XRD patterns of the films shown in Figure 2b of the article for low angles. Adapted and reproduced with permission from ref. 56 (copyright © 2019 Wiley-VCH Verlag GmBH & Co.).

The XRD patterns of both Li-V_2CT_x and Na-V_2CT_x films after one month (**Figure 5.8**) showed no change compared to the patterns of the as-fabricated films. **Figure 5.8 b** shows the V 2p XPS spectrum of a fresh Li-V_2CT_x film. It is interesting to note that in this film, vanadium is present in more reduced forms compare to d-V_2CTx films. Deconvolution of the XPS spectra of Li-V_2CT_x before and after argon etching shows that V^{2+} and V^{3+} species are dominant in this sample (~60-68%). As shown in **Figure 5.8 c,** in contrast to d-V_2CT_x, V^{5+} species were not detected in the XPS analysis of Li-V_2CT_x even after one month of storage in air. Also, as shown in **Figure 5.8 d** for Li-V_2CT_x, a freshly fabricated film is visually similar to those exposed to air at room temperature for one week and one month.

The combined evidence from a visual inspection of the films, the XRD data, and the XPS data imply that cation-driven assembly significantly suppresses the oxidation of the V_2CT_x flakes.

We suggest that the suppression of oxidation is related to a charge transfer from the inserted alkali ions to the MXene flakes. The charge density difference that occurs after Li insertion into the interlayer space of V_2CT_2 MXene with mixed -O and -F terminations, as calculated with density functional theory (DFT) is shown in **Figure 5.8 e**. A significant reduction in charge density is found close to the Li atom. Bader charge analysis[153] revealed that each Li atom loses 0.8e, which is transferred to the MXene layer. This charge is predominantly located on the terminating groups, particularly on the –F terminating atoms, which each gain approximately 0.2e while the –O terminating groups gain about 0.06e. On average, each V atom gains about 0.02e. This is in line with our XPS results that show the V species are in a more reduced state in Li-V_2CT_x compared to d-V_2CT_x. A similar charge transfer was previously calculated from sodium to V_2CT_2.[154]
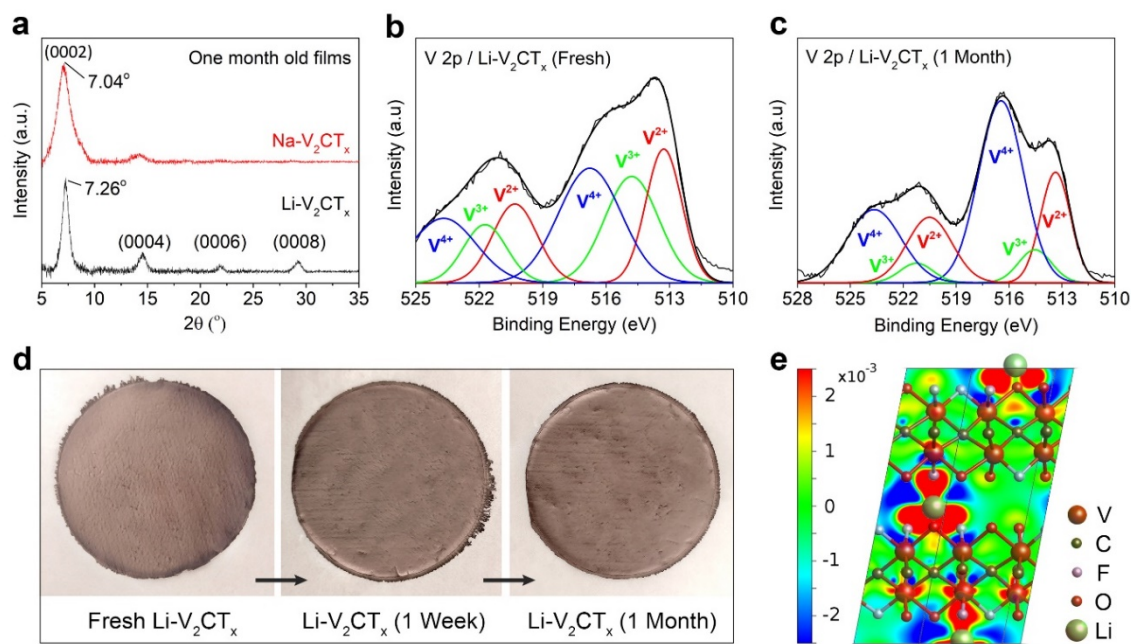
Figure 5.8. a) XRD patterns of the Li^+ and Na^+ assembled V_2CT_x films after one month. b) V 2p XPS spectrum of a fresh Li-V_2CT_x film. c) V 2p XPS spectrum of a Li-V_2CT_x after one month. d) Digital photographs of a Li-V_2CT_x film over time with no visual sign of degradation. e) Slices of charge density difference after lithiation, shown in a plane perpendicular to the MXene layer and through two intercalated Li atoms in the 3x3 unit cell. Here, red and blue colors indicate accumulation and depletion of charge density, respectively. The scale is in units of a.u.$^{-3}$. Adapted with permission from ref. 56 (copyright © 2019 Wiley-VCH Verlag GmBH & Co.).

Figure 5.9 also shows the shape of the V 2p XPS spectra shown in **Figure 5.8 b and c** before removal of the XPS Shirley background and their corresponding XPS fits. The end results and conclusions obtained from XPS analysis, however, are the same with or without removal of the Shirley background. In this figure also the C 1s XPS spectra for the two sample are provided. The C-C and C-O peaks are attributed to the adventitious contaminations.[16] As it can be seen, unlike the d-V_2CT_x sample, the V-C peak is present in the XPS spectra even after 1 month.
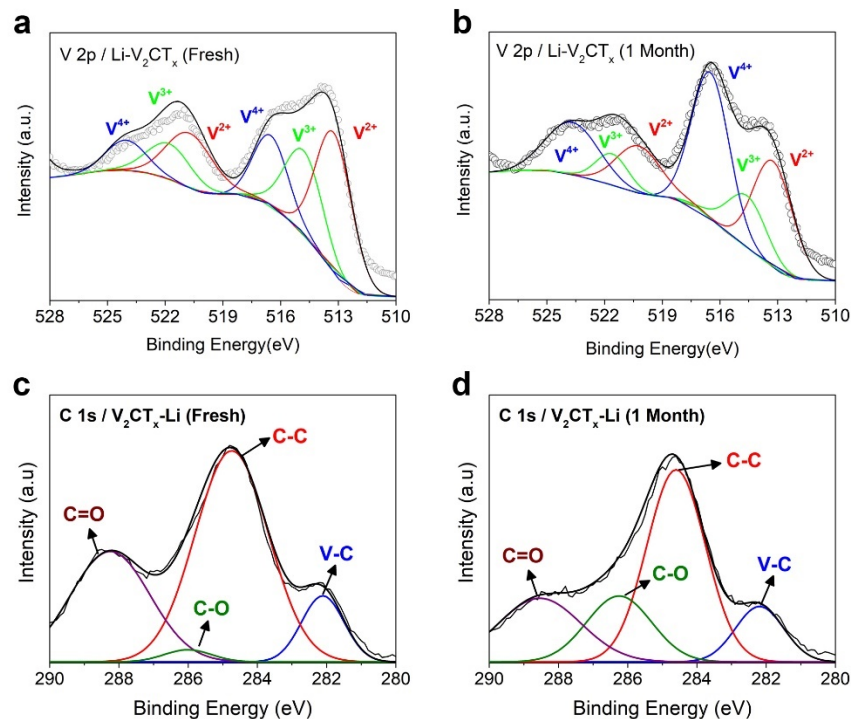
Figure 5.9. High-resolution V 2p XPS spectra of a) fresh d-V_2CT_x film and b) d-V_2CT_x film after one month (shown in the previous graph in panels a and b) before removal of the XPS Shirley background. C 1s spectra of c) fresh d-V_2CT_x film and d) d-V_2CT_x film after one month. Panels a and b are adapted and reproduced with permission from ref. 56 (copyright © 2019 Wiley-VCH Verlag GmBH & Co.).

The presence of alkali metals in the assembled C-V_2CT_x flakes (where C is Li, Na or Mg) was confirmed by energy dispersive X-ray spectroscopy (EDS) and, for the case of Li, by X-ray photoelectron spectroscopy (XPS) and inductively-coupled plasma mass spectroscopy (ICP-MS), as shown in **Figure 5.10**. Furthermore, high resolution scanning transmission electron microscopy (HR-STEM) images (shown in **Figure 5.11**) of these multilayered V_2CT_x flakes, assembled using either Li^+ or Na^+ cations (Li-V_2CT_x and Na-V_2CT_x), showed that the stacking number of the flakes ranges between 8-10 and 10-13, respectively. AFM analysis of the Li-V_2CT_x flakes (Shown in **Figure 5.12**) showed that in agreement with SEM and TEM analyses, they consist of several restacked MXene layers.
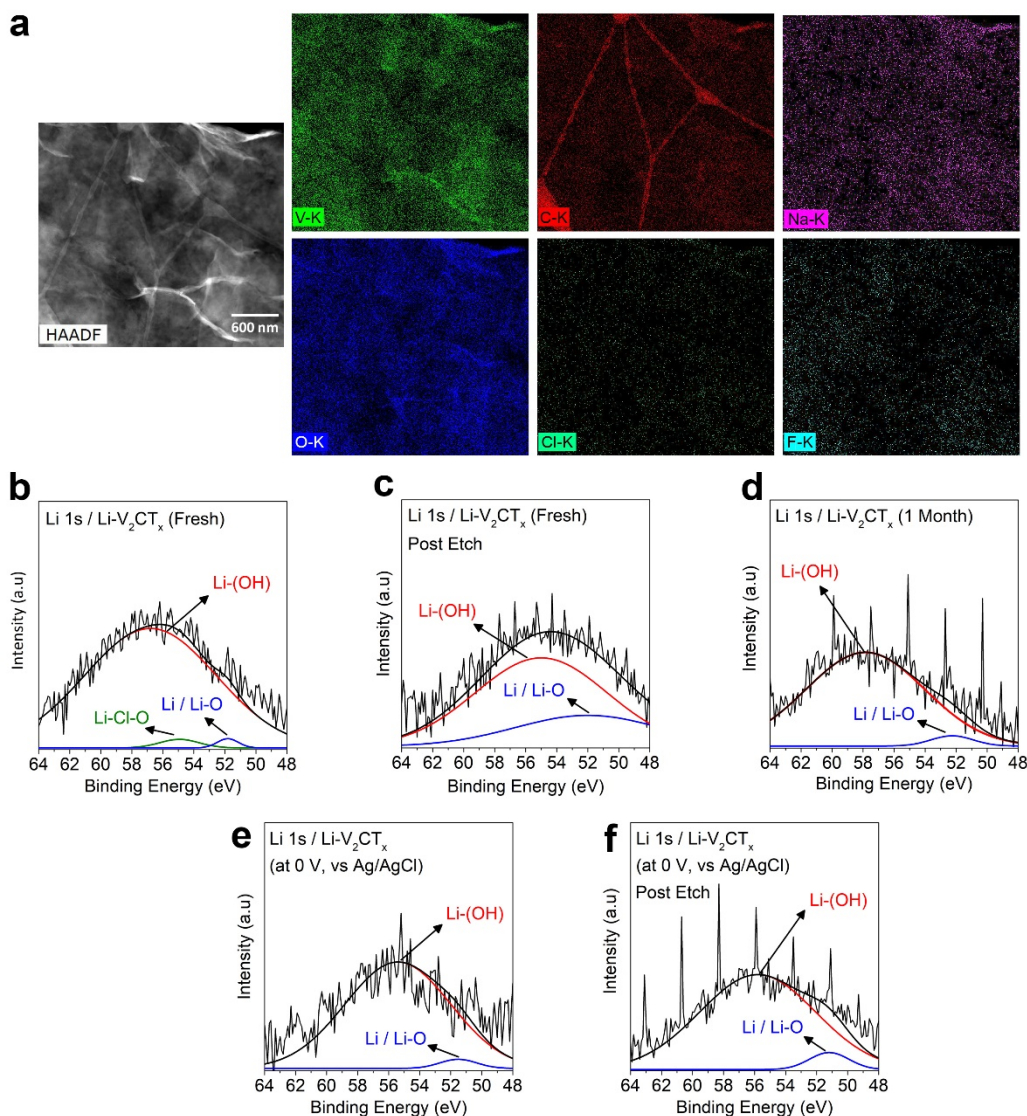
Figure 5.10. TEM/EDS and XPS results confirming the presence of Li and Na cations in the Li-V$_2$CT$_x$ and Na-V$_2$CT$_x$ flakes. a) TEM/EDS results of Na-V$_2$CT$_x$ confirming the presence of sodium in between the layers. b and c) XPS results for Li 1s region of a Li-V$_2$CT$_x$ sample, showing the presence of Li$^+$ in the sample before and after argon etching, respectively, indicating the presence of Li in the bulk of sample as well as its surface. d) High-resolution XPS results for Li 1s region of a Li-V$_2$CT$_x$ sample after one month. e and f) High-resolution XPS results for Li 1s region of a Li-V$_2$CT$_x$ sample charged to 0 V (V vs. Ag/AgCl) in 5 M LiCl before and after Argon etching, respectively. The XPS results show that the Li cations, placed in between the layers during the cation-driven assembly synthesis process, are very stable inside the structure and even after electrochemical deintercalation (charging of the electrode) some Li atoms remain in the electrode. Adapted with permission from ref. 56 (copyright © 2019 Wiley-VCH Verlag GmBH & Co.).
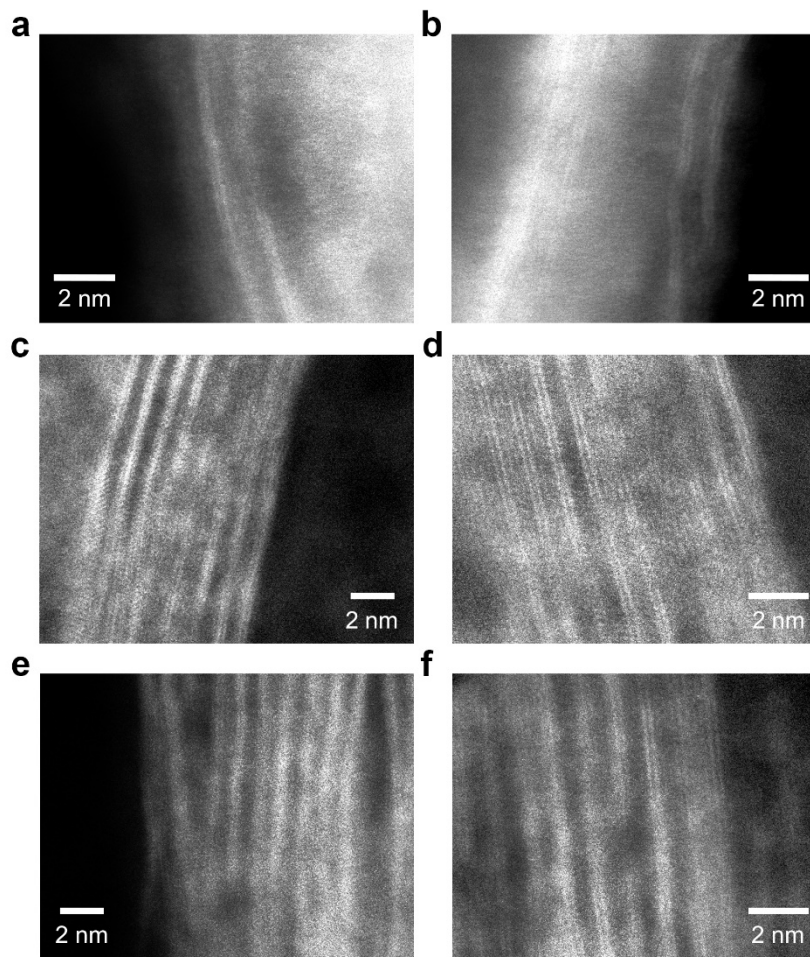
Figure 5.11. STEM images of V_2CT_x flakes. All TEM samples shown in this figure were prepared by drop casting the MXene solutions on a TEM grid to avoid directional ordering and assembly caused by vacuum filtration and be able to study the stacking and ordering of the flakes before and after cation-assembly. a and b) STEM images of delaminated V_2CT_x (d-V_2CT_x). The stacked (2 to 3) layers observed in the images are most probably due to self-restacking of delaminated flakes during drying on TEM grid. As seen in these images, d-V_2CT_x do not show ordered stacking. It is worth mentioning that d-V_2CT_x flakes were sensitive to the electron beam and at high magnifications their structure was degrading during their observation. Therefore, obtaining higher magnification images was not possible. c and d) STEM images of Li-V_2CT_x at different magnifications. In a good agreement with XRD results, TEM revealed higher ordering for V_2CT_x flakes restacked with Li^+ compared to other cations such as Na^+. The stacking number of flakes was around 8-10 for Li-V_2CT_x. e and f) STEM images of V_2CT_x flakes restacked with Na^+ (Na-V_2CT_x) at different magnifications. Na^+ restacked V_2CT_x showed less ordering (in good agreement with disappearance of (0006) and (0008) XRD peaks). Based on STEM images, the stacking number of Na-V_2CT_x sample was 10-13. Adapted with permission from ref. 56 (copyright © 2019 Wiley-VCH Verlag GmBH & Co.).
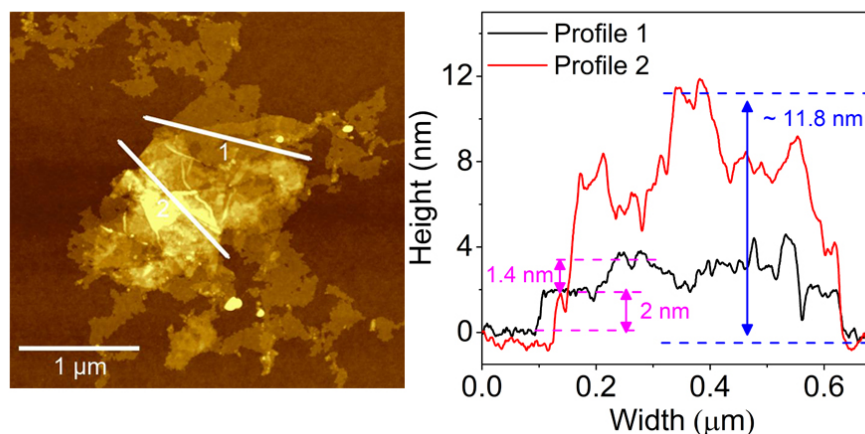
Figure 5.12. AFM image of Li-V$_2$CT$_x$ (V$_2$CT$_x$ assembled with Li$^+$) and the corresponding height profiles. Assembly of V$_2$CT$_x$ flakes is evident in the AFM image. The thickness of Li-V$_2$CT$_x$ flakes is around 11.8 nm, which corresponds to around 8 layers of MXene (thickness of first layer in contact with silicon wafer is around 2 nm, while AFM measurements on folded areas showed a thickness of ~ 1.4 nm for single layer V$_2$CT$_x$ on top of the first layer). Adapted with permission from ref. 56 (copyright © 2019 Wiley-VCH Verlag GmBH & Co.).

Also, in contrast to d-V$_2$CT$_x$ films, the C-V$_2$CT$_x$ films were very flexible (**Figure 5.13**) and showed superior chemical stability in the ambient condition.
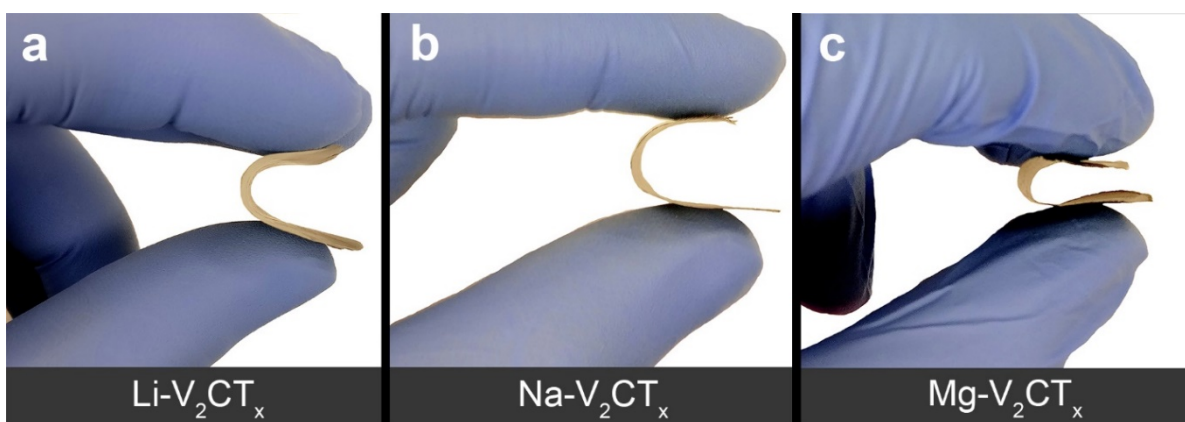
Figure 5.13. Photographs of the films fabricated using assembled C-V$_2$CT$_x$ flakes showing their flexibility. (a-d) Digital photographs of Li-, Na-, and Mg-V$_2$CT$_x$ MXene films showing their high flexibility similar to the Ti$_3$C$_2$T$_x$ MXene films.[41] Adapted with permission from ref. 56 (copyright © 2019 Wiley-VCH Verlag GmBH & Co.).

The effects of cation-driven assembly on the electrochemical properties of MXenes was studied using Li-V$_2$CT$_x$ and Na-V$_2$CT$_x$ electrodes, which showed the smallest and largest interlayer spacing among the C-V$_2$CT$_x$ films, respectively. **Figure 5.14 a** compares the CV profiles of d-V$_2$CT$_x$, Li-V$_2$CT$_x$, and Na-V$_2$CT$_x$ electrodes in a 5 M LiCl aqueous electrolyte. The CV responses of the electrodes are typical of intercalation based pseudocapacitive electrode materials, such as those previously reported for Ti$_3$C$_2$T$_x$ MXene,[62,70,71] but have not been demonstrated for V$_2$CT$_x$ before. In MXene electrodes the charge storage is accompanied by fast intercalation of ions allowing the redox reactions to occur in the bulk of the electrode and at the surface of individual MXene layers.[63] At the same scan rate of 2 mVs^{-1}, the area under the CV curves and the specific capacitance of Li-V$_2$CT$_x$ and Na-V$_2$CT$_x$ electrodes is significantly larger than that of the d-V$_2$CT$_x$ electrode. This can be explained by the pillaring effect of the cations between MXene layers and the more ordered structure of the assembled MXene electrodes which is expected to improve both ionic and electronic transport properties of the electrodes. As explained above, Na-V$_2$CT$_x$ had a larger interlayer spacing compared to Li-V$_2$CT$_x$ and, as a result, it showed better electrochemical properties, especially at higher scan rates (**Figure 5.14 c and Figure 5.15 a**). Nevertheless, the CV profiles of Li-V$_2$CT$_x$ and Na-V$_2$CT$_x$ were quite similar, offering a larger potential window (1V) than previously reported MXene electrodes tested in aqueous electrolytes.[15] An important property of assembled C-V$_2$CT$_x$ electrodes is that they can intercalate cations of different charges and sizes. CV profiles of Na-V$_2$CT$_x$ in various sulfate electrolytes (containing Li$^+$, Na$^+$, K$^+$, Mg^{2+}, Zn^{2+}, and Al^{3+} cations) are shown in **Figure 5.14 b**. Different CV shapes, as well as different capacitance values obtained in different electrolytes with similar anionic species, indicate that cation intercalation (and the associated redox reactions occurring at MXene surfaces upon their insertion) is the dominant charge storage mechanism in C-V$_2$CT$_x$ electrodes.

Gravimetric capacitances of Na-V$_2$CT$_x$ electrodes in different electrolytes are shown in **Figure 5.14 c**, at scan rates ranging from 2 to 100 mV s^{-1}. Depending on the electrolyte and intercalating cations, Na-V$_2$CT$_x$ electrodes showed specific capacitances ranging from ~120 F g^{-1} to ~285 F g^{-1}. These capacitance values are around three times higher than what has been reported for freestanding films of d-Ti$_3$C$_2$T$_x$ in electrolytes containing similar cations.[15]

Figure 5.14 d shows the cycle-life performance of Na-V$_2$CT$_x$ electrodes in different electrolytes at 10 A g^{-1}. Regardless of the electrolyte used and intercalating cations, Na-V$_2$CT$_x$ electrodes showed excellent cyclic performance with no capacity decay after 10,000 cycles and Coulombic efficiencies of about 100%. It is interesting to note that for electrolytes with larger cations, such as MgSO$_4$ and K$_2$SO$_4$, the specific capacitance of the electrodes initially increased before becoming constant. The CV profiles of Na-V$_2$CT$_x$ in these electrolytes showed a gradual increase in current during cycling. This can be explained by an initial slow diffusion or intercalation rate of the larger cations into the electrode, which improves during successive charge/discharge cycles. A similar behavior was reported for d-Ti$_3$C$_2$T$_x$ in a MgSO$_4$ electrolyte, where maximum capacity was achieved after 48h of continued cycling.[15]

To investigate the limits of rate handling and cyclic life of the assembled MXene electrodes, a Na-V$_2$CT$_x$ electrode was subjected to galvanostatic charge/discharge (GCD) cycling in a K$_2$SO$_4$ electrolyte at a current density of 100 A g^{-1} (**Figure 5.14 e).** At this high current rate, the Na-V$_2$CT$_x$ electrode showed a volumetric capacity of ~ 250 F cm^{-3} with capacitance retention of ~77% after one million cycles. To the best of our knowledge, no other pseudocapacitive material has been reported to date with such excellent cyclic performance and lifetime. Furthermore, CV profiles of Na-V$_2$CT$_x$ (shown in **Figure 5.16**) remained almost rectangular at scan rates of up to 1,000 mV s^{-1}, indicating their high-rate handling capability.[15]
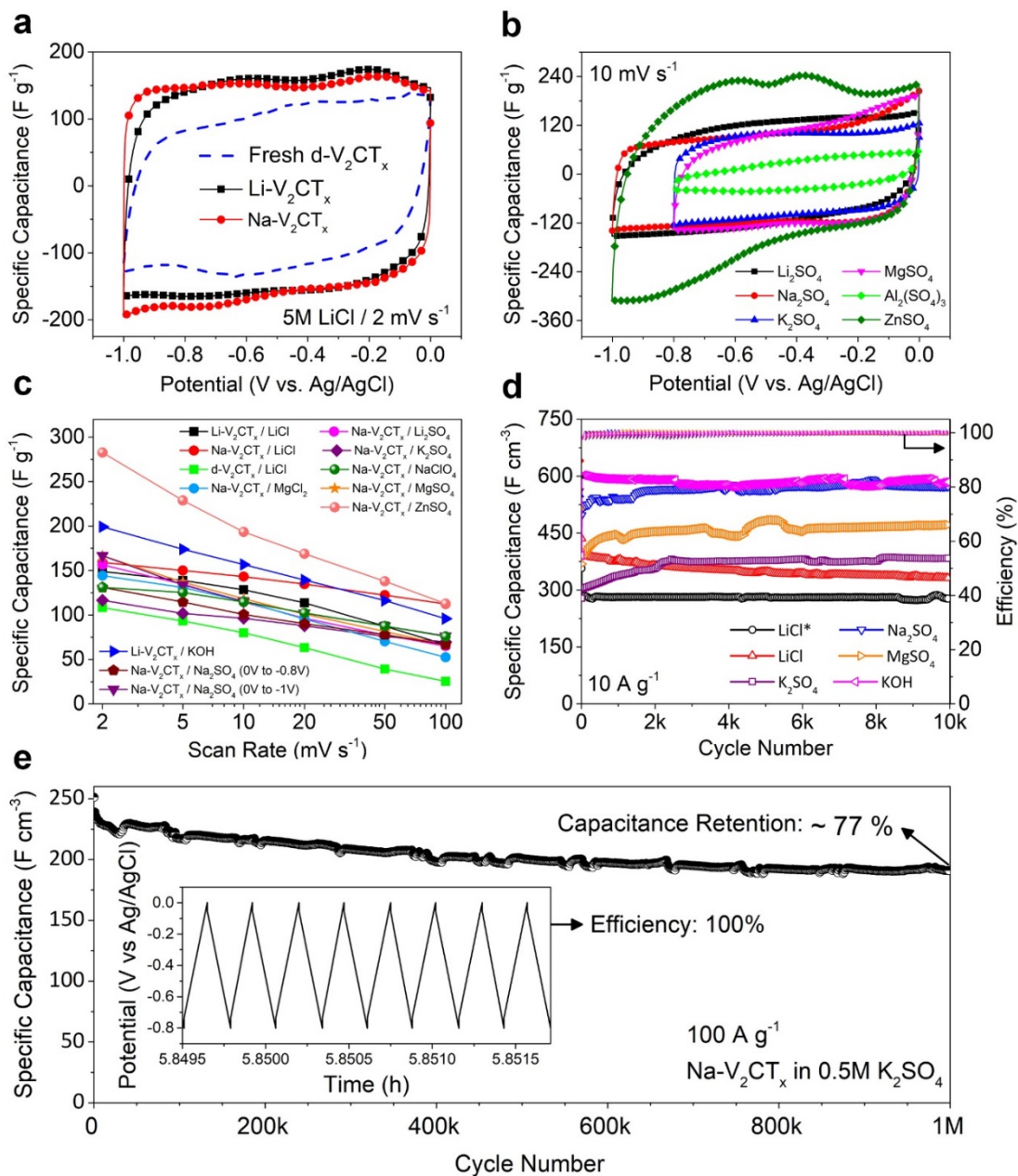
Figure 5.14. Electrochemical analyses and performance of Na-V$_2$CT$_x$. a) CV profiles of d-V$_2$CT$_x$, Li-V$_2$CT$_x$, and Na-V$_2$CT$_x$ electrodes in 5 M LiCl electrolyte (scan rate=2 mVs^{-1}). b) CVs of Na-V$_2$CT$_x$ in various electrolytes. c) Gravimetric capacitance of different V$_2$CT$_x$ electrodes in various salt electrolytes. d) Cyclic performance of Na-V$_2$CT$_x$ electrodes in various electrolytes at 10 A g^{-1}. (*) indicates working electrode was Li-V$_2$CT$_x$. e) Cycle life performance of an Na-V$_2$CT$_x$ electrode in a K$_2$SO$_4$ electrolyte with an efficiency of 100% and ~ 77% capacitance retention after one million cycles at a rate of 100 A g^{-1}. Adapted with permission from ref. 56 (copyright © 2019 Wiley-VCH Verlag GmBH & Co.).
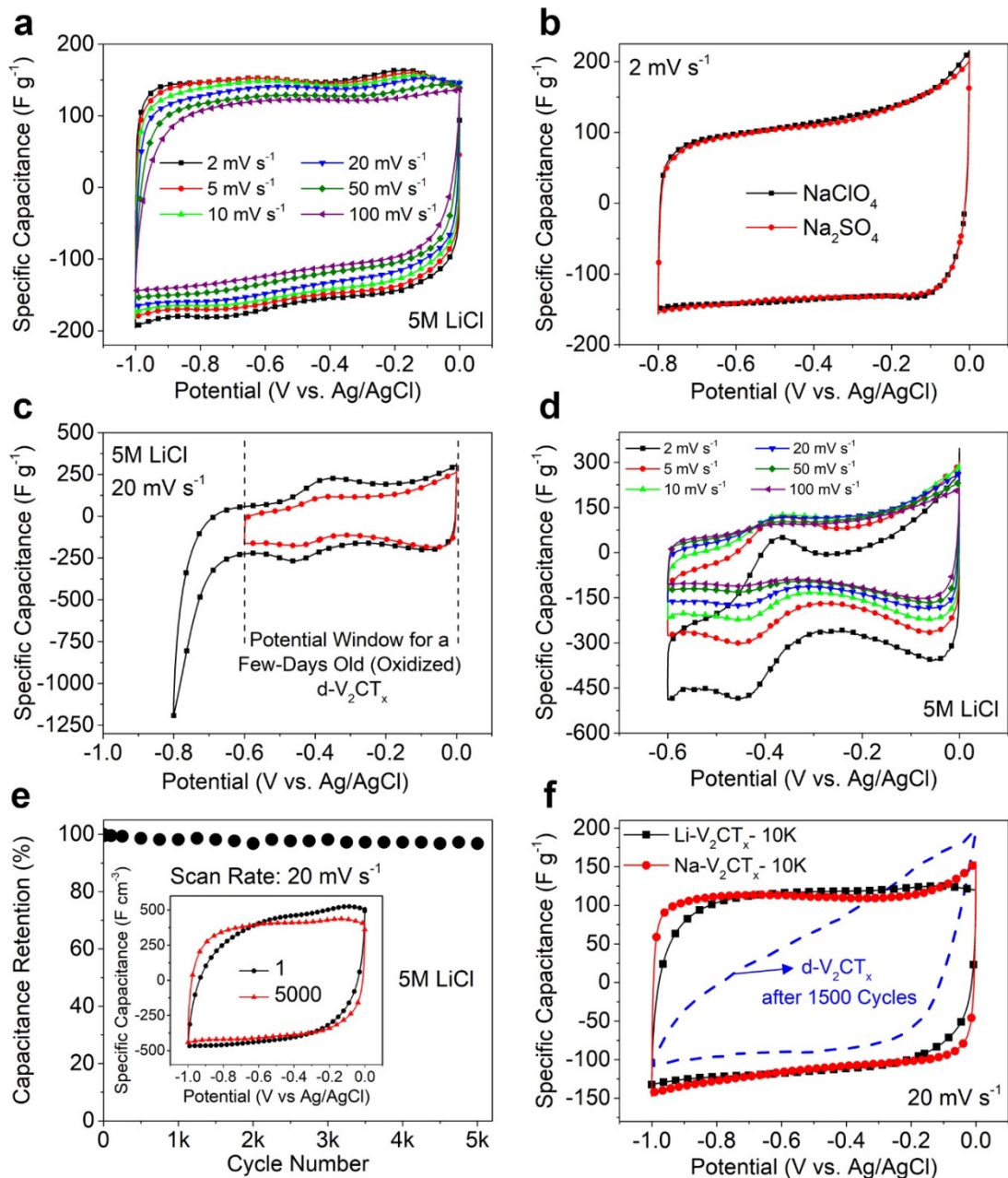
Figure 5.15. Electrochemical behavior of V_2CT_x: cycle life and cation intercalation. a) CV profiles of Na-V_2CT_x in 5 M LiCl at different scan rates of 2 to 100 mV s^{-1} s. b) CV profiles of Na-V_2CT_x in 1 M Na_2SO_4 and 1 M $NaClO_4$ electrolytes at 2 mV s^{-1}. c) CV of a few days old d-V_2CT_x (oxidized, similar to the one-week old black film). d) CVs of the oxidized d-V_2CT_x film at scan rates of 2 mV s^{-1} to 100 mV s^{-1} showing a large irreversibility in the CV curves. e) Cyclic performance of a 4 µm thick Li-V_2CT_x electrode at a scan rate of 20 mV s^{-1} in 5 M LiCl with no sign of degradation or capacitance loss after 5,000 cycles. f) CVs of Li-V_2CT_x and Na-V_2CT_x electrodes at a scan rate of 20 mV s^{-1} after 10,000 cycles in 5 M LiCl. Adapted with permission from ref. 56 (copyright © 2019 Wiley-VCH Verlag GmBH & Co.).

The similar shape of CVs as well as comparable capacitance of the electrodes in two different Na electrolytes with different anionic species (shown in **Figure 5.15 b**) further confirms the hypothesis that the intercalating ionic species are cations and not anions. As it can be seen in **Figure 5.15 c and d**, the oxidized films showed a much narrower potential window (0.6 V) compared to the freshly synthesized films (1V, similar to cation-assembled films). A long tail was observed in the CV at potentials lower than -0.6 V. Furthermore, as shown in **Figure 5.15 f**, the assembled V_2CT_x electrodes maintained their rectangular capacitive CV shape even after long cycling and showed superior stability and cycle life compared to d-V_2CT_x electrodes (shown by the dashed line), which drastically lost their capacitance in less than 1 500 cycles.
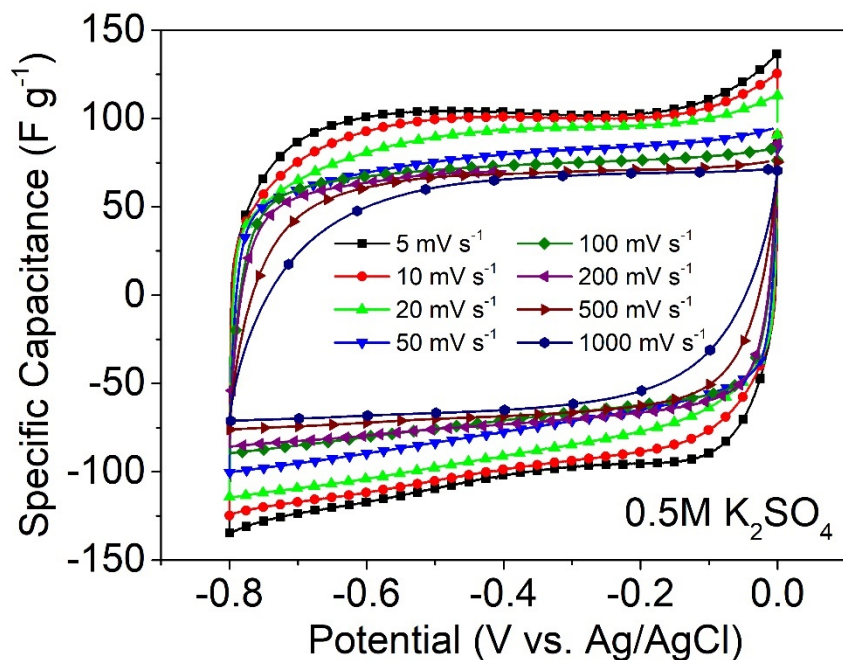
Figure 5.16. CV profiles of a Na-V_2CT_x electrode in 0.5 M K_2SO_4 electrolyte at scan rates ranging from 5 mV s^{-1} to 1000 mV s^{-1}. The CV curves remained near rectangular in all scan rates demonstrating the excellent rate capability of the assembled V_2CT_x MXene electrodes. Adapted with permission from ref. 56 (copyright © 2019 Wiley-VCH Verlag GmBH & Co.).

Based on the electrochemical analysis of the electrodes, we suggest that similar to $Ti_3C_2T_x$, the charge storage mechanism for V_2CT_x MXene is intercalation based pseudocapacitance. As shown in **Figure 5.17**, the fabricated electrodes have a relatively low surface area compared to activated carbon and other high surface area materials used as EDLC electrodes. Therefore, as previously shown in the case of $Ti_3C_2T_x$, the observed high capacitance is mainly related to fast redox reactions that follow the intercalation of ions between MXene layers and are accompanied by the change in the oxidation state of MXene's transition metal.[13,17,62] Previously, the high pseudocapacitance of $Ti_3C_2T_x$ in 3 M H_2SO_4 has been ascribed to intercalation of protons and change in the oxidation state of Ti, where this change was accompanied by protonation of the oxygen functional groups on the surface of MXene layers.[17,61,155] V_2CT_x MXene has very similar surface chemistry to that of $Ti_3C_2T_x$[16,142,156] and its electrochemical behavior in many electrolytes (e. g., CV curves in 3 M H_2SO_4 electrolyte as it will be discussed later) are similar to the general electrochemical behavior of $Ti_3C_2T_x$ with broad and distinct redox couples. We have clearly observed the intercalation of electrolyte ions into between MXene layers in XRD experiments (shown in Figure **5.18**), where change in the interlayer spacing was observed after ion intercalation. Ion intercalation is slower at the beginning of the charge-discharge process, but accessibility of the electrode interlayer spacing increases as the intercalation process continues. As a result, in some electrolytes (particularly those with larger and higher charge density cations) we observe a gradual increase in the capacitance and expansion of the area under CV curves during cycling (further explained in **Figure 5.19**). This behavior has been previously reported for other MXenes and together with XRD and electrochemical results discussed above confirm a charge storage mechanism based on intercalation pseudocapacitance.[17,61,62]
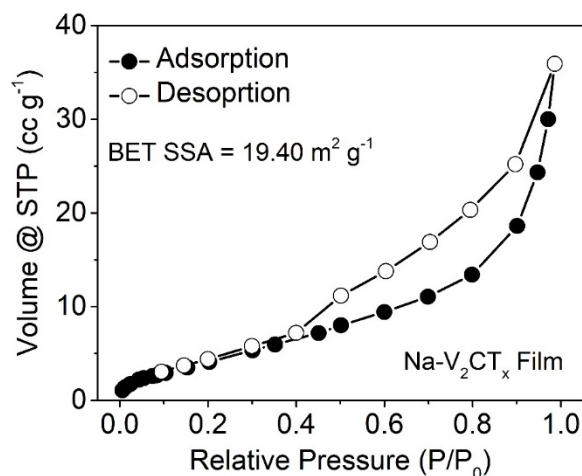
Figure 5.17. N_2 adsorption-desorption isotherms of a Na-V_2CT_x film. The Brunauer-Emmett-Teller (BET) specific surface area (SSA) was measured to be 19.40 m^2 g^{-1}. The pore size distribution of the sample was in the range of 10-70 nm and in the relative pressure range of 0.4-1.0, and the isotherm suggest that the MXene sample has slit-shaped pores.[20] Adapted with permission from ref. 56 (copyright © 2019 Wiley-VCH Verlag GmBH & Co.).
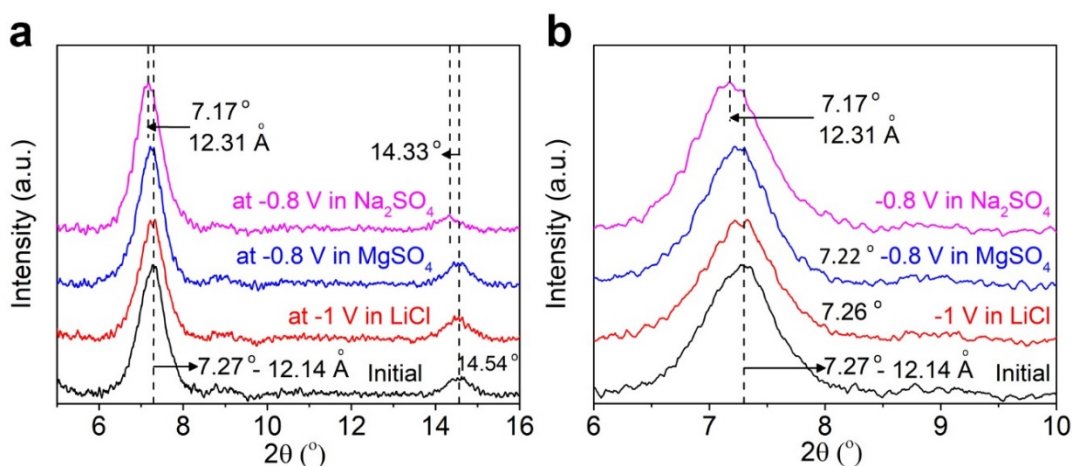
Figure 5.18. *Ex situ* XRD analysis of Li-V_2CT_x electrode after electrochemical intercalation of various cations. a) Shift of the peak related to the (0002) plane of Li-V_2CT_x electrodes after electrochemical intercalation of various cations. The electrodes were taken off the cells at the end of reduction portion of CV. The electrochemical intercalation of Mg^{2+} and Na$^+$ cations into Li-V_2CT_x (with initial d-spacing of 12.14 Å) resulted in a downshift in the position of (0002) peak toward lower angles corresponding to 0.09 Å and 0.18 Å increase in the d-spacing of MXene, respectively. Intercalation of Na$^+$ cations also resulted in downshift and broadening of the XRD peak for (0004) planes of MXenes. b) Enlarged version of XRD pattern between 6 and 10 degrees. Adapted with permission from ref. 56 (copyright © 2019 Wiley-VCH Verlag GmBH & Co.).
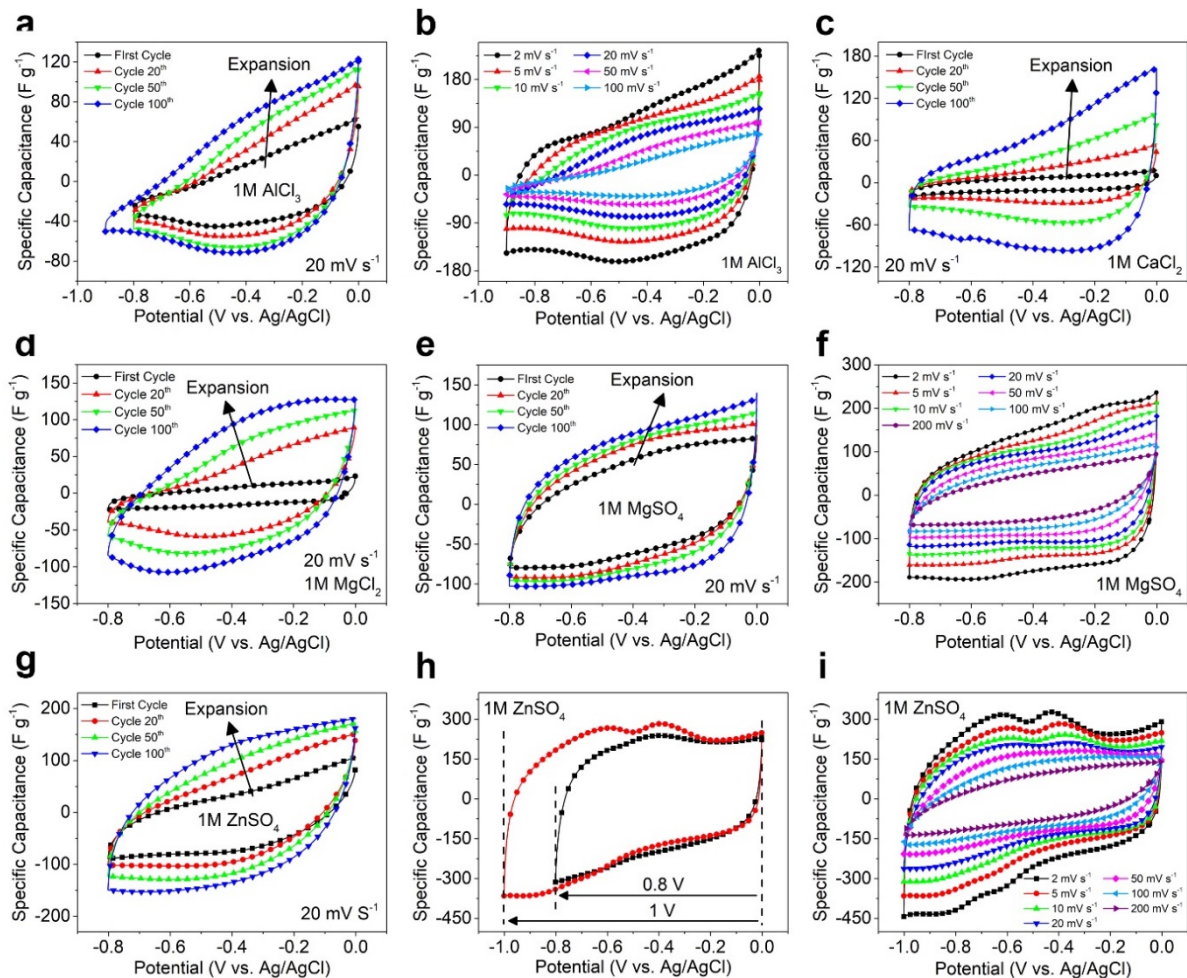
Figure 5.19. Increase in CV current of Na-V$_2$CT$_x$ electrodes during initial cycling in different electrolytes. a) Increase in CV currents and the expansion of areas under CV curves during the first 100 cycles in AlCl$_3$ electrolyte. b) CVs of Na-V$_2$CT$_x$ in AlCl$_3$ at scan rates from 2 mV s^{-1} to 100 mV s^{-1}. c) Expansion of CV area during the first 100 cycles in CaCl$_2$ electrolyte. d and e) Initial CVs in 1 M MgCl$_2$ and 1 M MgSO$_4$ electrolytes showing the expansion of CV area upon intercalation of Mg^{2+} during the first 100 cycles. f) CVs in 1 M MgSO$_4$ electrolyte at scan rate ranging from 2 mVs^{-1} to 200 mV s^{-1}. g) Initial expansion of CV in ZnSO$_4$ electrolyte upon Zn^{2+} intercalation. h) CVs in ZnSO$_4$ in two different lower cut-off potentials at scan rate of 5 mV s^{-1}. By increasing the lower potential to -1 V, another pair of oxidation (-0.7 V) and reduction (-0.85 V) peaks was observed. i) CVs in 1 M ZnSO$_4$ electrolyte at scan rates of 2 mV s^{-1} to 200 mV s^{-1}. Adapted with permission from ref. 56 (copyright © 2019 Wiley-VCH Verlag GmBH & Co.).

The electrochemical performance of Na-V_2CT_x electrodes in electrolytes containing various inorganic cations surpasses the reported performance of d-$Ti_3C_2T_x$ films. Previous studies, however, have shown that $Ti_3C_2T_x$ achieves its highest capacitance in H_2SO_4 electrolytes.[17,31,32,41,55,76] This high capacitance is due to the change in the oxidation state of Ti accompanied by the pronation of oxygen surface groups during redox reactions in the H_2SO_4 electrolytes.[61] As a results of the redox reactions, the CV curves of $Ti_3C_2T_x$ in H_2SO_4 electrolytes show distinct reversible redox peaks.[17,41] In order to make a direct comparison, we investigated the capacitive performance of Na-V_2CT_x electrodes in a 3 M H_2SO_4 electrolyte. CV tests of the electrodes (**Figure 5.20**) showed a pair of broad and highly reversible redox peaks at ~0 V (vs Ag/AgCl). The electrodes showed a highly capacitive response up to very high scan rates of 2 V s^{-1}. The highest specific capacitances, of ~1315 F cm^{-3} and ~420 F g^{-1}, were found at a scan rate of 5 mV s^{-1}. These volumetric and gravimetric capacitances are on average higher by about 400 F cm^{-3} and 150 F g^{-1}, respectively, than the capacitance of freestanding $Ti_3C_2T_x$ film electrodes with comparable thicknesses[41] and about two times higher than the specific capacitance of 1T MoS_2 electrodes.[157] For $Ti_3C_2T_x$, similar high-rate pseudocapacitive response has been only observed for structurally engineered hydrogel and porous electrodes.[17] GCD tests (shown in **Figure 5.21**) showed that the drop in the specific capacitance of the electrodes with increasing the current density is relatively small. At a very high current density of 100 A g^{-1}, the Na-V_2CT_x electrode showed an outstanding capacitance of ~200 F g^{-1}.

The volumetric capacitance and rate capability of Na-V_2CT_x electrodes in electrolytes comprised of sulfate anions and various cations are compared in **Figure 5.20 b**. While the highest specific capacitance at each scan rate was achieved in a H_2SO_4 electrolyte, the performance of the electrodes was very impressive in all of the considered electrolytes. For example, at a scan rate of

5 mV s^{-1} volumetric capacitances of ~852 F cm^{-3}, ~790 F cm^{-3}, ~664 F cm^{-3} was achieved in ZnSO$_4$, K$_2$SO$_4$, and MgSO$_4$ electrolytes, respectively. The excellent capacitive performance and ion transport properties of Na-V$_2$CT$_x$ electrodes in various electrolytes were also confirmed by electrochemical impedance spectroscopy (EIS) measurements (**Figure 5.22).**
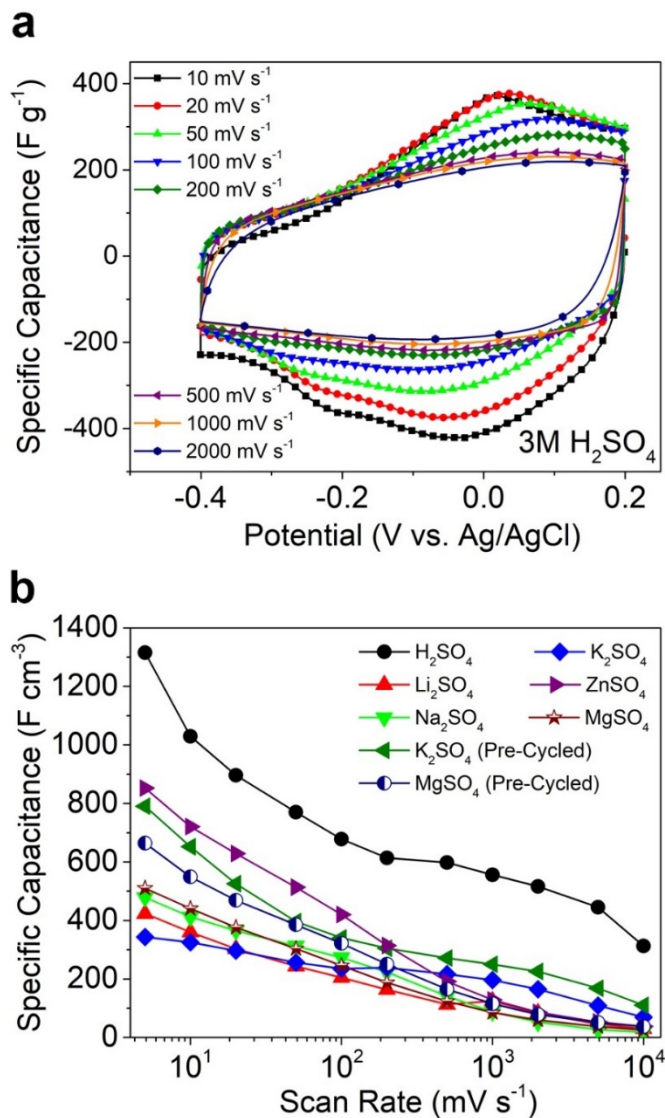
Figure 5.20. Performance of 2D vanadium carbide in sulfuric acid electrolyte. a) CV profiles of a Na-V$_2$CT$_x$ electrode in a 3 M H$_2$SO$_4$ electrolyte at scan rates from 10 mV s^{-1} to 2 V s^{-1}. b) Capacitance and rate performance of 3-4μm-thick Na-V$_2$CT$_x$ electrodes in various sulfate-based electrolytes. Adapted with permission from ref. 56 (copyright © 2019 Wiley-VCH Verlag GmBH & Co.).
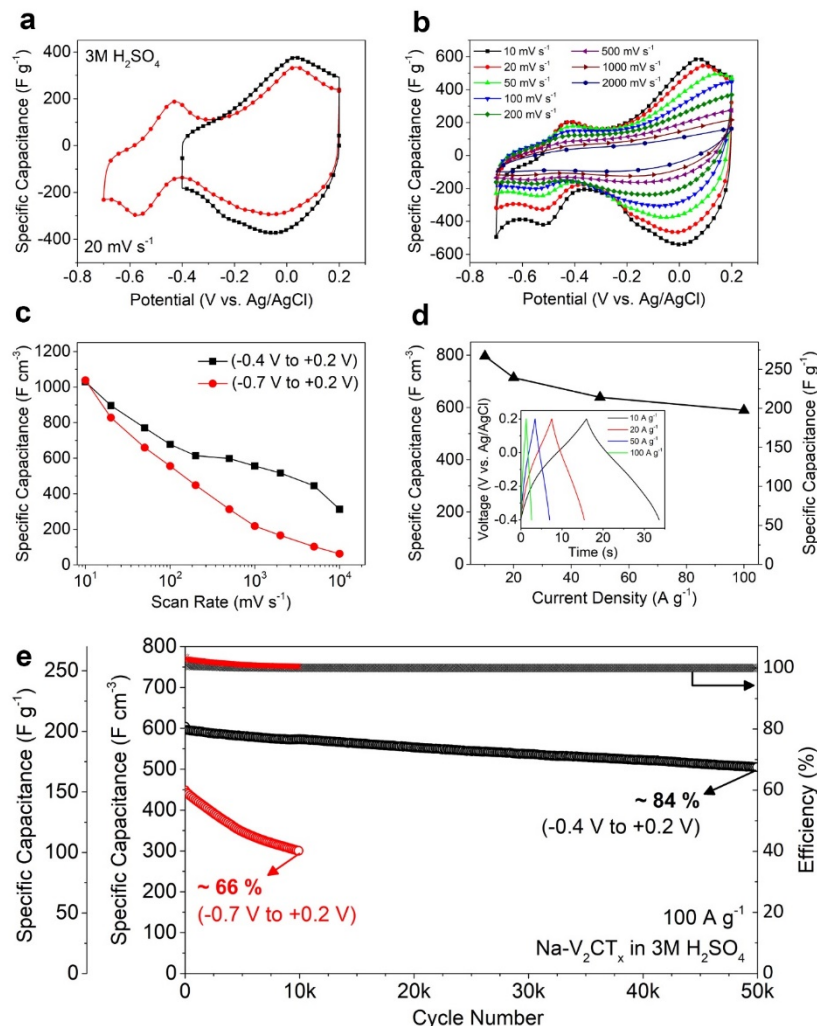
Figure 5.21. Potential window and cycle life performance of Na-V$_2$CT$_x$ electrode in 3 M H$_2$SO$_4$. a) CVs of Na-V$_2$CT$_x$ in two different potential windows in 3 M H$_2$SO$_4$ electrolyte. Increasing the lower cut off potential resulted in appearance of another redox pair with wider peak separation potentials and less reversibility. We believe these second redox peaks are due to an irreversible reaction of the MXene with the acidic electrolyte, which causes a rapid decay in the performance of the cell over cycling as well as at higher scan rates.[158] b) CV profiles of Na-V$_2$CT$_x$ at scan rates of 10 mV s^{-1} to 2000 mV s^{-1} in the larger potential window, showing rapid capacity decay at higher scan rates. c) Rate performance of Na-V$_2$CT$_x$ electrode in narrow and wide potential windows. d) Rate capability of Na-V$_2$CT$_x$ in 3 M H$_2$SO$_4$ at charge-discharge rates from 10 to 100 A g^{-1}. Inset shows charge-discharge (voltage vs. time) profiles. e) Cycle life performance of Na-V$_2$CT$_x$ electrode at 100 A g^{-1} in the narrow and wide potential windows. The electrode could withstand ~84% of the initial capacitance after 50 000 cycles in the narrow potential window while in the wider potential window the capacitance dropped to ~66% of the initial capacitance just after 10,000 cycles. It is important to note that in the H$_2$SO$_4$ electrolyte, unlike other tested electrolytes, the Na-V$_2$CT$_x$ electrodes showed the same high pseudocapacitive response from the initial cycles. This is due to the significantly smaller size of protons compared to alkali cations and their fast intercalation between MXene layers.[17,41] Adapted with permission from ref. 56 (copyright © 2019 Wiley-VCH Verlag GmBH & Co.).
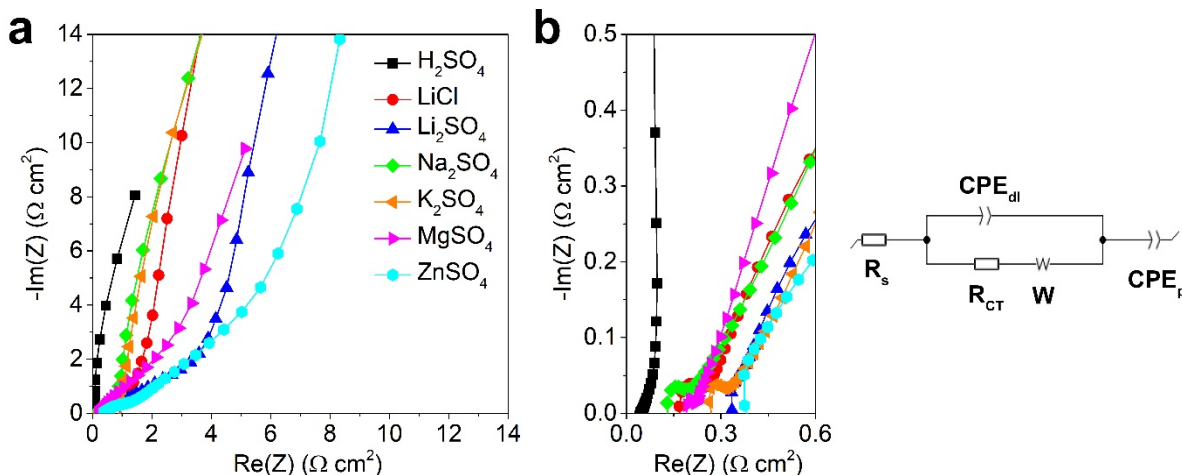
Figure 5.22. The results of electrochemical impedance spectroscopy (EIS) measurements of Na-V$_2$CT$_x$ film electrodes. a) Low-frequency region for Nyquist plots of the electrodes in various electrolytes (measurements were performed at OCV and for the frequency range of 100 mHz to 1000 kHz). b) High-frequency region of the Nyquist plots shown in (a) as well as the equivalent circuit used to fit the EIS data, where R$_s$ is the bulk electrolyte resistance, CPE$_{dl}$ is the double-layer capacitance which usually exists in parallel with R$_{CT}$, the charge transfer resistance, and W, a Warburg diffusion element[159,160], and CPE$_p$ is the pseudocapacitance element.[161,162] EIS results showed the capacitive performance of the electrodes in all electrolytes. However, for H$_2$SO$_4$ electrolyte the shape of the Nyquist plot is very close to an ideal capacitive response, with a short length of 45-degree linear part (Warburg impedance related to the ion transport resistance in the electrodes), and an almost vertically rising imaginary impedance at low frequencies.[17] The EIS data show that ion transport resistance in salt solutions is higher than in H$_2$SO$_4$ electrolyte. This is in line with our conclusions derived from CV tests, which reveal slower intercalation of alkali cations as compared to protons. For the electrodes tested in salt electrolytes, small semi-circles are observed in the low-frequency region of Nyquist plots. This is believed to stem from charge-transfer resistance arising from removal or rearrangement of the cation hydration shell during intercalation.[71,163] Adapted with permission from ref. 56 (copyright © 2019 Wiley-VCH Verlag GmBH & Co.).

The gravimetric capacitance of the cation assembled V$_2$CT$_x$ films are also shown in **Figure 5.23**. It is also important to note that similar to other 2D materials, the assembled V$_2$CT$_x$ MXene films showed a thickness dependent performance, however, the drop in capacitance was much less compared to the conventional 2D materials. This behavior is shown in **Figure 5.24.**
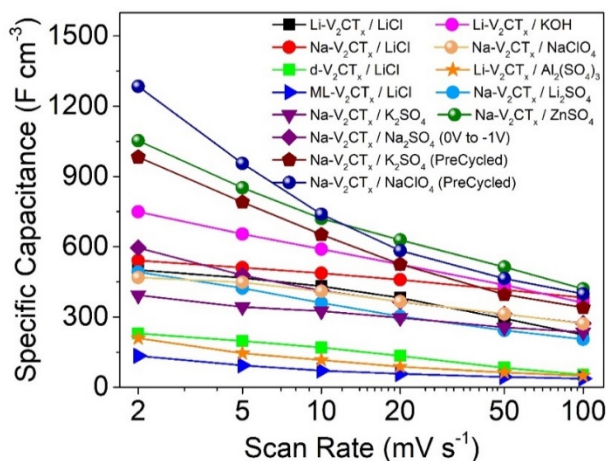
Figure 5.23. Volumetric capacitance of different V_2CT_x electrodes in various electrolytes. The term "Precycled" used for some electrodes indicates that those electrodes were cycled over 1000 cycles to reach their maximum capacitance and were then tested at different rates. Adapted with permission from ref. 56 (copyright © 2019 Wiley-VCH Verlag GmBH & Co.).
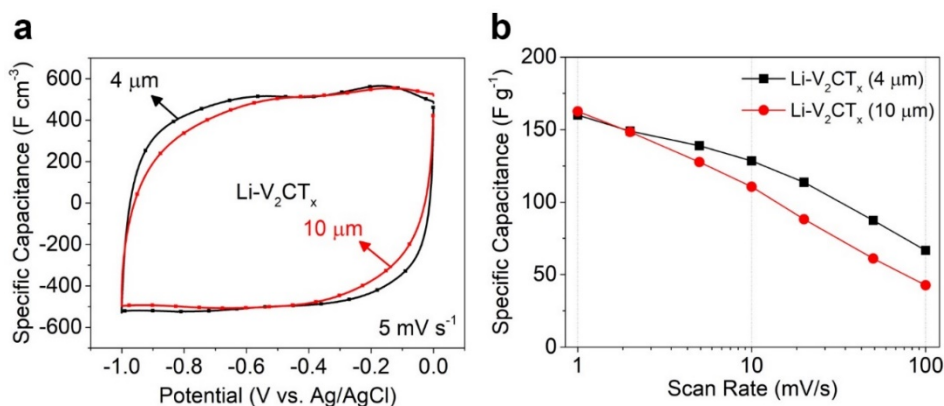
Figure 5.24. Effect of electrode thickness on electrochemical performance. The electrochemical performance of the freestanding films fabricated using 2D materials is often highly dependent on the thickness of the electrodes. The thickness dependent behavior has been previously observed for $Ti_3C_2T_x$ MXene and other 2D materials used as electrodes in ECs.[41,157] A severe drop in performance with increasing the thickness can make the electrode useless for practical applications. However, for assembled V_2CT_x, the drop in the performance with increasing thickness is very mild. (a) CV curves of a 4 µm and 10 µm thick Li-V_2CT_x electrodes at 5 mV s^{-1} in 5 M LiCl, showing very small change in the CV curve with increasing the thickness. (b) Comparison of the gravimetric capacitances of the 4 µm and 10 µm thick electrodes at different scan rates, showing the capacitance drop for the thicker electrode at higher scan rates. The diffusion (intercalation) of cations inside the thicker electrodes is slower and contributes to the lower capacitance at higher scan rates. Adapted with permission from ref. 56 (copyright © 2019 Wiley-VCH Verlag GmBH & Co.).

Figure 5.25 a compares the CV curves of Na-V_2CT_x symmetric supercapacitors in H_2SO_4,

Na_2SO_4, K_2SO_4, and LiCl electrolytes at a scan rate of 10 mV s^{-1} (**Figure 5.26 a-d** also show the

CV curves in these electrolytes at different scan rates). **Figure 5.25 b** shows a Ragone plot

comparing the volumetric performance of the Na-V_2CT_x symmetric supercapacitors with some of

the other notable symmetric supercapacitors and batteries reported in the literature. It should be

noted that the volumetric power (P) and energy (E) densities of Na-V_2CT_x symmetric cell in some

electrolytes, such as K_2SO_4, are an order of magnitude higher than those reported for symmetric

d-$Ti_3C_2T_x$ cells in the same electrolytes.[15] Moreover, Na-V_2CT_x symmetric cells in LiCl electrolyte

showed a power density of 1.46 W cm^{-3} at an energy density of 0.2 Wh cm^{-3}. The energy density

of the cell reached 0.04 Wh cm^{-3} at a high-power density of 28.15 W cm^{-3}. These promising results

place the V_2CT_x MXene among the best pseudocapacitive materials reported to date.[15,41,157,164–166]

The E and P values were calculated based on the total volume of the MXene electrodes.
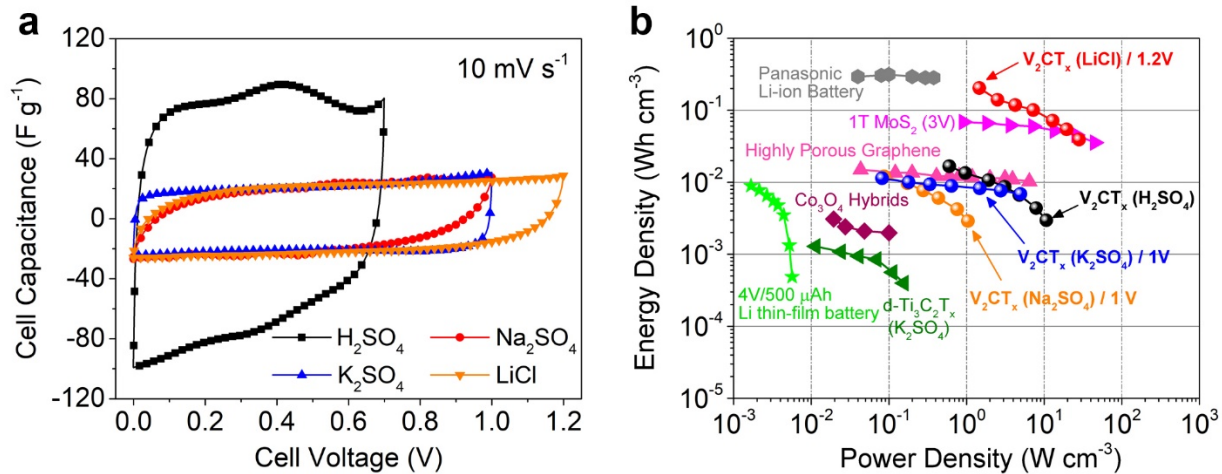
Figure 5.25. a) CV profiles of symmetric supercapacitors assembled using Na-V_2CT_x electrodes in various
electrolytes. b) Ragone plot of Na-V_2CT_x symmetric supercapacitors comparing the energy (E) and power
(P) density of symmetric Na-V_2CT_x cells to other supercapacitor and battery systems reported in the
literature: $Ti_3C_2T_x$ MXene,[5] Panasonic Li-ion batteries,[5,40] 1T MoS_2,[40] Co_3O_4/Co(OH)$_2$ hybrids,[167] highly
porous graphene,[40] Li-thin film battery.[5] Adapted with permission from ref. 56 (copyright © 2019 Wiley-
VCH Verlag GmBH & Co.).
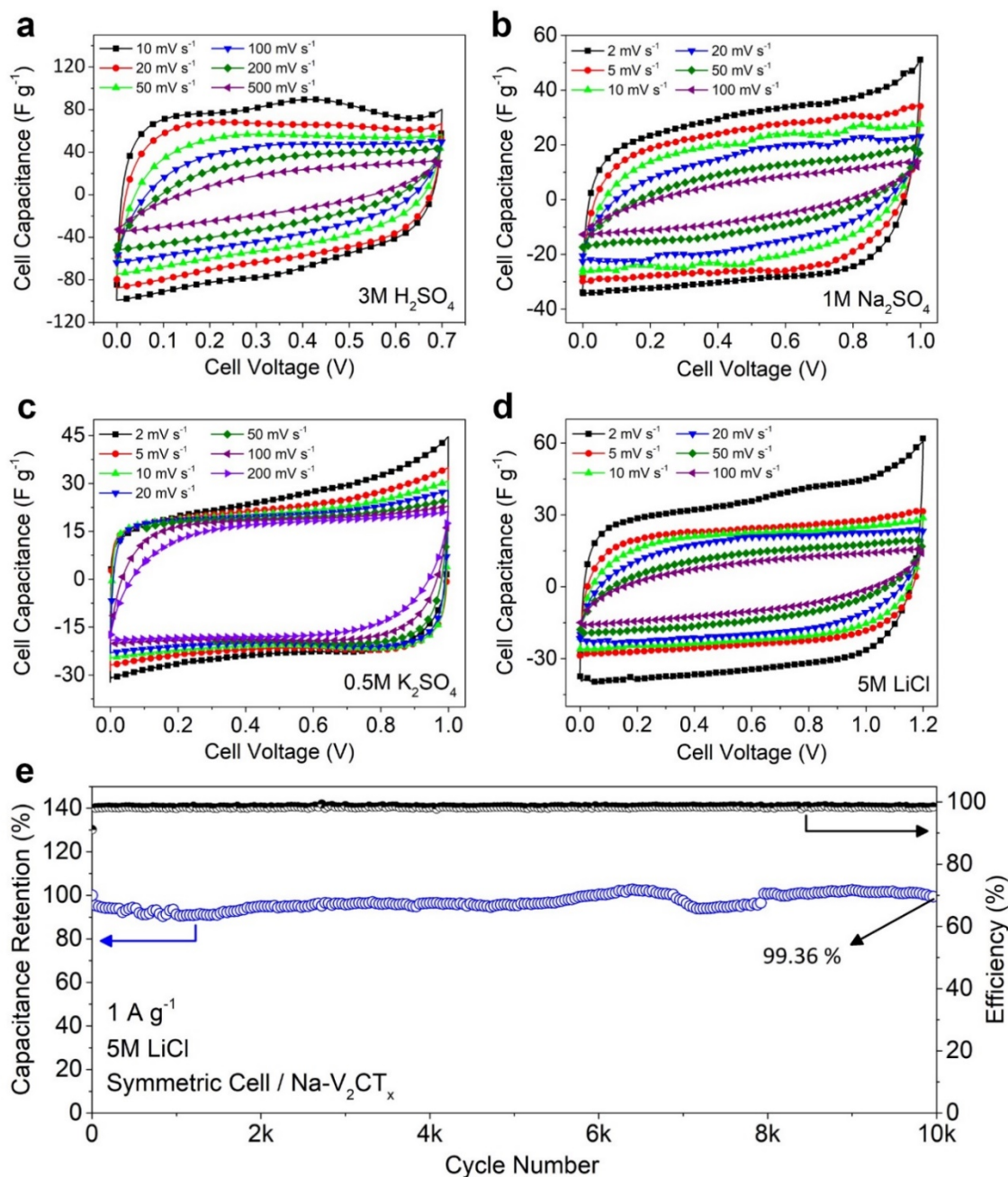
Figure 5.26. CV profiles and cycle performance of symmetric supercapacitors assembled using Na-V$_2$CT$_x$ electrodes at different scan rates. a) in 3 M H$_2$SO$_4$ electrolyte. b) in 1 M Na$_2$SO$_4$ electrolyte. c) in 0.5 M K$_2$SO$_4$ electrolyte. d) in 5 M LiCl electrolyte. e) Cycle life in 5 M LiCl electrolyte at current density of 1 A g^{-1} over 10K cycles with a capacitance retention of 99.36%. Adapted with permission from ref. 56 (copyright © 2019 Wiley-VCH Verlag GmBH & Co.).

As shown in **Figure 5.27**, I also applied the same assembly and electrode fabrication methods to delaminated Ti_2CT_x MXene (which, similarly to V_2CT_x, is also very unstable after delamination) and were able to fabricate freestanding $C-Ti_2CT_x$ films with capacitances of ~172 F g^{-1} and ~640 F cm^{-3} at 2 mV s^{-1} in an LiCl electrolyte, with no loss of capacity in over 10,000 cycles. **Figure 5.27 a (1-6)** show photographs of delaminated (concentrated) $d-Ti_2CT_x$ dispersion, diluted $d-Ti_2CT_x$ dispersion, assembly of $d-Ti_2CT_x$ with Li^+ cations, the corresponding $Li-Ti_2CT_x$ film produced with vacuum filtration, and photograph showing the flexibility of the produced film, respectively. In panel b of this graph, XRD patterns of the $d-Ti_2CT_x$ and $Li-Ti_2CT_x$ films are shown. **Figure 5.27 d** shows a SEM image of the $Li-Ti_2CT_x$ flakes on an alumina membrane. The flake wrinkling happens during drying on AAO membranes. CVs of the $Li-Ti_2CT_x$ electrode at different scan rates in 5 M LiCl electrolyte are shown in **Figure 5.27 e** and rate capability of the $Li-Ti_2CT_x$ electrode at different current densities are shown in **Figure 5.27 f**.

Figure 5.27 g compares the CVs of the $Li-Ti_2CT_x$ and $d-Ti_2CT_x$ electrodes at a scan rate of 5 mV s^{-1}. The $Li-Ti_2CT_x$ electrode shows a more rectangular CV curve and a higher capacitance compared to the delaminated $d-Ti_2CT_x$ electrode. These results are in good agreement with the effect of assembly on the electrochemical performance of V_2CT_x flakes. **Figure 5.27 h** shows the cycle life performance of $d-Ti_2CT_x$ and $Li-Ti_2CT_x$ electrodes at 10 A g^{-1}. Similar to our results on V_2CT_x MXene, the performance of the $d-Ti_2CT_x$ film degraded over cycling and its capacitance reached half of its initial value. The capacitance of the $Li-Ti_2CT_x$, however, increased over cycling. We speculate the increase in the capacity over cycling is due to the improved accessibility of cations to deeper intercalations sites inside the thick freestanding electrode. **Figures 5.27 i and j** show the charge storage contributions from surface and diffusion-controlled mechanisms for the $Li-Ti_2CT_x$ electrode at two scan rate of 2 mV s^{-1} and 20 mV s^{-1}.

117
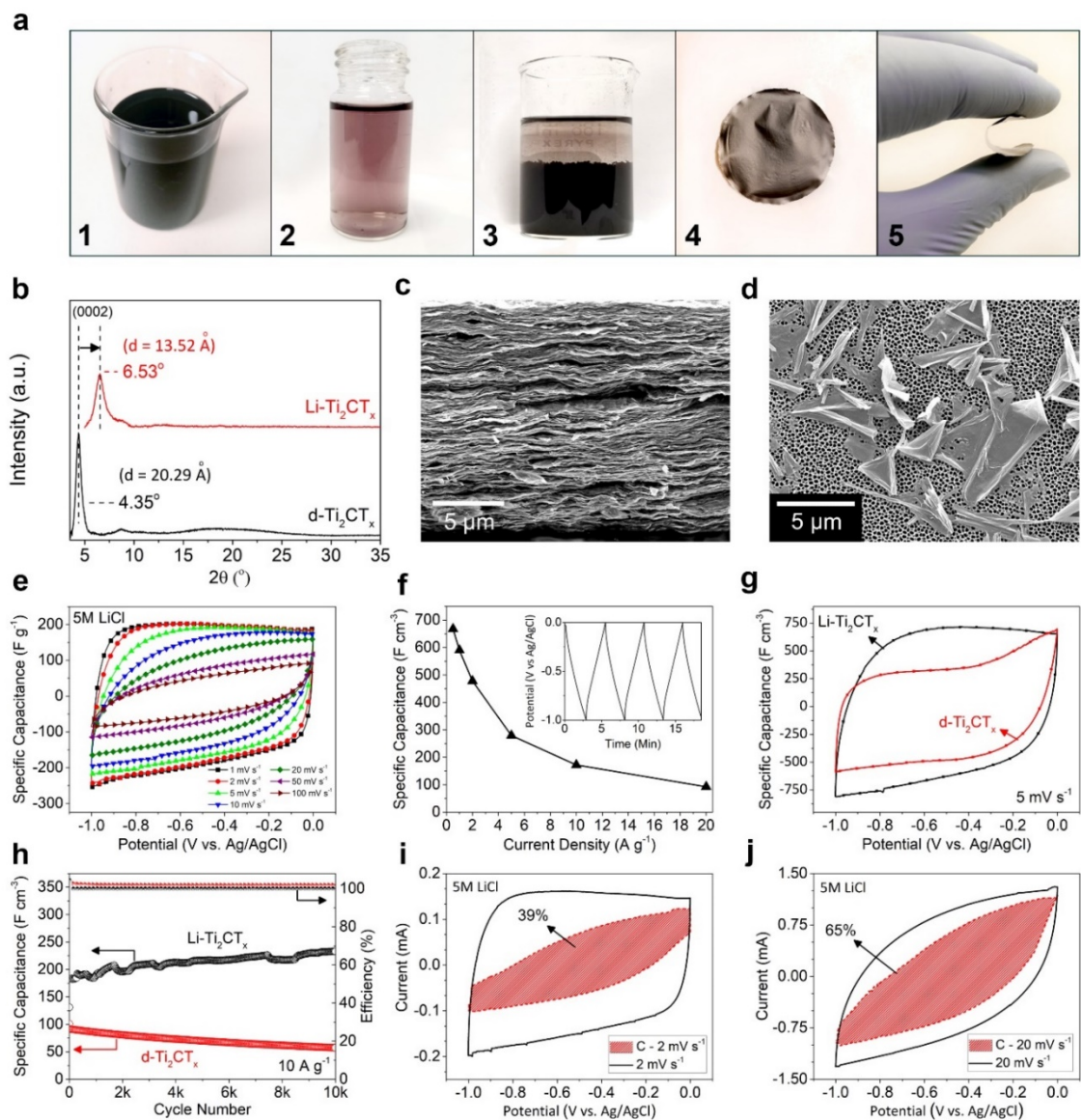
Figure 5.27. Cation-assisted assembly and electrochemical performance of Ti_2CT_x flakes. a 1-6), Photographs of delaminated (concentrated) d-Ti_2CT_x dispersion, diluted d-Ti_2CT_x dispersion, assembly of d-Ti_2CT_x with Li^+ cations, the corresponding Li-Ti_2CT_x film produced with vacuum filtration, and photograph showing the flexibility of the produced film, respectively. b) XRD patterns of the d-Ti_2CT_x and Li-Ti_2CT_x films. c) SEM image from the cross-section of the produced Li-Ti_2CT_x. d) SEM image of the Li-Ti_2CT_x flakes on an alumina membrane. e) CVs of the Li-Ti_2CT_x electrode at different scan rates in 5 M LiCl electrolyte. f) Rate capability of the Li-Ti_2CT_x electrode at different current densities. Inset shows the charge-discharge profiles of the Li-Ti_2CT_x in a 1V potential window. g) CVs of the Li-Ti_2CT_x and d-Ti_2CT_x electrodes at scan rate of 5 mV s^{-1}. h) Cycle life performance of d-Ti_2CT_x and Li-Ti_2CT_x electrodes at 10 A g^{-1}. i and j) Charge storage contributions from surface and diffusion-controlled mechanisms for the Li-Ti_2CT_x electrode at two scan rate of 2 mV s^{-1} and 20 mV s^{-1}. Adapted with permission from ref. 56 (copyright © 2019 Wiley-VCH Verlag GmBH & Co.).

5.4. Conclusions

In summary, the results presented in this chapter demonstrated a cation-driven assembly process to fabricate highly stable pseudocapacitive electrodes with superior electrochemical properties from otherwise unstable 2D V_2CT_x MXene flakes. Electrochemical tests in neutral electrolytes with various inorganic cations showed that the electrodes can be intercalated with cations of various sizes and charges. In a H_2SO_4 electrolyte, electrodes fabricated using the assembled V_2CT_x flakes showed outstanding specific capacitances, reaching values as high as ~420 F g^{-1} and ~1315 F cm^{-3}, and surpassing the performance of many state-of-the-art supercapacitor materials.[15,41,157,164,165] The C-V_2CT_x electrodes show excellent high-rate capability and deliver specific capacitances of ~180 F g^{-1} and ~100 F g^{-1} at high scan rates of 1 V s^{-1} and 10 V s^{-1}, respectively, higher than the calculated specific capacitances of d-$Ti_3C_2T_x$ film electrodes at these scan rates.[41] The impact of cation-driven assembly on the electrochemical stability and cyclic performance of V_2CT_x was also shown. The fabricated electrodes showed no capacitance decay after 10 000 cycles at 10 A g^{-1} and a capacitance retention of ~77% after one million cycles at a rate of 100 A g^{-1}, showcasing a new standard for pseudocapacitive materials with ultralong cycle life.

Chapter 6

Synthesis and Electrochemical Characterization of 2D MXene Heterostructures

Two-dimensional (2D) heterostructures that are built from vertical stacking of different 2D materials are among the promising electrode architectures for electrochemical energy storage devices. These materials offer interesting opportunities such as versatility in electrode-structure design and the possibility to overcome limitations of individual 2D building blocks in a new superlattice-like structure comprised of different 2D materials. The research presented in this chapter demonstrate a large-scale liquid phase assembly of 2D vertical heterostructures built from two different 2D transition metal carbide (MXene) compositions: $Ti_3C_2T_x$ and V_2CT_x. These materials were selected as a model for fabrication of vertical 2D heterostructures from MXenes. The cation-assisted assembly process developed in the previous chapter was used to fabricate MXene heterostructures. Detailed electrochemical characterization of the synthesized $Ti_3C_2T_x$ and V_2CT_x 2D heterostructures showed that it is possible to combine the capacitive performance of these two materials in a structure that offers a constant capacitive response over its entire potential window. The results presented in this chapter are currently under consideration and peer-review for publication in form of a research article titled: "MXene Vertical 2D Heterostructures for Electrochemical Energy Storage".

6.1. Introduction

Two-dimensional (2D) materials, due to their low-dimensionality and highly accessible and redox-active surfaces, offer interesting properties for electrochemical energy storage applications. Fast transport of ions, abundant intercalation sites, exceptional charge transport properties, and excellent mechanical robustness, are among the promising properties of 2D materials.[58] To date, however, no individual 2D material has shown to offer all of these properties together.[58,81,82] Additionally, in many cases inherent properties, as well as highly exposed surfaces of 2D materials, can result in unwanted side reactions with electrolyte and other cell components, resulting in their poor cyclic stability (i.e., many 2D metal oxides suffer from these issues).[58] Vertical stacking of different 2D materials to produce heterostructure is an approach that allows combining different atomically thin materials into hetero-layered structures with superior physical and (electro)chemical properties.[58,81,83–85] Such 2D heterostructures not only can potentially eliminate shortcomings of individual 2D materials, but also enable the realization of numerous new electrode compositions for batteries and supercapacitors.[58]

2D MXenes offer interesting properties such as high electrical conductivities, cation intercalation capability, and high-rate pseudocapacitive properties.[7,13,15,17,56] As it has been mentioned several times throughout my dissertation, MXenes distinguish themselves from other 2D materials by their versatile compositions as well as having different number of atomic layers in their structure. With a general formula of $M_{n+1}X_nT_x$ (M is a transition metal, X is carbon/nitrogen, n is 1-3, and T_x represents different surface functional groups),[7,9] to date, around 30 different MXenes are experimentally synthesized and many more theoretically predicted.[13,86] Therefore, utilizing this large family of 2D materials is an interesting avenue for the development of new 2D heterostructures.[13]

Recently, a few heterostructures of $Ti_3C_2T_x$ MXene with other 2D materials have been reported.[76,87–92] While these early studies have suggested enhanced properties for the final hetero (or composite) materials, they often do not demonstrate an ordered and uniform vertical stacking of the different 2D layers and only briefly discuss their structural properties. In addition, these early reports have only focused on the combination of 2D $Ti_3C_2T_x$ with graphene or 2D metal oxides and dichalcogenides; leaving behind other promising pseudocapacitive MXene compositions such as Ti_2CT_x and V_2CT_x, as well as the possibility of fabricating 2D heterostructures only based on vertical stacking of different MXene sheets. The lack of established methods for controlled synthesis and delamination of other MXenes as well as chemical instability of some of them are among underlying reasons for the former.

In the previous chapter, the exceptional performance of highly stable 2D vanadium carbide (V_2CT_x) multilayers were shown as supercapacitor electrode materials.[56] The notable performance of 2D V_2CT_x hints at the potential of other MXene compositions for pseudocapacitive energy storage. A recent computational study has in fact predicted superior pseudocapacitive properties for many other MXenes.[57] Therefore, it can be argued that proper stacking of different 2D MXene sheets into vertical heterostructures might enable practical heterolayered materials that address shortcomings of individual MXenes and result in dozens of new 2D heterostructures with superior properties. At the time of writing this dissertation, however, there are no reports on such all-MXene vertical 2D heterostructures. In the remaining sections of this chapter the results of my work on fabrication of such MXene 2D heterostructures are discussed.

6.2. Experimental Section

Synthesis and delamination of MXenes. Please refer to the methods explained for MAX and MXene synthesis in chapter 3.

Assembly of vertical MXene heterostructures from the liquid phase. To assemble MXene heterostructures, d-$Ti_3C_2T_x$ and d-V_2CT_x solutions were mixed in different ratios. This results in stable mixture solutions since both MXene solutions have similar negative zeta potentials.[45,52] Then a solution of saturated NaCl (similar to the cation-assembly method discussed in chapter 5) was added to the mixture solution while being stirred slowly (this can be done with other alkali solutions as well). This resulted in rapid assembly of MXene heterostructures and their precipitation at the bottom of the container. The supernatant was poured out, and the precipitates were washed several times to remove the excess salt. In order to fabricate the freestanding films, the hetero-layered powders were slightly shaken in water to obtain a uniform dispersion and then was vacuum filtered on top of a piece of Celgard membrane. The fabricated MXene heterostructures were labeled as Na-(Wt.% of $Ti_3C_2T_x$-Wt.% of V_2CT_x). For example, a heterostructure with $Ti_3C_2T_x$ to V_2CT_x weight ratio of 60:40 is labelled as Na-(60-40). Through this simple and rapid assembly hetero-layered powders up to 0.5 g could be produced in one batch.

Characterization techniques. XRD analyses were carried out at a scan speed of 0.2 seconds per 2θ step using Bruker X-ray diffractometer (D8 Discover) with 40 kV and 40 mA Cu-kα radiation. SEM/EDS analyses of the samples were done using a JEOL JSM-7000F scanning electron. To prepare samples for S/TEM analyses, initially, an FEI Scios dual beam system with gallium ion beam source was used to prepare lamellae from a cross-section of 2D MXene heterostructures films. Then, lamellas were thinned to a thickness of less than 100 nm and placed on a TEM grid. Imaging of lamellas was performed with a probe-corrected FEI Titan Thermis 300

S/TEM with ChemisSTEM technology in both HR-TEM and STEM imaging modes. TEM based EDS mapping was performed at 300 kV using a SuperX EDS system. The S/TEM analyses were performed by Dr. Wentao Liang and Mehrnaz Mojtabavi at Northeastern University.

Electrochemical measurements. Plastic Swagelok cells were used in all the electrochemical measurements. 3 M H_2SO_4 was used as the electrolyte in the cells except where indicated otherwise. After assembly of cells and before electrochemical measurements, they were rested for 1h and then cycled for at least 50 times at a scan rate of 20 mV s^{-1} to stabilize the cells. Cyclic Voltammetry (CV) experiments were carried out at scan rates ranging from 2 mV s^{-1} to 10 Vs^{-1}. Cycle life of the MXene heterostructures was examined by galvanostatic charge/discharge experiments at a current density of 10 A g^{-1} for 10 000 cycles. Electrochemical impedance spectroscopy (EIS) data were collected in the 100 mHz to 1,000 kHz frequency range. The applied potential amplitude was 10 mV. Symmetric supercapacitor devices (full cells) were assembled by using similar MXene heterostructures as both working and counter electrodes (two-electrode setup). In the full cells, the specific capacitance of the device was calculated considering the total weight (or volume) of both hetero-MXene electrodes.

6.3. Results and Discussion

$Ti_3C_2T_x$-V_2CT_x MXene heterostructures were fabricated through alkali cation-driven assembly[56,92] of negatively charged[41,45,52] MXene flakes in their water dispersions. This approach is fundamentally different than most recent reports on the liquid-phase fabrication of 2D heterostructures where they are prepared through self-assembly of two oppositely-charged 2D materials.[76,85,168,169] Despite the promise of this approach, it is not applicable to assemble different MXenes into heterostructures since the selective etching process, and aqueous exfoliation and

delamination of MXenes results in their negatively charged surfaces in water dispersions.[7] Therefore, because of their similarly charged surfaces, they will remain stable colloids upon mixing. In addition, although having two oppositely charged 2D materials seems to be favorable for assembly of unilamellar 2D heterostructures,[170,171] the large organic polycations (i.e., Polydiallyldimethylammonium chloride (PDDA)) that are usually used to prepare the positively charged 2D materials, result in large insulating gaps (and not an intimate contact) between assembled flakes, decreasing the electrical conductivity of the fabricated electrodes.[76] Also, they are not capable of precise single-layer assembly of ordered 2D multilayers either. In contrary, using molecules or elements with small sizes and high charge densities can enable fabrication of such structures. Therefore, in our approach, we used a small and high charge density alkali cation, Na^+, to self-assemble the negatively charged $Ti_3C_2T_x$ and V_2CT_x flakes into hetero-layered structures. Its noteworthy that we chose Na cations as a model for self-assembly of the MXene nanosheets. Similar results should be achieved through the use of other positively charged ions.[56,99,127] **Figure 6.1 a** schematically shows the suggested structure of the fabricated MXene heterostructures. **Figure 6.1 b** shows digital photographs of the freestanding films of Na-assembled pristine MXenes, Na- $Ti_3C_2T_x$ and Na- V_2CT_x, as well as the $Ti_3C_2T_x$-V_2CT_x heterostructure film with a weight ratio of 60:40 (referred to as Na-(60-40)). The pristine $Ti_3C_2T_x$ films have a dark grey color, and V_2CT_x films show a light brownish color, while the Na-(60-40) MXene heterostructure film shows a uniform and darker grayish brown color. No visual color variation/separation along the film could be seen, suggesting uniformly assembled 2D layers without apparent agglomeration of individual MXenes. A cross-sectional scanning electron microscopy (SEM) image of the heterostructure film (shown in **Figure 6.1 c**) showed layered vertical stacking of 2D nanosheets that are typical of vacuum filtered films.
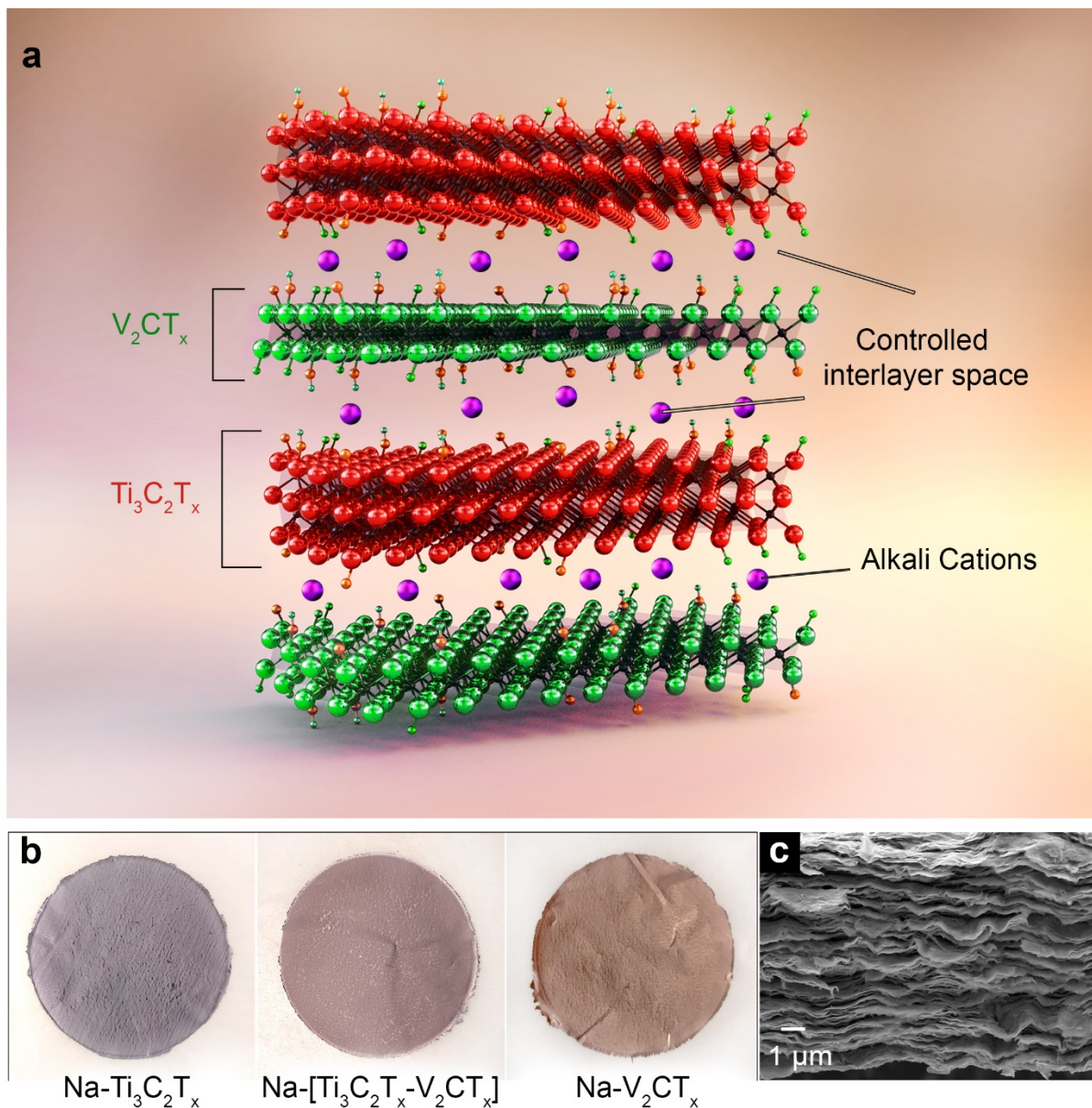
Figure 6.1. Synthesis process of MXene heterostructures. a) Schematic illustration of $Ti_3C_2T_x$ and V_2CT_x structures, and the cation-driven self-assembly process used for fabrication of the MXene heterostructures. b) Digital photographs of the freestanding binder free films of $Ti_3C_2T_x$, MXene heterostructure ($Ti_3C_2T_x$:V_2CT_x of 60:40), and V_2CT_x assembled with Na cations prepared by vacuum filtration. c) A cross-sectional SEM image of the Na-(60-40) MXene heterostructure film, demonstrating its layered structure.

126

X-ray diffraction (XRD) analysis was carried out to understand the structure and stacking order/sequence of the fabricated all-MXene heterostructures. **Figure 6.2 a** shows the XRD patterns of the pristine MXene films fabricated by vacuum filtration of the delaminated V_2CT_x (d-V_2CT_x) and d-$Ti_3C_2T_x$ MXene solutions, as well as their cation-assembled films which were prepared as control samples. Due to the intercalation of large TBA^+ cations in the delamination process, the d-V_2CT_x shows a very large interlayer spacing of 15.41 Å. In agreement with our previous results,[56] assembly of d-V_2CT_x with Na^+ cations resulted in a large upshift in the position of the peak corresponding to (0002) basal planes of V_2CT_x (from 5.73° to 8.47°, $\delta d_{(0002)} = 4.98$ Å), suggesting the exchange of larger TBA^+ ions with smaller high charge density Na^+ ions where the sodium cations pull the negatively charged MXene sheets together. In contrast, the Na-$Ti_3C_2T_x$ film showed a slightly larger d-spacing of 12.7 Å (compared to 12.49 Å for d-$Ti_3C_2T_x$), probably, as the result of the (partial) substitution of Li cations remained from etching and delamination process of $Ti_3C_2T_x$ with larger Na cations.[172]

The apparent optimal composition of the MXene heterostructure in which the surface area of the $Ti_3C_2T_x$ and V_2CT_x would match for a prefect assembly was calculated based on a hypothetical surface-area matching model suggested in earlier works.[168,169,171] For these calculations, we considered the previously reported approximate in-plane a-lattice parameters of ~0.305 Å for the $Ti_3C_2T_x$[173,174] and ~0.32 Å for the V_2CT_x[175]. Based on these values and the hexagonal in-plane structure of the MXenes, the 2D weight density of them can be calculate as follow:[168,169,171]

Theoretical 2D weight density (for in-plane hexagonal structures) $= \dfrac{M_{2D\ Material}}{a^2 \times \sin{(120°)} \times N_A}$

$M_{2D\ Material}$: Molecular weight of the material (g mol^{-1})

a: a-lattice parameter

N_A: Avogadro number

For Ti$_3$C$_2$T$_x$: $W_{Ti_3C_2T_x} = \dfrac{199.6}{(0.305)^2 \times sin\ (120°) \times 6.02 \times 10^{23}} = 1.23 \times 10^{-20}$ g Å^2

For V$_2$CT$_x$: $W_{V_2CT_x} = \dfrac{145.87}{(0.32)^2 \times sin\ (120°) \times 6.02 \times 10^{23}} = 8.15 \times 10^{-21}$ g Å^2

Therefore, the weight ratio between Ti$_3$C$_2$T$_x$ and V$_2$CT$_x$ would be:

$$\frac{m_{Ti_3C_2T_x}}{m_{V_2CT_x}} = \frac{W_{Ti_3C_2T_x}}{W_{V_2CT_x}} = \sim 1.5$$

This corresponds to a Ti$_3$C$_2$T$_x$:V$_2$CT$_x$ wt.% of 60:40.

Figure 6.2 b shows the evolution of the (0002) basal plane peaks of the different MXenes in the corresponding final heterostructures with the change in the ratio of Ti$_3$C$_2$T$_x$ to V$_2$CT$_x$. We chose the range of the compositions in our study based on a suggested hypothetical surface area-matching model[168,171] to calculate the initial composition for mixing Ti$_3$C$_2$T$_x$ and V$_2$CT$_x$ sheets. Accordingly, the weight ratio of Ti$_3$C$_2$T$_x$ to V$_2$CT$_x$ was calculated to be ~1.5 (60:40). Then we prepared other compositions with changing the ratio slightly toward higher weight percentages of V$_2$CT$_x$ compared to Ti$_3$C$_2$T$_x$. The corresponding peak for (0002) basal planes of the Na-Ti$_3$C$_2$T$_x$ and Na-V$_2$CT$_x$ showed almost a very marginal shift (corresponding to a δd$_{(0002)}$ = +0.4 Å and -0.4 Å, respectively) in all the fabricated heterostructure films with different ratios. Interestingly, the intensity of the (0002) peak for Na-V$_2$CT$_x$ increased gradually by increasing its weight ratio in the

assembled heterostructures while the intensity of the (0002) basal plane peak for the Na-Ti$_3$C$_2$T$_x$ decreased. These observations suggest a change in the stacking number of individual MXene sheets in the fabricated hetero-layered films, similar to the one-dimensional two-phase model proposed by Onada et al.[176] with no phase-separation. Interestingly, co-existence of the (0002) basal plane peaks was not observed in a control sample prepared by only mixing the two MXene solutions and vacuum filtration (**Figure 6.3**). This can be attributed to a completely random mixture of the two MXene compositions, which further signifies the role of counter-ions in the assembly of ordered hetero-layered structures.[176,177] The decreased intensity and broad nature of the (0002) peaks for the 2D MXene heterostructures, however, indicate imperfections in the stacking number and sequence of the Ti$_3$C$_2$T$_x$ and V$_2$CT$_x$ MXene sheets as well as the misorientation of (0002) planes with respect to each other.[85,168]

Atomic force microscopy (AFM) images and the corresponding height profiles of the single-layer Ti$_3$C$_2$T$_x$, V$_2$CT$_x$, and their Na-(60-40) heterostructures are shown in **Figure 6.2 c-e** (also **Figure 6.4**), respectively. The more than theoretical thicknesses of the single-layer MXenes measured from AFM images are in agreement with previous reports and originates from the trapped water molecules and inter-molecule interactions between MXene surfaces and the silicon substrate.[52,178] Nevertheless, vertical stacking of MXene nanosheets and the significantly higher thickness of the hetero-layered MXenes is obvious in **Figure 6.2 e**. Transmission electron microscopy (TEM), however, is a much better tool for detailed observation of the stacking sequence and the structure of the fabricated hetero-layers. Particularly, in this case, since V$_2$CT$_x$ is only three-atomic-layer thick and Ti$_3$C$_2$T$_x$ five-atomic-layer tick, these different MXenes are easily distinguishable in high-resolution or atomic-resolution TEM images.
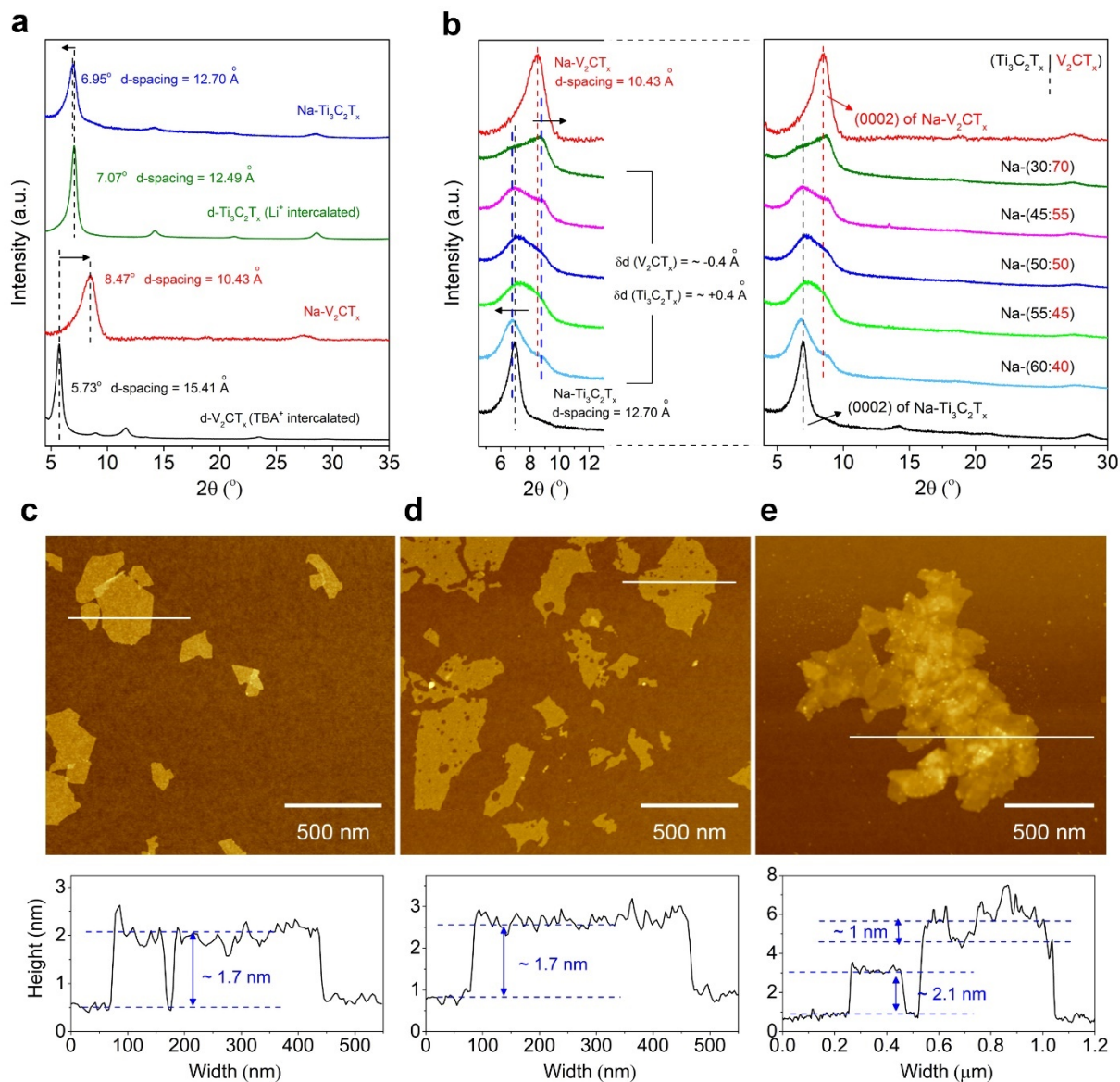
Figure 6.2. Structural characterization of the MXene heterostructures. a) XRD patterns of $Ti_3C_2T_x$ and V_2CT_x, and their Na-assembled films, showing the change in $d_{(0002)}$ upon self-assembly for the different MXenes. b) XRD patterns of the different MXene heterostructure films showing the evolution of the (0002) peak for $Ti_3C_2T_x$ and V_2CT_x MXenes with regard to the compositional variations in the hetero-layered films. AFM images and the corresponding height profiles of the (c) $Ti_3C_2T_x$, (d) V_2CT_x, and (e) MXene hetero flakes assembled with Na cations at the $Ti_3C_2T_x$ to V_2CT_x ratio of 60:40.

130
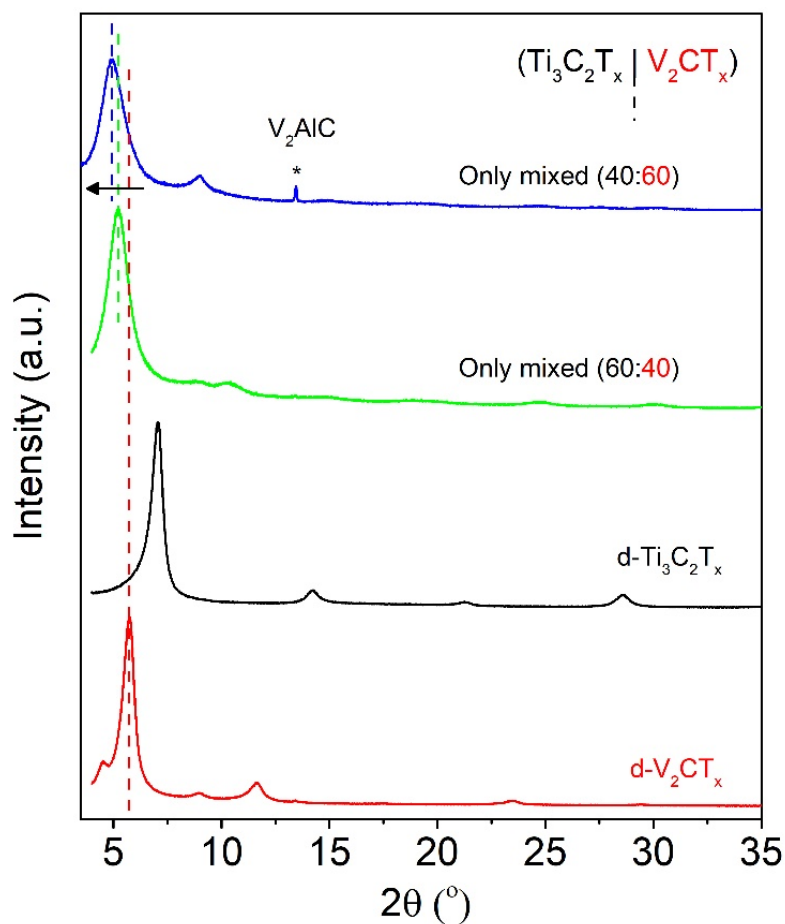
Figure 6.3. XRD patterns of the MXene mixture films prepared by simply mixing the aqueous solutions of $Ti_3C_2T_x$ and V_2CT_x in two different weight ratios of 60:40 and 40:60 compared to the pristine MXene films prepared by vacuum filtration of the as-prepared delaminated solutions. Unlike, the heterostructures prepared by cation-assembly process, the films prepared by only mixing the two different MXenes did not show the presence of two different peaks corresponding to (0002) basal planes of $Ti_3C_2T_x$ and V_2CT_x. Instead only one (0002) peak shifted toward lower angles which probably originates from the random mixture of these two MXenes was observed.
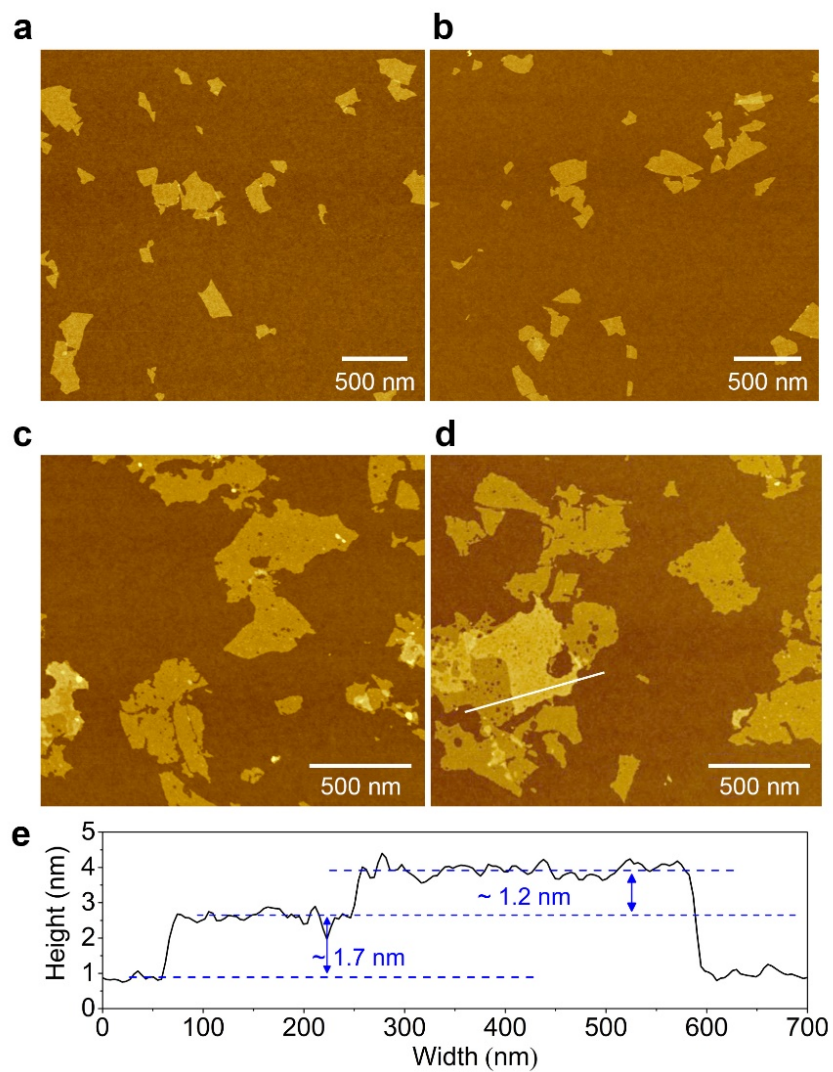
Figure 6.4. AFM images of d-Ti$_3$C$_2$T$_x$ (a and b) and d-V$_2$CT$_x$ (c and d), and the corresponding height profile of the d-V$_2$CT$_x$ on the silicon substrate for the line shown in panel d. Similar to previous reports on Ti$_3$C$_2$T$_x$ the exaggerated AFM measured thickness of the d-V$_2$CT$_x$ on silicon reduces to around 1.2 nm when the measurement is done on flakes placed on top of each other.

High-resolution TEM (HR-TEM) and scanning transmission electron microscopy (STEM) images of a Na-(60-40) heterostructure film are shown in **Figure 6.5 a-c**. These images demonstrate face-to-face vertical stacking of $Ti_3C_2T_x$ and V_2CT_x sheets inside the heterostructure films. In this composition, in a good agreement with XRD results, TEM images showed larger stacks of $Ti_3C_2T_x$ compared to the adjacent V_2CT_x layers. The average interlayer spacings for stacks of $Ti_3C_2T_x$ (~1.27 nm) and V_2CT_x (~1 nm) measured from STEM images correspond well to the values calculated from XRD patterns. Furthermore, from the STEM images, the average distance between the face-to-face $Ti_3C_2T_x$ and V_2CT_x layers was measured to be ~ 1.1 nm. A similar value (~ 1.15 nm) can be roughly calculated from XRD results considering the center of the broad (0002) peaks of the heterostructure films as the average representing distance for the assembled flakes (assuming perfect stacking where the two peaks merge into one broad peak).

Figure 6.5 d shows the HR-TEM image, and **Figure 6.5 e and f** show the STEM images of a Na-(45-55) heterostructure film. In this composition, a similar stacking of the flakes can be seen while in correlation to XRD results, here the number of V_2CT_x sheets per stack of them is larger than the adjutant $Ti_3C_2T_x$ sheets. **Figure 6.5 g and h** show TEM/EDS elemental maps of Na-(45-55) hetero film, confirming successive assembly of few-layer stacks of $Ti_3C_2T_x$ and V_2CT_x. **Figure 6.5 h** also shows the presence of Na atoms. It's noteworthy that we performed TEM analysis on a $Ti_3C_2T_x$ and V_2CT_x (60-40) mixture film (without assembly with cation, shown in **Figure 6.6**) where, as expected, the stacking of these two MXenes were found to be random with no obvious pattern.
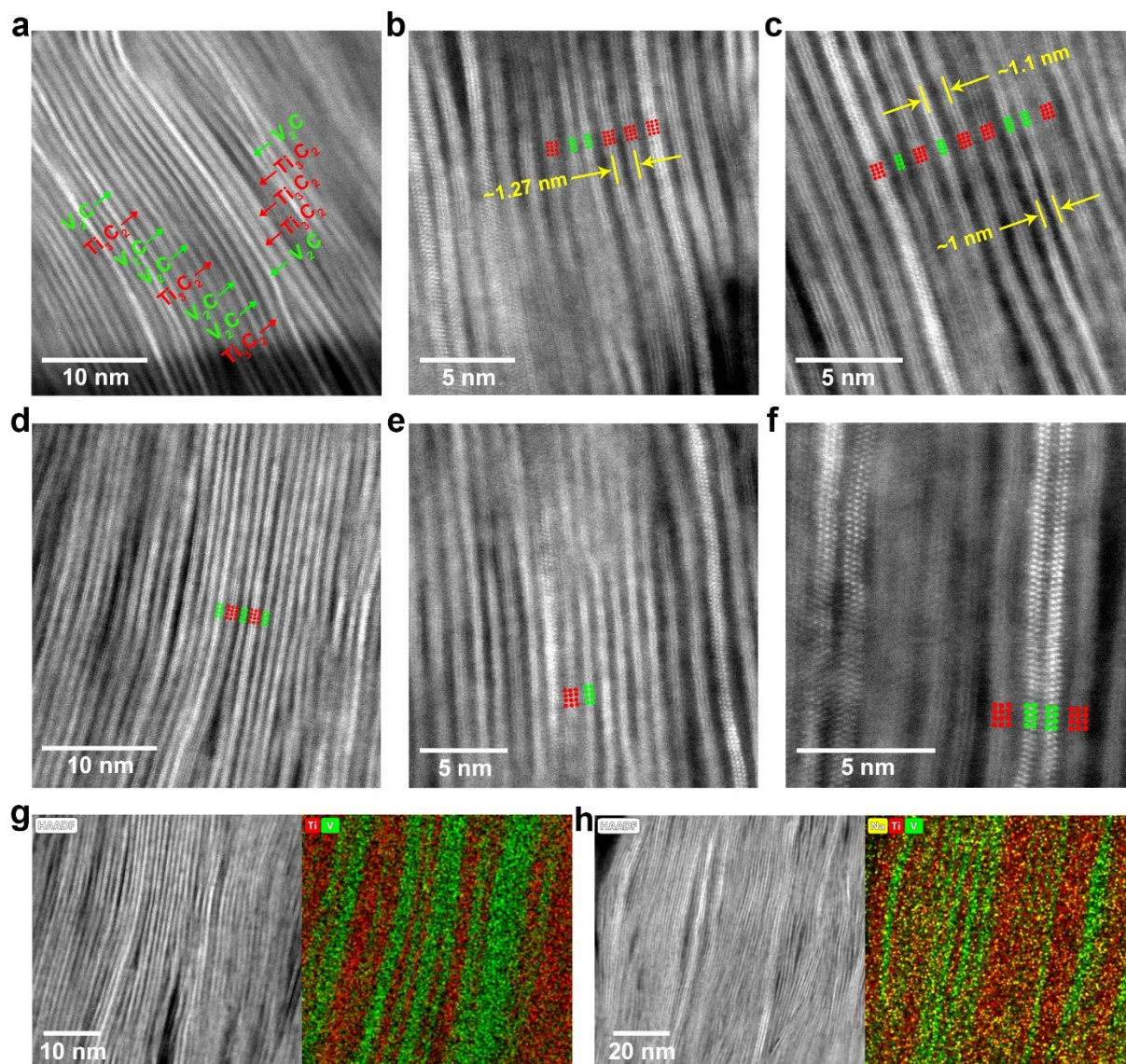
Figure 6.5. Transmission electron microscopy (TEM) analysis of the MXene heterostructures. a) The high-resolution TEM image of Na-assembled MXene heterostructure films at the $Ti_3C_2T_x$ to V_2CT_x weight ratio of 60:40, referred to as Na-(60-40), showing the alternating sequence of the two MXene compositions along the cross-section of the film. b) STEM atomic-resolution images of the Na-(60-40) films and the measured average spacings between individual $Ti_3C_2T_x$ and V_2CT_x stackings as well as the spacing between face-to-face $Ti_3C_2T_x$ and V_2CT_x sheets. d) High-resolution TEM and (e-f) STEM atomic-resolution images of a Na-(45-55) MXene heterostructure film, showing the difference in the sequencing and the stacking number of the $Ti_3C_2T_x$ and V_2CT_x MXene sheets compared to the Na-(60-40) composition. High-angle annular dark-field (HAADF) TEM images and EDS maps of the g) Na-(60-40) and h) Na-(45-55) heterostructure films.
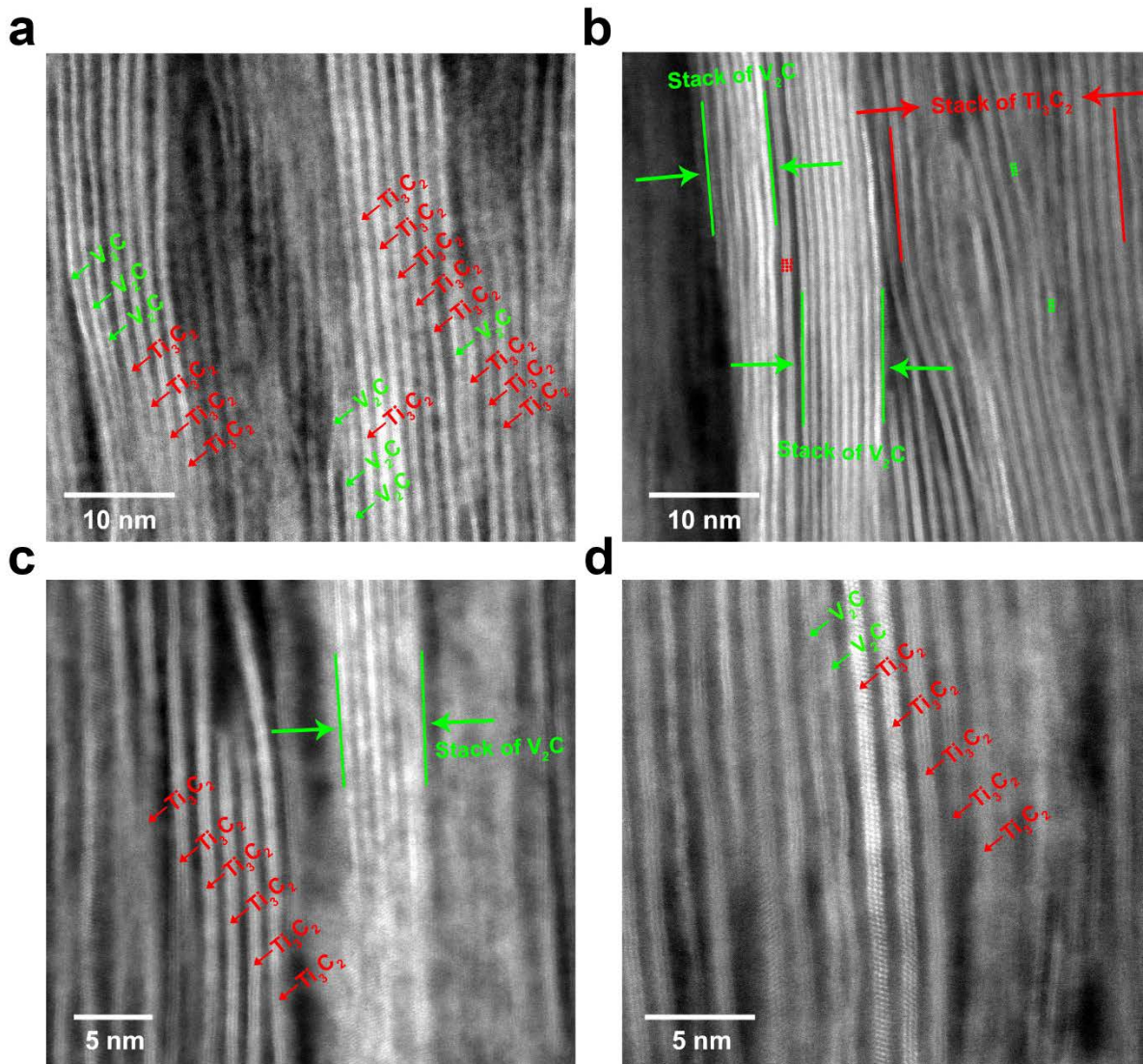
Figure 6.6. a-d) STEM images of a 60:40 $Ti_3C_2T_x$ to V_2CT_x MXene mixture film produced by vacuum filtration. It is evident from these images that simple mixing cannot result in ordered and sequential stacking of hetero-layered MXene sheets. It rather only results in a complete random mixture of these two MXene flakes. Large piles of stacked V_2CT_x or $Ti_3C_2T_x$ are marked on these images which clearly show the difference between the mixture film and the sequential stacking of hetero-layered MXenes when assembled by cations. In addition, it is noteworthy that as we have recently shown[56] in these images since V_2CT_x flakes are not assembled using cations, they were very unstable under electron beam and could be easily damaged by a few seconds of exposure. Therefore, these flakes appear cloudier and blurrier in these images compared to those of cation-assembled heterostructures where individual V_2CT_x flakes could be observed sharply.

Previously assembly of individual $Ti_3C_2T_x$[99] or V_2CT_x[56] MXenes into multilayered structures with alkali cations were reported to show outstanding pseudocapacitive performances (particularly in the acidic H_2SO_4 electrolyte), as well as, in case of V_2CT_x, superior chemical stability. Therefore, the electrochemical properties of the freestanding MXene heterostructure films were investigated in a three-electrode supercapacitor setup using 3 M H_2SO_4 as the electrolyte. **Figure 6.7 a** shows how the electrochemical response of the $Ti_3C_2T_x$ and V_2CT_x have merged to give the MXene heterostructure film a new and improved electrochemical response with a cyclic voltammogram (CV) that resembles a combination of those of individual MXenes. The CV of MXene heterostructure film, indeed, shows an interesting and promising feature that most pseudocapacitive materials lack behind delivering it, which is an almost constant capacitance throughout their potential window. Most conventional pseudocapacitive materials deliver their maximum capacitance at a narrow peak potential range (particularly in acidic electrolytes). This is evident in the CV profile of the $Ti_3C_2T_x$ which delivers a large portion of its capacitance only in between -0.45 V and -0.2 V (V vs. Ag/AgCl), highlighted in blue, and the Na-V_2CT_x which delivers most of its capacitance from -0.2 V and +0.25 V (V vs. Ag/AgCl), highlighted in red (shown in **Figure 6.7 b**). The CV of MXene heterostructure film, however, combines these two potential ranges and delivers a constant capacitance in over whole potential window (from -0.45 V to +025 V). To better demonstrate this concept, we calculated the potential-limited capacitance (C) per total capacitance obtained in the whole potential window(C_{total}) for each of these electrodes and plotted the obtained values at different scan rates (shown in **Figure 6.7 c**) in the potential ranges of -0.45 V to -0.2 V (referred to as P-I) and -0.2 V to +0.25 V (referred to as P-II). An ideal supercapacitor electrode is expected to deliver similar capacitance values at different potential ranges for constant and uniform power output at all voltages.[65,70] In this plot, such behavior can be

translated to a ~50% C/C_{Total} ratio, meaning that the electrode is delivering relatively similar capacitance (current output) at different potential points in its operating voltage window. This graph clearly shows that in the P-I range, the performance of V_2CT_x is almost negligible while $Ti_3C_2T_x$ delivers most of its capacitance, and in P-II range this is exactly opposite. The Na-(50-50) MXene heterostructure electrode, however, shows a C/C_{Total} value of close to ~50% in both potential ranges indicating its constant performance over the whole potential window. This feature can enable the development of new pseudocapacitive materials that are capable of delivering their peak performance over their entire operating voltage window.

Figure 6.7 d shows CV profiles of a Na-(50-50) electrode at scan rates ranging from 2 mV s^{-1} to 1000 mV s^{-1} demonstrating the high-rate capability of the fabricated heterostructure electrodes. Figure 6.7 e shows the evolution of the CV profiles and the corresponding redox peaks associated with V_2CT_x[56] and $Ti_3C_2T_x$[17] in a similar fashion to that observed in the XRD patterns (an increase of the contributions from V_2CT_x redox couples with an increase of its weight ratio in the electrode structure). We chose the (50-50) ratio for our different electrochemical analysis as it showed the best combination of $Ti_3C_2T_x$ and V_2CT_x pseudocapacitive responses. Nevertheless, all other compositions showed the new CV features as well, with small variations upon the change of heterostructure composition (Figure 6.8 shows the CVs of different compositions at different scan rates). The pronounced presence of redox couples of both MXenes, however, was not present in the CV when $Ti_3C_2T_x$ and V_2CT_x MXenes were simply mixed without cation assembly process. Figure 6.7 f compares the CVs of a simply mixed and a Na assembled heterostructure film with $Ti_3C_2T_x$ to V_2CT_x weight ratio of 60:40. While the electrode film prepared by simple mixing of the two MXenes still shows an improved pseudocapacitive behavior compared to the individual MXenes, it is easily noticeable that unlike the heterostructure film, its CV does not feature the

pronounced redox couples of V_2CT_x at more positive potentials. Also, the ultra-large interlayer spacing of the mixed film caused by intercalation of present TBA^+ cations from V_2CT_x solution resulted in its poor volumetric capacitance. **Figure 6.7 g** compares the volumetric capacitance of the various heterostructure and pristine MXene electrodes. A highest volumetric capacitance of ~1473 F cm^{-3} and a gravimetric capacitance of ~ 410 F g^{-1} was achieved for Na-(50-50) heterostructure film with a thickness of 6 µm at a scan rate of 2 mV s^{-1}. The heterostructure showed a good rate capability with retaining ~70% (~1020 F cm^{-3}) and ~30% (~436 F cm^{-3}) of its initial capacitance at scan rates of 100 mV s^{-1} and 1000 mV s^{-1}, respectively. Although, similar to other freestanding MXene electrodes, the capacitance of the heterostructure films showed a thickness-dependent behavior, because of the increased ion accessibility of these electrodes as well as the synergistic effects between the two MXene layers, they could still deliver high capacitances at relatively higher thickness. For example, a heterostructure film with composition of Na-(40-60) and a thickness of ~15 µm could deliver capacitances of ~1273 F cm^{-3} and ~402 F g^{-1} at a scan rate of 2 mV s^{-1}. These numbers are very similar to those of a 7 µm-thick pristine $Ti_3C_2T_x$ (~1319 F cm^{-3}, ~390 F g^{-1}) and a ~5 µm-thick Na-V_2CT_x (~1437 F cm^{-3}, ~423 F g^{-1}) at the same scan rate. Alongside their improved capacitances and rate-capability, the heterostructure MXene electrodes showed an exceptional cycle life performance. For example, a Na-(50-50) electrode showed no capacitance decay, and in fact, around 8% capacitance increase (capacitance retention of ~108%) after 50 000 charge-discharge cycles at a high rate of 100 A g^{-1} (compared to $Ti_3C_2T_x$ and Na-V_2CT_x electrodes (**Figure 6.9**) which showed capacitance retentions of ~91% and 92%, respectively).
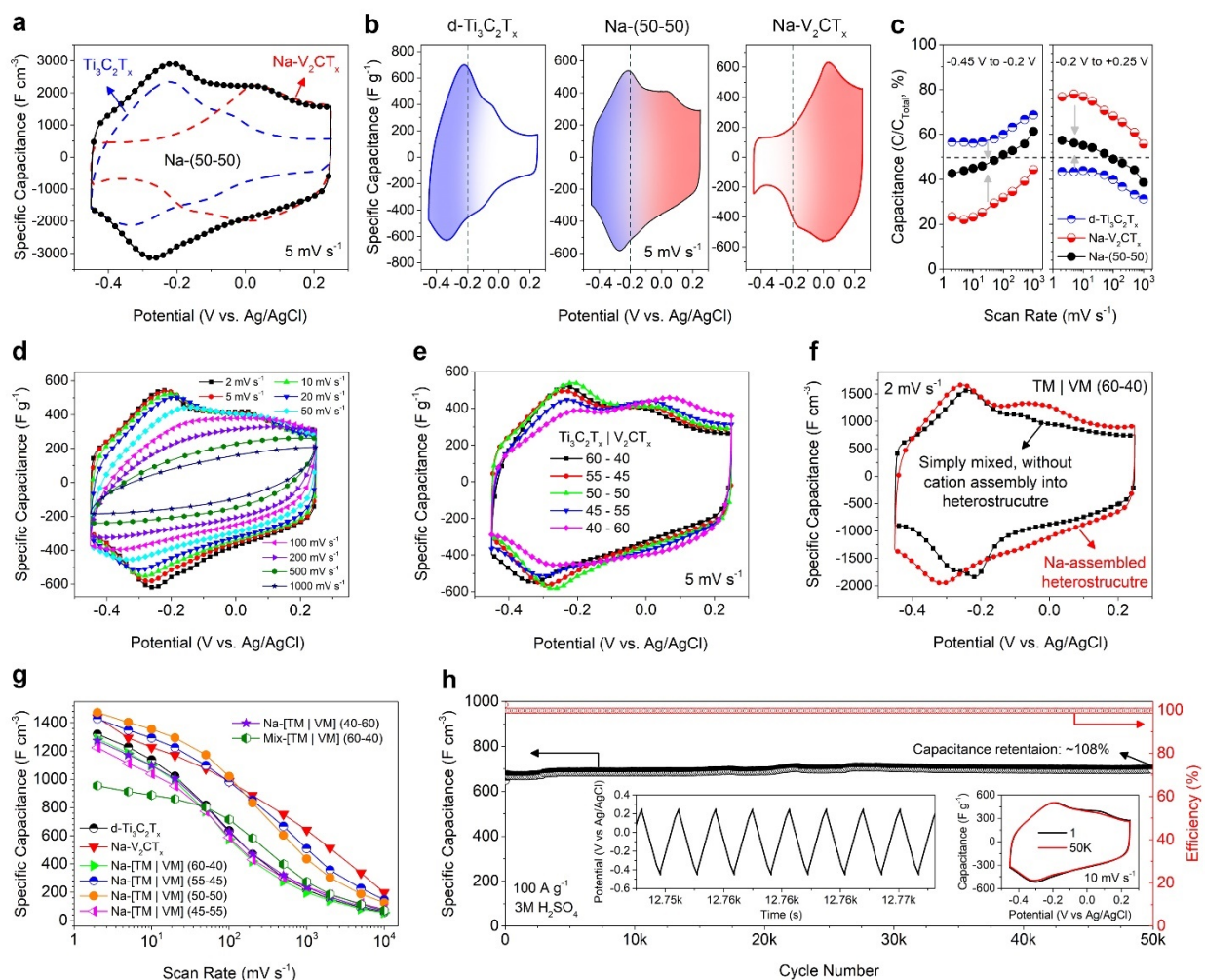
Figure 6.7. Electrochemical characterization of MXene heterostructure electrodes in 3M H_2SO_4. a) Comparison between cyclic voltammograms (CVs) of $Ti_3C_2T_x$, Na-V_2CT_x, and Na-(50-50) MXene heterostructure at a scan rate of 5 mV s^{-1}, demonstrating the new electrochemical response for the heterostructure electrode. b) Highlighted CVs of $Ti_3C_2T_x$, Na-V_2CT_x, and Na-(50-50) at the potential ranges in which these electrodes show their highest electrochemical activity. c) Potential-limited capacitance to the total capacitance of $Ti_3C_2T_x$, Na-V_2CT_x, and Na-(50-50) at two potential ranges of (PI), -0.45 V to -0.2 V and (PII), -0.2 V to +0.25 V (V vs. Ag/AgCl) showing constant electrochemical response of the MXene heterostructure compared to $Ti_3C_2T_x$ MXene which delivers most of its capacitance only in PI and Na-V_2CT_x, which is mostly active only in PII. d) CVs of Na-(50-50) at scan rates from 2 mV s^{-1} to 1000 mV s^{-1}. e) CVs of MXene heterostructures with different compositions at 5 mV s^{-1}. f) Comparison between CVs of Na-assembled (60-40) MXene heterostructure and a film prepared by simply mixing $Ti_3C_2T_x$ and V_2CT_x in 60:40 wt.%. g) Volumetric capacitances of different electrodes tested in this study. "TM" is $Ti_3C_2T_x$ MXene and "VM" is V_2CT_x MXene h) Cyclic performance of the Na-(50-50) electrode at a current density of 100 A g^{-1}.

139
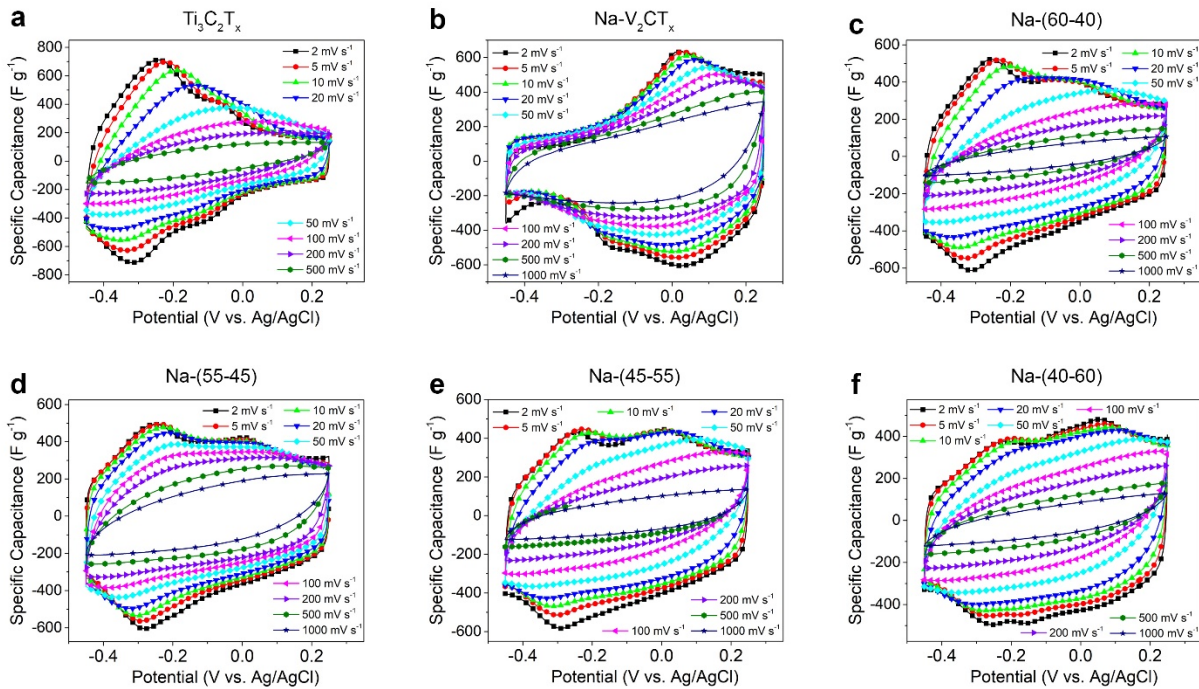
Figure 6.8. CV profiles of the different freestanding electrodes in 3 M H_2SO_4 at scan rates of 2 mVs^{-1} to 1000 mV s^{-1}. a) d-$Ti_3C_2T_x$, b) Na-V_2CT_x, and MXene heterostructures with $Ti_3C_2T_x$ to V_2CT_x weight ratio of c) Na-(60-40), d) Na-(55-45), e) Na-(45-55), and f) Na-(40-60).
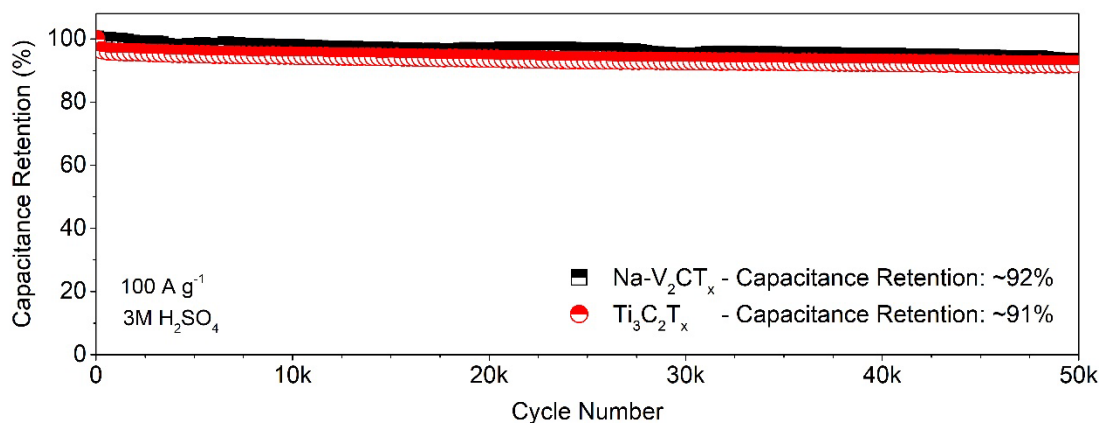
Figure 6.9. Cycle life of $Ti_3C_2T_x$ and Na-V_2CT_x electrodes in the 3M H_2SO_4 electrolyte at a current density of 100 A g^{-1}.

The kinetics of the surface-controlled (capacitive) and diffusion-limited charge storage contributions in Na-(50-50) heterostructure electrode were evaluated and compared to those of $Ti_3C_2T_x$ and $Na-V_2CT_x$ electrodes with similar thicknesses through considering a power-law relationship between the current (i) and scan rate (v), $i=av^b$. [63,133] In this equation, b = ~0.5 corresponds to diffusion-limited reactions while b = ~1 corresponds to surface-controlled reactions (capacitive).[133] **Figure 6.10 a and b** show the capacitive contributions (hatched portions of the CVs) to the total charge stored in a Na-(50-50) heterostructure electrode at two scan rates of 2 and 20 mV s^{-1}. Around 86% and 95% of the total charge stored in the heterostructure film at these scan rates originate from fast surface-controlled reactions suggesting the better accessibility of electrolytes' ions to the redox-sites at the surface Ti and V transition metal atoms. This analysis clearly show an improved capacitive performance for the heterostructure electrode compared to the pristine $Ti_3C_2T_x$ or V_2CT_x electrodes. For example, at a scan rate of 2 mV s^{-1} only 69% and 80% of the capacitances of $Ti_3C_2T_x$ and V_2CT_x come from capacitive contributions, respectively (charge analyses are shown in **Figure 6.11-13**). **Figure 6.10 c** shows the capacitive contributions for the three different electrodes at scan rates of 2, 5, 10, and 20 mV s^{-1}. It is evident that at all scan rates the heterostructure film shows a better capacitive performance. This improvement stems from the sequential vertical assembly of $Ti_3C_2T_x$ and V_2CT_x sheets in the hetero-layered architecture which hampers self-restacking of these individual MXene sheets and therefore, increases the accessible redox-active surface of the electrode.[76,92,168] Electrochemical impedance spectroscopy results (**Figure 6.14**) further confirmed the improved ion and charge transport properties of the heterostructure electrodes.
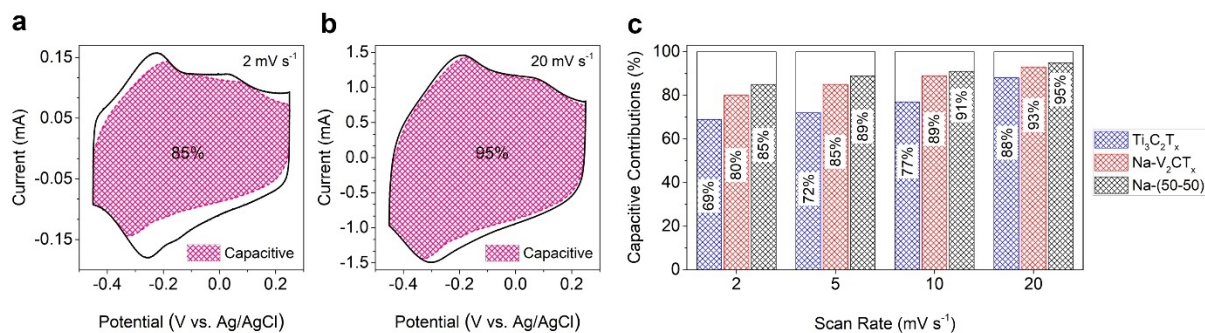
Figure 6.10. Charge storage analysis and performance of the MXene heterostructure films in symmetrical supercapacitor cells. Surface-controlled (capacitive) charge storage contributions to the overall charge stored at two scan rates of a) 2 mV s^{-1} and b) 20 mV s^{-1}. c) Comparison between capacitive contributions in the overall charge storage performance of Ti$_3$C$_2$T$_x$, Na-V$_2$CT$_x$, and Na-(50-50) electrodes at scan rates of 2, 5, 10, and 20 mV s^{-1}, showing the improved capacitive response of the MXene heterostructure electrodes.
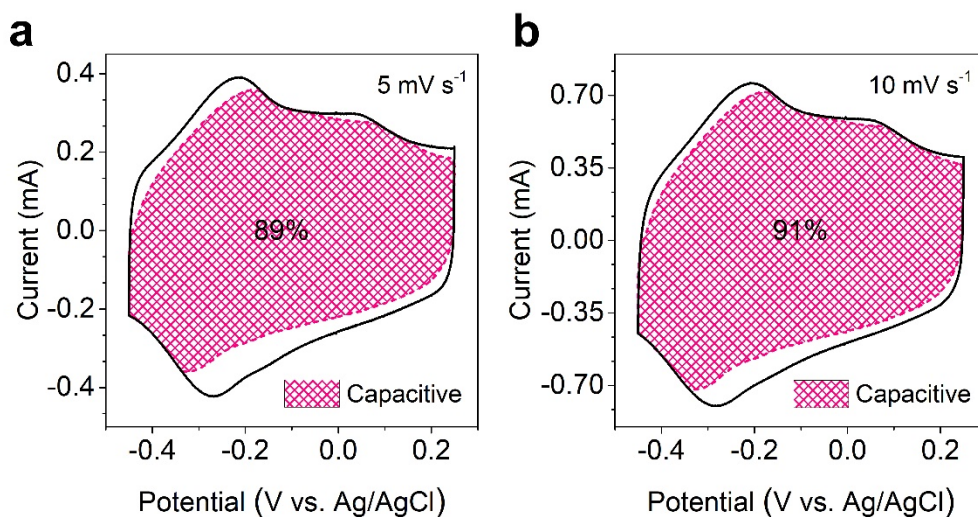
Figure 6.11. Analysis of the capacitive charge storage contributions from the Na-(50-50) MXene heterostructure at different scan rates of a) 5 mV s^{-1} and b) 10 mV s^{-1}. Hatched portions shown on the graph show the surface-controlled (capacitive) contributions.

142
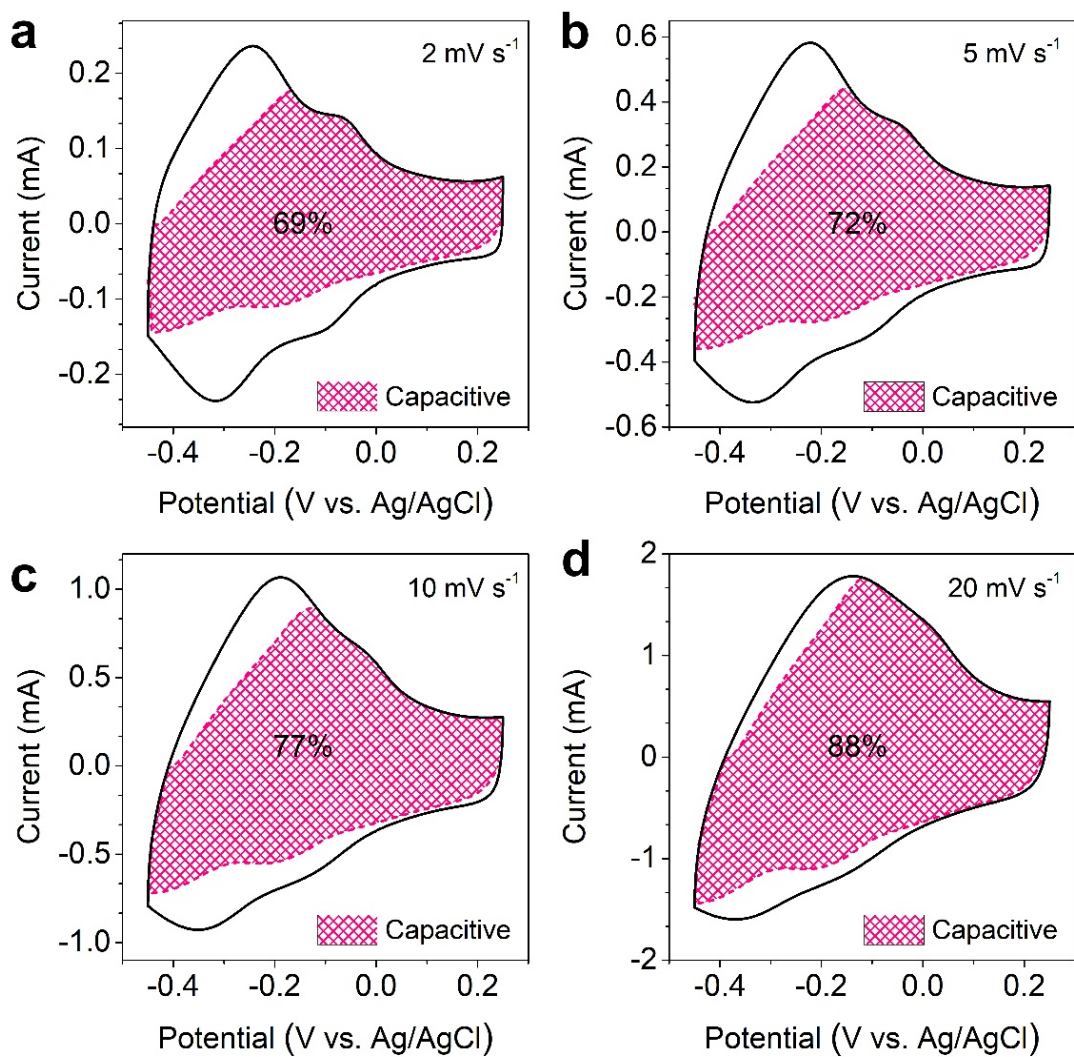
Figure 6.12. Analysis of the capacitive charge storage contributions from the CV for d-Ti$_3$C$_2$T$_x$ at different scan rates of a) 2 mV s^{-1}, b) 5 mV s^{-1}, c) 10 mV s^{-1}, and d) 20 mV s^{-1}. Hatched portions shown on the graph show the surface-controlled (capacitive) contributions.
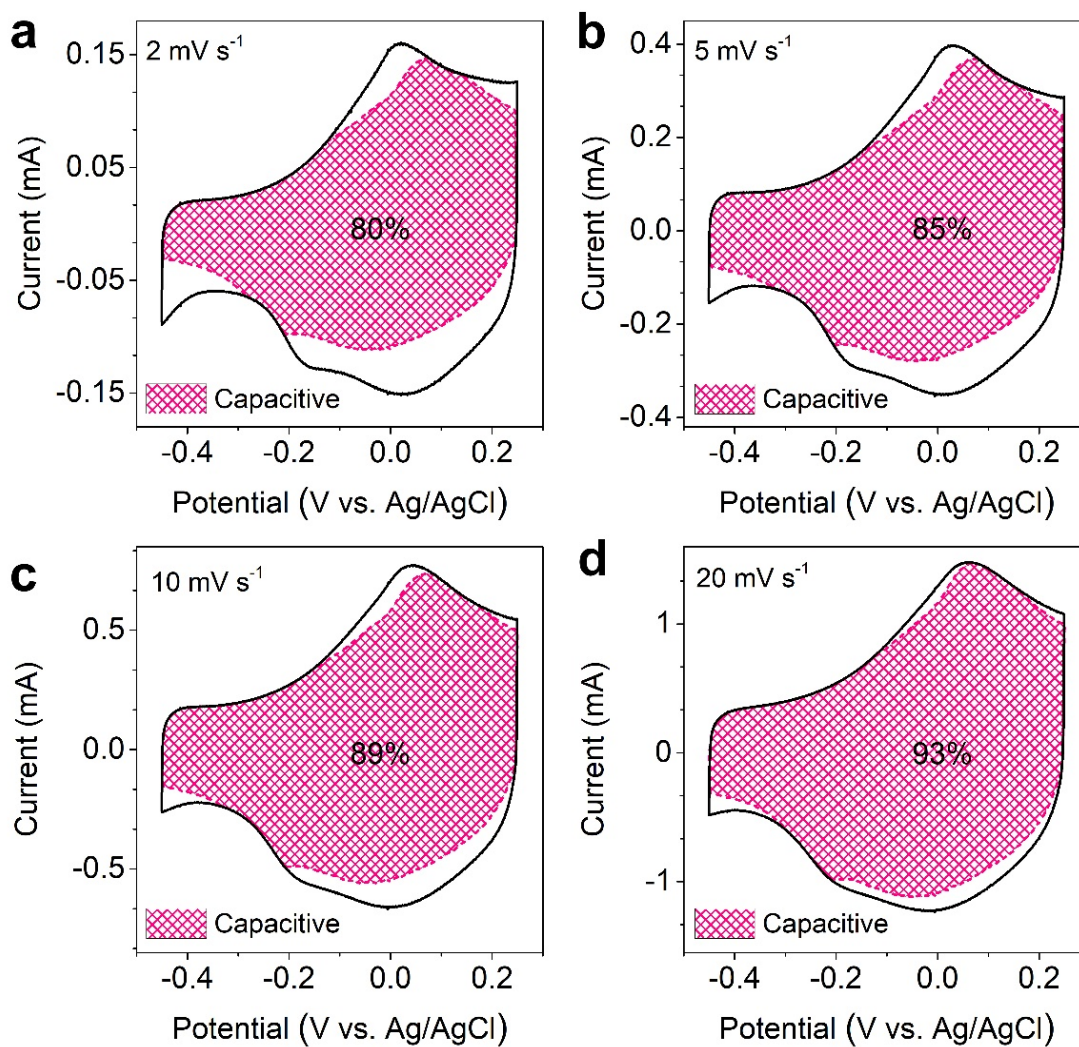
Figure 6.13. Analysis of the capacitive charge storage contributions from the CV for Na-V$_2$CT$_x$ at different scan rates of a) 2 mV s^{-1}, b) 5 mV s^{-1}, c) 10 mV s^{-1}, and d) 20 mV s^{-1}. Hatched portions shown on the graph show the surface-controlled (capacitive) contributions.
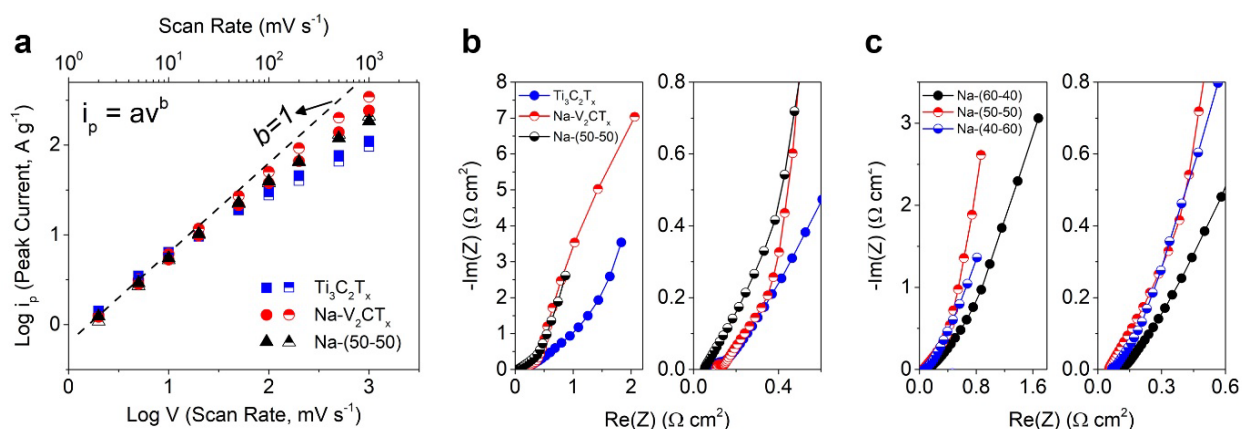
Figure 6.14. Electrochemical analyses and EIS results. a) Logarithm of cathodic (solid symbols) and anodic (half-filled symbols) peak currents at logarithm of scan rates from 2 mV s^{-1} to 1000 mV s^{-1} for Ti$_3$C$_2$T$_x$, Na-V$_2$CT$_x$, and Na-(50-50) heterostructure electrodes with comparable thicknesses. In parallel to CV charge analyses, the heterostructure film showed an improved capacitive performance at scan rates higher than 100 mV s^{-1} compared to pristine Ti$_3$C$_2$T$_x$ electrode with a similar high rate capacitive performance to that of already promising Na-V$_2$CT$_x$.[56] b) Electrochemical impedance spectroscopy (EIS) results for Ti$_3$C$_2$T$_x$, Na-V$_2$CT$_x$, and Na-(50-50) heterostructure electrodes. At high frequencies the heterostructure electrode showed improved charge transfer properties, while at lower frequencies it showed high ion-transport properties similar to that of Na-V$_2$CT$_x$ and significantly better than Ti$_3$C$_2$T$_x$. c) EIS results for heterostructure electrodes with different compositions. As it can be seen in the graphs, all electrodes showed similarly improved ion and charge transfer properties compared to those of individual pristine MXene electrodes. The slightly different increase in the imaginary resistances (corresponding to ion-transport properties) at high frequency region for different electrodes could originate from the differences in their thicknesses. As indicated in the paper and known in literature, Freestanding MXene electrodes prepared by vacuum filtration usually show a thickness-dependent performance. As discussed, however, this thickness-dependent performance showed a considerable improvement in heterostructure electrodes where they could deliver similar capacitances and rate-performances at thicknesses relatively higher than those of pristine MXene electrodes.

To investigate the real-device performance of the MXene heterostructures, we fabricated symmetrical supercapacitor cells from Na-(50-50) electrodes using 3 M H_2SO_4 as the electrolyte. **Figure 6.15 a** shows the CV profiles of the symmetrical supercapacitor in a 0.8 V voltage window at scan rates from 2 to 500 mV s^{-1}. The energy and power densities of the Na-(50-50) symmetric cell are shown in **Figure 6.15 b,** displaying an improvement over our previous work on high-performance symmetric cells based on Na-V_2CT_x in the same electrolyte.[56] The fabricated cell could deliver a power density of 0.03 W cm^{-3} at an energy density of ~0.22 Wh cm^{-3}. A maximum energy density of ~12.3 Wh cm^{-3} could be achieved at a power density of ~0.007 W cm^{-3}, placing the MXene heterostructure symmetric cell among the best reported aqueous symmetric supercapacitors reported. Importantly, the fabricated MXene heterostructure symmetric device showed exceptional capacitance retention of ~89.3% after 100 000 charge-discharge cycles at a rate of 1 A g^{-1}. This outstanding cyclic performance renders MXene heterostructures as promising electrodes for practical devices that require ultralong cycle life.
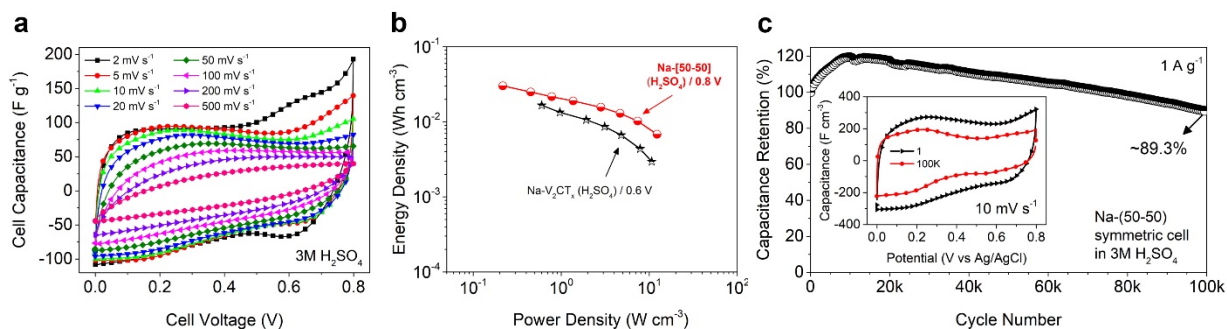
Figure 6.15. Symmetric supercapacitors with MXene heterostructures. a) CVs of symmetric supercapacitor cell with Na-(50-50) electrode in 3 M H_2SO_4 electrolyte. b) Ragone plot comparing the power and energy densities of the Na-(50-50) MXene heterostructure symmetric cell to that of the previously reported state-of-the-art Na-V_2CT_x symmetric cell. c) Cycle life of Na-(50-50) MXene heterostructure symmetric supercapacitor at a current density of 1 A g^{-1} with capacitance retention of ~89.3% after 100 000 cycles.

6.4. Conclusions

In summary, the results of this chapter demonstrated rational self-assembly of two negatively charged MXene nanosheets: $Ti_3C_2T_x$ and V_2CT_x, into vertical 2D heterostructures through a liquid phase assembly with the possibility to produce large amounts of the hetero-layered material. The assembled all-MXene heterostructures showed an ordered sequential stacking of few-layers $Ti_3C_2T_x$ and V_2CT_x in their structure confirmed by XRD and S/TEM analyses. The fabricated freestanding binder-free MXene heterostructure films showed new and improved electrochemical behavior in 3 M H_2SO_4 electrolyte with an exceptional cycle life performance with no capacity decay after 50 000 cycles, a high volumetric capacitance of ~1473 F cm^{-3}, and maximum volumetric power and energy densities of 0.03 W cm^{-3} and ~12.3 Wh cm^{-3}, respectively.

Chapter 7

MXenes' as Cathode Materials for Non-Aqueous Rechargeable Aluminum Batteries

Multivalent-ion batteries are considered as potential alternative systems to current lithium-ion batteries (LiBs) because of their higher theoretical capacities. Among various multivalent systems, rechargeable aluminum batteries (AlBs) can potentially be safer, cheaper, and deliver higher energy densities compared to commercial LIBs. Because of the high charge density of Al^{3+} cations and their strong interaction with the host lattice, however, very few cathode materials are known to be able to reversibly intercalate these ions. In this chapter, my research results on electrochemical properties of 2D MXenes in non-aqueous rechargeable aluminum batteries are presented. The fabrication of aluminum batteries in the laboratory scale, is different than conventional coin cell setups used for LiB experiments. Therefore, this chapter initially discusses challenges for fabricating an aluminum battery and different components of it. The electrochemical properties of MXene cathodes is then presented in this emerging battery technology. The results presented in this chapter are published as a peer-reviewed article (ref. 19) titled: "Two-Dimensional Vanadium Carbide (MXene) as a High Capacity Cathode Material for Rechargeable Aluminum Batteries", in the Journal of ACS Nano, 2017, 11 (11), 11135-11144.

7.1. Introduction

Rapid growth in the development of the portable electronic devices, the expanding market for the electric vehicles (EVs), and advances in the production of electricity from renewable sources have increased the demand for safe and low-cost energy storage devices. The application of Li-ion batteries (LIBs) in the future is overshadowed by their high cost and safety issues as well as the concerns about access to the lithium metal resources in the future.[107] This has challenged scientists worldwide to actively pursue the development of the so-called "beyond Li-ion" batteries. Recently, rechargeable aluminum batteries (Al-batteries) have received attention as promising alternatives to LIBs for applications such as electrics vehicles (EVs) and gird-scale storage. This is due to the high theoretical capacity of aluminum metal anode (8040 mAh cm^{-3} and 2980 mAh g^{-1}) stemming from its relatively light weight and three-electron redox capability. The standard reduction potential of aluminum metal, however is less negative compared to lithium (-1.7 V *versus* -3.0 V), which can result in a lower energy density of Al-battery systems.[107] Despite this drawback, aluminum is the most abundant metal in Earth's crust and can be handled in air, which may reduce the battery cost and facilitate battery fabrication processes.[107,179–181] However, the development of Al-batteries is hindered by the lack of high capacity and voltage cathode materials that can host trivalent Al^{3+} cations.[107,182,183]

Al-batteries based on graphite, few-layer graphene, or graphitic foam as cathode materials have been introduced in the last few years and their electrochemical behavior have been studied.[181,184,185] The operation of these batteries is based on the reversible (de)intercalation of chloroaluminate anions in between graphene layers.[181,185,186] The studied graphite-based cathodes can deliver capacities as high as 70 mAh g^{-1} at a very high rate of 4000 mA g^{-1}. However, the highest specific capacity reported so far for carbon-based cathodes is around 120 mAh g^{-1} for

graphene nanoribbons directly grown on highly porous 3D graphene structures. [184] Despite their high-rate capabilities, most of the reported graphite and graphene based cathodes show poor Coulombic efficiencies at low rates.[181,184,186] Also, the intercalation of anions instead of Al^{3+} cations in these cathode materials limits the achievable capacity.[181,185,186] In addition, it is suggested that the dual-ion (Cl^-, $Al_xCl_y^-$) insertion mechanism into some carbon-based cathodes results in depletion of anions during charging and limits the energy density of the battery.[187] Conversion-type cathode materials based on sulfur (S) or metal sulfides (such as Ni_3S_2 and CuS) have also been reported for Al-batteries. These cathodes store charge by conversion reactions that result in the formation of Al_2S_3 during discharge and its reversible conversion to sulfur and/or sulfur compounds during the charging process.[187–189] Similar to their Li counterparts, such cathode materials suffer from low cyclic life and show huge capacity decays over only a few cycles.[187,188,190] So far, only a few materials have been reported that can reversibly intercalate Al^{3+} cations into their structures.[187] V_2O_5 was the first reported intercalation-type cathode material for Al-batteries and has been extensively studied in recent years.[107,179] Depending on the electrode structure and test methods, specific capacities in the range of 50 mAh g^{-1} to more than 200 mAh g^{-1} and insertion potentials of less than 1 V are reported for V_2O_5 cathodes.[179,191–194] A recent study has shown that the charge storage in V_2O_5 is based on a combination of intercalation and phase change at the surface of the electrode. [193] Other reported cathode materials for Al-batteries generally suffer from poor cyclic performance, exhibit low capacities even at very slow (dis)charging rates, and have low insertion potentials (e. g. Mo_6S_8 Chevrel phase, around 0.55 V vs Al/Al^{3+}).[179,191,195–198]

In this chapter of my dissertation, it is demonstrated that MXenes can act as potential cathode materials for rechargeable aluminum batteries. Initially, and as or fist attempt, we

fabricated a rechargeable Al-battery with two-dimensional (2D) and layered vanadium carbide MXene (V_2CT_X) as the cathode, aluminum metal as the anode, and a non-flammable ionic liquid consisting of a mixture of aluminum chloride ($AlCl_3$) and 1-ethyl-3-methylimidazolium chloride ([EMIm]Cl) as the electrolyte. As battery electrode materials, various MXenes have shown high performance as anodes for lithium and sodium ion batteries. It is important to note that despite all these promising performances of MXenes in LiBs and NaBs, as well as the common knowledge that the charge storage in MXenes is based on the intercalation of cations, [199] MXenes have mostly shown capacitor-type behaviors without distinct charge-discharge plateaus when tested as battery electrodes.[13,18,42] This capacitive behavior of MXenes has unfortunately, cast shadow on the potential performance of these materials as true battery electrodes. The results of this chapter show that in the aluminum battery systems, in contrast to LiBs and NaBs, MXenes display a more battery-type behavior with distinct charge and discharge plateaus.

7.2. Experimental Section

Synthesis of MAX Phases. Please refer to chapter 3 for synthesis of MAX Phases.

Synthesis of MXenes. Multilayered (ML) MXene powders were prepared according to the procedure explained in chapter 3.

In case of initial experiments for V_2CT_x, the few layer V_2CT_x (FL- V_2CT_x) was produced by dispersion of ML-V_2CT_x powder in 1-Methyl-2-pyrrolidinone (NMP, 99+%, Alfa Aesar) and stirring at high speeds (1000-1200 rpm) on a hotplate at 60 ºC for 24h. TBAOH intercalation was done by dispersion of the ML-V_2CT_x powder in a 40 % w/w aqueous solution of TBAOH (Alfa Aesar) in a ration of 1g to 12.5 mL (MXene powder to TBAOH solution) for 4h at room temperature. The intercalated powder was then filtered and rinsed with DI water and absolute

ethanol several times to remove the residual TBAOH and dried at room temperature under vacuum overnight. To produce the TBAOH-FL-V$_2$CT$_X$ MXene, the TBAOH treated powder was stirred at 100 rpm in NMP for at least 12 h at 60 ℃ prior to electrode fabrication.

Preparation of the Ionic Liquid Electrolyte. The chloroaluminate ionic liquid electrolyte was prepared by mixing 1-ethyl-3-methylimidazolium chloride ([EMIm]Cl - 98+%, Alfa Aesar) and anhydrous high-purity aluminum chloride (AlCl$_3$ - 99.999+%, Alfa Aesar) at room temperature in an argon filled glove box with oxygen and moisture levels below 0.1 ppm. Prior to mixing, the [EMIm]Cl ionic liquid was completely dried under vacuum at 150 ℃ for at least 24 h. The high purity AlCl$_3$ powder was directly used without any purification. To prepare the electrolyte, the AlCl$_3$ was slowly added to the dried [EMIm]Cl ionic liquid in a 1.3:1 molar ratio to avoid excessive heat generation. The resulting yellowish electrolyte was then stirred for 30 minutes to dissolve the remaining AlCl$_3$ powder. Molecular sieves were used to further decrease the water contents in the electrolyte. To further purify the electrolyte, a piece of polished high purity aluminum foil was placed in the prepared electrolyte and kept for at least one week before using the electrolyte. The final electrolyte used in the experiments was light yellow or colorless.

Cell Fabrication and Electrochemical Measurements. All electrochemical experiments were carried out in custom made Teflon cells or plastic pouch cells to avoid possible reactions of the electrolyte with the stainless-steel coin cells. To prepare the cathodes, the synthesized V$_2$CT$_X$ MXene powder was mixed with carbon black (Super P, 99+%, Alfa Aesar) and polyvinylidene fluoride (PVDF Binder, 99.5%, MTI) in a ratio of 80:10:10 using NMP (99+%, Alfa Aesar) as the solvent and stirring for 24 h to achieve uniform mixture. The resulting slurry was directly casted on a piece of carbon paper (P50, Fuel Cell Earth) and was dried at 120 ℃ under vacuum for 24 h. The mass loading of the active material was ~ 0.5-2 mg cm^{-2}. High-purity Molybdenum foil

(99.95%, 3-7 micron thick, Alfa Aesar) or Tantalum foil (99.95%, 0.025 mm thick, Alfa Aesar) were used as the current collector for the cathode side and high-purity aluminum foil (99.9995%, 0.2 mm thick, Alfa Aesar) was used as both the anode and current collector for the anode side of the cells. The aluminum foil electrodes were thoroughly polished and cleaned with absolute ethanol before use. Two layers of Celgard ® microporous membranes (3501) were used as separators and the $AlCl_3$:[EMIm]Cl ionic liquid with a molar ratio of 1.3:1 was used as the electrolyte in the cell. The cell components were completely dried under vacuum overnight prior to cell fabrication and the cell fabrication process was carried out in an argon filled glovebox.

Cyclic voltammetry (CV) and galvanic charge-discharge experiments were carried out using BioLogic VMP3 potentiostat. The aluminum batteries were tested in a 1.7 V voltage window (0.1 V – 1.8 V vs. Al/Al^{3+}). The carbon paper used as the cathode substrate was inactive in this potential window. This was demonstrated by performing CV and charge/discharge experiments on a cell using bare carbon paper as the cathode and at a scan rate of 1 mV/s, and applied current density of 5 mA g^{-1} in the same 1.7 V potential window. All Galvanostatic charge-discharge experiments were carried out between 0.1 V and 1.8 V at different current densities (based on the total mass of the active material (MXene) in the electrode).

Characterization Techniques. The structure and morphology of the synthesized MAX and MXene powders and electrodes were characterized using Bruker X-ray diffractometer with 40 kV and 40 mA Cu-kα radiation in 0.4º 2θ steps and JEOL JSM-7000F scanning electron microscope equipped with an energy dispersive spectrometer (EDS detector). A dual beam focused ion beam (FEI Helios Nanolab 460F1) was used to prepare the lamellae from V_2CT_x electrodes at different charge states. After thinning, the lamellae were imaged using a Talos F200x transmission electron microscope equipped with a super-X SDD EDXS at 200 kV. HRTEM/STEM imaging

modes were used to study the morphology and the structure of the samples. TEM/EDS mapping was used to confirm the presence of different elements. The TEM analyses were performed by Dr. Ali Hadjikhani at university of Connecticut. To investigate the structural and morphological changes of the electrodes after cycling, the battery cells were opened in a glovebox after six successive charge and discharge cycles at current density of 50 mA g^{-1}. The fully charged (to 1.8 V) and discharged (0.1 V) electrodes were thoroughly washed with anhydrous ethanol and dried in the glovebox for at least 12 h before further analysis. For XRD and SEM analysis, the washed and dried electrodes were quickly transferred out of the glovebox and were analyzed. For XPS analysis, the samples were completely sealed in plastic bags inside the glovebox to avoid any reaction with air, and then were transferred out of glovebox and XPS analysis was performed as soon as samples were received.

Photoemission measurements were performed in a Kratos AXIS 165 surface analysis system equipped with a 165-mm hemispherical analyzer (HAS). XPS spectra were recorded in the fixed analyzer transmission (FAT) mode using a monochromatic aluminum source at 12 mA and 15 kV. The step size was set to 0.05 eV with 500 ms dwell time (700 for V) and 2 sweeps across each energy range. The chamber was purged with nitrogen. For Argon etching of the surface of the samples, Ar sputtering was done for 10 minutes at 4 kV, with a large spot size ($\sim$2 mm^2). The resolution of the instrument at the operating parameters was measured from FWHM of the Ag3d$_{5/2}$ peak to be 1.0 eV. The XPS energy scale was calibrated by setting the Ag3d$_{5/2}$ line on clean silver to exactly 368.3 eV referenced to the Fermi level. The angle of the incidence of the x-ray beam relative to the specimen normal was 54.7°. All analyses were performed on the original electrode, fully discharged (0.1 V), and fully charged (1.8 V) electrodes.

7.3. Results and Discussions

7.3.1. Ionic Liquid electrolyte and AlB Battery Cell Setup

Preparation of the ionic liquid-based electrolyte that is currently being used in the literature is not as straightforward as the common carbonate-based electrolytes used for Li- and Na-ion batteries. The ionic liquids (for example, [EMIm]Cl or [BMIm]Cl) are very sensitive to air and moisture and in their as-synthesized form contain significant amounts of water. Therefore, initially and as the starting point, I developed a protocol to dry these ionic liquids and prepare the desired electrolyte composition through the addition of $AlCl_3$ salt. Details of electrolyte preparation can be found in the experimental section of this chapter. **Figure 7.1** shows the differences between a high quality (light yellowish liquid shown in **Figure 7.1 a**) and a low quality (dark or light green liquid shown in **Figure 7.1 b**) electrolyte prepared using EMImCl ionic liquid and $AlCl_3$ salt. The low quality (greenish) electrolyte was prepared with a lower purity (99.9%) $AlCl_3$ and less dried ionic liquid. This shows the importance of the drying step and the purity of the Al salt in preparation of this electrolyte.

In the $AlCl_3$/[EMIm]Cl ionic liquid electrolyte, the main anionic species are $[AlCl_4]^-$ and $[Al_2Cl_7]^-$ chloroaluminates, where the concentration of the latter is higher in acidic mixtures ($AlCl_3$ to [EMIm]Cl ratio of higher than 1), enabling reversible platting and stripping of the aluminum.[107,180] The capability of aluminum deposition and dissolution of the prepared ionic liquid-based electrolyte (yellow/high quality one) is shown in **Figure 7.2.** In this figure the voltage window stability of this electrolyte is also shown using Mo foil as the current collector on the cathode (positive electrode) side. confirms its usability for preparation of the MXene-based aluminum battery cells.

155
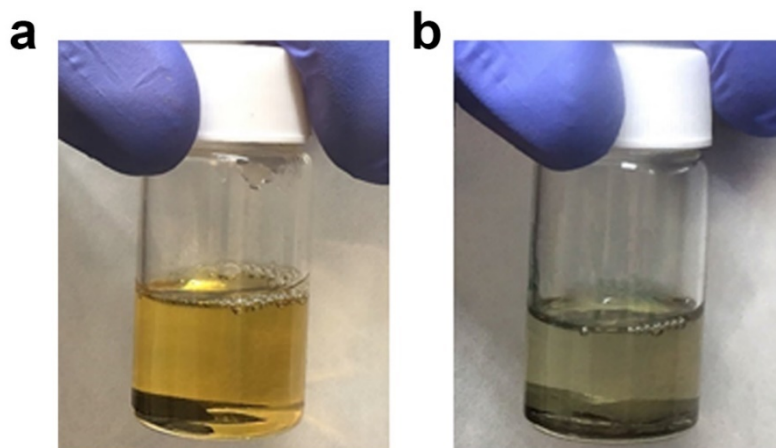
Figure 7.1. Aluminum battery electrolyte. a) High-quality and carefully dried [EMIm]Cl:AlCl$_3$ ionic liquid electrolyte. b) The same electrolyte, prepared without enough pre-drying of the ionic liquid, showing a greenish color (low-quality electrolyte). It is noteworthy that the low-quality electrolyte was dried after preparation using molecular sieves as well as polished aluminum pieces and before drying it had a dark green color.
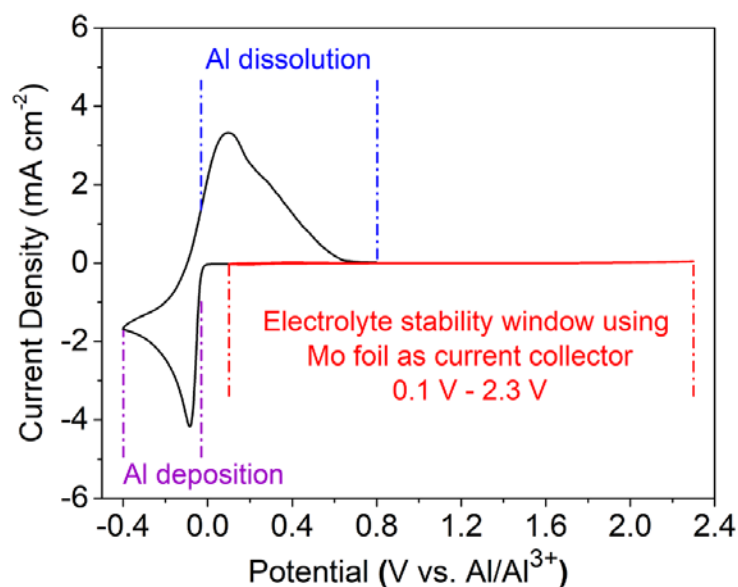
Figure 7.2. Al deposition and dissolution using the AlCl$_3$:[EMIm]Cl (1.3:1 molar ratio) ionic liquid electrolyte and stability of the same electrolyte using Mo foil as working electrode and Al foil as reference and counter electrode in a three-electrode setup cell at a scan rate of 10 mV s^{-1}. Adapted with permission from ref. 19 (Copyright © 2017 American Chemical Society).

156

It should be noted that the common coin cell setup that is widely used for Li- and Na-ion battery tests and experiments in laboratories cannot be used to test the aluminum batteries that contain this ionic liquid electrolyte. The developed EMimCl:AlCl$_3$ electrolyte is very corrosive and severely reacts with and corrodes the stainless steel coin cell casings during the electrochemical cycling.[107] Therefore, I developed a hand-made setup in which either polymer coated aluminum pouch cells or pieces of Teflon sheets were used as the casing for fabrication of aluminum batteries. When the Teflon sheets were used, the cells were sealed with Parafilm pieces and tested inside the glovebox to ensure that the electrolyte does not degrade as the result of side reaction with oxygen or moisture. **Figure 7.3** shows the different components used for fabrication of the aluminum battery cells.
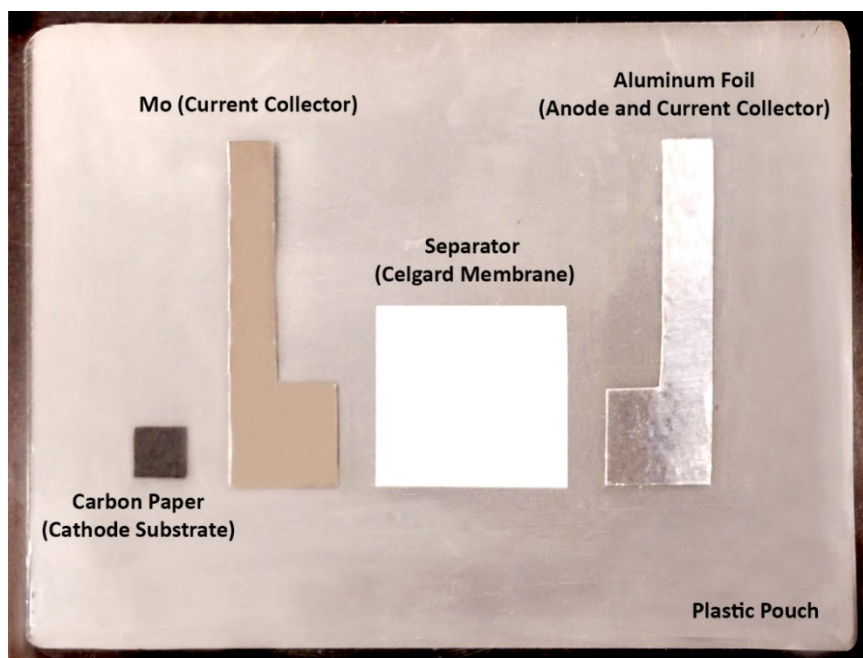
Figure 7.3. Different components of the handmade aluminum battery cells we have designed in our laboratory.[19] Adapted with permission from ref. 19 (Copyright © 2017 American Chemical Society).

Another problem regarding the development of aluminum batteries is the choice of current collector and the substrate for preparation of the cathode electrode. Again, because of the corrosive nature of the electrolyte here, the common copper foil substrate that is being used for Li-ion batteries cannot be used for aluminum battery systems as it will result in severe side reactions.[107] I examined a wide variety of metallic current collectors and substrates in the assembled aluminum battery cell setups.

Figure 7.4 shows the voltage stability of different metallic substrates in the prepared ionic liquid electrolyte. Mo and Ta foils show the best stability in the aluminum battery electrolyte and the widest potential window can be achieved using them (please note to the lower current values at the lower and upper cut-off potentials in **Figure 7.4 b and c**). Therefore, either Mo or Ta were used as the current collector on that cathode (MXene electrode) side. It was also found that carbon cloth used as the porous substrate for preparation of the cathode electrode, is electrochemically inactive up to around 1.9 V vs. Al/Al^{3+}. Therefore, the carbon cloth will not contribute to the charge storage in the voltage window of 0.1 V to 1.8 V (V vs. Al/Al^3) which the MXene electrodes were tested.

Using the developed electrolyte and cell setup, I was able to fabricate working aluminum battery cells based on the the MXene cathodes and study their electrochemical properties in the $EMImCl:AlCl_3$ ionic liquid electrolyte against Aluminum metal anode. In the continues of this chapter, my comprehensive results on electrochemical performance of MXenes (with focus on V_2CT_x composition, since it has one of the highest theoretical capacities in this system) in the AlB system is shown and the suggested mechanism for charge storage is discussed in detail.
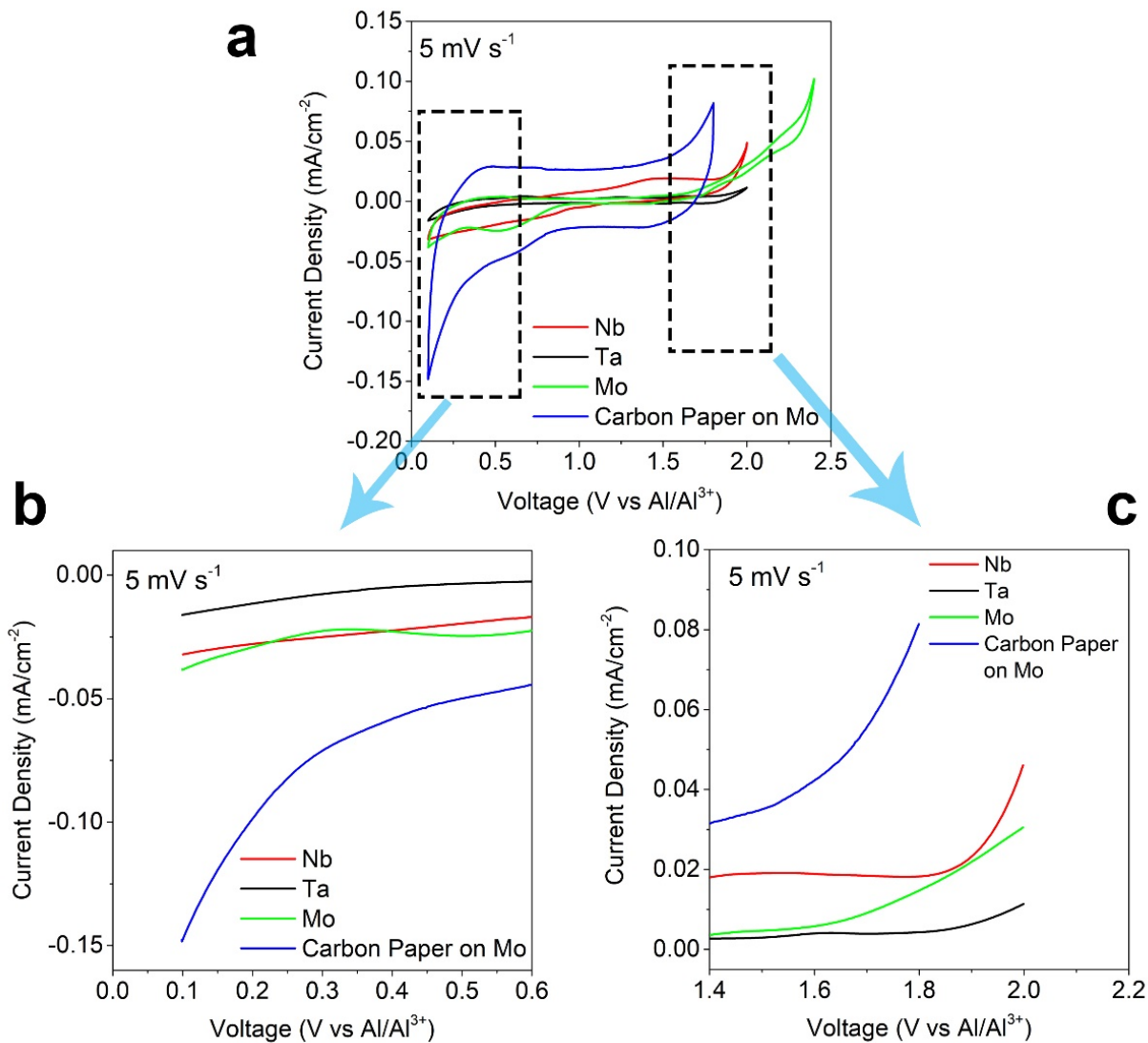
Figure 7.4. Stability and reactivity of different metal current collectors in Al-battery electrolyte. a) Cyclic voltammetry of different metal current collectors at 5 mV s⁻¹ in AlCl₃:[EMIm]Cl (1.3:1 molar ratio) electrolyte. b) Zoomed in the portion for the lower cut-off potential. c) Zoomed in the portion for the upper cut-off potential.

7.3.2. Theoretical Capacities of MXene Phases in Aluminum Batteries

In order to have a better understanding of potential performance and achievable capacities of different MXenes as aluminum battery cathodes, initially theoretical capacities of several known MXenes were calculated. The results of these calculations are shown in **Table 7.1**. As it can be seen, among different MXenes, V_2CT_x offers one of the highest theoretical capacities upon intercalation of Al^{3+} cations. Therefore, we chose this MXene composition at the beginning to perform detailed electrochemical studies in the aluminum battery system.

The theoretical capacities shown in **Table 7.1** are calculated similar to the following example shown for V_2CT_x compositions. Based on the total mass of the cathode and a three-electron charge transfer, the theoretical capacity of V_2C MXene can be calculated as follow:

The cathode discharge reaction in the Al-battery is (considering maximum intercalation of 1 mole Al per unit cell of MXene):

$$V_2C + Al \rightleftarrows V_2AlC$$
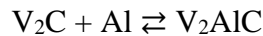
And the theoretical capacity (C) of the cathode can be calculated as:

$$C = \frac{nF}{M_{V_2C}} = \frac{3 \times 26800\,\frac{mAh}{mole}}{2 \times 51\,\frac{g}{mole} + 1 \times 12\,\frac{g}{mole}} = 705.263\,mAh\,g^{-1}$$

Similar method can be performed to calculate the theoretical capacities of other MXenes as well as MXenes with certain surface functional groups (please see **Table 7.1**).

Table 7.1. Theoretical capacity of some 2D MXenes (considering three different formulas with F, O, and OH terminating surface groups for simplicity) as potential cathode materials for rechargeable aluminum batteries. Adapted with permission from ref. 19 (Copyright © 2017 American Chemical Society).

Type	Parent MAX Phase	Corresponding MXene	Theoretical Capacity (mAh g^{-1})
Carbides	Sc$_2$AlC	Sc$_2$CF$_2$ **	574.69
		Sc$_2$CO$_2$ **	600.44
		Sc$_2$C(OH)$_2$ **	591.60
	Ti$_2$AlC	Ti$_2$CF$_2$	551.73
		Ti$_2$CO$_2$	575.42
		Ti$_2$C(OH)$_2$	567.30
	V$_2$AlC	V$_2$CF$_2$	529.39
		V$_2$CO$_2$	551.16
		V$_2$C(OH)$_2$	543.71
	Nb$_2$AlC	Nb$_2$CF$_2$	340.96
		Nb$_2$CO$_2$	349.87
		Nb$_2$C(OH)$_2$	346.85
	-	Mo$_2$CF$_2$ *	332.41
		Mo$_2$CO$_2$ *	340.87
		Mo$_2$C(OH)$_2$ *	338.00
	Cr$_2$AlC	Cr$_2$CF$_2$ **	522.14
		Cr$_2$CO$_2$ **	543.31
		Cr$_2$C(OH)$_2$ **	536.06
	Ti$_3$AlC$_2$	Ti$_3$C$_2$F$_2$	391.05
		Ti$_3$C$_2$O$_2$	402.80
		Ti$_3$C$_2$(OH)$_2$	398.81
Nitrides	Ti$_2$AlN	Ti$_2$NF$_2$ **	544.27
		Ti$_2$NO$_2$ **	567.31
		Ti$_2$N(OH)$_2$ **	559.42
	V$_2$AlN	V$_2$NF$_2$ **	522.52
		V$_2$NO$_2$ **	543.72
		V$_2$N(OH)$_2$ **	536.47
	Cr$_2$AlN	Cr$_2$NF$_2$ **	515.45
		Cr$_2$NO$_2$ **	536.08
		Cr$_2$N(OH)$_2$ **	529.02

* Mo$_2$C MXene is synthesized from a non-Al based MAX phase (Mo$_2$Ga$_2$C), however, for the calculation of the theoretical capacity we consider the final structure to be like a "211" Al-based MAX phase.

** Synthesis of these MXenes have not yet been reported but their corresponding MAX phases are available.

7.3.3. Performance of V_2CT_x MXene in Rechargeable Aluminum Batteries

Figure 7.1 a schematically shows the synthesis method of V_2CT_x MXene, where Al atoms are selectively etched from V_2AlC structure through immersing the MAX phase powder in a concentrated hydrofluoric (HF) acid solution at room temperature. **Figure 7.5 b and c** show scanning electron microscopy (SEM) images of typical V_2AlC particles before and after etching in hydrofluoric acid (HF) for 92h, respectively.

The typical accordion-like multilayered structure observed for the etched MAX phases indicates the successful synthesis of V_2CT_x MXenes. This sample was denoted as multilayered (ML) V_2CT_x. Upon etching V_2AlC powder and the removal of Al layers from V_2AlC, the XRD pattern of etched particles showed a peak corresponding to (0002) plane of V_2CT_x MXene, while the intensity of the MAX phase peaks (JCPDS # 29-0101) decreased significantly (**Figure 7.5 d**). The presence of small peaks corresponding to V_2AlC in the XRD pattern of the etched powder indicates the existence of a small amount of unreacted MAX phase in the final product, consistent with previous reports on the synthesis of V_2CT_x.[16,103,200]

The synthesized V_2CTx powder was casted on porous carbon paper substrate and used as the cathode in an Al-battery cell, where high-purity aluminum foil was the anode and $AlCl_3$/[EMIm]Cl ionic liquid (with $AlCl_3$:[EMIm]Cl molar ratio of 1.3) was used as the electrolyte. **Figure 7.6** schematically shows the components and the suggested operation mechanism of the fabricated aluminum batteries. Please note that the V_2CT_x is a model material from the MXene family here and we speculate similar charge storage mechanism occurs for other MXene compositions as well.
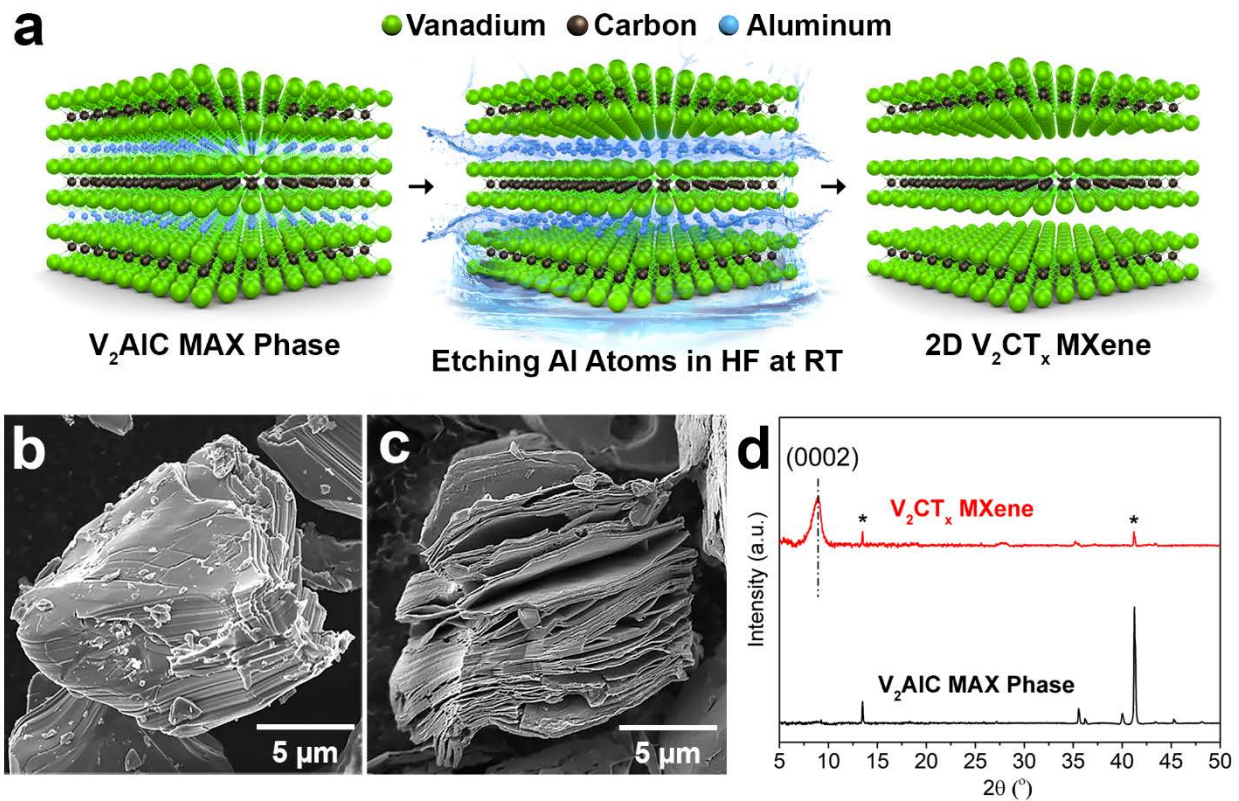
Figure 7.5. Schematic illustration of 2D vanadium carbide MXene synthesis and its structural characterizations. a) Schematic illustration of the selective etching process used to synthesize V_2CT_x MXene from V_2AlC MAX Phase. b) SEM image of V_2AlC MAX phase particle. c) SEM image of V_2AlC treated with 50% HF for 92h at RT. d) XRD patterns of V_2AlC before and after HF treatment (V_2CT_x MXene). (*) denotes the remaining MAX phase residual in the etched powder. Adapted with permission from ref. 19 (Copyright © 2017 American Chemical Society).
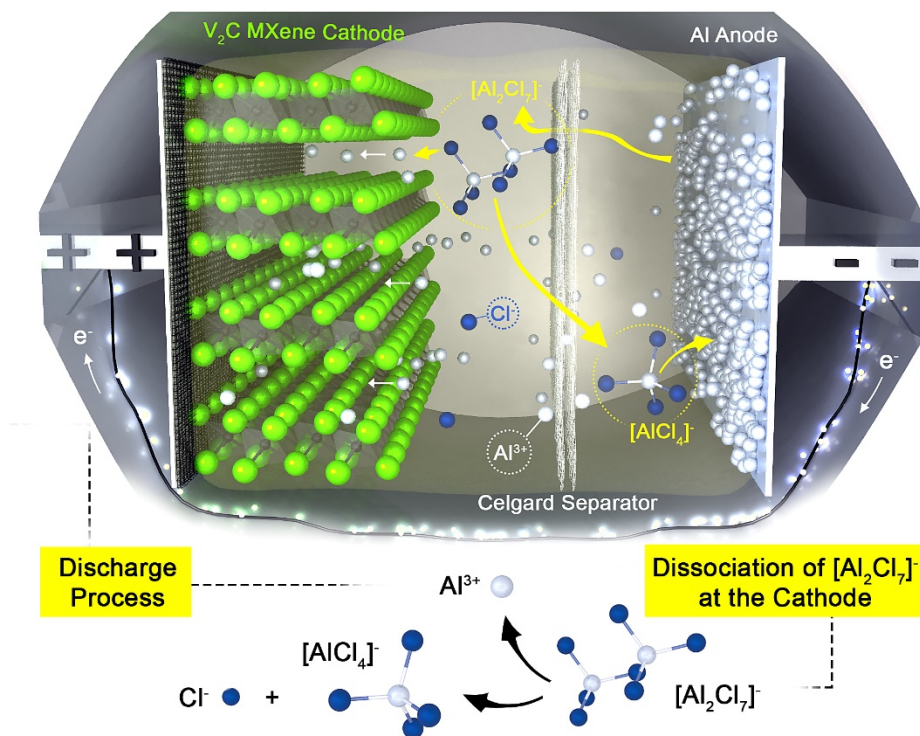
Figure 7.6. Schematic illustration of the proposed mechanism for an Al-battery with V_2CT_x MXene as the cathode during discharge in 1.3:1 $AlCl_3$:[EMIm]Cl ionic liquid electrolyte. Adapted with permission from ref. 19 (Copyright © 2017 American Chemical Society).

During the discharge process, $[Al_2Cl_7]^-$ anions dissociate at the electrode/electrolyte interface (Eq. 7.1) and Al^{3+} cations intercalate between the MXene layers (Eq. 7.2). Meanwhile, on the anode side of the cell, aluminum metal reacts with $[AlCl_4]^-$ anions to form $[Al_2Cl_7]^-$ anions and release three electrons (Eq. 7.3).

Proposed cathode Reactions:

$$4\ Al_2Cl_7^- \rightleftarrows Al^{3+} + 7\ AlCl_4^- \qquad (7.1)$$

$$V_2CT_x + y\ Al^{3+} + 3y\ e^- \rightleftarrows V_2Al_yCT_x \qquad (7.2)$$

Anode Reaction:

$$Al + 7\ AlCl_4^- \rightleftarrows 4\ Al_2Cl_7^- + 3\ e^- \qquad (7.3)$$
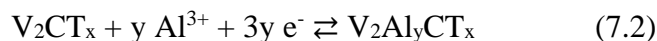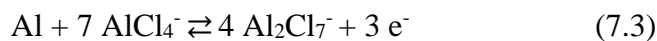
Figure 7.7 a shows the charge-discharge profiles of an ML-V_2CT_x cathode at a current density of 10 mAg^{-1}. In the initial discharge, a large irreversible capacity of ~335 mAhg^{-1} was observed, possibly due to dissociation of chloroaluminate anions and other electrolyte components that may form a solid electrolyte interface (SEI). The initial discharge capacity dropped to about 178 mAh g^{-1} in the first cycle (corresponding to $V_2Al_{0.26}CT_x$). The charge and discharge profiles of the cell in the first cycle show broad plateaus that correspond to the observed cathodic and anodic peaks in the cyclic voltammetry (CV) tests. The CV curve of the cell (**Figure 7.7 b**) shows two broad cathodic peaks at 1.2-1 V (I) and 0.9-0.8 V (II) and corresponding anodic peaks at ~ 1 V (III) and 1.4 V (IV). After the first cycle, the specific capacity decreased at a much lower rate down to 112 mAhg^{-1} after 20 cycles (**Figure 7.7 d**). Also, the Coulombic efficiency of the cell dropped from 100% in the first few cycles to around 90% in the fourth cycle. *Ex-situ* X-ray diffraction (XRD) analysis of the electrodes after discharging to 0.1 V and after charging to 1.8 V did not show any change from the original pattern of the 2D V_2CT_x cathode (**Figure 7.7 c**), suggesting the absence of phase transition and a storage mechanism based on the intercalation of ions into the cathode. After discharge, the peak corresponding to the (0002) plane of the V_2CT_x MXene (originally at 2θ=9.21º) downshifted to 2θ=9.11º, which corresponds to about 0.21 Å increase in the c-lattice parameter (c-LP) of the V_2CT_x upon discharge. Since a unit cell of MXene contains two layers of V_2CT_x, this increase in c-LP corresponds to about 0.10 Å increase in the interlayer distance. However, no change in the c-LP of the electrode was observed after the subsequent charge. Interestingly, the increase in the interlayer spacing of V_2CT_x is much lower compared to the change observed for MXenes intercalated with other cations (such as Li$^+$ and Na$^+$).[15,18,103] For instance, Dall'Agnese et al. have reported that a V_2CT_x electrode shows up to 4.6 Å increase in its c-LP when intercalated with Na ions.[103]
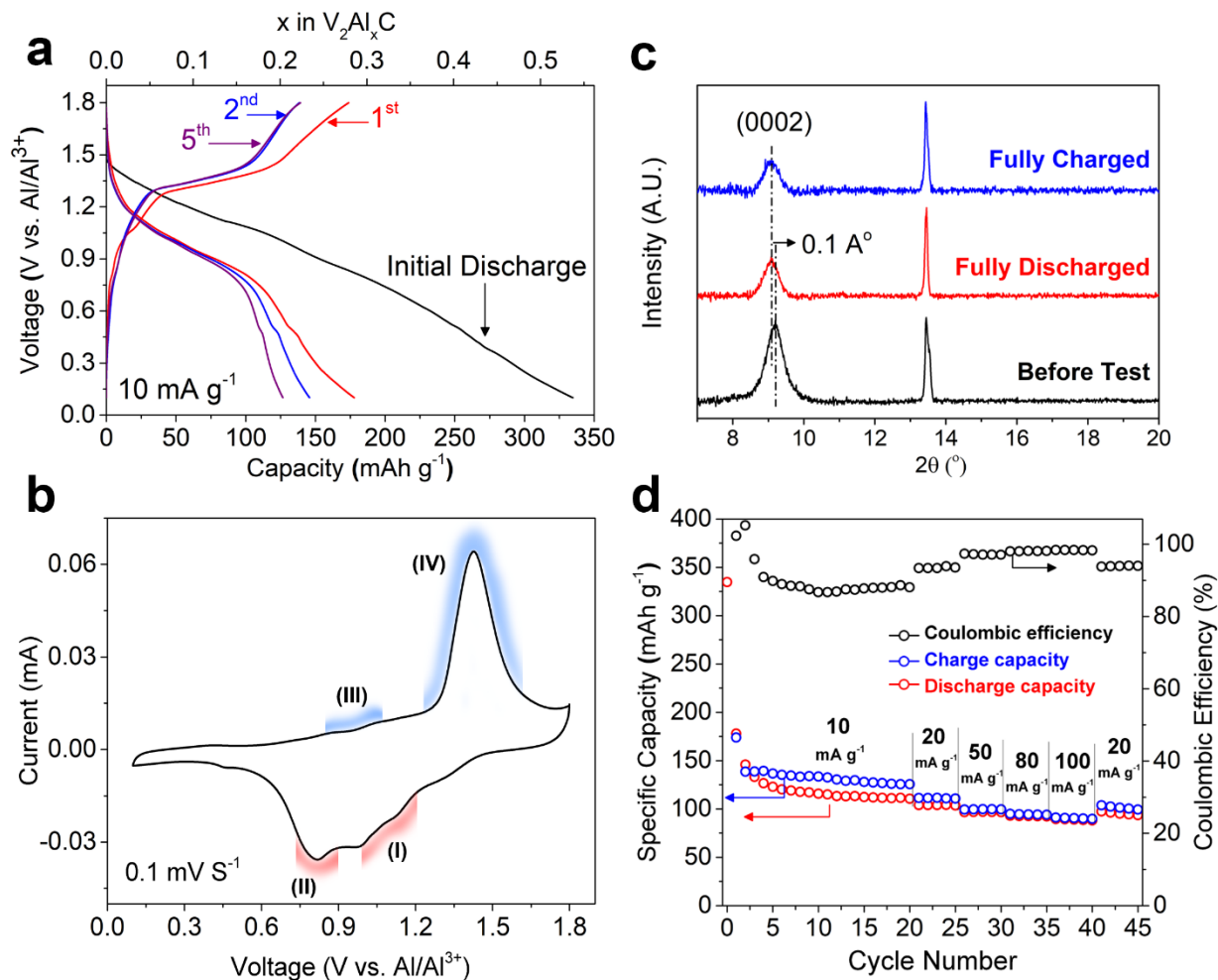
Figure 7.7. Electrochemical performance of ML-V_2CT_x cathode. a) Initial discharge and the following charge-discharge cycles of a ML-V_2CT_x cathode for the first, second, and the fifth cycles at a current density of 10 mA g^{-1}. b) CV curve of a ML-V_2CT_x cathode at a scan rate of 0.1 mV s^{-1} in a voltage range of 0.1 V – 1.8 V (V vs. Al/Al^{3+}). c) XRD patterns of V_2CT_x electrodes in different states of charge showing a negligible increase (~0.1 Å) in the d-spacing upon Al^{3+} intercalation. d) Cyclic performance and rate capability of a ML-V_2CT_x cathode at different current densities, showing a discharge capacity of around 112 mAh g^{-1} with Coulombic efficiency of ~ 90% after 20 cycles at a current density of 10 mA g^{-1}. Adapted with permission from ref. 19 (Copyright © 2017 American Chemical Society).

Based on these observations and other evidence discussed below, we suggest that Al^{3+} cations are the main intercalating species into MXene cathodes. Therefore intercalation (or co-intercalation) of large $[AlCl_4]^-$ and $[Al_2Cl_7]^-$ chloroaluminate anions (~5.28, ~7.02 Å, respectively) or EMI^+ cations (~ 7 Å),[65,201] which is observed for some of the other Al-battery cathode materials,[181,184–186] may not happen in the case of MXenes.

High-resolution transmission electron microscopy (HRTEM) images of the V_2CT_x electrodes before testing and after discharge and charge are shown in **Figure 7.8**. A very marginal increase in the d-spacing of the V_2CT_x was observed upon discharge, while no change in the interlayer spacing (ca. ~ 0.97 nm) or structure of the V_2CT_x MXene was observed after subsequent charge which is in good agreement with the XRD results. The lack of a large increase in the interlayer spacing can also be related to the very high charge density of Al^{3+} intercalation, which can attract the negatively charged MXene sheets. Previous studies have even suggested reduction of interlayer spacing of MXenes ($Ti_3C_2T_x$ in this case) upon intercalation of cations with high charge densities in aqueous electrolytes.[62] It is also worth noting that the intercalation of Al^{3+} into layered TiS_2 has been reported to slightly decrease the interlayer spacing. Reduced repulsion between sulfur layers in TiS_2 structure caused by intercalation of high charge density Al^{3+} cations is cited as the reason for the reduction in interlayer spacing.[202] Li_3VO_4 is also reported to show only around 0.03 Å increase in its d-spacing upon Al^{3+} intercalation.[203]

Similarly, we hypothesize that Al^{3+} intercalation into V_2CT_x structure reduces the repulsion between negatively charged functionalized MXene surfaces, resulting in a very small change in the interlayer spacing after ion intercalation.
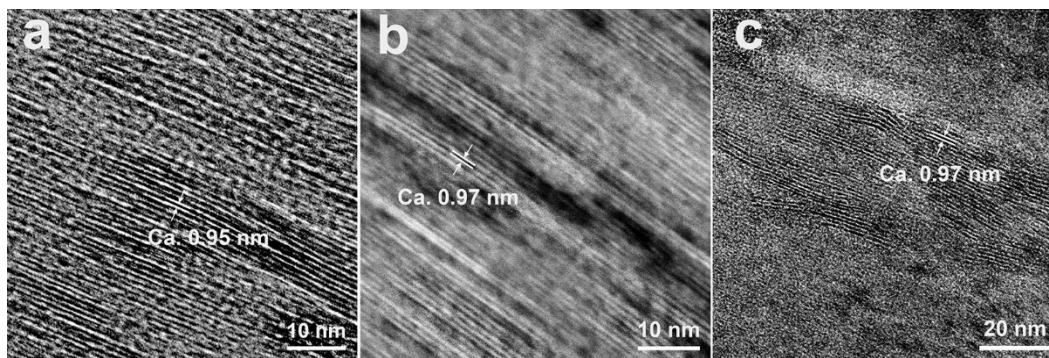
Figure 7.8. HRTEM images of V_2CT_x electrodes. a) before test, b) discharged to 0.1 V, and c) charged to 1.8 V. Adapted with permission from ref. 19 (Copyright © 2017 American Chemical Society).

Investigation of the composition of the electrodes before and after discharge with energy dispersive spectroscopy (EDS) consistently showed large increases in the Al content and very small increases in the Cl content of the MXenes after discharge. Representative SEM images and the corresponding EDS results of MXene particles before testing, after discharge to 0.1 V vs. Al/Al^{3+}, and after charge to 1.8 V (V vs. Al/Al^{3+}) are shown in **Figure 7.9**. It should be noted that the Al content of a typical V_2CT_x MXene particle was measured to be as high as 6.82 atomic % upon discharge (shown in **Figure 7.9**), while the Cl content is only 0.61 atomic %. The average Al/V atomic ratio of V_2CT_x MXene electrodes after second charge and discharge cycles was calculated by performing EDS measurements on 20 different MXenes particles. As shown in **Table 7.2** the Al/V ratio increased from 0.063 to 0.16 upon discharging the electrodes at 50 mA g^{-1}, corresponding to an Al content of x=0.22 ($V_2Al_{0.22}CT_x$). This is in a good agreement with the calculated Al content from the electrochemical measurement (x= 0.18, considering the presence of F, O, and OH functional groups; please see supplemental document for more details). The pronounced presence of Al after discharge was also shown by TEM/EDS analyses which are shown in **Figure 7.10 and 11**.
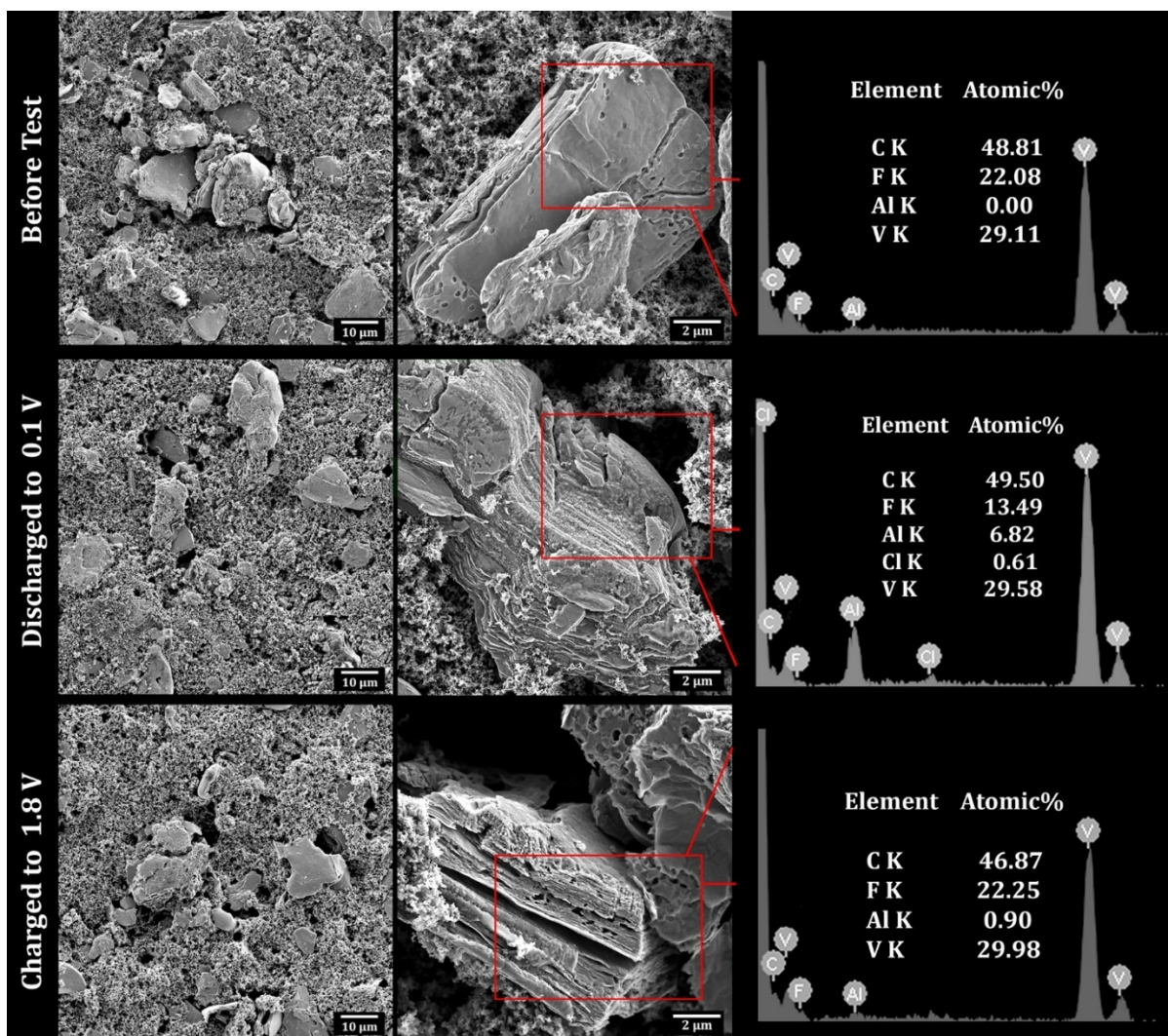
Figure 7.9. SEM and EDS analysis of multilayered (ML)-V_2CT_x electrodes at different charge states. EDS results clearly show the increase in the aluminum content of the MXene particles upon discharge and its decrease after charge. On "before test" and "charged" samples, no chlorine was detected on or between the layers of MXene particles. The negligible amount of the chlorine detected in the discharged sample could be due to presence of the residual electrolyte at the surface of MXene or Cl as the result of the dissociation of $[Al_2Cl_7]^-$ anion at the surface of the cathode during the discharge process. Adapted with permission from ref. 19 (Copyright © 2017 American Chemical Society).
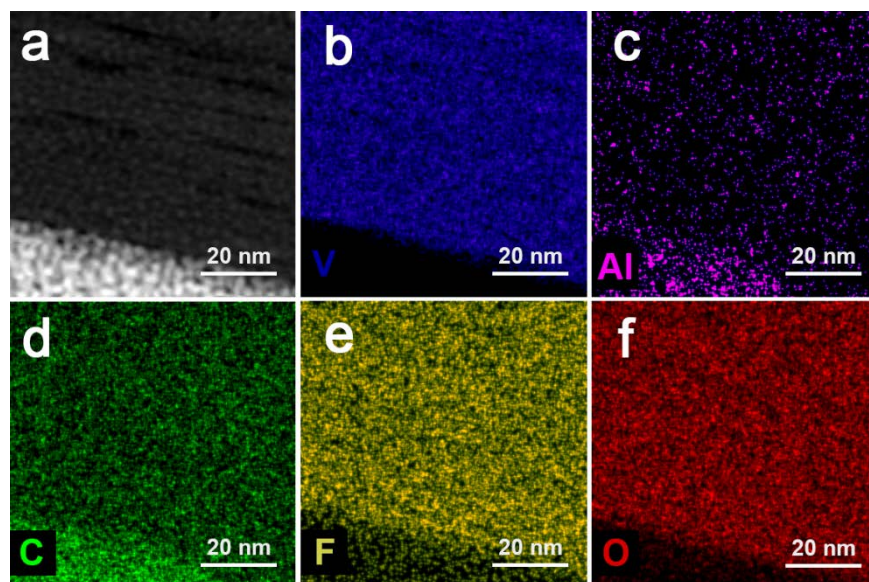
Figure 7.10. a-f) STEM images of V_2CT_x electrode before the test and the corresponding elemental mappings for V, Al, C, F, and O, respectively. Adapted with permission from ref. 19 (Copyright © 2017 American Chemical Society).
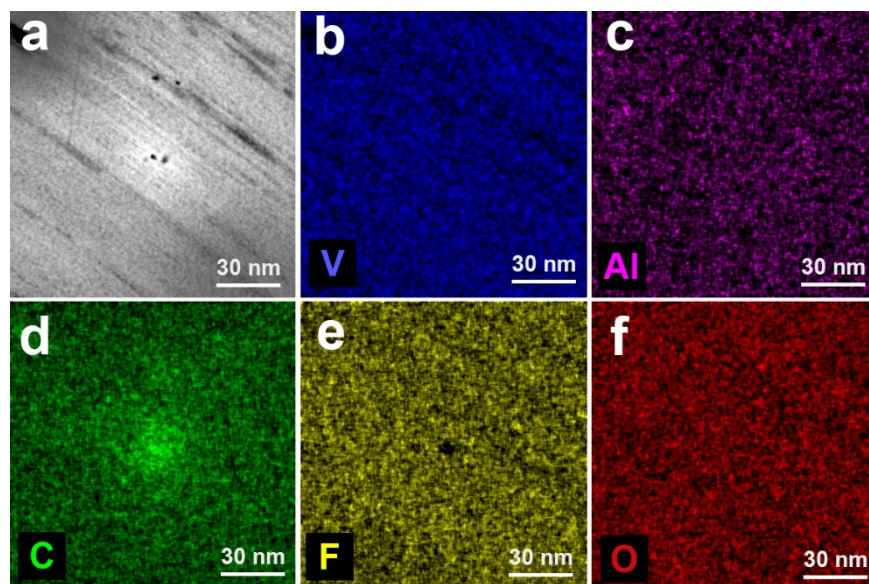
Figure 7.11. a-f) STEM images of a V_2CT_x electrode discharged to 0.1 V (V vs Al/Al^{3+}) and the corresponding elemental mappings for V, Al, C, F, and O, respectively. Adapted with permission from ref. 19 (Copyright © 2017 American Chemical Society).

Table 7.2. Average atomic ratio of aluminum to vanadium in MXene particles/flakes (average of 20 particles per sample) of ML-V_2CT_x electrode at different charge states (charging/discharging rate = 50 mA g^{-1}). Adapted with permission from ref. 19 (Copyright © 2017 American Chemical Society).

		Before Test	Discharged to 0.1 V	Charged to 1.8 V
Obtained from EDS	Al / V Ratio	0.063	0.166	0.099
	x Value	0.11	0.33	0.19
Experimental Obtained Discharge Capacity		90 mAh g^{-1}		
Based on Discharge Capacity	x in $V_2Al_xCF_2$	0.175		
	x in $V_2Al_xCO_2$	0.168		
	x in $V_2Al_xC(OH)_2$	0.170		

Despite the lack of irreversible structural changes or phase transformation, V_2CT_x electrodes showed a small but continuous decrease in their specific capacities and Coulombic efficiencies during successive cycles (**Figure 7.7 d**). This can be attributed to Al ion trapping in the large MXene particles as EDS also showed a small amount of Al^{3+} cations remain in the MXene particles after charging (about 0.9 atomic% for the example shown in **Figure 7.9**). However, the capacity loss and the low Coulombic efficiency of the MXene electrodes can be partly related to the possible side reactions of electrolytes with water molecules that exist between the V_2CT_x layers. It is known that water molecules intercalate between MXene layers during the etching and exfoliation processes and some interlayer water may remain even after drying in a vacuum furnace at 110-140 °C.[7,16,152] Thermogravimetric analysis (TGA) performed on the pre-dried MXene samples in my experiments also showed presence of water in these samples (**Figure 7.12**).
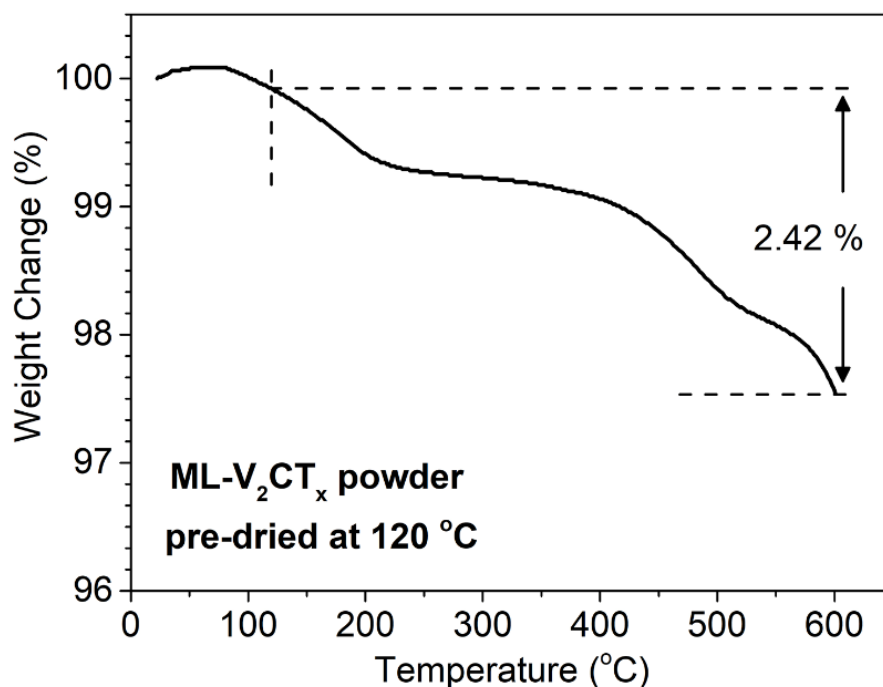
Figure 7.12. Thermogravimetric analysis (TGA) data of the ML-V_2CT_x powder pre-dried at 120 °C for 24h under vacuum. The results show that even after drying the powder, there is still about 2.42 wt.% of water in the MXene powder. Adapted with permission from ref. 19 (Copyright © 2017 American Chemical Society).

To better understand the charge storage mechanism of V_2CT_x, X-ray photoelectron spectroscopy (XPS) was carried out on three similar electrodes before testing, after discharging to 0.1 V, and after charging to 1.8 V (both versus Al/Al^3). Deconvolution of the V2p peak region of the electrode before testing (**Figure 7.13 a**) mostly showed vanadium in its V^{4+} oxidation state (516.3 eV) due to the presence of a monolayer oxide/vanadium oxide mixture on the surface of vanadium carbide nanosheets. Similar result was suggested by a previous study on the surface chemistry of V_2CT_x MXene.[16]

The existence of some V^{2+} species was also observed, which can be attributed to the remaining unreacted MAX phase in the produced MXenes.[16] For the discharged electrode (**Figure**

172

7.13 b), the V2p$_{3/2}$ peak develops a shoulder and shows V^{3+} species (515.6 eV) along with V^{4+} (shifted to 516.7 eV), which demonstrates the reduction of vanadium during discharge. After charging to 1.8 V vs. Al/Al^{3+} (**Figure 7.13 c**), vanadium is mostly present in its V^{4+} oxidation state (516.3 eV) with some V^{3+} remaining in the XPS spectra indicating that charging cannot revert all the V^{3+} to V^{4+}.

Figures **7.13 e and f** show the XPS spectra of discharged and charged samples after Ar sputtering, which can be used to understand the chemical environment inside the V$_2$CT$_x$ cathodes and eliminate the possible effects of residual electrolyte on the electrode surface. After Ar sputtering, some V^{3+} could be detected in the V2p peak of the original electrode, which is slightly shifted toward lower energies (V^{4+} shifted down to 516.1 eV; **Figure 7.13 d**). These spectra show a much higher ratio of V^{3+} to V^{4+} in the discharged samples, indicating the charge storage in V$_2$CT$_x$ is based on the change in the oxidation state of the vanadium, similar to the charge storage mechanism observed for V$_2$O$_5$ cathodes used in Al-batteries.[191,193]

As shown in **Figure 7.13 e**, the major oxidation state of the vanadium in V$_2$CT$_x$ when it is discharged to 0.1 V (vs. Al/Al^{3+}) is V^{3+}, indicating the electrochemical reaction is not limited to the surface of V$_2$CT$_x$ and exists in the bulk of the material as well (intercalation and diffusion of Al^{3+}). The spectra of the charged electrode after Ar etching (**Figure 7.13 f**) confirms that some vanadium with V^{3+} oxidation state remain in V$_2$CT$_x$ after charging. This could be attributed to trapped Al^{3+} ions in between MXene layers (meaning not all of the inserted Al^{3+} can reversibly be extracted) or possible surface phase transition as has been reported for V$_2$O$_5$.[193] Further studies are required to completely understand the reason for the irreversible change in the oxidation state of vanadium.

Figure 7.14 shows the overall survey XRD spectra of these three electrodes, respectively. **Figure 7.15** also shows the same XPS graphs shown in **Figure 7.13** before removal of the XPS Shirley background for the demonstration of the original shape of the graphs before the background was removed, and their corresponding peak deconvolutions. In this figure the deconvolution results are significantly improved. The end results and conclusions (more reduced state of V in discharged) obtained from XPS analyses, however, are the same with or without removal of the background.
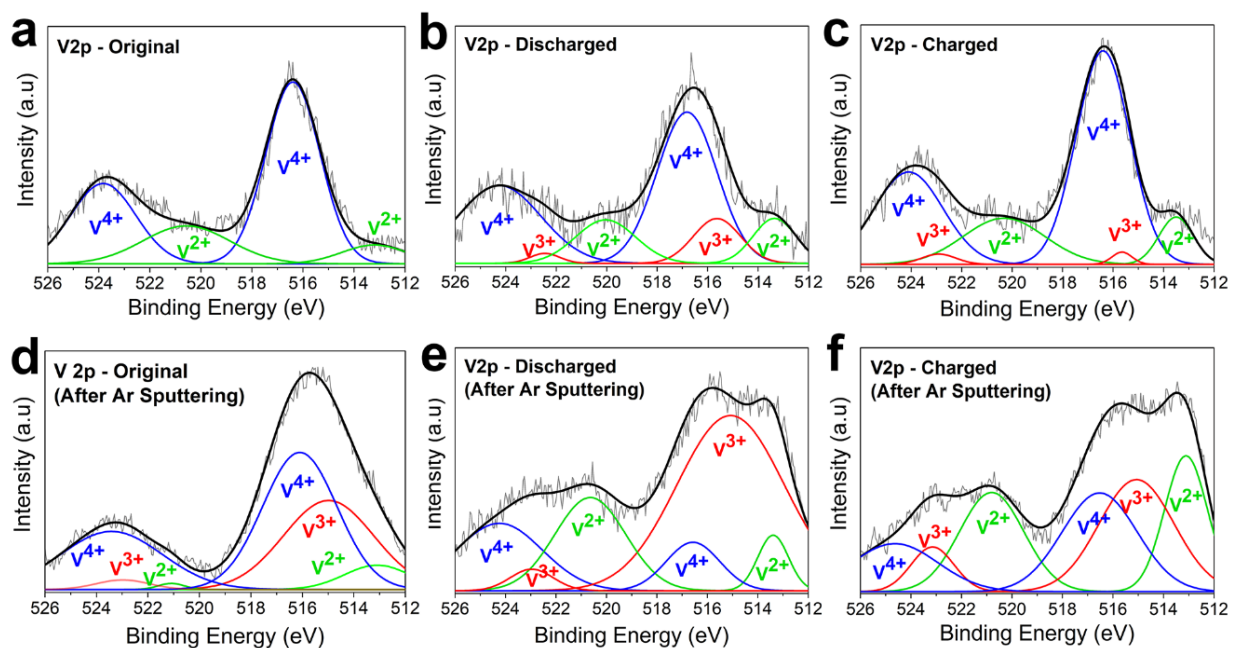
Figure 7.13. High resolution XPS spectra of V2p region of V_2CT_x. a) original electrode before test. b) discharged to 0.1 V vs. Al/Al^{3+}. c) charged to 1.8 V vs. Al/Al^{3+}, showing the change in the oxidation state of vanadium at each charge/discharge state. d, e, and f) XPS spectra of V2p region for original, discharged, and charged electrodes after Argon etching for 10 min, respectively. Adapted with permission from ref. 19 (Copyright © 2017 American Chemical Society).
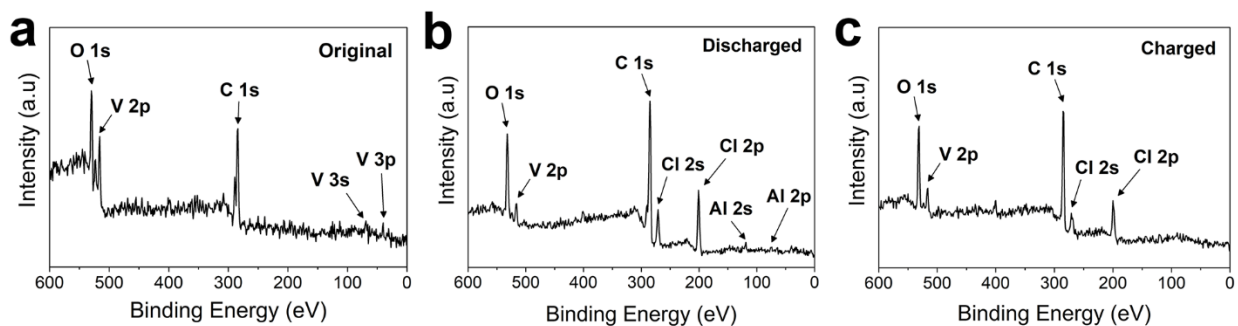
Figure 7.14. Survey XPS spectra of the electrodes. a) original, b) discharged to 0.1 V, and c) charged to 1.8 V ML-V_2CT_x electrodes. The high-resolution spectra of V 2p region and the related peak deconvolutions are shown in Figure 7.10 and 11. The Cl peaks shown in "b" and "c" are most probably due to electrolyte remains on the surface of the discharged and charges electrodes. Adapted with permission from ref. 19 (Copyright © 2017 American Chemical Society).
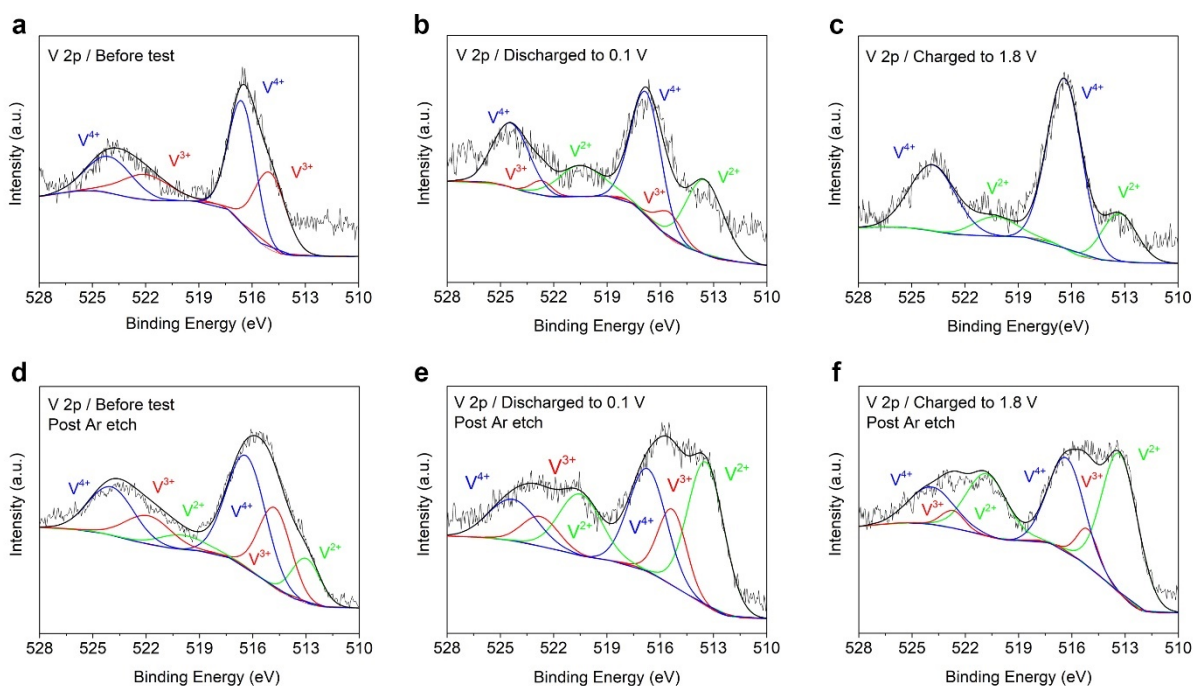
Figure 7.15. The same high-resolution V 2p XPS spectra region of V_2CT_x electrodes shown in Figure 7.13 before removal of the XPS Shirley background, and their corresponding deconvolutions. a) original electrode before test. b) discharged to 0.1 V vs. Al/Al^{3+}. c) charged to 1.8 V vs. Al/Al^{3+}, showing the change in the oxidation state of vanadium at each charge/discharge state. d, e, and f) XPS spectra of V2p region for original, discharged, and charged electrodes after Argon etching for 10 min, respectively. Adapted and reproduced with permission from ref. 19 (Copyright © 2017 American Chemical Society).

175

Diffusion of ions into the structure is usually the rate-limiting step for the intercalation of ions in the host materials. The ionic diffusion coefficient (D), diffusion length (l), and diffusion time (τ) are related according to $\tau = l^2/D$. Since D is constant for materials with the same structural parameters, τ is proportional with l^2 and decreasing the particle size of the host material can decrease intercalation time and increase the rate capability of the battery.[204,205] The role of particle size on the performance of the electrode is even more pronounced in the case of multivalent-ion batteries due to the generally slower diffusion of multivalent ions in the structure of the host materials.[108] The ML-V_2CT_x MXenes studied here have a particle size of about 10-15 microns, which is very large for battery electrode materials. This large particle size may result in a large energy barrier for the diffusion of Al^{3+} ions and reduce the capacity of the electrodes, particularly at high (dis)charge rates. Previous studies on the electrochemical performance of MXenes have shown the improvement of rate capability by delamination of multilayered MXenes into single or few-layer sheets.[16,42,43,206] Therefore, as the next step of the project I explored improving the electrochemical performance of the V_2CT_x MXene cathodes by their delamination.

Naguib et al. have reported that the spontaneous intercalation of MXenes (including V_2CT_x) by large organic bases such as tetrabutylammonium hydroxide (TBAOH), choline hydroxide, or n-butylamine results in a large increase in their interlayer spacing. [45] The interlayer expanded MXenes can be delaminated by dispersion in water followed by rigorous handshaking. However, they also found that delaminated V_2CT_x has a strong susceptibility to oxidation when dispersed in water. [45] To avoid oxidation of MXene during processing and to facilitate the electrode fabrication process, we tried to delaminate MXene in 1-Methyl-2-pyrrolidinone (NMP) instead of water.

In our first attempt, we simply dispersed ML-V_2CT_x MXenes in NMP by high speed stirring at moderate temperatures. Interestingly, after 24 hours of stirring a dispersion of delaminated V_2CTx sheets was formed. Examining the delaminated sheets with atomic force microscopy (AFM) and SEM showed that the delaminated V_2CTx sheets may have a large distribution in their size and number of layers (ranging from 4-5 layers and few hundred nanometer lateral dimensions to tens of individual layers and a few micron lateral dimensions) and single-layer sheets were not observed (**Figures 7.16**). Thus, the delaminated MXenes were labeled as few-layer (FL) V_2CTx.
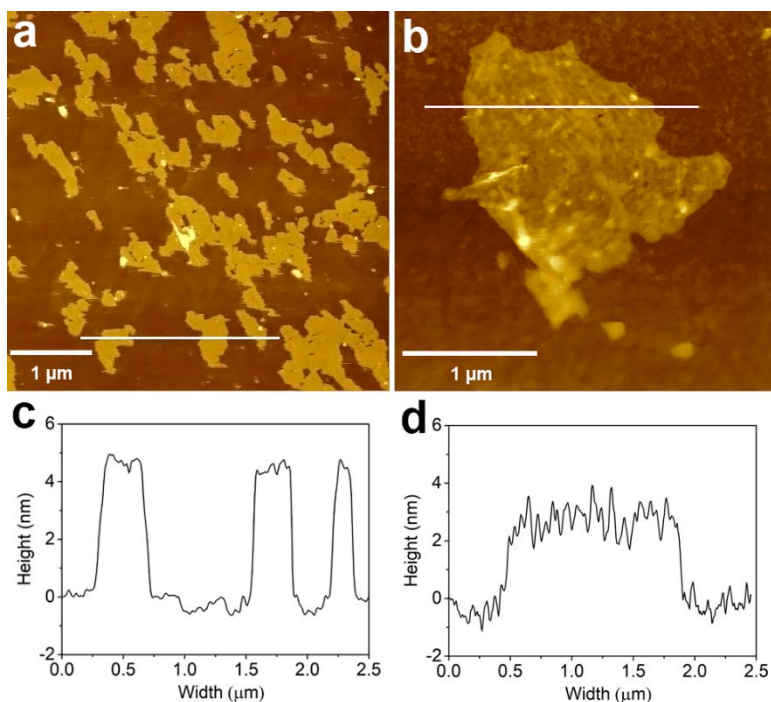
Figure 7.16. Atomic force microscopy (AFM) images of a) TBAOH-FL-V_2CT_x (delaminated in NMP) and b) TBAOH-V_2CT_x delaminated in water. c) Height profile of the trace line in "a". d) Height profile of the trace line in "b". The V_2CT_x flakes that were first intercalated with TBAOH and then delaminated in NMP are generally bi- or a few layers thick, while direct delamination of V_2CT_x right after TBAOH treatment in water results in single and bi-layer flakes. Adapted with permission from ref. 19 (Copyright © 2017 American Chemical Society).

Next, the dispersion of FL-V$_2$CT$_x$ in NMP was directly used for the electrode fabrication process by adding conductive additives and binder.

As shown in **Figure 7.17 a**, FL-V$_2$CT$_x$ cathode showed a large irreversible initial discharge capacity of 482 mAh g^{-1} and a first cycle discharge capacity of about 162 mAh g^{-1} at a high current density of 100 mA g^{-1} with a Coulombic efficiency of ~88 % (note that ML-V$_2$CT$_x$ showed a discharge capacity of about 90 mAhg^{-1} at the same current density). Similar to the ML-V$_2$CT$_x$ cathodes, however, the specific capacity of FL-V$_2$CT$_x$ cathodes declined in the next few cycles, but at a comparatively slower rate. The measured capacity of the electrode after 100 cycles was about 90 mAhg^{-1} (**Figure 7.17 b**).

The voltage profiles of a FL-V$_2$CT$_x$ electrode (dis)charged at different current densities (**Figure 7.18 a**), indicated the high-rate capability of the electrodes. For example, a specific capacity of ~50 mAh g^{-1} was measured at a very high rate of 5000 mA g^{-1}.

In addition, my experiments (**Figure 7.18 b**) showed that the FL-V$_2$CT$_x$ cathodes can be charged at considerably high rates (1000 mA g^{-1}) and discharged at slower rates (100 mA g^{-1}), and still deliver an appreciable discharge capacity of 76 mAh g^{-1} after 100 cycles with a Coulombic efficiency of ~96.6 %. This behavior has only been reported for graphite and graphene based Al-batteries thus far.[181,186]
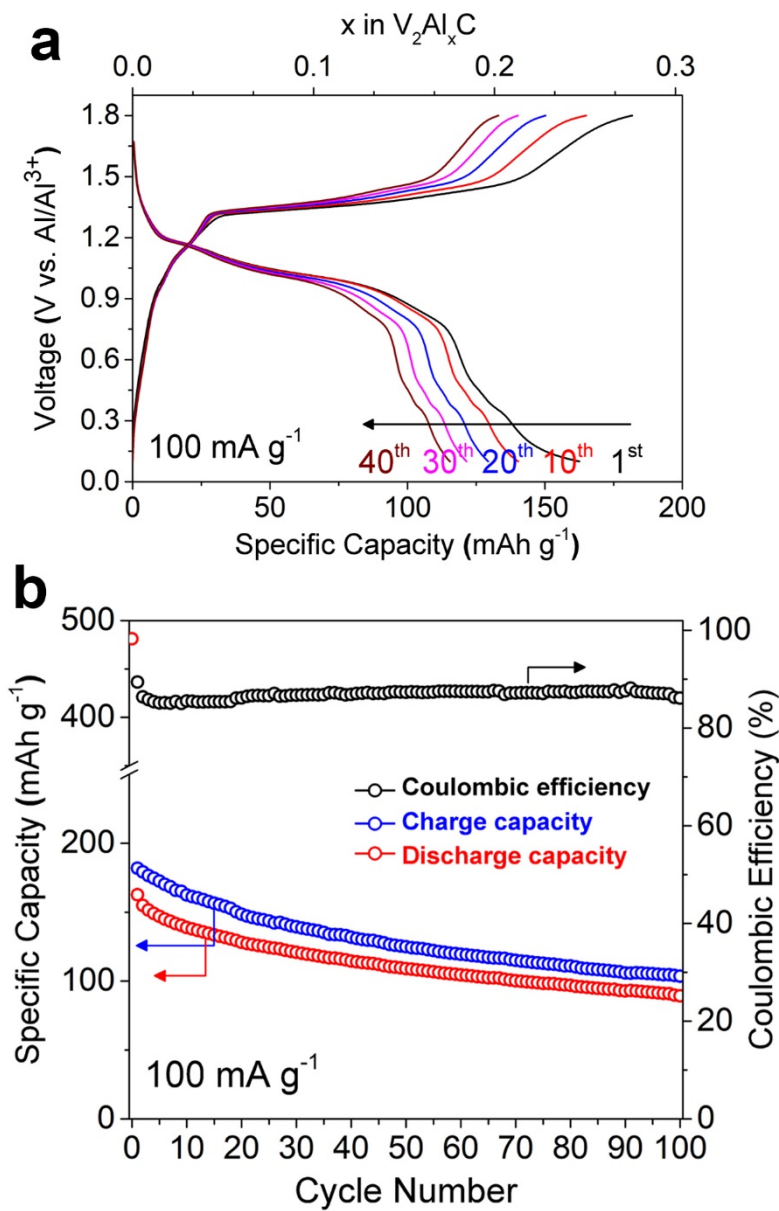
Figure 7.17. a) Charge-discharge profiles of FL-V$_2$CT$_x$ electrodes. b) Cyclic performance of FL-V$_2$CT$_x$ cathode over 100 cycles at a current density of 100 mA g^{-1}. Adapted and reproduced with permission from ref. 19 (Copyright © 2017 American Chemical Society).
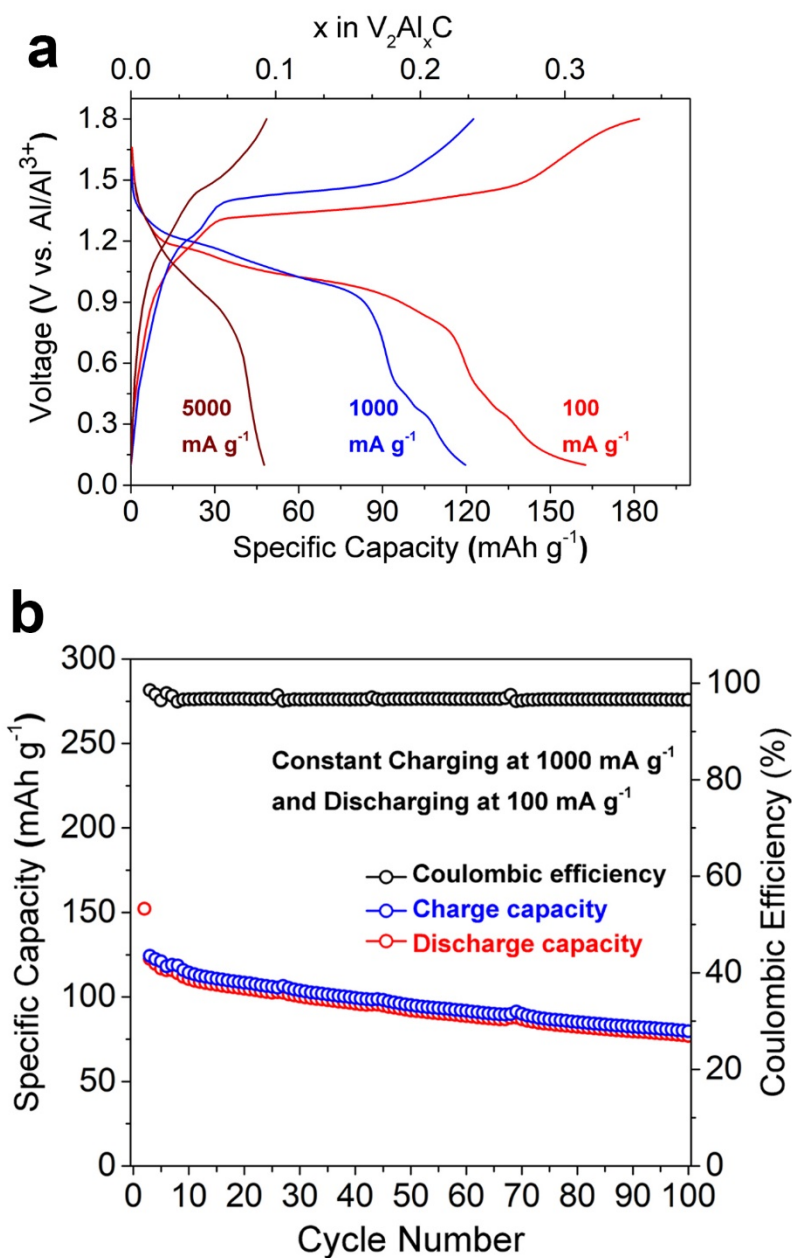
Figure 7.18. Electrochemical performance of FL-V_2CT_x cathode. a) Charge-discharge profiles of the FL-V_2CT_x at different current densities, showing specific capacities as high as 50 mAh g^{-1} at very high rate of 5000 mA g^{-1}. b) Cyclic performance of the FL-V_2CT_x charged at 1000 mA g^{-1} and discharged at 100 mA g^{-1}, demonstrating fast-charging capabilities of FL-V_2CT_x electrodes. Adapted and reproduced with permission from ref. 19 (Copyright © 2017 American Chemical Society).

To further investigate the effects of V_2CT_x delamination on the electrode performance, we attempted to improve the delamination process by combing the method reported by Naguib et al.[45] (also explained in details in chapter 3, as well as chapter 5 for preparation of delaminated V_2CT_x MXene) with the process explained above for preparation of FL-V_2CT_x samples. First, TBAOH was intercalated between the MXene layers to increase the interlayer spacing of ML-V_2CT_x (**Figure 7.19 a** shows a schematic representation of TBAOH intercalation and interlayer expansion of ML-V_2CT_x).

Figure 7.19 b shows the XRD pattern of the original ML-V_2CT_x and V_2CT_x treated with TBAOH for 4h. The peak corresponding to (0002) plane of MXenes showed a large downshift after TBAOH treatment, corresponding to a 11.46 Å increase in the c-LP. In addition, a new peak corresponding to (0004) plane of V_2CT_x appeared, which is in good agreement with the XRD results reported by Naguib et al.[45]

After TBAOH intercalation, the interlayer expanded ML-V_2CT_x powder was dried and subsequently delaminated in NMP by high speed stirring at 60 °C. This time a uniform dispersion of delaminated V_2CT_x with only a small amount of non-delaminated particles were achieved. However, AFM and SEM studies showed that even after TBAOH-assisted delamination the resulting sheets consist of several MXene layers.

We studied the electrochemical performance of delaminated MXenes (denoted as TBAOH-FL-V_2CT_x), by directly fabricating electrodes from their NMP dispersions and performing electrochemical tests. **Figure 7.20** shows the first five cycles of the cyclic voltammograms (CVs) of the TBAOH-FL-V_2CT_x electrode in the aluminum battery cell.
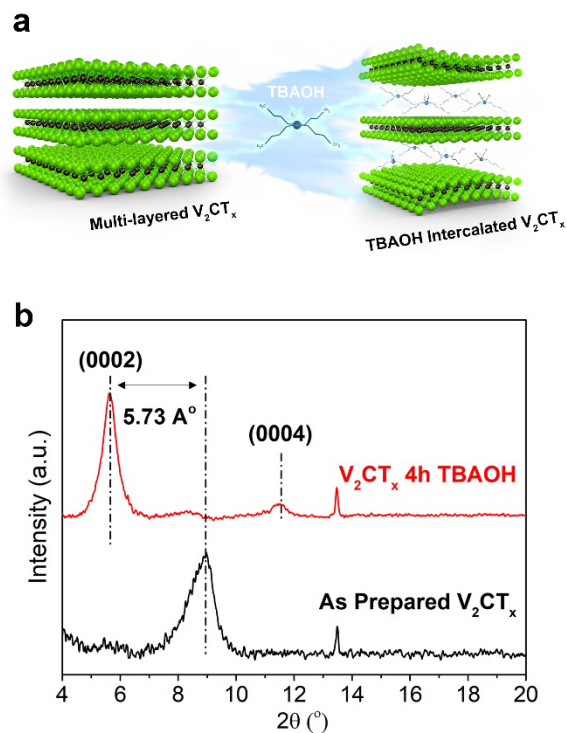
Figure 7.19. a) Schematic illustration of interlayer expansion of ML-V_2CT_x MXene through TBAOH intercalation. b) XRD patterns of ML-V_2CT_x and ML-V_2CT_x treated with a TBAOH solution for 4h at RT, showing an increase of about 5.73 Å in the interlayer spacing after TBAOH intercalation. Adapted and reproduced with permission from ref. 19 (Copyright © 2017 American Chemical Society).
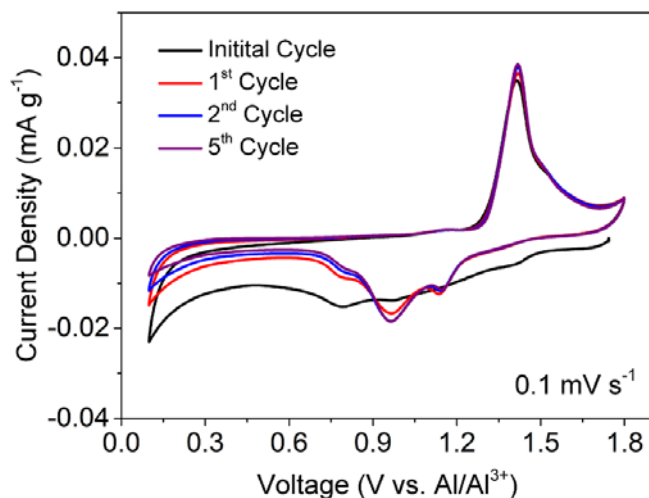
Figure 7.20. First five cycles of the cyclic voltammograms of TBAOH FL-V_2CT_x cathode at scan rate of 0.1 mV s^{-1}. Adapted with permission from ref. 19 (Copyright © 2017 American Chemical Society).

For a visual comparison, the microstructure of the three different electrodes (ML-V_2CT_x, FL-V_2CT_x, and TBAOH-FL-V_2CT_x) are shown in **Figure 7.21**. Also, their CVs are shown in **Figure 7.22**, which shows the difference between the intensity of their redox couples as well as their current-voltage profiles.
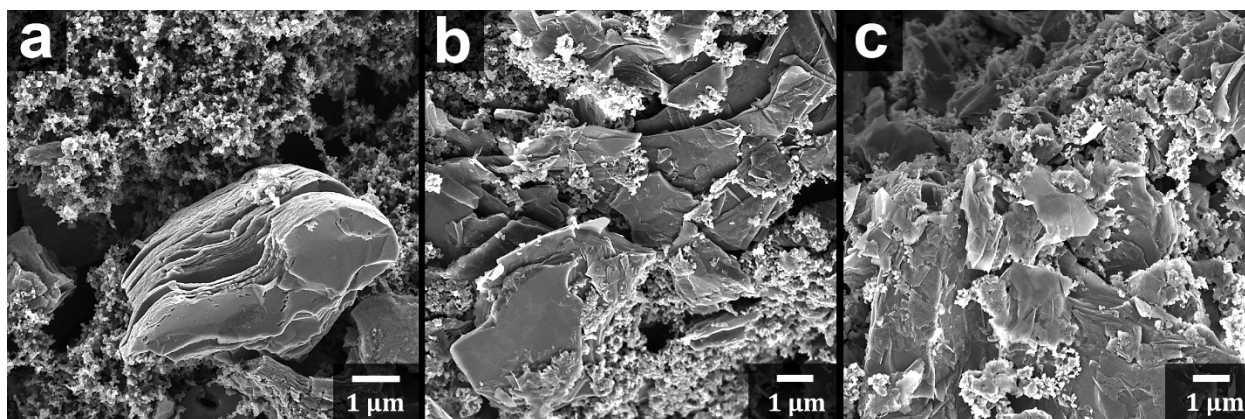
Figure 7.21. SEM images of different V_2CT_x MXene electrode structures. a) ML-V_2CT_x. b) FL-V_2CT_x. c) (interlayer expanded) TBAOH-FL-V_2CT_x. Adapted with permission from ref. 19 (Copyright © 2017 American Chemical Society).
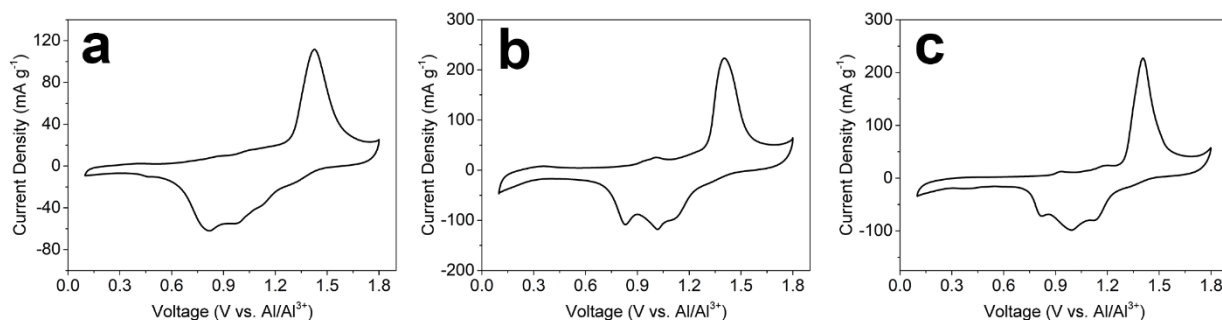
Figure 7.22. Cyclic voltammograms of (a) ML-V_2CT_x, (b) FL-V_2CT_x, and (c) TBAOH FL-V_2CT_x at scan rate of 0.1 mV s^{-1} after 50 Cycles. Adapted with permission from ref. 19 (Copyright © 2017 American Chemical Society).

As shown in **Figure 7.23 a**, after a very large initial discharge capacity of 922 mAh g^{-1}, the TBAOH-FL-V$_2$CT$_X$ electrodes showed an unprecedented specific capacity of ~392 mAh g^{-1} at a current density of 100 mA g^{-1} for their first cycle. However, the first cycle shows signs of electrolyte decomposition near the cutoff potentials. After the first cycle, the measured specific capacities for the following four cycles were about 300 mAhg^{-1}. To the best of our knowledge, this is the highest specific capacity reported for an intercalation type cathode material for Al-batteries.[107,182]

The cyclic performance tests performed at a high current density of 200 mA g^{-1} (**Figure 7.23 b**) showed that the electrodes still suffer from capacity loss during cycling at high charge/discharge rates. It is worth noting that the rate of the capacity loss for the studied V$_2$CT$_X$ MXenes is much lower than most of the previously reported Al-battery cathodes.[189–192,195] However, an in-depth understanding of the reasons for the observed capacity decay requires further investigation. Testing the electrodes at various current densities confirmed the excellent rate capability of the TBAOH-FL-V$_2$CT$_X$ cathodes, which maintained a capacity of about 150 mAh g^{-1} with a Coulombic efficiency of 95% at a high current density of 300 mA g^{-1} (**Figure 7.23 c**). As mentioned above, the lower Coulombic efficiency at lower (dis)charge rates is possibly due to the Al ion trapping in the electrodes or a slight decomposition of the electrolyte at the surface of the electrode at cut-off potentials. We attribute the improved performance of TBAOH-FL-V$_2$CT$_X$ compared to FL-V$_2$CT$_X$ to the higher delamination yield and possibly a more uniform delamination of the former. As shown in **Figure 7.22**, CV curves of the FL-V$_2$CT$_X$ showed bolder cathodic peaks (at around 1.1 V, 0.95 V, and 0.8 V) and corresponding anodic peaks (at 0.9, 1.1, and 1.4 V) compared to ML-V$_2$CT$_X$ or FL-V$_2$CT$_X$, suggesting the facilitated access of Al^{3+} cations to the intercalation sites between MXene layers.
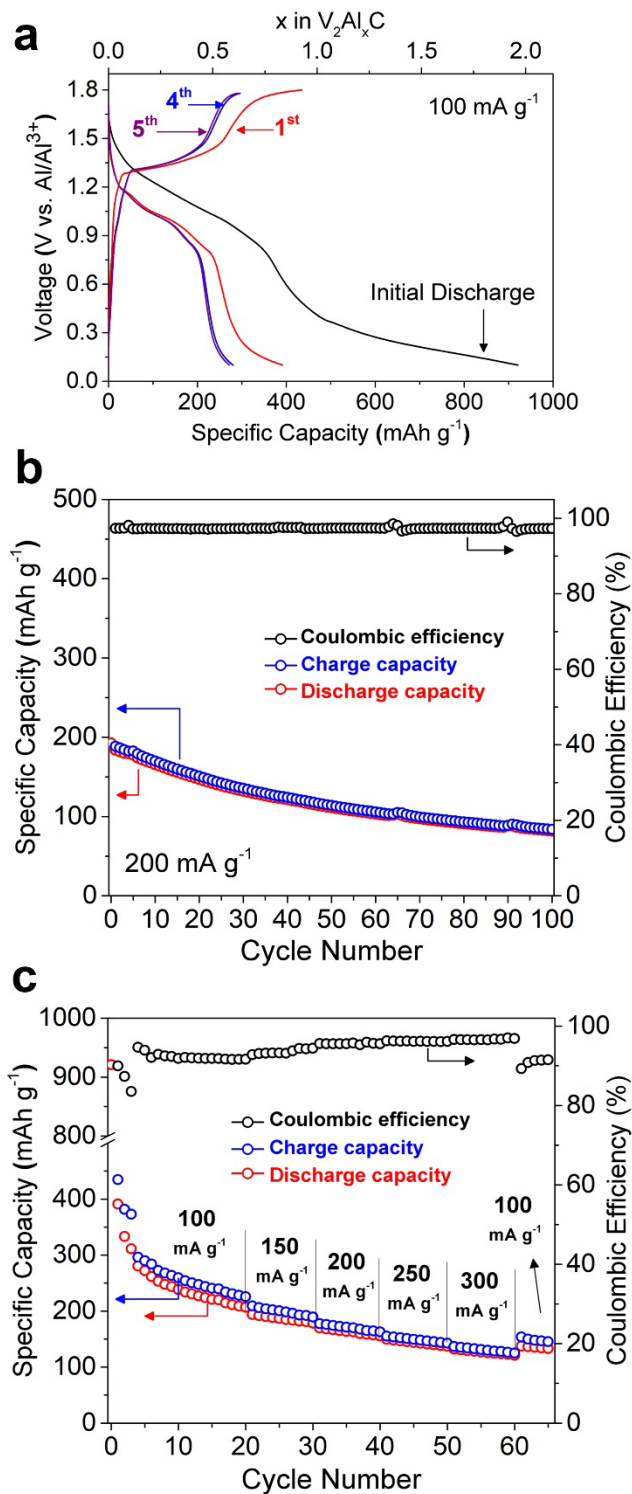
Figure 7.23. a) Charge-discharge curves of TBAOH-FL-V$_2$CT$_x$ for the first 5 cycles. b) Cyclic performance of TBAOH-FL-V$_2$CT$_x$ cathode over 100 cycles at a current density of 200 mA g^{-1}. c) Rate-capability of a TBAOH-FL-V$_2$CT$_x$ cathode. Adapted and reproduced with permission from ref. 19 (Copyright © 2017 American Chemical Society).

Figure 7.24 compares the charge-discharge (voltage vs. time) profiles of the ML-V_2CT_x and TBAOH-FL-V_2CT_x electrodes. As it can be seen in this figure, and in a good agreement with CV profiles shown in **Figure 7.22**, the TBAOH-FL-V_2CT_x electrode shows more distinct and sharper plateaus compared to the ML-V_2CT_x.

Again, here I would like to emphasize that the porous carbon substrate that different V_2CT_x electrodes were cast on it, is electrochemically inactive n the potential window (0.1 V t0 1.8 V vs. Al/Al^{3+}) that the MXene electrodes were tested. This is shown in **Figure 7.25**.
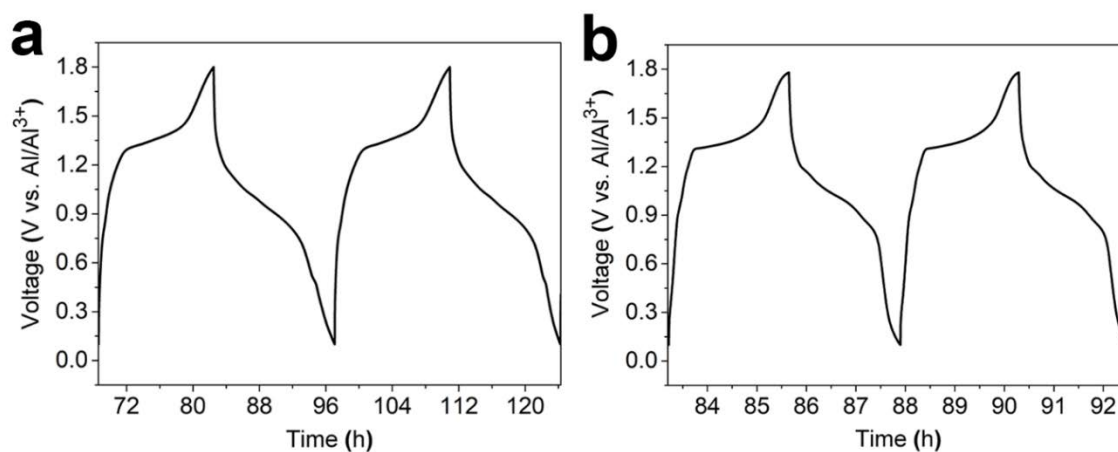
Figure 7.24. Voltage-time profile of a) ML-V_2CT_x cathode at current density of 10 mA g^{-1} and b) TBAOH FL-V_2CT_x cathode at current density of 100 mA g^{-1}. Adapted with permission from ref. 19 (Copyright © 2017 American Chemical Society).
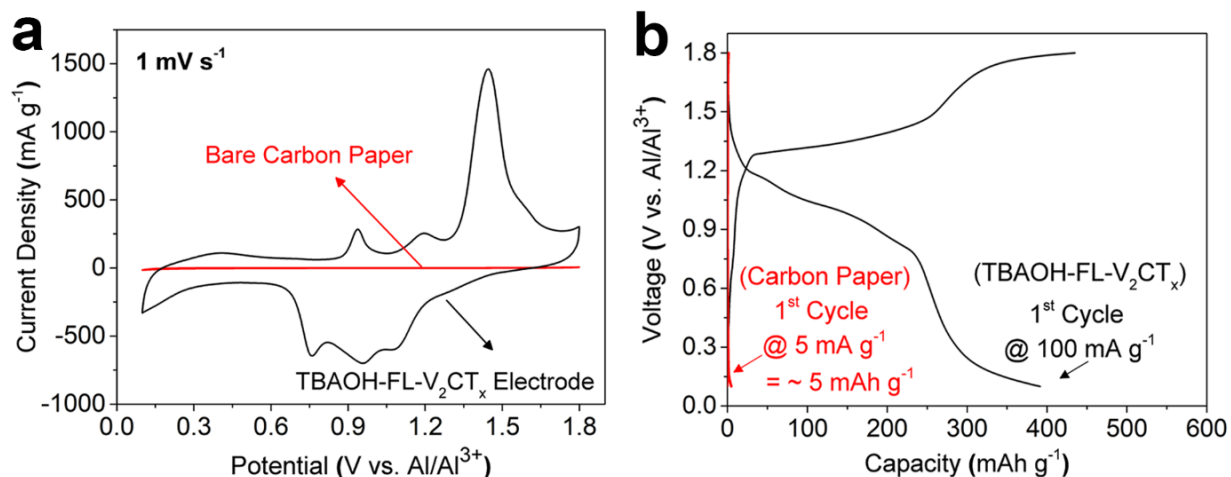
**Figure 7.25.** CVs of bare carbon paper used as cathode substrate and V_2CT_x casted on carbon paper, showing the inactivity of the carbon paper in the tested voltage window (shown in a). b) Charge-discharge curves in the first cycle for bare carbon paper used as the substrate at 5 mA g^{-1} and TBAOH FL-V_2CT_x at 100 mA g^{-1}. Adapted with permission from ref. 19 (Copyright © 2017 American Chemical Society).

The interlayer expanded V_2CT_x electrodes were also capable of fast charging and slow discharging while delivering high capacities. This is shown in Figure **7.26**, were at a constant charging rate of 1000 A g^{-1}, different discharge rates resulted in different discharge times.
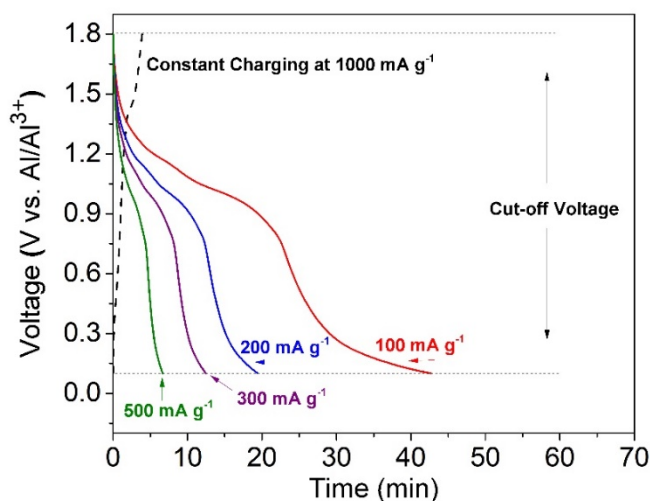
Figure 7.26. Constant charging of the TBAOH FL-V_2CT_x electrode at 1000 mA g^{-1} and discharging at various current densities, demonstrating fast charging and slow discharging capabilities of the 2D vanadium carbide cathode. Adapted with permission from ref. 19 (Copyright © 2017 American Chemical Society).

187

It should be possible to further improve the performance of the V_2CT_x electrodes by optimizing the delamination process and controlling the lateral size and number of layers of V_2CT_x MXenes. In fact, the combination of high specific capacity and relatively high discharge potential of V_2CT_x renders these materials as one the best reported cathode materials for rechargeable Al-batteries. **Figure 7.27** compares the average discharge potentials (insertion potentials) and the reported specific capacities of various aluminum battery cathodes tested in literature. Ideally, the materials that place on the top right of this graph (higher discharge potential and higher capacities) are favorable for practical battery applications. As it can be seen the performance of 2D V_2CT_x MXene is equal or surpasses most of the previously reported cathode materials for rechargeable aluminum batteries.
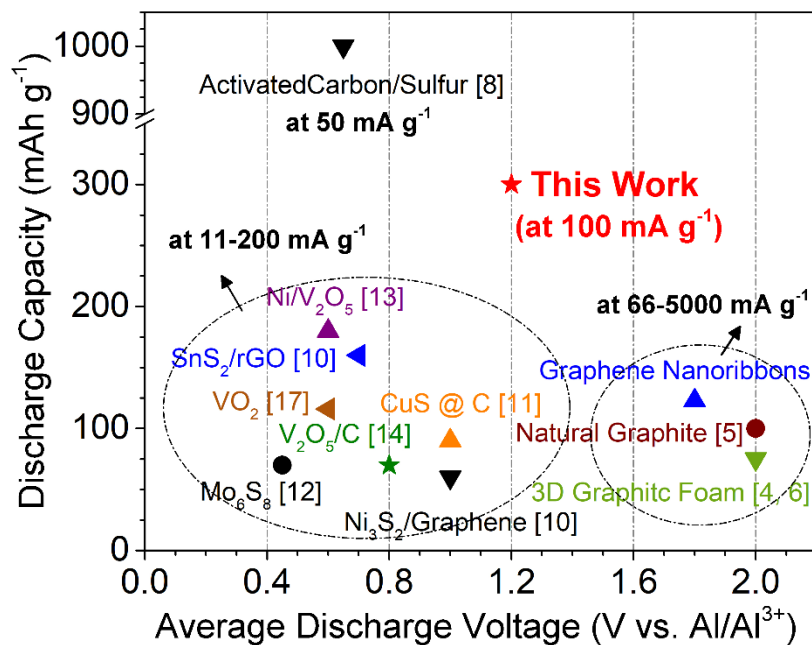
Figure 7.27. Comparison of the performance of V_2CT_x MXene cathodes with some of the notable previously reported cathode materials for rechargeable Al-batteries. The specific capacity is calculated based on the weight of the active material in the $TBAOH-FL-V_2CT_x$ cathodes. Adapted with permission from ref. 19 (Copyright © 2017 American Chemical Society).

7.4. Conclusions

The results of this chapter provide important fundamental understandings for applications of MXenes in batteries with multivalent-ion chemistry, i.e. as shown here rechargeable aluminum batteries. V_2CT_x MXene was investigated as a high capacity intercalation-type cathode material for rechargeable Al-batteries. Based on the presented results we suggest that that Al^{3+} cations are the only intercalating species between the layers of MXene, however, further *in situ* studies are required to completely understand the intercalation mechanism. Also, the intercalation of Al^{3+} cations did not have much effect on the structure of ML-V_2CT_x materials and only a very small increase in the interlayer spacing of MXene was observed after ion intercalation. As expected, it was demonestrated that the electrochemical performance of the MXenes can be improved by delamination of ML-V_2CT_x to few-layer sheets. Further improvement of the specific capacity was achieved for MXenes delaminated after pre-intercalation with TBAOH. This delamination method resulted in a higher delamination yield and the TBAOH-FL-V_2CT_x cathodes delivered exceptionally high specific capacities of more than 300 mAh g^{-1} at a high (dis)charging current density of 100 mA g^{-1}. The specific capacity, intercalation potential, and cycle lifetime efficiency of V_2CT_x MXenes is among the best performances reported so far for intercalation-type Al-battery cathodes.

Chapter 8

Future Work

Since 2011, 2D MXenes have presented some unique properties and exceptional performances in variety of applications, particularly as electrode materials in different energy storage systems. In fact, the discovery of MXenes have led to numerous significant research projects in the field of energy storage materials world-wide. As discussed in the beginning of my dissertation, MXenes are an emerging family of 2D materials that until today comprise of around 30 different compositions that are experimentally made and many more theoretically predicted. Versatility of MXenes, by itself, distinguishes them from other 2D materials such as graphene, phosphorene, silicene, and even TMDCs, which all are only available in a handful number of compositions. Therefore, investigation of MXenes for different applications as well as understanding their fundamental properties can result in significant advances in the ongoing field of 2D materials. With that in mind and the general interest in applications of MXenes in energy storage systems, developing new electrode architectures and electrochemical systems based on MXenes, and providing an understanding about the behavior of these materials in energy applications can significantly contribute to first, development of MXenes, and second, development of high-performance energy storage systems. I hope the research results presented in my dissertation as well as my publications will eventually serve as a specific guideline for other researchers to expand the research on 2D MXenes in related research directions.

Based on my experience from working on 2D MXenes during the past 4 years, I propose the following directions as potential and important future research opportunities, relevant to my Ph.D. work, which can eventually advance small portion of the ongoing research on 2D MXenes.

- Understanding the basic differences in the selective etching process of MXenes with certain transition metals in their structure and providing effective solutions for controlling etching's selectivity toward "A" layer elements only.

- Preparation of delaminated form of new MXene compositions and scientific understanding about underlying reasons for the different approaches required for delamination of MXenes with different compositions.

- Fabrication of vertical 2D heterostructures based on 2D MXenes and understanding the chemistry at the prepared 2D heterointerfaces.

- Preparation of stable electrode architectures based on 2D MXenes for pseudocapacitive charge storage.

- Direct assessment of charge storage mechanism for MXene cathodes in rechargeable multivalent-ion batteries such as the MXene-based aluminum batteries presented in this dissertation.

References

1. Naguib, M. & Gogotsi, Y. Synthesis of two-dimensional materials by selective extraction. *Acc. Chem. Res.* **48**, 128–135 (2015).

2. Xiao, X., Wang, H., Urbankowski, P. & Gogotsi, Y. Topochemical synthesis of 2D materials. *Chem. Soc. Rev.* **47**, 8744–8765 (2018).

3. Novoselov, K. S. *et al.* Two-dimensional atomic crystals. *Proc. Natl. Acad. Sci.* **102**, 10451–10453 (2005).

4. KS, N. *et al.* Electric Field Effect in Atomically Thin Carbon Films. *Science (80-.).* **306**, 666–669 (2004).

5. Geim, A. K. & Novoselov, K. S. The rise of graphene. *Nat. Mater.* **6**, 183–191 (2007).

6. Mas-Ballesté, R., Gómez-Navarro, C., Gómez-Herrero, J. & Zamora, F. 2D materials: To graphene and beyond. *Nanoscale* **3**, 20–30 (2011).

7. Naguib, M., Mochalin, V. N., Barsoum, M. W. & Gogotsi, Y. 25th anniversary article: MXenes: A new family of two-dimensional materials. *Adv. Mater.* **26**, 992–1005 (2014).

8. Coleman, J. N. *et al.* Two-dimensional nanosheets produced by liquid exfoliation of layered materials. *Science (80-.).* **331**, 568–571 (2011).

9. Naguib, M. *et al.* Two-dimensional transition metal carbides. *ACS Nano* **6**, 1322–1331 (2012).

10. Naguib, M. *et al.* Two-dimensional nanocrystals produced by exfoliation of Ti 3AlC 2. *Adv. Mater.* **23**, 4248–4253 (2011).

11. Nicolosi, V., Chhowalla, M., Kanatzidis, M. G., Strano, M. S. & Coleman, J. N. Liquid exfoliation of layered materials. *Science (80-.).* **340**, 1226419 (2013).

12. Barsoum, M. W. The M ,, AXN Phases : A New Class of Solids. *Prog. Solid State Chem.* **28**, 201–281 (2000).

13. Anasori, B., Lukatskaya, M. R. & Gogotsi, Y. 2D metal carbides and nitrides (MXenes) for energy storage. *Nat. Rev. Mater.* **2**, 16098 (2017).

14. Zhao, M.-Q. *et al.* Synthesis of Carbon/Sulfur Nanolaminates by Electrochemical Extraction of Titanium from Ti $_2$ SC. *Angew. Chemie Int. Ed.* **54**, 4810–4814 (2015).

15. Lukatskaya, M. R. *et al.* Cation intercalation and high volumetric capacitance of two-dimensional titanium carbide. *Science (80-.).* **341**, 1502–1505 (2013).

16. Naguib, M. *et al.* New two-dimensional niobium and vanadium carbides as promising materials for li-ion batteries. *J. Am. Chem. Soc.* **135**, 15966–15969 (2013).

17. Lukatskaya, M. R. *et al.* Ultra-high-rate pseudocapacitive energy storage in two-dimensional transition metal carbides. *Nat. Energy* **6**, 1–6 (2017).

18. Wang, X. *et al.* Pseudocapacitance of MXene nanosheets for high-power sodium-ion hybrid capacitors. *Nat. Commun.* **6**, 6544 (2015).

19. Vahidmohammadi, A., Hadjikhani, A., Shahbazmohamadi, S. & Beidaghi, M. Two-Dimensional Vanadium Carbide (MXene) as a High-Capacity Cathode Material for Rechargeable Aluminum Batteries. *ACS Nano* **11**, 11135–11144 (2017).

20. Xie, X. *et al.* Porous heterostructured MXene/carbon nanotube composite paper with high volumetric capacity for sodium-based energy storage devices. *Nano Energy* **26**, 513–523 (2016).

21. Ahmed, B., Anjum, D. H., Gogotsi, Y. & Alshareef, H. N. Atomic layer deposition of

SnO2on MXene for Li-ion battery anodes. *Nano Energy* **34**, 249–256 (2017).

22. Peng, Y.-Y. *et al.* All-MXene (2D titanium carbide) Solid-State Microsupercapacitors for On-Chip Energy Storage. *Energy Environ. Sci.* (2016). doi:10.1039/C6EE01717G

23. Eames, C. & Islam, M. S. Ion Intercalation into Two-Dimensional Transition-Metal Carbides: Global Screening for New High-Capacity Battery Materials. *J. Am. Chem. Soc.* (2014). doi:10.1021/ja508154e

24. Shahzad, F. *et al.* Electromagnetic interference shielding with 2D transition metal carbides (MXenes). *Science (80-.).* **353**, 1137–1140 (2016).

25. Weng, G. M. *et al.* Layer-by-Layer Assembly of Cross-Functional Semi-transparent MXene-Carbon Nanotubes Composite Films for Next-Generation Electromagnetic Interference Shielding. *Adv. Funct. Mater.* **1803360**, 1–9 (2018).

26. Liu, G. *et al.* Ultrathin two-dimensional MXene membrane for pervaporation desalination. *J. Memb. Sci.* **548**, 548–558 (2018).

27. Srimuk, P. *et al.* MXene as a novel intercalation-type pseudocapacitive cathode and anode for capacitive deionization. *J. Mater. Chem. A* (2016). doi:10.1039/C6TA07833H

28. Lee, E. *et al.* Room Temperature Gas Sensing of Two-Dimensional Titanium Carbide (MXene). *ACS Appl. Mater. Interfaces* **9**, 37184–37190 (2017).

29. Kim, S. J. *et al.* Metallic $Ti_3C_2T_x$ MXene Gas Sensors with Ultrahigh Signal-to-Noise Ratio. *ACS Nano* **12**, acsnano.7b07460 (2018).

30. Sarycheva, A. *et al.* 2D titanium carbide (MXene) for wireless communication. *Sci. Adv.* **4**, eaau0920 (2018).

31. Boota, M. *et al.* Pseudocapacitive Electrodes Produced by Oxidant-Free Polymerization of Pyrrole between the Layers of 2D Titanium Carbide (MXene). *Adv. Mater.* **28**, 1517–1522

(2016).

32.   VahidMohammadi, A. *et al.* Thick and Freestanding MXene/PANI Pseudocapacitive Electrodes with Ultrahigh Specific Capacitance. *J. Mater. Chem. A* 22123–22133 (2018). doi:10.1039/C8TA05807E

33.   Ding, L. *et al.* MXene molecular sieving membranes for highly efficient gas separation. *Nat. Commun.* **9**, 155 (2018).

34.   Zhou, L., Meng, F., Anasori, B., Gogotsi, Y. & El-Deiry, W. S. Abstract 3210: Photothermal therapy of malignant mesothelioma with delaminated MXene Ti<sub>3</sub>C<sub>2</sub> *Cancer Res.* **78**, 3210 LP – 3210 (2018).

35.   Han, X. *et al.* 2D Ultrathin MXene-Based Drug-Delivery Nanoplatform for Synergistic Photothermal Ablation and Chemotherapy of Cancer. *Adv. Healthc. Mater.* **7**, 1701394 (2018).

36.   Liu, Z. *et al.* 2D superparamagnetic tantalum carbide composite MXenes for efficient breast-cancer theranostics. *Theranostics* **8**, 1648–1664 (2018).

37.   Lin, H., Wang, X., Yu, L., Chen, Y. & Shi, J. Two-Dimensional Ultrathin MXene Ceramic Nanosheets for Photothermal Conversion. *Nano Lett.* acs.nanolett.6b04339 (2016). doi:10.1021/acs.nanolett.6b04339

38.   Meng, F. *et al.* MXene Sorbents for Removal of Urea from Dialysate: A Step toward the Wearable Artificial Kidney. *ACS Nano* acsnano.8b06494 (2018). doi:10.1021/acsnano.8b06494

39.   Anasori, B. *et al.* Two-Dimensional, Ordered, Double Transition Metals Carbides (MXenes). *ACS Nano* **9**, 9507–9516 (2015).

40. Voigt, C. A., Ghidiu, M., Natu, V. & Barsoum, M. W. Anion Adsorption, Ti3C2T z MXene Multilayers, and Their Effect on Claylike Swelling. *J. Phys. Chem. C* **122**, 23172–23179 (2018).

41. Ghidiu, M., Lukatskaya, M. R., Zhao, M. Q., Gogotsi, Y. & Barsoum, M. W. Conductive two-dimensional titanium carbide 'clay' with high volumetric capacitance. *Nature* **516**, 78–81 (2015).

42. Byeon, A. *et al.* Two-Dimensional Titanium Carbide MXene As a Cathode Material for Hybrid Magnesium/Lithium-Ion Batteries. *ACS Appl. Mater. Interfaces* acsami.6b04198 (2016). doi:10.1021/acsami.6b04198

43. Mashtalir, O. *et al.* Intercalation and delamination of layered carbides and carbonitrides. *Nat. Commun.* **4**, 1716 (2013).

44. Lipatov, A. *et al.* Effect of Synthesis on Quality, Electronic Properties and Environmental Stability of Individual Monolayer Ti3C2 MXene Flakes. *Adv. Electron. Mater.* **2**, 1600255 (2016).

45. Naguib, M., Unocic, R. R., Armstrong, B. L. & Nanda, J. Large-scale delamination of multi-layers transition metal carbides and carbonitrides "MXenes". *Dalt. Trans.* **44**, 9353–9358 (2015).

46. Seh, Z. W. *et al.* Two-Dimensional Molybdenum Carbide (MXene) as an Efficient Electrocatalyst for Hydrogen Evolution. *ACS Energy Lett.* **1**, 589–594 (2016).

47. Yang, Y., Umrao, S., Lai, S. & Lee, S. Large-Area Highly Conductive Transparent Two-Dimensional Ti $_2$ CT $_x$ Film. *J. Phys. Chem. Lett.* **8**, 859–865 (2017).

48. Byeon, A. *et al.* Lithium-ion capacitors with 2D Nb2CTx (MXene) – carbon nanotube electrodes. *J. Power Sources* 1–9 (2016). doi:10.1016/j.jpowsour.2016.03.066

49.   Bao, W. *et al.* Porous Cryo-Dried MXene for Efficient Capacitive Deionization. *Joule* **2**, 778–787 (2018).

50.   Lee, J., Kim, S., Kim, C. & Yoon, J. Hybrid capacitive deionization to enhance the desalination performance of capacitive techniques. *Energy Environ. Sci.* **7**, 3683–3689 (2014).

51.   Zhao, J. *et al.* Hydrophobic Surface Enabled Salt-blocking 2D Ti3C2 MXene Membrane for Efficient and Stable Solar Desalination. *J. Mater. Chem. A* (2018). doi:10.1039/C8TA05569F

52.   Mojtabavi, M., Vahidmohammadi, A., Liang, W., Beidaghi, M. & Wanunu, M. Single-Molecule Sensing Using Nanopores in Two-Dimensional Transition Metal Carbide (MXene) Membranes. *ACS Nano* **13**, 3042–3053 (2019).

53.   Tarascon, J. M. & Armand, M. Issues and challenges facing rechargeable lithium batteries. *Nature* **414**, 359–67 (2001).

54.   Mendoza-Sánchez, B. & Gogotsi, Y. Synthesis of Two-Dimensional Materials for Capacitive Energy Storage. *Adv. Mater.* 6104–6135 (2016). doi:10.1002/adma.201506133

55.   Xia, Y. *et al.* Thickness-independent capacitance of vertically aligned liquid-crystalline MXenes. *Nature* **557**, 409–412 (2018).

56.   VahidMohammadi, A., Mojtabavi, M., Caffrey, N. M., Wanunu, M. & Beidaghi, M. Assembling 2D MXenes into Highly Stable Pseudocapacitive Electrodes with High Power and Energy Densities. *Adv. Mater.* **31**, 1806931 (2019).

57.   Zhan, C. *et al.* Computational Screening of MXene Electrodes for Pseudocapacitive Energy Storage. *J. Phys. Chem. C* acs.jpcc.8b11608 (2018). doi:10.1021/acs.jpcc.8b11608

58.   Pomerantseva, E. & Gogotsi, Y. Two-dimensional heterostructures for energy storage. *Nat.*

Energy **2**, 17089 (2017).

59. Xie, Y. *et al.* Prediction and characterization of MXene nanosheet anodes for non-lithium-ion batteries. *ACS Nano* **8**, 9606–15 (2014).

60. Shan, Q. *et al.* Two-dimensional vanadium carbide (V2C) MXene as electrode for supercapacitors with aqueous electrolytes. *Electrochem. commun.* **96**, 103–107 (2018).

61. Lukatskaya, M. R. *et al.* Probing the Mechanism of High Capacitance in 2D Titanium Carbide Using in Situ X-Ray Absorption Spectroscopy. *Adv. Energy Mater.* **5**, 1500589 (2015).

62. Levi, M. D. *et al.* Solving the Capacitive Paradox of 2D MXene using Electrochemical Quartz-Crystal Admittance and In Situ Electronic Conductance Measurements. *Adv. Energy Mater.* **5**, 1400815 (2015).

63. Augustyn, V. *et al.* High-rate electrochemical energy storage through Li+ intercalation pseudocapacitance. *Nat. Mater.* **12**, 518–22 (2013).

64. Augustyn, V., Simon, P. & Dunn, B. Pseudocapacitive oxide materials for high-rate electrochemical energy storage. *Energy Environ. Sci.* **7**, 1597–1614 (2014).

65. Simon, P. & Gogotsi, Y. Materials for electrochemical capacitors. *Nat. Mater.* **7**, 845–854 (2008).

66. Lukatskaya, M. R., Dunn, B. & Gogotsi, Y. Multidimensional materials and device architectures for future hybrid energy storage. *Nat. Commun.* **7**, 1–13 (2016).

67. Choi, D., Blomgren, G. E. & Kumta, P. N. Fast and reversible surface redox reaction in nanocrystalline vanadium nitride supercapacitors. *Adv. Mater.* **18**, 1178–1182 (2006).

68. Zheng, J. P., Cygan, P. J. J. & Jow, T. R. R. Hydrous ruthenium oxide as an electrode material for electrochemical capacitors. *J. Electrochem. Soc.* **142**, 2699–2703 (1995).

69. Geng, P. *et al.* Transition Metal Sulfides Based on Graphene for Electrochemical Energy Storage. *Adv. Energy Mater.* **8**, 1–26 (2018).

70. Gogotsi, Y. & Penner, R. M. Energy Storage in Nanomaterials – Capacitive, Pseudocapacitive, or Battery-like? *ACS Nano* **12**, 2081–2083 (2018).

71. Okubo, M., Sugahara, A., Kajiyama, S. & Yamada, A. MXene as a Charge Storage Host. *Acc. Chem. Res.* **51**, 591–599 (2018).

72. Chen, C. *et al.* Charge Transfer Induced Polymerization of EDOT Confined between 2D Titanium Carbide Layers. *J. Mater. Chem. A* **00**, 1–6 (2017).

73. Zhao, M. Q. *et al.* Flexible MXene/carbon nanotube composite paper with high volumetric capacitance. *Adv. Mater.* **27**, 339–345 (2015).

74. Hu, P. *et al.* Topological-structure modulated polymer nanocomposites exhibiting highly enhanced dielectric strength and energy density. *Adv. Funct. Mater.* **24**, 3172–3178 (2014).

75. C. E. Ren, M.-Q. Zhao, T. Makaryan, J. Halim, M. Boota, S. Kota, B. Anasori, M. W. Barsoum, Y. G. Porous Two-Dimensional Transition Metal Carbide (MXene) Flakes for High-Performance Li-Ion Storage,. *ChemElectroChem* **3**, 689–693 (2016).

76. Yan, J. *et al.* Flexible MXene/Graphene Films for Ultrafast Supercapacitors with Outstanding Volumetric Capacitance. *Adv. Funct. Mater.* **27**, 1701264 (2017).

77. Xu, S., Wei, G., Li, J., Han, W. & Gogotsi, Y. Flexible MXene-graphene electrodes with high volumetric capacitance for integrated co-cathode energy conversion/storage devices. *J. Mater. Chem. A* **5**, 17442–17451 (2017).

78. Kumar, N. A. *et al.* Polyaniline-Grafted Reduced Graphene Oxide for E ffi cient Electrochemical. *ACS Nano* **25**, 1715–1723 (2012).

79. Wang, D. W. *et al.* Fabrication of graphene/polyaniline composite paper via in situ anodic

electropolymerization for high-performance flexible electrode. *ACS Nano* **3**, 1745–1752 (2009).

80. Zhang, K., Zhang, L. L., Zhao, X. S. & Wu, J. Graphene/polyaniline nanofiber composites as supercapacitor electrodes. *Chem. Mater.* **22**, 1392–1401 (2010).

81. Novoselov, K. S., Mishchenko, A., Carvalho, A. & Castro Neto, A. H. 2D materials and van der Waals heterostructures. *Science (80-.).* **353**, aac9439–aac9439 (2016).

82. Geim, A. K. & Grigorieva, I. V. Van der Waals heterostructures. *Nature* **499**, 419–425 (2013).

83. Jariwala, D., Marks, T. J. & Hersam, M. C. Mixed-dimensional van der Waals heterostructures. *Nat. Mater.* **16**, 170–181 (2017).

84. Kang, K. *et al.* Layer-by-layer assembly of two-dimensional materials into wafer-scale heterostructures. *Nature* **550**, 229–233 (2017).

85. Xiong, P. *et al.* Two-Dimensional Unilamellar Cation-Deficient Metal Oxide Nanosheet Superlattices for High-Rate Sodium Ion Energy Storage. *ACS Nano* **12**, 12337–12346 (2018).

86. Frey, N. C. *et al.* Prediction of Synthesis of 2D Metal Carbides and Nitrides (MXenes) and Their Precursors with Positive and Unlabeled Machine Learning. *ACS Nano* acsnano.8b08014 (2019). doi:10.1021/acsnano.8b08014

87. Chen, C. *et al.* MoS2-on-MXene Heterostructures as Highly Reversible Anode Materials for Lithium-Ion Batteries. *Angew. Chemie - Int. Ed.* **57**, 1846–1850 (2018).

88. Zhao, M.-Q. *et al.* Scalable Manufacturing of Large and Flexible Sheets of MXene/Graphene Heterostructures. *Adv. Mater. Technol.* **1800639**, 1800639 (2019).

89. Dong, X. *et al.* Layer-by-layer self-assembled two-dimensional MXene/layered double

hydroxide composites as cathode for alkaline hybrid batteries. *J. Power Sources* **390**, 208–214 (2018).

90. Zhao, R. *et al.* Molecular-Level Heterostructures Assembled from Titanium Carbide MXene and Ni-Co-Al Layered Double-Hydroxide Nanosheets for All-Solid-State Flexible Asymmetric High-Energy Supercapacitors. *ACS Energy Lett.* **3**, 132–140 (2018).

91. Wang, X. *et al.* Heterostructures of Ni−Co−Al layered double hydroxide assembled on V$_4$C$_3$ MXene for high-energy hybrid supercapacitors. *J. Mater. Chem. A* 1–3 (2019). doi:10.1039/C8TA11249E

92. Jin, X. *et al.* Superior role of MXene nanosheet as hybridization matrix over graphene in enhancing interfacial electronic coupling and functionalities of metal oxide. *Nano Energy* **53**, 841–848 (2018).

93. Kim, S. J. *et al.* High mass loading, binder-free MXene anodes for high areal capacity Li-ion batteries. *Electrochim. Acta* **163**, 246–251 (2015).

94. Ahmed, B., Anjum, D. H., Gogotsi, Y. & Alshareef, H. N. Atomic Layer Deposition of SnO2 on MXene for Li-Ion Battery Anodes. *Nano Energy* (2017). doi:10.1016/j.nanoen.2017.02.043

95. Liu, Y. T. *et al.* Self-Assembly of Transition Metal Oxide Nanostructures on MXene Nanosheets for Fast and Stable Lithium Storage. *Adv. Mater.* **30**, 1–9 (2018).

96. Zhao, M. Q. *et al.* 2D titanium carbide and transition metal oxides hybrid electrodes for Li-ion storage. *Nano Energy* **30**, 603–613 (2016).

97. Xie, X. *et al.* Porous Ti$_3$C$_2$T$_x$ MXene for Ultrahigh-Rate Sodium-Ion Storage with Long Cycle Life. *ACS Appl. Nano Mater.* acsanm.8b00045 (2018). doi:10.1021/acsanm.8b00045

98. Wang, Y. *et al.* Three-dimensional porous MXene / layered double hydroxide composite

for high performance supercapacitors. *J. Power Sources* **327**, 221–228 (2016).

99.   Zhao, D. *et al.* Alkali-induced crumpling of Ti3C2Tx (MXene) to form 3D porous networks for sodium ion storage. *Chem. Commun.* **54**, 4533–4536 (2018).

100.   Luo, J. *et al.* Sn $^{4+}$ Ion Decorated Highly Conductive Ti $_3$ C $_2$ MXene: Promising Lithium-Ion Anodes with Enhanced Volumetric Capacity and Cyclic Performance. *ACS Nano* acsnano.5b07333 (2016). doi:10.1021/acsnano.5b07333

101.   Luo, J. *et al.* Pillared Structure Design of MXene with Ultra-Large Interlayer Spacing for High Performance Lithium-Ion Capacitors. *ACS Nano* acsnano.6b07668 (2016). doi:10.1021/acsnano.6b07668

102.   Zhao, M. Q. *et al.* Hollow MXene Spheres and 3D Macroporous MXene Frameworks for Na-Ion Storage. *Adv. Mater.* **29**, 1702410 (2017).

103.   Dall'Agnese, Y., Taberna, P.-L., Gogotsi, Y. & Simon, P. Two-Dimensional Vanadium Carbide (MXene) as Positive Electrode for Sodium-Ion Capacitors. *J. Phys. Chem. Lett.* 2305–2309 (2015). doi:10.1021/acs.jpclett.5b00868

104.   Tang, Q., Zhou, Z. & Shen, P. Are MXenes promising anode materials for Li ion batteries? Computational studies on electronic properties and Li storage capability of Ti3C2 and Ti3C2X2 (X = F, OH) monolayer. *J. Am. Chem. Soc.* **134**, 16909–16 (2012).

105.   Zhao, M.-Q. *et al.* Magnesium-Ion Storage Capability of MXenes. *ACS Appl. Energy Mater.* acsaem.8b02253 (2019). doi:10.1021/acsaem.8b02253

106.   Xu, M. *et al.* Opening Magnesium Storage Capability of Two-Dimensional MXene by Intercalation of Cationic Surfactant. *ACS Nano* **12**, 3733–3740 (2018).

107.   Elia, G. A. *et al.* An Overview and Future Perspectives of Aluminum Batteries. *Adv. Mater.* 1–16 (2016). doi:10.1002/adma.201601357

108. Canepa, P. *et al.* Odyssey of Multivalent Cathode Materials: Open Questions and Future Challenges. *Chem. Rev.* **117**, 4287–4341 (2017).

109. Huicong Yang, Hucheng Li, Juan Li, Zhenhua Sun, Kuang He, Hui-Ming Cheng, F. L. The Rechargeable Aluminum Battery: Opportunities and Challenges. *Angew. Chemi* (2019). doi:10.1016/j.dyepig.2010.03.014

110. Peng, L., Zhu, Y., Chen, D., Ruoff, R. S. & Yu, G. Two-Dimensional Materials for Beyond-Lithium-Ion Batteries. *Adv. Energy Mater.* **6**, 1–21 (2016).

111. Muldoon, J., Bucur, C. B. & Gregory, T. Quest for Nonaqueous Multvalent Secondary Batteries: Magnesium and Beyond. *Chem. Rev.* **114**, 11683–11720 (2014).

112. Guduru, R. & Icaza, J. A Brief Review on Multivalent Intercalation Batteries with Aqueous Electrolytes. *Nanomaterials* **6**, 41 (2016).

113. Xu, C. *et al.* Secondary batteries with multivalent ions for energy storage. *Sci. Rep.* **5**, 14120 (2015).

114. Zhang, Y., Liu, S., Zhang, Y. & Zhang, Y. Emerging Nonaqueous Aluminum-Ion Batteries: Challenges, Status, and Perspectives. *Adv. Mater.* **1706310**, (2018).

115. Liang, Y. *et al.* Interlayer-expanded molybdenum disulfide nanocomposites for electrochemical magnesium storage. *Nano Lett.* **15**, 2194–2202 (2015).

116. Zhang, L., Chen, L., Luo, H., Zhou, X. & Liu, Z. Large-Sized Few-Layer Graphene Enables an Ultrafast and Long-Life Aluminum-Ion Battery. *Adv. Energy Mater.* **2**, 1700034 (2017).

117. Chen, H. *et al.* Ultrafast all-climate aluminum-graphene battery with quarter-million cycle life. *Sci. Adv.* (2017).

118. Chen, H. *et al.* A Defect-Free Principle for Advanced Graphene Cathode of Aluminum-Ion Battery. *Adv. Mater.* **29**, (2017).

119. Li, Z., Niu, B., Liu, J., Li, J. & Kang, F. A Rechargeable Aluminum-Ion Battery Based on MoS2 Microsphere Cathode A Rechargeable Aluminum-Ion Battery Based on MoS 2 Microsphere Cathode. *ACS Appl. Mater. Interfaces* (2018). doi:10.1021/acsami.8b00100

120. Alhabeb, M. *et al.* Guidelines for Synthesis and Processing of Two-Dimensional Titanium Carbide (Ti3C2TxMXene). *Chem. Mater.* **29**, 7633–7644 (2017).

121. Bak, S. M. *et al.* Na-Ion Intercalation and Charge Storage Mechanism in 2D Vanadium Carbide. *Adv. Energy Mater.* **7**, 1700959 (2017).

122. Tian, W. *et al.* Layer-by-layer self-assembly of pillared two-dimensional multilayers. *Nat. Commun.* **10**, 2558 (2019).

123. Bhadra, S., Khastgir, D., Singha, N. K. & Lee, J. H. Progress in preparation, processing and applications of polyaniline. *Prog. Polym. Sci.* **34**, 783–810 (2009).

124. Yang, L. *et al.* Hierarchical MoS2/polyaniline nanowires with excellent electrochemical performance for lithium-ion batteries. *Adv. Mater.* **25**, 1180–1184 (2013).

125. Jeong, J.-M. *et al.* Hierarchical Hollow Spheres of Fe2O3@Polyaniline for Lithium Ion Battery Anodes. *Adv. Mater.* **25**, 6250–6255 (2013).

126. Xu, J., Wang, K., Zu, S. Z., Han, B. H. & Wei, Z. Hierarchical nanocomposites of polyaniline nanowire arrays on graphene oxide sheets with synergistic effect for energy storage. *ACS Nano* **4**, 5019–5026 (2010).

127. Natu, V., Clites, M., Pomerantseva, E. & Barsoum, M. W. Mesoporous MXene powders synthesized by acid induced crumpling and their use as Na-ion battery anodes. *Mater. Res. Lett.* **6**, 230–235 (2018).

128. Xue, Q. *et al.* Photoluminescent Ti 3 C 2 MXene Quantum Dots for Multicolor Cellular Imaging. *Adv. Mater.* 1604847 (2017). doi:10.1002/adma.201604847

129. Wang, H. *et al.* Surface modified MXene Ti3C2multilayers by aryl diazonium salts leading to large-scale delamination. *Appl. Surf. Sci.* **384**, 287–293 (2016).

130. Feng, X. M. *et al.* One-step electrochemical synthesis of graphene/polyaniline composite film and its applications. *Adv. Funct. Mater.* **21**, 2989–2996 (2011).

131. Gospodinova, N. & Terlemezyan, L. Conducting polymers prepared by oxidative polymerization: polyaniline. *Prog. Polym. Sci.* **23**, 1443–1484 (1998).

132. Simon, P. & Gogotsi, Y. Capacitive Energy Storage in Nanostructured Carbon-Electrolyte Systems. *Acc. Chem. Res.* **46**, 1094–1103 (2013).

133. Wang, J., Polleux, J., Lim, J. & Dunn, B. Pseudocapacitive Contributions to Electrochemical Energy Storage in TiO $_2$ (Anatase) Nanoparticles. *J. Phys. Chem. C* **111**, 14925–14931 (2007).

134. Beidaghi, M. & Gogotsi, Y. Capacitive energy storage in micro-scale devices: Recent advances in design and fabrication of micro-supercapacitors. *Energy Environ. Sci.* **7**, 867–884 (2014).

135. Yu, X. *et al.* Emergent Pseudocapacitance of 2D Nanomaterials. *Adv. Energy Mater.* **8**, 1–33 (2018).

136. Kresse, G. & Furthmüller, J. Efficient iterative schemes for ab initio total-energy calculations using a plane-wave basis set. *Phys. Rev. B - Condens. Matter Mater. Phys.* **54**, 11169–11186 (1996).

137. Joubert, D. From ultrasoft pseudopotentials to the projector augmented-wave method. *Phys. Rev. B - Condens. Matter Mater. Phys.* **59**, 1758–1775 (1999).

138. Blöchl, P. E. Projector augmented-wave method. *Phys. Rev. B* **50**, 17953–17979 (1994).

139. Perdew, J. P., Burke, K. & Ernzerhof, M. Generalized gradient approximation made simple.

Phys. Rev. Lett. **77**, 3865–3868 (1996).

140. Pack, J. D. & Monkhorst, H. J. 'special points for Brillouin-zone integrations'-a reply. *Phys. Rev. B* **16**, 1748–1749 (1977).

141. Brooks, B. R. *et al.* CHARMM: The Biomolecular Simulation Program B. *J. Comput. Chem.* **30**, 1545–1614 (2009).

142. Xie, Y. *et al.* Role of surface structure on li-ion energy storage capacity of two-dimensional transition-metal carbides. *J. Am. Chem. Soc.* **136**, 6385–6394 (2014).

143. Yu, Y.-X. Prediction of Mobility, Enhanced Storage Capacity, and Volume Change during Sodiation on Interlayer-Expanded Functionalized Ti $_3$ C $_2$ MXene Anode Materials for Sodium-Ion Batteries. *J. Phys. Chem. C* **C**, acs.jpcc.5b10366 (2016).

144. Zhang, C. J. *et al.* Oxidation Stability of Colloidal Two-Dimensional Titanium Carbides (MXenes). *Chem. Mater.* **29**, 4848–4856 (2017).

145. Lotfi, R., Naguib, M., Yilmaz, D. E., Nanda, J. & van Duin, A. C. T. A comparative study on the oxidation of two-dimensional Ti 3 C 2 MXene structures in different environments. *J. Mater. Chem. A* **199**, 393–403 (2018).

146. Lim, J., Jin, X., Jo, Y. K., Lee, S. & Hwang, S. J. Kinetically Controlled Layer-by-Layer Stacking of Metal Oxide 2D Nanosheets. *Angew. Chemie - Int. Ed.* **56**, 7093–7096 (2017).

147. Lu, K. *et al.* Cation Intercalation in Manganese Oxide Nanosheets: Effects on Lithium and Sodium Storage. *Angew. Chemie - Int. Ed.* **55**, 10448–10452 (2016).

148. Cheng, Q., Yang, T., Li, Y., Li, M. & Chan, C. K. Oxidation-reduction assisted exfoliation of LiCoO2into nanosheets and reassembly into functional Li-ion battery cathodes. *J. Mater. Chem. A* **4**, 6902–6910 (2016).

149. Shasha Zheng, Huaiguo Xue, H. P. Supercapacitors based on metal coordination materials

Shasha. *Coord. Chem. Rev.* **373**, 2–21 (2018).

150. Heising, J. & Kanatzidis, M. G. Exfoliated and restacked MoS2 and WS2: Ionic or neutral species? Encapsulation and ordering of hard electropositive cations. *J. Am. Chem. Soc.* **121**, 11720–11732 (1999).

151. Ghidiu, M. *et al.* Ion-Exchange and Cation Solvation Reactions in Ti3C2 MXene. *Chem. Mater.* **28**, 3507–3514 (2016).

152. Osti, N. C. *et al.* Effect of Metal Ion Intercalation on the Structure of MXene and Water Dynamics on its Internal Surfaces. *ACS Appl. Mater. Interfaces* **8**, 8859–8863 (2016).

153. Henkelman, G., Arnaldsson, A. & Jónsson, H. A fast and robust algorithm for Bader decomposition of charge density. *Comput. Mater. Sci.* **36**, 354–360 (2006).

154. Caffrey, N. M. Effect of mixed surface terminations on the structural and electrochemical properties of two-dimensional Ti3C2T2 and V2CT2 MXenes multilayers. *Nanoscale* **10**, 13520–13530 (2018).

155. Hu, M. *et al.* High-Capacitance Mechanism for Ti3C2TxMXene by in Situ Electrochemical Raman Spectroscopy Investigation. *ACS Nano* **10**, 11344–11350 (2016).

156. Harris, K. J., Bugnet, M., Naguib, M., Barsoum, M. W. & Goward, G. R. Direct measurement of surface termination groups and their connectivity in the 2D MXene V_2CT_x using NMR spectroscopy. *J. Phys. Chem. C* **119**, 13713–13720 (2015).

157. Acerce, M., Voiry, D. & Chhowalla, M. Metallic 1T phase MoS 2 nanosheets as supercapacitor electrode materials. *Nat. Nanotechnol.* **10**, 313–318 (2015).

158. Lu, X. *et al.* High energy density asymmetric quasi-solid-state supercapacitor based on porous vanadium nitride nanowire anode. *Nano Lett.* **13**, 2628–2633 (2013).

159. Horng, Y. Y. *et al.* Flexible supercapacitor based on polyaniline nanowires/carbon cloth with both high gravimetric and area-normalized capacitance. *J. Power Sources* **195**, 4418–4422 (2010).

160. Niu, Z. *et al.* Compact-designed supercapacitors using free-standing single-walled carbon nanotube films. *Energy Environ. Sci.* **4**, 1440–1446 (2011).

161. Xia, Q. X. *et al.* Bismuth Oxychloride/MXene symmetric supercapacitor with high volumetric energy density. *Electrochim. Acta* **271**, 351–360 (2018).

162. Huang, Y. *et al.* A carbon modified MnO2nanosheet array as a stable high-capacitance supercapacitor electrode. *J. Mater. Chem. A* **1**, 9809–9813 (2013).

163. Shpigel, N. *et al.* Direct Assessment of Nanoconfined Water in 2D Ti3C2 Electrode Interspaces by a Surface Acoustic Technique. *J. Am. Chem. Soc.* **140**, 8910–8917 (2018).

164. El-Kady, M. F. *et al.* Engineering three-dimensional hybrid supercapacitors and microsupercapacitors for high-performance integrated energy storage. *Proc. Natl. Acad. Sci.* **112**, 4233–4238 (2015).

165. Wen, Z. *et al.* Crumpled nitrogen-doped graphene nanosheets with ultrahigh pore volume for high-performance supercapacitor. *Adv. Mater.* **24**, 5610–5616 (2012).

166. Wang, L. *et al.* Flexible solid-state supercapacitor based on a metal-organic framework interwoven by electrochemically-deposited PANI. *J. Am. Chem. Soc.* **137**, 4920–4923 (2015).

167. Pang, H. *et al.* One-pot synthesis of heterogeneous Co3O4-nanocube/Co(OH)2-nanosheet hybrids for high-performance flexible asymmetric all-solid-state supercapacitors. *Nano Energy* **35**, 138–145 (2017).

168. Xiong, P., Ma, R., Sakai, N. & Sasaki, T. Genuine Unilamellar Metal Oxide Nanosheets

Confined in a Superlattice-like Structure for Superior Energy Storage. *ACS Nano* **12**, 1768–1777 (2018).

169. Xiong, P., Ma, R., Sakai, N., Nurdiwijayanto, L. & Sasaki, T. Unilamellar Metallic MoS2/Graphene Superlattice for Efficient Sodium Storage and Hydrogen Evolution. *ACS Energy Lett.* **3**, 997–1005 (2018).

170. Xiong, P., Ma, R., Wang, G. & Sasaki, T. Progress and perspective on two-dimensional unilamellar metal oxide nanosheets and tailored nanostructures from them for electrochemical energy storage. *Energy Storage Mater.* 1–18 (2018). doi:10.1016/j.ensm.2018.12.011

171. Cai, X. *et al.* Tuning the surface charge of 2d oxide nanosheets and the bulk-scale production of superlatticelike composites. *J. Am. Chem. Soc.* **137**, 2844–2847 (2015).

172. Ghidiu, M. *et al.* Alkylammonium cation intercalation into Ti3C2 (MXene) - effects on properties and ion-exchange capacity estimation. *Chem. Mater.* **2**, acs.chemmater.6b04234 (2017).

173. Shi, C. *et al.* Structure of Nanocrystalline Ti_3C_2 MXene Using Atomic Pair. *Phys. Rev. Lett.* **112**, 125501 (2014).

174. Wang, H.-W., Naguib, M., Page, K., Wesolowski, D. J. & Gogotsi, Y. Resolving the Structure of $Ti_3C_2T_x$ MXenes through Multi-Level Structural Modeling of the Atomic Pair Distribution Function. *Chem. Mater.* acs.chemmater.5b04250 (2015). doi:10.1021/acs.chemmater.5b04250

175. Champagne, A., Shi, L., Ouisse, T., Hackens, B. & Charlier, J. C. Electronic and vibrational properties of V2 C -based MXenes: From experiments to first-principles modeling. *Phys. Rev. B* **97**, 1–11 (2018).

176. Onoda, M., Liu, Z., Ebina, Y., Takada, K. & Sasaki, T. X-ray diffraction study on restacked flocculates from binary colloidal nanosheet systems Ti0.91O2-MnO2, Ca 2Nb3O10-Ti0.91O2, and Ca2Nb3O10-MnO2. *J. Phys. Chem. C* **115**, 8555–8566 (2011).

177. Jin, X. *et al.* Superior role of MXene nanosheet as hybridization matrix over graphene in enhancing interfacial electronic coupling and functionalities of metal oxide. *Nano Energy* **53**, 841–848 (2018).

178. Lipatov, A. *et al.* Elastic properties of 2D Ti $_3$ C $_2$ T $_x$ MXene monolayers and bilayers. *Sci. Adv.* **4**, eaat0491 (2018).

179. Jayaprakash, N., Das, S. K. & Archer, L. a. The rechargeable aluminum-ion battery. *Chem. Commun.* **47**, 12610 (2011).

180. Li, Q. & Bjerrum, N. J. Aluminum as anode for energy storage and conversion: A review. *J. Power Sources* **110**, 1–10 (2002).

181. Lin, M.-C. *et al.* An ultrafast rechargeable aluminium-ion battery. *Nature* **520**, 324–328 (2015).

182. Ambroz, F., Macdonald, T. J. & Nann, T. Trends in Aluminium-Based Intercalation Batteries. *Adv. Energy. Mater.* **201602093**, (2017).

183. Das, S. K. K., Mahapatra, S. & Lahan, H. Aluminium-ion Batteries: Developments and Challenges. *J. Mater. Chem. A* (2017). doi:10.1039/C7TA00228A

184. Yu, X., Wang, B., Gong, D., Xu, Z. & Lu, B. Graphene Nanoribbons on Highly Porous 3D Graphene for High-Capacity and Ultrastable Al-Ion Batteries. *Adv. Mater.* 1–8 (2016).

doi:10.1002/adma.201604118

185. Wu, Y. *et al.* 3D Graphitic Foams Derived from Chloroaluminate Anion Intercalation for Ultrafast Aluminum-Ion Battery. *Adv. Mater.* 1–5 (2016). doi:10.1002/adma.201602958

186. Wang, D.-Y. *et al.* Advanced rechargeable aluminium ion battery with a high-quality natural graphite cathode. *Nat. Commun.* **8**, 14283 (2017).

187. Gao, T. *et al.* A Rechargeable Al/S Battery with an Ionic-Liquid Electrolyte. *Angew. Chemie Int. Ed.* **55**, 9898–9901 (2016).

188. Wang, S. *et al.* A Novel Aluminum-Ion Battery: Al/AlCl3-[EMIm]Cl/Ni3S2@Graphene. *Adv. Energy Mater.* **6**, 2–11 (2016).

189. Hu, Y. *et al.* An Innovative Freeze-Dried Reduced Graphene Oxide Supported SnS $_2$ Cathode Active Material for Aluminum-Ion Batteries. *Adv. Mater.* 1606132 (2017). doi:10.1002/adma.201606132

190. Wang, S. *et al.* High-Performance Aluminum-Ion Battery with CuS@C Microsphere Composite Cathode. *ACS Nano* acsnano.6b06446 (2016). doi:10.1021/acsnano.6b06446

191. Chiku, M., Takeda, H., Matsumura, S., Higuchi, E. & Inoue, H. Amorphous Vanadium Oxide/Carbon Composite Positive Electrode for Rechargeable Aluminum Battery. *ACS Appl. Mater. Interfaces* **7**, 24385–24389 (2015).

192. Wang, H. *et al.* Binder-free V2O5 cathode for greener rechargeable aluminum battery. *ACS Appl. Mater. Interfaces* **7**, 80–84 (2015).

193. Gu, S. *et al.* Confirming reversible Al3+ storage mechanism through intercalation of Al3+ into V2O5 nanowires in a rechargeable aluminum battery. *Energy Storage Mater.* **6**, 9–17 (2017).

194. Wang, H. *et al.* Anion-effects on electrochemical properties of ionic liquid electrolytes for

rechargeable aluminum batteries. *J. Mater. Chem. A* **3**, 22677–22686 (2015).

195. Geng, L., Lv, G., Xing, X. & Guo, J. Reversible Electrochemical Intercalation of Aluminum in Mo_6S_8. *Chem. Mater.* **27**, 4926–4929 (2015).

196. Reed, L. D., Ortiz, S., Xiong, M. & Menke, E. J. A Rechargeable Aluminum-ion Battery Utilizing a Copper Hexacyanoferrate Cathode in an Organic Electrolyte. *Chem. Commun.* **51**, 1–4 (2015).

197. Hudak, N. & Ingersoll, D. Conductive Polymers as Positive Electrodes in Rechargeable Aluminum Batteries. *223rd ECS Meet. (May 12-17, 2013)* 2013 (2013).

198. Wang, W. *et al.* A new cathode material for super-valent battery based on aluminium ion intercalation and deintercalation. *Sci. Rep.* **3**, 3383 (2013).

199. Come, J. *et al.* A Non-Aqueous Asymmetric Cell with a Ti2C-Based Two-Dimensional Negative Electrode. *J. Electrochem. Soc.* **159**, A1368–A1373 (2012).

200. Chen, J. *et al.* CO2 and temperature dual responsive 'Smart' MXene phases. *Chem. Commun.* **51**, 314–7 (2015).

201. Takahashi, S., Koura, N., Kohara, S., Saboungi, M.-L. & Curtiss, L. a. Technological and scientific issues of room-temperature molten salts. *Plasmas Ions* **2**, 91–105 (1999).

202. Geng, L. *et al.* Titanium Sulfides as Intercalation-Type Cathode Materials for Rechargeable Aluminum Batteries. *ACS Appl. Mater. Interfaces* **9**, 21251–21257 (2017).

203. Jiang, J. *et al.* Investigation of the Reversible Intercalation/Deintercalation of Al into the Novel Li3VO4@C Microsphere Composite Cathode Material for Aluminum-Ion Batteries. *ACS Appl. Mater. Interfaces* **9**, 28486–28494 (2017).

204. Okubo, M. *et al.* Nanosize effect on high rate Li-ion intercalation in $LiCoO_2$ electrode. *J. Am. Chem. Soc.* **129**, 7444–7452 (2007).

205. Hu, Z., Liu, Q., Chou, S.-L. & Dou, S.-X. Advances and Challenges in Metal Sulfides/Selenides for Next-Generation Rechargeable Sodium-Ion Batteries. *Adv. Mater.* **1700606**, 1700606 (2017).

206. Liu, F. *et al.* Preparation of High-Purity V $_2$ C MXene and Electrochemical Properties as Li-Ion Batteries. *J. Electrochem. Soc.* **164**, A709–A713 (2017).